

ADA 081 949

AFML-TR-79-4131

LEVEL

2
B.S.

**FATIGUE RESISTANT ALUMINUM
P/M ALLOY DEVELOPMENT**

*R. E. SANDERS, JR.
W. L. OTTO, JR.
R. J. BUCCI*

*ALUMINUM COMPANY OF AMERICA
ALCOA TECHNICAL CENTER
ALCOA CENTER, PA 15069*

1979 SEPTEMBER

TECHNICAL REPORT AFML-TR-79-4131
Final Report for Period 1977 September — 1979 September

DTIC
TE
MAR 13 1980
C

Approved for public release; distribution unlimited.

DDC FILE COPY

AIR FORCE MATERIALS LABORATORY
AIR FORCE WRIGHT AERONAUTICAL LABORATORIES
AIR FORCE SYSTEMS COMMAND
WRIGHT-PATTERSON AIR FORCE BASE, OHIO 45433

80 3 7 054

NOTICE

When Government drawings, specifications, or other data are used for any purpose other than in connection with a definitely related Government procurement operation, the United States Government thereby incurs no responsibility nor any obligation whatsoever; and the fact that the government may have formulated, furnished, or in any way supplied the said drawings, specifications, or other data, is not to be regarded by implication or otherwise as in any manner licensing the holder or any other person or corporation, or conveying any rights or permission to manufacture, use, or sell any patented invention that may in any way be related thereto.

This report has been reviewed by the Information Office (OI) and is releasable to the National Technical Information Service (NTIS). At NTIS, it will be available to the general public, including foreign nations.

This technical report has been reviewed and is approved for publication.

Walter M. Griffith

WALTER M. GRIFFITH, Project Engineer
Structural Metals Branch
Metals & Ceramics Division

FOR THE COMMANDER

L. R. Bidwell

LAWRENCE R. BIDWELL, ACTG CHIEF,
Structural Metals Branch
Metals & Ceramics Division

"If your address has changed, if you wish to be removed from our mailing list, or if the addressee is no longer employed by your organization please notify AFML/LLS, W-PAFB, OH 45433 to help us maintain a current mailing list."

Copies of this report should not be returned unless return is required by security considerations, contractual obligations, or notice on a specific document.

UNCLASSIFIED

SECURITY CLASSIFICATION OF THIS PAGE (When Data Entered)

19 REPORT DOCUMENTATION PAGE		READ INSTRUCTIONS BEFORE COMPLETING FORM
1. REPORT NUMBER 18 AFML-TR-79-4131	2. GOVT ACCESSION NO.	3. RECIPIENT'S CATALOG NUMBER
4. TITLE (and Subtitle) 6 FATIGUE RESISTANT ALUMINUM P/M ALLOY DEVELOPMENT	5. TYPE OF REPORT & PERIOD COVERED 9 FINAL TECHNICAL REPORT SEP 1977-SEP 1979	6. PERFORMING ORG. REPORT NUMBER 14 56-79-AF11
7. AUTHOR(s) 10 B. E. SANDERS, JR. O. OTTO, JR. R. J. BUCCI	8. CONTRACT OR GRANT NUMBER(s) 15 F33615-77-C-5174	
9. PERFORMING ORGANIZATION NAME AND ADDRESS ALUMINUM COMPANY OF AMERICA ALCOA TECHNICAL CENTER ALCOA CENTER, PA 15069	10. PROGRAM ELEMENT, PROJECT, TASK AREA & WORK UNIT NUMBERS 16 24180104 17 01	
11. CONTROLLING OFFICE NAME AND ADDRESS AIR FORCE MATERIALS LABORATORY AIR FORCE SYSTEMS COMMAND WRIGHT-PATTERSON AIR FORCE BASE, OH 45433	12. REPORT DATE 1979 SEPTEMBER	13. NUMBER OF PAGES 176 11 Sep 79
14. MONITORING AGENCY NAME & ADDRESS (if different from Controlling Office) 12 277	15. SECURITY CLASS. (of this report) UNCLASSIFIED	
16. DISTRIBUTION STATEMENT (of this Report) APPROVED FOR PUBLIC RELEASE; DISTRIBUTION UNLIMITED.		
17. DISTRIBUTION STATEMENT (of the abstract entered in Block 20, if different from Report)		
18. SUPPLEMENTARY NOTES		
19. KEY WORDS (Continue on reverse side if necessary and identify by block number) 7XXX aluminum alloys Fatigue crack growth Powder metallurgy CT91 Microstructure Residual stresses Forging Crack closure Extrusion DELTA - Square root of M		
20. ABSTRACT (Continue on reverse side if necessary and identify by block number) An investigation was undertaken to study the effects of fabrication practice, alloy chemistry, aging treatment, and residual stress relief on the fatigue crack growth (FCG) resistance of 7XXX P/M hand forgings and extrusions. Testing was performed in both humid air (R.H. > 90%) and salt fog atmosphere. FCG rates of the P/M extrusions were slightly higher than those of a 7050-T76511 control material at ΔK values below 4 MPa \sqrt{m} . From 4-10 MPa \sqrt{m} , FCG resistance of the P/M extrusions were approximately equivalent to those of the 7050 control. Overaging was beneficial to the FCG resistance of the P/M		

DD FORM 1473 EDITION OF 1 NOV 68 IS OBSOLETE
1 JAN 73

UNCLASSIFIED

SECURITY CLASSIFICATION OF THIS PAGE (When Data Entered)

409868

UNCLASSIFIED

SECURITY CLASSIFICATION OF THIS PAGE(When Data Entered)

20. extrusions. Scatter in the FCG data for the hand forgings prevented any definite conclusions regarding effects of chemistry or aging treatment on crack growth in these materials. FCG testing of stress-relieved and nonstress-relieved forgings showed that compressive residual stresses can markedly affect effective ΔK levels and measured FCG rates. The introduction of crack closure concepts to the data analysis allowed for a computation of effective ΔK values to correct for the presence of residual stresses in FCG specimens.

DELTA

PREFACE

This investigation was performed for the Air Force Materials Laboratory, Wright-Patterson Air Force Base, Ohio, under Contract No. F33615-77-C-5174. Mr. W. M. Griffith served as contract monitor for the Air Force.

The experimental design for the program was conceived and the investigation initiated under the direction of Mr. R. R. Sawtell and Mr. J. T. Staley of the Alloy Technology Division. Mr. D. A. Mauney served as project manager for the latter part of the investigation. The experimental efforts of Messrs W. R. Graff, P. H. Jacobus, and B. J. Johnson are gratefully acknowledged.

Accession For	
NTIS GPO	<input checked="" type="checkbox"/>
DOC TAB	<input type="checkbox"/>
Unannounced	<input type="checkbox"/>
Justification	
By _____	
Distribution/	
Availability Codes	
Dist	Avail and/or special
A	

TABLE OF CONTENTS

	<u>Page</u>
INTRODUCTION-----	1
MATERIALS AND PROCEDURES-----	2
POWDER PREPARATION-----	2
BILLET COMPACTION-----	3
EXTRUSION-----	4
FORGING-----	5
HEAT TREATMENT-----	6
MECHANICAL PROPERTY EVALUATION-----	7
MICROSTRUCTURE-----	9
PHASE I-----	9
RESULTS-----	9
Tensile Properties-----	9
Fatigue Crack Growth-----	10
Microstructure-----	11
DISCUSSION-----	13
PHASE II-----	14
RESULTS-----	14
Tensile Properties-----	14
Fatigue Crack Growth-----	15
Microstructure-----	16
Fractography-----	16
DISCUSSION-----	17
Microstructure and FCG Resistance of High-Strength 7XXX Alloys-----	19
PHASE III-----	25
BACKGROUND-----	25
EXPERIMENTATION-----	27
RESULTS-----	30
Residual Stresses - Parent Slab-----	30
Mechanical Properties-----	31
Fatigue Crack Growth-----	32
Residual Stresses in CT FCG Specimens---	33

TABLE OF CONTENTS (CONTINUED)

	<u>Page</u>
DISCUSSION-----	34
CONCLUSIONS-----	38
PHASE I-----	38
PHASE II-----	39
PHASE III-----	40
REFERENCES-----	42
TABLES-----	44
FIGURES-----	60
APPENDIX-----	137

LIST OF ILLUSTRATIONS

<u>No.</u>		<u>Page</u>
1.	Schematic diagram of 21.4 cm hot compacting cylinder-----	60
2.	Sectioning layout for testing of Phase I hot-pressed billets-----	61
3.	Extrusion load versus ram displacement for Phase I P/M extrusions-----	62
4.	Forging sequence for production of A-upset and draw hand forgings-----	63
5.	Forging sequence for production of ABC-upset and draw hand forgings-----	64
6.	Slabs removed from Phase III A-upset and draw hand forgings for subsequent heat treatment and mechanical testing-----	65
7.	CCT specimen geometry used for Phase I and Phase II fatigue crack growth tests, L-T orientation----	66
8.	Fatigue crack growth data for Phase I hand forgings tested in salt fog atmosphere-----	67
9.	Fatigue crack growth data for Phase I extrusions tested in salt fog atmosphere-----	68
10.	Fatigue crack growth data for T-L specimens from Phase I A-upset and draw hand forgings tested in humid air-----	69
11.	Fatigue crack growth data for T-L specimens from Phase I medium Z extrusions tested in humid air---	70
12.	Scanning electron micrographs of as-atomized alloy 0.4 Co (CT91) powder-----	71
13.	Optical micrograph of polished and etched atomized CT91 powder particles-----	72
14.	Optical microstructure of P/M billet, S-356452, 0.0 Co-----	73
15.	Optical microstructure of P/M billet, S-356453, 0.4 Co (CT91)-----	74
16.	Optical microstructure of P/M billet, S-356454, 0.3 Co-----	75

LIST OF ILLUSTRATIONS (CONTINUED)

<u>No.</u>		<u>Page</u>
17.	Optical microstructure of P/M billet, S-356455, blend-----	76
18.	Optical microstructure of 0.0 Co A-upset and draw hand forging, S-356452-2T-----	77
19.	Optical microstructure of 0.0 Co ABC-upset and draw hand forging, S-356452-3T-----	78
20.	Optical microstructure of 0.4 Co A-upset and draw hand forging, S-356453-2T (CT91)-----	79
21.	Optical microstructure of 0.4 Co ABC-upset and draw hand forging, S-356453-3T (CT91)-----	80
22.	Optical microstructure of 0.8 Co A-upset and draw hand forging, S-356454-2T-----	81
23.	Optical microstructure of 0.8 Co ABC-upset and draw hand forging, S-356454-3T-----	82
24.	Optical microstructure of blended powder A-upset and draw hand forging, S-356455-2T-----	83
25.	Optical microstructure of blended powder ABC-upset and draw hand forging, S-356455-3T-----	84
26.	Optical microstructure of 0.0 Co medium Z extrusion, S-356452-6G-----	85
27.	Optical microstructure of 0.4 Co medium Z extrusion, S-356453-6G (CT91)-----	86
28.	Optical microstructure of 0.8 Co medium Z extrusion, S-356454-5G-----	87
29.	Optical microstructure of blended powder medium Z extrusion, S-356455-5G-----	88
30.	Longitudinal micrographs of Phase I high and low Z extrusions-----	89
31.	Transmission electron micrographs of Phase I high Z extrusions in T7X1 temper-----	91
32.	Pole figures showing degree of preferred orientation for CT91 hot-pressed billet, S-356453-----	93

LIST OF ILLUSTRATIONS (CONTINUED)

<u>No.</u>	<u>Page</u>
33. Pole figures showing degree of preferred orientation for CT91 A-upset and draw hand forging, S-356453-2T-----	94
34. Pole figures showing degree of preferred orientation for CT91 ABC-upset and draw hand forging, S-356453-3T-----	95
35. Pole figures showing degree of preferred orientation for CT91 high Z extrusion, S-356453-4AG-----	96
36. Pole figures showing degree of preferred orientation for CT91 low Z extrusion, S-356453-7G-----	97
37. Rockwell B hardness versus second-step aging time at 163°C (325°F) for Phase II extrusions-----	98
38. Electrical conductivity versus second-step aging time at 163°C (325°F) for Phase II extrusions-----	99
39. Fatigue crack growth data for Phase II hand forgings tested in humid air-----	100
40. Fatigue crack growth data for Phase II extrusions tested in humid air-----	101
41. Fatigue crack growth data for Phase II hand forgings tested in salt fog atmosphere-----	102
42. Fatigue crack growth data for Phase II extrusions tested in salt fog atmosphere-----	103
43. Optical microstructure of MA88 A-upset and draw hand forging, S-493706-----	104
44. Optical microstructure of MA90 A-upset and draw hand forging, S-493705-----	105
45. Optical microstructure of MA88 extrusion, S-493706-1G-----	106
46. Optical microstructure of MA90 extrusion, S-493705-1G-----	107
47. Optical microstructure of commercially-produced 7050-T76511 extrusion-----	108

LIST OF ILLUSTRATIONS (CONTINUED)

<u>No.</u>	<u>Page</u>
48. Macrophotographs of fractured FCG specimens from salt fog tests-----	109
49. Fractographs of CT91 extrusion FCG specimens tested in salt fog atmosphere-----	110
50. Fractographs of MA88-T7X2 and MA90-T7X2 extrusion FCG specimens tested in salt fog atmosphere-----	111
51. Fractographs of 7050-T76511 FCG specimens tested in salt fog atmosphere-----	113
52. Schematic diagram of monotonic plastic zone size (r_p) as a function of ΔK -----	114
53. Micrographs depicting monotonic plastic zone size relative to microstructural feature size-----	115
54. FCG data for short-transverse specimens taken from P/M hand forgings, Reference 3-----	117
55. Residual stress distribution in 7075 cylinder quenched in cold water spray-----	118
56. Proposed explanation for observed effect of specimen type on FCG rates established from nonstress-relieved 7XXX P/M extruded rod-----	119
57. Location of Phase III test specimens and residual stress measurements in parent slab-----	120
58. Location and orientation of X-ray residual stress measurements on FCG test specimens-----	121
59. Effect of residual stresses on load-COD trace in bulk material surrounding the crack tip-----	122
60. Location of displacement measurements in CT specimen blanks simulating FCG by progressive sawcuts-----	123
61. Average residual stress measurements in parent slabs-----	124
62. Through-thickness residual stress distribution which causes crack curvature in nonstress- relieved materials-----	125

LIST OF ILLUSTRATIONS (CONTINUED)

<u>No.</u>	<u>Page</u>
63. Effect of stress relief on S-L FCG rates in MA87-T7X2 hand forging-----	126
64. Effect of stress relief on S-L FCG rates in 7XXX-T7X2 hand forging-----	127
65. Comparison of S-L FCG rates in stress-relieved P/M and I/M hand forgings-----	128
66. Typical residual stress distribution on rectangular section "A-A"-----	129
67. Effect of longitudinal residual stress on FCG measurement in S-L CT specimen taken from non-stress-relieved material-----	130
68. Stress redistribution following sawcuts to simulate a propagating crack-----	131
69. Characteristic load-COD traces established on stress-relieved and nonstress-relieved P/M FCG specimens-----	133
70. Characteristic load-COD traces established on stress-relieved and nonstress-relieved I/M FCG specimens-----	134
71. Corrected FCG rates in nonstress-relieved P/M hand forgings-----	135
72. Corrected FCG rates in nonstress-relieved I/M hand forgings-----	136

LIST OF TABLES

<u>No.</u>		<u>Page</u>
1.	Melt Analysis-----	44
2.	Powder Size and Distribution-----	45
3.	Extrusion Conditions - Phases I, II-----	46
4.	Tensile and Notch Tensile Properties of Hot Pressed Billets-----	47
5.	Uniaxial Tensile Properties of P/M Billets-----	48
6.	Uniaxial Tensile Properties of P/M Forgings-----	49
7.	Uniaxial Tensile Properties of P/M Extrusions-----	50
8.	Cyclic Lives of P/M Billets Over Various Regimes of Crack Growth-----	51
9.	Cyclic Lives of P/M Forgings Over Various Regimes of Crack Growth-----	52
10.	Cyclic Lives of P/M Extrusions Over Various Regimes of Crack Growth-----	53
11.	Results of Aging Study for Selection of Alloy Tempers for Phase II Extrusions-----	54
12.	Tensile Properties of Phase II Materials-----	55
13.	Crack Lengths at Fracture for CCT Specimens from Phase II Hand Forgings-----	56
14.	Calculated Plane Strain Monotonic Plastic Zone Sizes for Experimental Materials-----	57
15.	Short-Transverse Mechanical Properties of Phase III Hand Forgings-----	58
16.	Average X-ray Residual Stress Indications on FCG Specimens-----	59

SUMMARY

PHASE I

Forgings and extrusions fabricated for Phase I showed similar tensile properties, FCG resistance, and microstructures, regardless of Co content or fabrication practice (A vs ABC forging, or "Z" level for extrusions). The Phase I billets displayed lower FCG resistance, particularly at high ΔK levels, due to the low degree of hot deformation received during hot pressing. Compared to the 7050 control material, Phase I extrusions tested in salt fog had somewhat higher da/dN values at low ΔK values. Above $4 \text{ MPa}\sqrt{\text{m}}$, however, data for the P/M extrusions fell mostly within the scatterband for commercial 7050-T76511 extrusions.

PHASE II

FCG testing of Phase II materials showed that changes in alloy chemistry had no significant effects on crack growth rates in salt fog or humid air over the range of ΔK levels studied. Overaging the materials to a lower strength T7X2 temper measurably increased FCG resistance of the P/M extrusions. Scatter in the data obtained for Phase II hand forgings prevented an accurate assessment of alloy chemistry and temper effects on FCG in these materials.

The microstructural characteristics in both P/M and I/M materials were discussed in order to analyze their possible effects on FCG mechanisms. The discussion was based on a comparison of feature size to monotonic plastic zone

size (r_p) at various levels of ΔK . When r_p was significantly larger than the size of the basic microstructural unit, grain or subgrain size, the material behaved as a continuum and microstructure had virtually no effect on FCG. At lower levels of ΔK , where r_p was small, it was felt that the inhomogeneous structures of I/M materials could act to divert fatigue cracks from their macroscopic growth direction, leading to lower da/dN values. The fine, uniform P/M microstructures, however, offered no features to divert the growing fatigue crack, and led to higher observed crack growth rates at low stress intensities.

PHASE III

High residual stresses were mainly responsible for early data which showed extremely slow FCG rates in P/M alloys. Though FCG data were established in accordance with ASTM recommended practice (E647-78T), failure to recognize influence of residual stresses was shown to give misleading interpretation of results in nonstress-relieved materials. The introduction of crack closure concepts to the data interpretation brought nonstress-relieved results more in line with data from stress-relieved materials.

Comparison of CT specimen FCG rates from stress-relieved P/M and I/M Phase III forgings indicated comparable FCG resistance for both materials at $2.5 \text{ MPa}\sqrt{\text{m}}$, slightly better I/M resistance at intermediate ΔK , and higher resistance for P/M at ΔK levels greater than $10 \text{ MPa}\sqrt{\text{m}}$.

Though FCG data established by the chosen test procedure for stress-relieved forgings are more representative of commercial product behavior, some caution is still warranted in the quantitative ranking of P/M vs I/M performance. Reasons cited for the needed caution were: (1) differences in fracture surface morphology that result in different ΔK_{EFF} in the two materials for identical applied ΔK ; and (2) incomplete residual stress removal in stress-relieved samples.

INTRODUCTION

The development of powder metallurgy (P/M) technology at Alcoa Laboratories has resulted in the production of 7XXX aluminum alloys with superior combinations of strength and corrosion resistance compared to alloys produced by conventional ingot metallurgy (I/M) techniques (1,2). At equivalent levels of stress-corrosion cracking resistance, P/M alloys have been shown to exhibit equivalent fracture toughness, with higher strength and exfoliation resistance than the high performance I/M alloys 7050 and 7475 (2,3). P/M alloys CT90 and CT91 have been developed as potential candidates for a wide variety of aerospace applications including forgings, extrusions, and rolled plate (4).

The purpose of this AFML-sponsored investigation is to determine the interrelationships among fabrication practice, microstructure, and fatigue crack growth resistance of high-strength 7XXX P/M alloys similar to alloy CT91 (formerly MA87). The original design of the present program was based on data generated by AFML Contract No. F33615-74-C-5077. The results of this investigation, reported in AFML TR-76-60, showed that hand forgings fabricated by an ABC upset and draw sequence exhibited markedly slower fatigue crack growth (FCG) rates in dry air at cyclic stress intensities below $11 \text{ MPa}/\sqrt{\text{m}}$ than standard I/M alloys such as 7050 (3). Furthermore, Co content and fabrication practice were shown to affect FCG rates in P/M extrusions (3).

Initial results of the present program were unable to reproduce the dramatic improvements in FCG rates documented in AFML TR-76-60. Humid air testing of P/M alloys showed only marginally slower FCG rates than I/M 7075. A detailed re-evaluation of the fabrication practices used for the original materials (AFML TR-76-60) revealed that the hand forgings had not been stress-relieved following quenching, and hence, probably contained large residual quenching stresses. The compressive stress-relief operation applied to the forgings tested in the current program were thought to produce lower, and more uniform, residual stresses. Consequently, it was determined to redesign the program in order to: (1) fully evaluate the effects of residual stresses on FCG rates in these materials, and (2) study changes in composition and alloy temper which may yield improved FCG resistance in P/M alloys.

The redesigned program was organized into three phases: Phase I, which evaluated effect of Co content and distribution; Phase II, which studied effects of Zn/Mg ratio, Cu content, and aging treatment; and Phase III, designed to study the effects of residual stresses on FCG rates in hand forgings. This report serves to describe the results of the completed investigation.

MATERIALS AND PROCEDURE

POWDER PREPARATION

Four types of powders were prepared for use in Phase I. The first three powder lots were prepared by air atomizing alloy melts with an aim base composition of 6.5 wt% Zn, 2.5 wt% Mg,

and 1.5 wt% Cu and nominal Co additions of 0.0, 0.4, or 0.8 wt%. Average melt analyses for these powders are shown in Table 1. The fourth powder lot was produced by blending equal amounts of the 0.0 and 0.8% Co powders to yield a nominal 0.4% Co level. Particle size distributions from samples of each powder lot, as determined by a U.S. standard screen analysis, and APD measurements from a Fisher Sub-Sieve Sizer are presented in Table 2.

Two Al-Zn-Mg-Cu-Co alloy powder lots were air atomized for the second phase of the program. The melt analyses and powder size descriptions are shown in Tables 1 and 2, respectively. These alloys represent variations in zinc (S493705) and copper (S493706) relative to the base CT91 alloy composition of Al-6.5 Zn-2.5 Mg-1.5 Cu-0.4 Co. All of the alloys had a 0.40 weight percent nominal cobalt content.

One powder lot of the CT91 composition without cobalt was air atomized for Phase III of the program. Tables 1 and 2 show the melt analysis and particle size information for the powder. A 22.9 cm diameter ingot of the cobalt-free CT91 composition with a Cr addition was cast using the direct chill technique. The melt analysis of the ingot is included in Table 1. The cast ingot was homogenized at 471°C for 48 hours prior to scalping to 18.4 cm diameter.

BILLET COMPACTION

Portions of each powder lot were cold isostatically pressed at 207 MPa in a wet bag system to form 66 Kg cylindrical compacts, 18.7 cm diameter by 109.2 cm long. Cold pressed density was ~75% of theoretical.

The cold compacts were encapsulated in a welded 3003 aluminum alloy can and preheated to 521°C using a dynamic vacuum level of 10 μm of Hg. Total preheat cycle time ranged from 7.0 to 8.0 hr with about 1 hr at 521°C±2.8°C. At completion of the preheat cycle, the compacts were removed from the furnace and the evacuation lines were sealed. The compacts were then hot pressed in a closed end compaction cylinder (Figure 1) at a nominal axial pressure of 621 MPa which was maintained for one minute. The hot pressed compacts were then air cooled to room temperature and scalped to 18.4 cm diameter.

Problems in maintaining vacuum were encountered in the preheat-hot press cycle of S356454-3. Consequently, this billet was cooled to room temperature, the can rewelded, and reheated.

One billet of each Phase I composition was sectioned for evaluation in the as-hot pressed condition. Two slabs, 3.8 cm thick and 33 cm long, were removed as shown in Figure 2. The remaining billets were extruded or forged as described below.

EXTRUSION

Three hot pressed billets of each composition were extruded to a 1.3 cm x 16.5 cm cross-section bar using a 23.5 cm diameter extrusion cylinder. Extrusion conditions corresponded to three levels of temperature compensated strain rate (Z), namely, 4.3×10^8 , 2.5×10^{10} , and 1.50×10^{12} cm/cm-sec. The values of Z were calculated from the expression:

$$Z = \dot{\epsilon} \exp \frac{H}{RT}$$

where: $\dot{\epsilon}$ = average strain rate,
H = activation energy for self diffusion,
R = universal gas constant,
T = average billet temperature.

The extrusion parameters corresponding to the three Z levels are shown in Table 3. The extrusion ram loads and displacements were continuously recorded for each extrusion. Typical load displacement plots for extrusions at the three Z levels are shown in Figure 3. Extrusion press capacity limitations required that the high Z (1.5×10^{12} cm/cm-sec) extrusions be produced from 33 cm billet lengths; therefore, duplicate extrusions were fabricated for each alloy. The remaining extrusions were produced from 66 cm long billets.

The load-displacement history for each extrusion was examined to select portions of each bar representative of steady-state extrusion.

One extrusion of the 1.3 cm x 16.5 cm cross-section was produced for each of the Phase II alloys. Extrusion conditions corresponding to the 2.5×10^{10} cm/cm-sec temperature compensated strain rate were used.

FORGING

Two hot pressed billets of each composition were forged into a 5.1 cm x 17.8 cm x 99.1 cm slab by both an A-upset and draw and an ABC upset and draw forging sequence, as depicted in Figures 4 and 5. The initial billet temperatures were 371°C with 260°C die temperatures. The workpiece temperature increased initially

during upset forging to 387°C and decayed to 371°C at the end of the squaring operation. The workpiece temperature continued to decay to 327°C during draw forging to 6.4 cm for the A dimension. The forgings were reheated to 371°C prior to finish forging to the slab configuration. Final workpiece temperatures were approximately 327°C at the completion of forging.

The A-upset and draw forging sequence was used to fabricate each of the Phase II alloys to the 5.1 cm x 17.8 cm x 99.1 cm slab configuration. Temperature histories similar to the Phase I forging process were observed.

Both the P/M and I/M alloys of Phase III were forged by the A-upset and draw sequence to a 10.2 cm x 15.2 cm x 55.9 cm slab configuration (see Figure 6). Processing temperatures comparable to that of Phase I were used. Each forging was sectioned per Figure 6 prior to final heat treatment.

HEAT TREATMENT

Portions of each billet, slab, extrusion, and forging were solution heat treated 2 hr at 488°C and quenched in cold running water. The billets, slabs, and forgings were then compressed ~2.0% permanent set in the short dimension for relief of residual quenching stresses. The extrusions were stretched ~2.0% permanent set in the longitudinal direction after quenching, also for stress relief. Each of the products was subsequently aged four days at room temperature followed by artificial aging at 121°C for 24 hours. Portions of the products were aged for additional times at 163°C to bring them to desired levels of

strength and conductivity. Final temper selections for the forgings and extrusions were designated T7X1 for the higher strength condition and T7X2 for the more overaged temper (Table 11).

Prior to solution heat treatment (SHT) of the Phase III materials, two 3.8 cm (1.5 in.) thick slabs were removed at the short transverse-longitudinal plane of the forging, as shown in Figure 6. After SHT and quench, one of the two pieces was compressively stress relieved by 3 to 5% permanent reduction in the shortest dimension (3.8 cm) of the slab. Each slab was then aged to the T7X1 temper. With exception of the stress relief, this procedure reproduced the fabrication history of the P/M A-upset and draw material of the previous AFML-sponsored program (3).

MECHANICAL PROPERTY EVALUATION

In an attempt to assess billet quality, uniaxial and notched tensile properties of heat treated samples were determined in the radial direction of the hot-compacted materials. Samples were aged 24 hours at 121°C + 14 hours at 163°C prior to testing. The tensile tests were performed in accordance with ASTM E8-69 using 0.64 cm diameter round specimens. Notched tensile properties were obtained using 1.27 cm diameter round specimens in accordance with ASTM E602-76-T.

The results of these tests are shown in Table 4. Only one billet, 356452-4, developed an abnormally low NTS/YS ratio. The poor toughness of this material probably resulted from a loss of vacuum before or during the hot compaction operation. This billet was extruded and heat treated before the test results were available and could not be replaced.

Longitudinal tensile properties of the billets, extrusions, and hand forgings were determined using 0.91 cm diameter round specimens as per ASTM E8-69.

Fatigue crack growth (FCG) tests were performed using center-cracked specimens 10.2 cm wide and 0.64 cm thick. Specimens produced for measurement of L-T crack growth properties were 37.6 cm in length as shown in Figure 7. T-L specimens were as long as the width of the wrought products: 16.5 cm for the extrusions and 17.8 cm for the hand forgings. Tests were conducted under constant amplitude loading in salt fog or high humidity (R.H. >90%) air. A minimum stress/maximum stress (R) ratio of 1/3 was used for all tests. Crack length was measured either visually or through the use of continuity-type crack propagation grids spaced 0.25 cm apart. Crack lengths were monitored between 1.02 cm and 3.3 cm.

In order to allow more efficient analysis of the Phase I data, the raw crack length versus cycles (a vs N) data were fitted using a least squares cubic spline function with three knot points. This function allowed for the calculation of cyclic lives over a given range of crack growth and for the determination of FCG rates (da/dN). Since different loading conditions were used for many of the tests later in the program, these data were analyzed and reported as plots of log da/dN versus log ΔK , where ΔK represents the cyclic stress intensity range during a fatigue cycle.

Experimental procedures and techniques used for the determination of residual stresses and FCG data in Phase III are described in a later section of this report.

MICROSTRUCTURE

Microstructures of the finished products were examined using standard optical and transmission electron metallographic (TEM) procedures. For optical examination of the wrought P/M products, an etchant of 84.0 ml H₂O, 15.5 ml HNO₃, 0.5 ml HF, and 3.0 g CrO₃ was found to be preferable to the traditionally used Keller's reagent. Scanning electron microscopy (SEM) was used for examination of atomized powders and fatigue specimen fracture surfaces. An automated X-ray texture goniometer was used to obtain data on preferred orientation in the wrought P/M products.

PHASE I

RESULTS

Tensile Properties

Uniaxial tensile properties of the billets, forgings, and extrusions fabricated for Phase I are shown in Tables 5, 6, and 7, respectively. Average yield and tensile strengths for the hot-pressed billets and hand forgings were approximately equal. Ductility values, as evidenced by both elongation and R.A., were significantly higher for the hand forgings than for the billets. Average strengths for the extrusions were 41 to 55 MPa (6-8 ksi) higher than for the forgings or billets. Co content, forging sequence (A vs ABC), or extrusion parameters,

as measured by "Z," did not appear to affect strength or ductility of the P/M materials.

Fatigue Crack Growth

Initial results of Phase I FCG tests in humid air covered cyclic stress intensity ranges (ΔK) from approximately 6 to 15 MPa \sqrt{m} . Since these test conditions produced unexpectedly high FCG rates ($>10^{-5}$ cm/cycle), loads were reduced for subsequent testing of Phase I materials. These tests employed lower applied ΔK values and resulted in FCG rates in the range of 10^{-5} to 10^{-3} cm/cycle.

Results of the humid air FCG tests are summarized in Tables 8 through 10. Crack length versus number of cycles for individual tests are shown in Appendix I. These data show that no significant differences in FCG resistance existed among the forgings or extrusions fabricated in the program. The cyclic lives of the billets tended to decrease with increasing Co content and were, on average, significantly shorter than lives for the forgings or extrusions.

Figures 8 and 9 show FCG results for Phase I materials tested in a salt fog environment. In these tests, changes in Co content had no significant effect on FCG resistance of A upset and draw hand forgings (Figure 8) or medium Z extrusions (Figure 9). No salt fog FCG testing of Phase I billets was performed. Results of FCG tests of T-L specimens taken from alloys 356453 (0.4 Co) and 356454 (0.8 Co) are shown in Figures 10 ("A" hand forgings) and 11 (medium Z extrusions).

Microstructure

Scanning electron micrographs of typical CT91 atomized powder particles are shown in Figure 12. The as-atomized powders were fine (APD $\sim 13 \mu\text{m}$) and irregular in shape. Extremely fine dendritic structures were produced during solidification of these powders as shown by the optical microstructures in Figure 13. The dendrite arm spacings ($\sim 0.5 \mu\text{m}$) generally observed in the atomized powders produced in this program are indicative of cooling rates in the 10^5 - 10^6 °C/sec range (5).

Consolidation and subsequent fabrication of the atomized powders resulted in products with extremely fine microstructures such as those shown in Figures 14 through 30. The structures of the billets, Figures 14 through 17, were considerably coarser than those of the wrought products, showing evidence of prior powder particle boundaries in the hot-pressed condition. The forgings and extrusions were mostly unrecrystallized, with extremely fine, elongated structural features. The dimensions of these features were 1-5 μm in the ST direction, up to 30 μm in the LT direction, and varied widely in the longitudinal direction.

The microstructures of the hand forgings were relatively nonuniform and exhibited more variability than seen for the extrusions. The structures of the A-upset and draw forgings were considerably finer as Co content increased from 0.0 to 0.8 percent. Evidence of recrystallization was seen in some of the lower Co forgings, e.g., Figures 18 and 21. The microstructures of the

medium Z extrusions were fine and uniform, making it extremely difficult to distinguish between grains and subgrains at optical magnifications. Increasing Co content from 0.0 to 0.8 percent produced finer structures. However, the effect was not as pronounced as observed for the "A" type hand forgings. Figure 30 shows that temperature-compensated strain rate (Z) also affected the structures of the P/M extrusions. The low Z extrusions consistently had coarser microstructures than the high Z materials, regardless of Co content or distribution. The fine microstructures of these materials again made it difficult to determine the exact nature of these structural differences. Such observations probably reflect either an increased amount of recrystallization or a different type of recovered substructure in extrusions fabricated at the higher extrusion temperature (low Z).

Typical structures observed by TEM of the Phase I wrought products in the T7X1 temper are shown in Figure 31. Readily apparent in these micrographs are Co_2Al_9 particles, oxides, and strengthening precipitates. The Co_2Al_9 particles were spherical, generally 0.1-0.5 μm in diameter. The distribution of small ($<0.1 \mu\text{m}$) oxides was observed to be very inhomogeneous with particles often appearing clumped together or arranged as stringers. Dislocation debris was often seen in areas where large densities of oxides were present.

Pole figures obtained for the CT91 materials are shown in Figure 32 through 36. The P/M billet exhibited no discernible preferred orientation, as shown in Figure 32. However, both P/M

forgings, Figures 33 and 34, showed some degree of preferred orientation (probably cube) and the ABC forging seemed to develop a slightly sharper texture than the A forging. The CT91 extrusions, Figures 35 and 36, showed a $(110)[11\bar{2}]$ texture typical of unrecrystallized structures often observed in wrought 7XXX I/M alloys. The temperature-compensated strain rate, Z , did not produce major differences in texture of the CT91 extrusions.

DISCUSSION

The forgings and extrusions tested in Phase I exhibited similar FCG resistance, while the billets showed faster crack growth rates, particularly at higher ΔK levels. The poor FCG resistance of the hot-pressed billets is probably related to the coarse microstructures and relatively low toughness of these materials. Comparison of Figures 14 through 17 shows that the billets received considerably less hot deformation than either the hand forgings or extrusions. Powder particle boundaries are still evident in the billet structure, Figure 14, but were completely eliminated in the wrought products. The more highly worked structures of the forgings and extrusions resulted in higher ductility, increased toughness, and improved FCG resistance relative to the P/M billets. Previous work has also reported similar improvements in ductility and fracture properties of P/M materials with increased amounts of hot deformation (3,6).

The tensile and FCG results for the wrought products showed a marked insensitivity to the changes in Co level and different fabricating practices used in Phase I. Humid air FCG

resistance of the A-upset and draw hand forgings, when calculated on the basis of the cubic spline fit, Table 9, was increased somewhat by increasing Co content. However, this improvement was observed only in these initial tests at high ΔK levels and was not reflected in $da/dN-\Delta K$ data obtained in subsequent tests. Figures 8 through 11 show no clear-cut effect of Co content on FCG of the wrought materials in either humid air or salt fog.

The similarity in FCG resistance of Phase I materials is probably related to the relatively small differences in microstructure noted during the metallographic examinations. The effects of microstructure on FCG resistance of the P/M materials will be discussed in more detail in a separate section dealing with the development of structure in P/M alloys. This topic will be discussed in conjunction with the results of Phase II.

PHASE II

RESULTS

Tensile Properties

An aging study was conducted to select appropriate tempers (T7X1 and T7X2) for Phase II materials. Hardness and electrical conductivity (EC) measurements were made on specimens of CT91 (S-356453), MA88 (S-493706), and MA90 (S-493705) extrusions. The specimens were aged for various times at 163°C after an initial aging step of 24 hours at 121°C. Results of Rockwell B hardness tests, Figure 37, and EC, Figure 38, show that alloy chemistry affected precipitation kinetics in the

three alloys. Final aging practices were selected in an attempt to produce similar yield strengths for the three alloys in the T7X1 and T7X2 tempers. Tensile properties obtained in the aging study are shown in Table 11. The results of tensile tests of T7X1 and T7X2 materials after final temper selection are listed in Table 12. Also included in Table 12 are tensile properties for a 7050-T76511 extrusion, which was tested as an I/M control for the Phase II FCG tests.

Fatigue Crack Growth

Results of the Phase II humid air FCG tests of P/M hand forgings and extrusions are shown in Figures 39 and 40. Salt fog test results for the experimental materials are plotted in Figures 41 and 42. Results of FCG tests for the 7050-T76511 control material are included in Figures 40 and 42 for comparison. The FCG results for the P/M extrusions are also compared to scatterbands of data for commercial 7050 extrusions obtained in previous investigations (7,8). Overaging the P/M alloys to the T7X2 temper generally improved FCG resistance, particularly in the extrusions.

At ΔK levels from 4 to 10 $\text{MPa}\sqrt{\text{m}}$, FCG rates of the P/M extrusions aged to the T7X2 temper were quite similar to those of 7050-T76511. Alloy chemistry generally had little effect on FCG resistance of the Phase II extrusions, as evidenced by the similarity of data for the alloys aged to similar strength levels. The MA88-T7X1 extrusion, however, had poorer FCG resistance than the other two alloys when tested in high humidity air (Figure 40).

Due to a considerable amount of scatter in FCG data obtained for the hand forgings, firm conclusions cannot be drawn regarding effects of alloy chemistry or overaging on the FCG resistance of these materials. A possible explanation for the scatter in the hand forging data will be discussed in the "DISCUSSION" section of this report.

Microstructure

Optical micrographs of the structures of the MA88 and MA90 wrought products fabricated in the Phase II investigation are shown in Figures 43 through 46. The microstructure of the hand forgings, Figures 43 and 44, and extrusions, Figures 45 and 46, were quite similar to those of the CT91 products described earlier. Figure 47 shows a typical microstructure of the 7050-T76511 control material tested in Phase II.

Fractography

The FCG fracture surfaces of the P/M extrusions and the 7050 control materials were examined using optical metallography and SEM. The P/M specimens exhibited rather smooth, featureless fractures on a macroscopic level. By contrast, the 7050 fracture surfaces were rough and faceted in appearance. An optical comparison of the fracture appearances is shown in Figure 48. Scanning electron micrographs, Figures 49 through 51, confirm the macroscopic observations. The P/M FCG fracture surfaces are smooth, with little evidence of plateaus, ledges, or secondary cracking typically found in I/M materials. The 7050 specimen, Figure 51, showed a much rougher, more tortuous fracture appearance than observed for FCG specimens of the P/M materials.

DISCUSSION

The lack of noticeable alloy chemistry effects on FCG resistance of the Phase II materials is probably related to the overriding effect of the fine, uniform structure in these alloys. Though increasing Cu content, MA88 vs CT91, has been shown to increase FCG resistance of I/M alloys (9,10), this result was not found for the P/M alloys in the tempers selected for the present study. Alloy MA88 showed no advantage in FCG resistance compared to CT91, particularly in the higher strength temper (Figure 40). The beneficial effects of overaging to a T7X2 temper on FCG resistance were similar to those reported previously for I/M alloys (9). Overaging the P/M materials results in decreased sensitivity to environmental effects on FCG and increased resistance to plastic strains, i.e., a larger plastic zone size.

The considerable amount of scatter observed in the FCG data obtained for the hand forgings prevents any definite conclusions regarding the effects of alloy chemistry on overaging. The reason for this lack of consistency in the hand forging FCG data may be due to the nature of the processing received by such products. Nonuniform grain flow in forgings often results in large variability in microstructure and mechanical properties of these materials. Differences in grain size, shape, and preferred orientation in different locations of the forgings could have affected the response of the forgings to FCG. A possibly more important source of variability of properties in these materials is the compressive residual stress operation experienced

by the hand forgings. Even though the quenching stresses were relieved to some extent by the application of 2-3% compression, measurable residual stresses are generally encountered in such forgings (See Phase III RESULTS). Furthermore, compressive stress relief does not necessarily eliminate residual stresses in all directions of the product.

An examination of the a vs N data for FCG samples from the forgings showed that the growth of the fatigue crack was not uniform from both sides of the notch in the CCT specimens, Figure 7. At fracture, differences of up to 1.8 cm (0.75 in.) were noted in the length of the cracks on either side of the notch. This eccentricity of the cracks at fracture, reported in Table 13, was not observed in the a vs N data for the extrusions. Even though this type of eccentric crack growth behavior does not violate a specific ASTM test standard, it is known to have an effect on the effective stress intensity level in CCT specimens (11). Since the extent of eccentricity varied widely from specimen to specimen, it appears likely that residual stress patterns in the specimens taken from the hand forgings are responsible for the nonuniform crack growth and variability in the FCG data. Consequently, any interpretation of alloy or temper effects on FCG of the hand forgings is not warranted on the basis of the data presented in Figures 39 and 41.

In light of the FCG data obtained in both Phase I and II of the present investigation, the dominant factor in determining FCG resistance of these alloys is the fine, uniform

microstructure produced by P/M processing. It seems evident that the FCG process in P/M alloys must be related to structural features by similar mechanisms to those determined for I/M materials (9,10). A brief discussion will be undertaken to contrast the development of microstructures in I/M and P/M materials and to explain how the structures of the wrought products may differ in their resistance to fatigue crack growth.

Microstructure and FCG Resistance of High-Strength 7XXX Alloys

The structures observed in the wrought P/M products have their origins in the rapidly solidified powders shown in Figures 12 and 13. The fine particle size (13 μm , APD) and irregular shape of these powders are beneficial to the compaction and densification of the P/M materials (3), allowing for the attainment of 100% density after vacuum hot compaction. Further hot work produces recovered structures, e.g., Figures 18-30, with microstructural features in the 1-5 μm range.

A second effect of P/M processing is the suppression of constituent particle formation by the high solidification rates during atomizing. Large (up to 30 μm) insoluble constituents, such as $\text{Al}_7\text{Cu}_2\text{Fe}$ or Mg_2Si , are formed during casting of commercial purity I/M alloys. These large particles, known to be detrimental to toughness and, hence, high ΔK FCG resistance in high strength 7XXX alloys (9,10), are not normally observed in the P/M materials. A more subtle effect of the lack of constituents in P/M alloys may be reflected in their lack of

sensitivity to the processing variations of the present investigation. An ongoing program has shown that constituent particles play an important role in the response of I/M alloys to thermomechanical processing (12). The absence of large constituents coupled with the presence of fine oxides, probably overrides to some extent the effects of Co content or processing variations on the microstructures of P/M wrought products. It should be remembered, however, that a certain minimum amount of hot work is necessary for the development of fine structures as shown by the relatively coarse structures of the hot-pressed billets. Additionally, more severe degrees of deformation processing, e.g., low temperature/high reduction rolling practices, would probably result in significant recrystallization and much coarser grain structures (13).

Though the role of oxides in the development of microstructure in P/M materials is not clearly understood at present, these particles seem to be important in maintaining fine subgrain structures in P/M wrought products. The TEM evidence, Figure 31, suggests that the oxides serve to pin dislocations and subgrain boundaries. This observation is supported by previous work on SAP materials (14) and mechanically alloyed products (15). The fact that the oxide distribution is quite nonhomogeneous probably contributes, in part, to the highly variable structural size observed in some of the Co-free wrought products, e.g., Figure 18.

The important features of the P/M microstructures relative to the present FCG investigation are summarized below:

1. Fine, mostly unrecrystallized structures.
2. Grain/subgrain size - 1 to 5 μm .
3. No coarse constituent particles.
4. Fine, inhomogeneous distribution of oxides and Co_2Al_9 .
5. Structure somewhat insensitive to Co content, processing.

By contrast, the structure of a typical I/M wrought material such as the 7050-T76511 extrusion shown in Figure 47 is described as:

1. Partially recrystallized structure.
2. Duplex structure with fine subgrains ($\sim 5 \mu\text{m}$) and larger recrystallized grains which may be greater than 200 μm in the extrusion direction.
3. Constituent particles (approximately 1 vol.%) generally 2-20 μm in size.
4. Structure variable with processing conditions.

A comparison of the FCG behavior of these two materials may be made in terms of these microstructural features and fractographic observations of FCG specimens.

In an attempt to understand the FCG behavior of high strength 7XXX alloys, the monotonic plastic zone size (r_p) relative to pertinent structural features should be taken into account (16). The value of r_p depends on yield strength, K_{max} , and the state of stress (plane stress/plane strain conditions) experienced by the specimen. An estimate of r_p may be calculated according to the equation below:

$$r_p = \frac{1}{6\pi} \frac{K_{\max}^2}{\sigma_{ys}}$$

where: r_p = monotonic plastic zone size,

K_{\max} = maximum stress intensity during a fatigue cycle,

σ_{ys} = yield strength.

Values of r_p (plane strain) calculated for ΔK levels of interest in the present investigation are listed in Table 14. Figure 52 serves to illustrate the magnitude of change in r_p at various levels of ΔK .

When values of r_p are significantly greater than a given microstructural feature, e.g., grain size, interparticle spacing, that feature should have relatively little effect on FCG resistance. The microstructure essentially behaves as a continuum, obeying relationships calculated from linear elastic fracture mechanics (LEFM). The micrographs in Figure 53 suggest that, even at ΔK levels as low as $3.0 \text{ MPa}\sqrt{\text{m}}$, the P/M microstructures are significantly finer than the monotonic plastic zone size. By contrast, some of the larger recrystallized grains in the 7050 extrusion (Figure 53(b)) are considerably larger than r_p in the low ΔK regime.

This type of analysis may be used to explain the observed FCG behavior of P/M and I/M materials. At low ΔK levels, where r_p values are small, large grains (17) or constituent particles (18) may serve to divert cracks from the preferred crack growth path normal to the applied stress. In large-grained I/M materials, crystallographic crack growth may serve to significantly reduce

measured FCG rates at low ΔK levels (10). The fine structures of the P/M materials, however, are still small relative to r_p and offer no features to divert the crack from the macroscopic growth direction. Consequently, somewhat higher FCG rates were measured for the P/M materials below $\sim 5 \text{ MPa}\sqrt{\text{m}}$. At higher stress intensity levels, where r_p values are larger, both P/M and I/M microstructures act as a continuum and display similar FCG rates. This observation is in agreement with previous work which has shown that 7XXX I/M alloys are relatively insensitive to microstructural changes at intermediate ($5\text{-}15 \text{ MPa}\sqrt{\text{m}}$) ΔK levels (9). Recent attempts to develop predictive microstructure/FCG relationships have also shown that a reduction in grain size is generally detrimental to the crack growth resistance of high-strength structural alloys (19).

The fractographic observations of Figure 48 through 51 support the above analysis of microstructural effects on FCG of P/M and I/M materials. The P/M fracture surfaces are relatively smooth and featureless over the range of ΔK examined, with no evidence of diversion from the crack growth direction. The 7050 fracture surface, Figure 51, is rather tortuous in appearance with evidence of secondary cracking and local deviations in crack path. This type of fracture morphology would be expected to result in slower FCG rates, particularly at low stress intensities.

More detailed fractography is necessary to properly determine the complex interrelationships between the various microstructural features of P/M materials and FCG mechanisms.

Such a fundamental analysis is beyond the scope of the present investigation, but is being pursued by various university research programs (20-22). More complete evaluations of the roles played by oxides, Co_2Al_9 , and the fine grain and subgrain structures in controlling the accumulation of fatigue damage and local fracture processes will aid in the production of improved fatigue-resistant P/M aluminum alloys.

PHASE III - EFFECT OF RESIDUAL STRESS ON
FATIGUE CRACK GROWTH OF 7XXX
P/M ALLOY

BACKGROUND

Early research aimed at understanding of metallurgical variables affecting the mechanical properties of P/M alloys pointed to their extremely attractive FCG resistance. In this work large decreases in FCG rates (da/dN) at low and intermediate cyclic stress intensity factor (ΔK) were demonstrated on several occasions.

A program conducted for the Air Force Materials Laboratory (AFML) characterized short-transverse* FCG rates of MA87 alloy and several of its variants (3). Plots of da/dN vs ΔK established from compact type (CT) specimen tests indicated that certain processing variants produced FCG rates about an order of magnitude slower than commercial high strength I/M alloys, Figure 54. Subsequent work at AFML verified the slow FCG rates with CT specimens cut from the same P/M forgings (23). The improved FCG resistance appeared to be a function of interactions between fabricating practice and dispersed phases in the alloy microstructure. However, the data were somewhat erratic, and it was not clear which metallurgical variables were responsible for the excellent FCG resistance.** The present AFML sponsored program was, therefore, undertaken to determine the interrelationship among fabrication practices,

*S-L orientation per ASTM Standard Method E399-78.

**In some CT specimens the fracture path deviated from a plane normal to the direction of loading with increasing crack extension. The magnitude of the deviation varied with specimen.

microstructure and FCG resistance of high strength 7XXX P/M alloys similar to CT91 (formerly MA87).

Initial FCG results of the present program were unable to reproduce the dramatic improvements in FCG resistance demonstrated in the earlier Reference 3. Humid air testing of P/M alloys showed only marginally slower FCG rates than I/M 7075. None of the P/M alloys tested showed equivalent FCG resistance to I/M 7050. These results were totally unexpected and in direct conflict with results of previous AFML-sponsored work and internal Alcoa results.

Because of the observed discrepancies, the FCG test procedures employed in current work were re-examined and found to be in perfect order. Growth rates established from replicate specimens of Phase I materials were demonstrated to be highly reproducible. A detailed reevaluation of the fabrication practices for original materials in Reference 3 revealed that the hand forgings had not been stress relieved following quenching and, hence, probably contained large residual stresses. The compressive stress relief operation applied to forgings tested in the current program should produce a lower magnitude, and more uniform, residual stress state.*

Other early P/M FCG testing at Alcoa Laboratories was conducted on laboratory scaled, nonstress-relieved, extruded rod (24).

*The plane of fracture in stress-relieved FCG specimens was typically normal to the loading direction, as expected.

Longitudinal single edge notched (SEN) specimens from these rods suggested high FCG resistance. After the question of residual stress was raised, it was decided to test an alternate center crack tension (CCT) specimen configuration for identical material. The distribution of quenching residual stresses in the extruded P/M rod was assumed similar to those measured in a quenched 7075-T6 cylinder, Figure 55. This distribution of residual stresses was hypothesized as being largely responsible for the different FCG rates observed in the two specimen types removed from identical P/M material, Figure 56. For the SEN specimen, residual stresses normal to the crack plane were initially in compression and initial FCG rates were slower than those of the CCT specimen, where residual stress normal to the crack plane is tensile.

Because of the confounding of early data by residual stress, and incomplete information regarding specimen location and residual stress distributions, the superior P/M FCG resistance observed in the early work could not be confirmed or refuted. It was, therefore, proposed that this investigation be conducted with the goal of (1) reproducing the original good FCG resistance of Reference 3 and (2) evaluating the effect of residual stress on FCG measurement.

EXPERIMENTATION

Residual stress and mechanical properties were determined for the four material conditions, viz, P/M and I/M with and without stress relief. The location of test specimens and surface

X-ray residual stress measurements made on the parent slab are indicated in Figure 57.

For each material condition, the following tests were conducted according to the designated ASTM standard test practice (25).

<u>Quantity</u>	<u>Type of Test</u>	<u>Specimen Type</u>	<u>ASTM Practice</u>
2	Tensile	6.35 mm (1/4 in.) dia.	E-8
2	Cylindrical Notch Tensile	12.7 mm (1/2 in.) dia.	E602-76T
1	Fracture Toughness	CT Specimen 38.1 mm (1-1/2 in.) Thk.	E399
3	FCG Rate	CT Specimen 6.35 mm (1/4 in.) Thk.	E647-78T

Specimen locations, Figure 57, and test parameters were selected to replicate test conditions studied in Reference 3. The FCG tests were conducted in dry air (relative humidity <10%) at stress ratio (R) equal to 1/3. All other tests were conducted in ambient air. Compact FCG specimens were removed from material at the mid-thickness (T/2) plane and both surfaces of the parent slab to check whether possible nonsymmetry of grain flow or residual stress in the parent slab influence test results.

To better quantify effect of residual stress on FCG measurement, residual stresses in FCG specimens were established by the X-ray method prior to testing. The location and stress orientation of these measurements are indicated in Figure 58. The X-ray measurements obtained in the original parent slab and test specimens were analyzed statistically. Residual stress indications were determined to be reproducible with ± 28 MPa (4 ksi) at the 95% confidence level. Main and interaction effects

of material type, state of stress relief, stress orientation, and measurement location were identified using the Yates' algorithm supplemented by general linear modeling techniques. Statements of significance, unless otherwise stated, are at the 95% confidence level.

Crack propagation rates (da/dN) were determined from visual crack length measurements. A crack opening displacement (COD) gauge was used to monitor compliance change with crack extension in FCG specimens removed from the T/2 and one surface plane of each material condition. A crack opening load (P_{op}) was estimated from the load-COD trace obtained in the instrumented tests, as in Figure 59. The opening load is required to offset compression at the crack tip caused by the superposition of clamping forces attributed to residual stress in the bulk material and forces caused by wedging action of residual deformation left in the wake of the propagating crack, as described by Elber (26). The residual stress influence on da/dN can, therefore, be evaluated using the concept of effective cyclic stress intensity factor (ΔK_{EFF}), which assumes that propagation occurs only when the crack is completely open. For a constant applied cyclic load (ΔP), any internal force system which increases P_{op} above the minimum cyclic load would decrease ΔK_{EFF} , and thus decrease da/dN .

Two rectangular blanks having identical thickness and plan size as the FCG specimens were removed from I/M material at comparable locations to the instrumented FCG tests, but from the opposite end of the parent slab, as indicated in Figure 57. The

redistribution of residual stresses following progressive sawcuts, simulating a growing crack, was determined from displacements measured at the locations indicated in Figure 60.

RESULTS

Residual Stresses - Parent Slab

The X-ray residual stress measurements made at each numbered location of the parent slab, Figure 57, represented a 2^3 factorial experiment which considered material (I/M vs P/M), state of residual stress (with and without stress relief) and stress orientation (L vs S or T). The following conclusions were determined from statistical analysis of the X-ray measurements:*

1. State of stress relief had the largest effect on magnitude of the residual stress. Residual stress magnitudes were consistently larger in nonstress-relieved materials.
2. Residual stress magnitudes in both the stress-relieved and nonstress-relieved materials were significantly different from zero.
3. Neither a main effect nor interaction effect of material (I/M vs P/M) on residual stress magnitude was detected.
4. Residual stress magnitudes were influenced by a significant interaction between residual stress state and stress orientation. The stress relief was more effective at reducing internal stress in the S direction than it was in the L direction.

*Main and interaction effects were determined by the Yates' algorithm.

5. A main effect of residual stress orientation (i.e., non-biaxial residual stress state) was detectable. This trend was smaller than that noted in 1 and 4 above and could only be confirmed at the 80% confidence level.
6. For a comparable state of stress relief no difference in residual stress distribution could be detected between location 2 and location 6, Figure 57; i.e., nonsymmetry of residual stresses was not detected between the left and right hand portion of the billets.
7. No difference in residual stress magnitudes between locations 2 and 5, Figure 57, was detected for stress-relieved material. However, differences were detected between these two locations in nonstress-relieved material; i.e., the residual stress redistribution through the slab thickness was nonsymmetrical in nonstress-relieved material.

The above main and interaction effects of stress-relief state and stress orientation are indicated in the comparison of mean residual stress levels at selected locations, Figure 61.

Mechanical Properties

Short-transverse tensile and fracture toughness properties of Phase III materials and a comparable MA87 P/M material from Reference 3 are given in Table 15. Valid fracture toughness, K_{IC} , numbers were established for stress-relieved materials, while results of nonstress-relieved materials were invalid due to excessive fatigue precrack curvature caused by the residual stress distribution indicated in Figure 62. The nonvalid

K_Q values, however, can be used for relative toughness comparison of nonstress-relieved material. Both notch yield ratio (NTS/YS) and K_Q results, Table 15, indicate higher toughness in P/M than in I/M having comparable stress-relief state.

Fatigue Crack Growth

The comparison of stress-relieved vs nonstress-relieved FCG behavior (da/dN vs ΔK) is shown respectively for P/M and I/M alloys in Figures 63 and 64. Data from triplicate tests of identical stress-relieved material were in good agreement. For identical applied ΔK , the FCG rates in nonstress-relieved material were significantly slower than rates in stress-relieved material, particularly at low ΔK . In nonstress-relieved material the measured response depended upon sample location within the parent slab, e.g., Figure 63, while in stress-relieved material sample location was not a factor.

The results of nonstress-relieved materials, Figures 63 and 64, indicated that significant internal stresses altered the crack tip stress intensity factor, thereby causing the disagreement with stress-relieved behavior. The recommended standard FCG test practice (ASTM E647-78T) assumes internal stresses to be zero, and uses external loads only to compute ΔK . Hence, though FCG results of nonstress-relieved materials are completely accurate and valid according to ASTM practice,* the data should not be considered representative of the true material behavior.

*With exception of that data where the fatigue crack grew out of plane.

The stress-relieved data are more typical of the FCG resistance of the subject alloys when fabricated by commercial-type processing operations. Comparison of stress-relieved results, Figure 65, indicate P/M FCG resistance to be comparable to I/M at the lowest ΔK established ($\sim 2.5 \text{ MPa}\sqrt{\text{m}}$), slightly inferior to I/M at intermediate ΔK , and superior to I/M at high ΔK because of the improved toughness.

Residual Stresses in CT FCG Specimens

The X-ray residual stress measurements made at the indicated CT specimen locations, Figure 58, were analyzed as a 2^5 factorial experiment of the following variables: material (I/M vs P/M), residual stress state (with and without stress relief), stress orientation (L vs S), specimen origin from parent material (T/2 vs surface*), and specimen face-to-face variation (i.e., side A vs side B, Figure 58). The following conclusions were determined by statistical analysis:

1. The residual stress magnitude in both the stress-relieved and nonstress-relieved CT specimens were significantly different from zero.
2. The main effects of residual stress state (stress-relieved vs nonstress-relieved) and stress orientation had the largest effect on residual stress magnitudes. On the average, stresses in the S direction were algebraically 30 MPa (4.3 ksi) greater than stresses in the L direction,

*Only one surface specimen was examined with sufficient replication to permit statistical comparisons.

and stresses in nonstress-relieved samples were algebraically 25 MPa (3.6 ksi) greater than stress-relieved samples.

3. A significant second order interaction between residual stress state and stress orientation was detected. The magnitude of residual stress change with stress relief was generally greatest for stresses oriented in the S direction.
4. A significant second order interaction between residual stress state and specimen origin was also detected. The effect of sample location on residual stress magnitudes was greatest in nonstress-relieved material.
5. Residual stress varied as a main effect with the specimen face on which the measurement was made. Typically, there was about 14 MPa (2 ksi) difference in indicated residual stress from one specimen surface to the other.
6. Neither a main effect nor interaction effect of material (I/M vs P/M) on residual stress magnitude was detected.

Table 16 summarizes average X-ray residual stress indications made at selected locations on the FCG specimens.

DISCUSSION

Residual stresses are produced during quenching by deformation associated with shrinkage during cooling. Generally, the first portion of the sample to cool is left in residual compression and the last portion to cool is left in residual tension. This is true of the cylinder indicated in Figure 55

where residual compression along the outer surface is balanced by a core of residual tension at the center.

Using the above rationale, the principle of equilibrium, and the boundary condition that stresses normal to a free surface must be zero, the distribution of S and L residual stresses in a nonstress-relieved rectangular cross section would be similar to that illustrated in Figure 66. This typical distribution was verified by X-ray measurements of the nonstress-relieved parent materials. Longitudinal surface compression is greatest at the corners, since these locations are the first to cool.

The full section thickness nonstress-relieved S-L fracture toughness samples demonstrated that compressive S stresses at the surface caused the crack to grow slower than at the T/2 plane where the S residual stress was tensile. Machining FCG specimens to a thickness of 6.35 mm (0.25 in.) sufficiently reduced S stress variation through the thickness such that excessive crack front curvature was no longer a problem.

Residual stress in the L direction had the greatest effect on valid measurement of FCG resistance in nonstress-relieved CT specimens. Figure 67 illustrates that crack tip compression results from a clamping moment caused by the stress unbalance which develops upon introduction of the crack starter slot. This force system is relatively uniform through the thickness, and therefore, its occurrence cannot be detected by excessive curvature in the propagating fatigue crack. That is, by failing to recognize this residual stress system, one would

be likely to interpret FCG measurements as valid according to ASTM Method E647-78T.

A simple technique to determine whether a clamping moment exists is to measure surface displacement before and after the introduction of the machined starter notch. For example, following a sawcut simulating the crack starter slot in a CT blank, Figure 50, mechanical gauge marks initially spaced 51 mm (2.0 in.) apart closed respectively by 0.18 and 0.20 mm (0.007 and 0.008 in.) in blanks removed from the T/2 and surface plane of the parent nonstress-relieved I/M slab. Comparable measurements made on stress-relieved I/M blanks indicated the initial gauge locations spread apart by 0.05 mm (0.002 in.) for both the T/2 and surface locations. The latter observation indicates that FCG rates established in stress-relieved specimens could actually be greater than those expected in residual stress-free material, because of increased mean stress at the crack tip.

Stress redistribution in a CT specimen following a series of sawcuts to simulate a growing fatigue crack was measured by strain gauges mounted just below the fracture plane, Figure 50. Measurements made in nonstress-relieved material indicated significant compression stress in material at and ahead of the propagating crack front, Figure 68. Crack propagation would, therefore, be retarded by the forces tending to close the crack. Stresses ahead and at the simulated crack tip in stress-relieved material were either slightly positive at short crack length or zero at large crack length. Crack growth may, therefore, be either

accelerated or unaffected by the residual stress system present in the original stress-relieved blank.

Clear differences were observed in the load-COD traces established in instrumented FCG tests of stress-relieved vs non-stress-relieved samples. Typical test records for P/M and I/M samples removed from the T/2 plane are indicated in Figures 69 and 70, respectively. Comparable test records were reproduced in test specimens removed from the surface plane of the parent slab. For simplicity, the crack opening load, P_{op} , was determined at the intersection of two traces which divide the test record into two linear segments. At relatively short specimen crack length, P_{op} in nonstress-relieved material was of the order of the maximum applied load, P_{max} , in tests of stress-relieved material. This explains why nonstress-relieved samples required P_{max} about double that in stress-relieved samples to propagate a crack at equivalent rate early in the test. In nonstress-relieved samples, decrease in P_{op} resulted from the stress relief which occurred with crack extension. This explains the near equivalence of da/dN vs ΔK data in stress-relieved and nonstress-relieved samples at high ΔK (long crack length).

Nonstress-relieved FCG rates were corrected using the effective ΔK concept of Figure 60. The adjusted results from nonstress-relieved material agreed very well with data established in the stress-relieved samples, e.g., Figures 71 and 72. Thus, it is concluded that residual stresses were largely responsible for the extremely low FCG rates observed in original MA87 data reported in Reference 3.

A finite crack opening load was detected in stress-relieved I/M samples, while no opening load could be detected in P/M samples of comparable residual stress state, e.g., compare Figures 69 and 70. In I/M material the opening load is most likely attributable to closure forces produced by wedging action of deformed material contacting on the fractures surface, as demonstrated by Elber (26). Macroscopic fatigue fracture surface morphology of P/M samples was typically smoother (flatter) than observed in I/M fractures, e.g., Figures 48-51. Using the Elber concept, closure forces in P/M material attributed to deformation in the wake of the propagating crack would be significantly less in P/M than in the I/M material. Therefore, if ΔK_{EFF} rather than ΔK applied were applied to correlate growth rate, then the FCG resistance of I/M would depreciate relative to that of P/M material.* In actual components a significant portion of the FCG life is spent in the propagation of very small flaws (27). Crack growth life of very small cracks is better correlated by ΔK_{EFF} since there is little or no contact surface to develop closure forces.

CONCLUSIONS

PHASE I

1. Changes in Co content between 0.0 and 0.8% did not significantly affect tensile properties of Phase I hand forgings or extrusions.

*The magnitude of the change would depend on R-ratio.

2. Difference in forging sequence, A-upset and draw vs ABC upset and draw, had no effect on tensile properties of Phase I hand forgings.
3. Changes in temperature-compensated strain rate (Z) between $4.3 \times 10^{-8} \text{ sec}^{-1}$ and $1.5 \times 10^{-12} \text{ sec}^{-1}$ did not affect tensile properties of Phase I extrusions.
4. Salt fog FCG resistance of Phase I hand forgings or extrusions in the T7X1 temper was not sensitive to Co variations from 0.0 to 0.8% over the range of ΔK studied.
5. The FCG resistance of billets tested in humid air was significantly less than that of hand forgings or extrusions.
6. FCG rates for the P/M extrusions tested in salt fog were slightly higher or in the upper range of the scatterband for 7050-T76511 data.

PHASE II

1. FCG resistance of Phase II extrusions in humid air or salt fog was not significantly affected by the changes in alloy chemistry studied.
2. Overaging the Phase II extrusions to a lower strength T7X2 temper was beneficial to FCG resistance in both humid air and salt fog.
3. Scatter in the data for Phase II hand forgings prevented an unambiguous conclusion regarding alloy or temper effects on FCG in these materials.

4. The FCG rates of Phase II extrusions in the T7X2 temper fell within a scatterband for 7050-T76511 materials at ΔK levels above $4 \text{ MPa}\sqrt{\text{m}}$ (salt fog) or above $6 \text{ MPa}\sqrt{\text{m}}$ (humid air).
5. FCG rates for T7X1 extrusions were generally above or in the upper end of the range of data in the 7050-T76511 scatterbands.
6. At ΔK values below $4 \text{ MPa}\sqrt{\text{m}}$, FCG rates of all P/M materials were higher than that of the 7050-T76511 material tested in this investigation.
7. The FCG resistance of both P/M and I/M materials may be explained on the basis of plastic zone size relative to the size of the basic microstructural units.

PHASE III

1. Residual stresses were mainly responsible for the observed slow FCG rates reported in Reference 3.
2. The compressive stress relief operation produced significantly lower levels of residual stress than found in non-stress-relieved materials. However, measurements indicated that, even after stress relief, residual stresses were still significantly different from zero.
3. Response of the hand forgings to residual stress relief was similar for both I/M and P/M materials.
4. Crack closure concepts could be used to correct nonstress-relieved data to account for residual stresses on the basis of effective ΔK levels.

5. Though FCG data obtained in Phase III for stress-relieved materials are more representative of commercial products, caution is still warranted in the quantitative comparison of P/M and I/M data due to:

- (1) differences in material response to crack closure, and
- (2) incomplete stress relief in stress-relieved hand forgings.

REFERENCES

1. A. P. Haarr, "Development of Aluminum-Base Alloys, Section III," Contract DA-36-034-ORD-3559RD, AD487764, 1966 May 31.
2. J. P. Lyle, and W. S. Cebulak, "Powder Metallurgy Approach for Control in High Strength Aluminum P/M Products," presented at TMS-AIME Spring Meeting, Philadelphia, PA, 1973 June.
3. W. L. Otto, Jr., "Metallurgical Factors Controlling Structure in High Strength Aluminum P/M Products," AFML TR-76-60, 1976 May.
4. W. S. Cebulak, "Program to Develop High Strength Aluminum Powder Metallurgy Products, Phase IV - Scale-Up to 3200 lb Billet," Final Report, Contract DAAA25-72-C0593, 1977 April.
5. H. Matyja, B. C. Giessen, and N. J. Grant, J. Inst. Metals, Vol 96, 1968, pp 30-32.
6. H. W. Antes, Ph.D. Thesis, Drexel University, Philadelphia, PA, 1979 June.
7. J. T. Staley, J. E. Jacoby, R. E. Davies, G. E. Nordmark, J. D. Walsh, and F. R. Rudolph, "Aluminum Alloy 7050 Extrusions," AFML TR-76-129, 1977 March.
8. R. E. Davies, G. E. Nordmark, and J. D. Walsh, "Design Mechanical Properties, Fracture Toughness, Fatigue Properties, Exfoliation and Stress-Corrosion Resistance of 7050 Sheet, Plate, Hand Forgings, Die Forgings and Extrusions," Final Report, Contract N00019-72-C-0512, 1975 July.
9. W. G. Truckner, J. T. Staley, R. J. Bucci, and A. B. Thakker, "Effects of Microstructure on Fatigue Crack Growth of High Strength Aluminum Alloys," AFML-TR-76-169, 1976 August.
10. T. H. Sanders, Jr., and J. T. Staley, "Review of Fatigue and Fracture Research on High Strength Aluminum Alloys," presented at 1978 ASM Materials Science Seminar, Fatigue and Microstructure, St. Louis, MO, 1978 October 14-15.
11. G. R. Irwin, H. Liebowitz, and P. C. Paris, Compendium in Eng. Fract. Mech., Vol 1, 1968, pp 235-36.
12. T. H. Sanders, Jr., NASC Contract N00019-77-C-0499, Final Report in preparation, 1979.
13. D. P. Voss, "Development of Improved High Strength Aluminum Powder Metallurgy Products," Progress Report, AFOSR Grant 77-3440, 1978 December 31.

14. R. J. Towner, "Atomized Powder Alloys of Aluminum," Metal Progress, 1958 May, p 70.
15. S. J. Donachie, "New Developments in Dispersion Strengthened P/M Aluminum Products," ASM Materials Conference, Paper No. 64, 1977.
16. J. Lankford, D. L. Davidson, and T. S. Cook, "Fatigue Crack Tip Plasticity," Cyclic Stress-Strain and Plastic Deformation Aspects of Fatigue Crack Growth, ASTM STP 637, American Society for Testing and Materials, 1977, pp 36-55.
17. M. E. Fine and R. O. Ritchie, "Fatigue Crack Initiation and Slow Crack Growth," presented at 1978 ASM Materials Science Seminar, Fatigue and Microstructure, St. Louis, MO, 1978 October 14-15.
18. T. H. Sanders, Jr., R. R. Sawtell, J. T. Staley, R. J. Bucci, and A. B. Thakker, "Effect of Microstructure on Fatigue Crack Growth of 7XXX Aluminum Alloys Under Constant Amplitude and Spectrum Loading," Final Report, NADC Contract N00019-76-C-0482, 1978 April.
19. S. B. Chakraborty, Office of Naval Research Tech. Report 78-2, 1978 May.
20. M. J. Koczak and A. Lawley, Drexel University, Annual Tech. Report, AFOSR Grant 77-3247, 1978 April.
21. M. E. Fine, Northwestern University, ongoing AFOSR-sponsored research, 1979.
22. E. A. Starke, Jr., Georgia Institute of Technology, ongoing research supported by Lockheed-Georgia Company, ARRADCOM, 1979.
23. W. M. Griffith, Air Force Materials Laboratory, Private communication, 1976 July.
24. Alcoa Laboratories, unpublished results, 1976.
25. 1978 Annual Book of ASTM Standards, Part 10, American Society for Testing and Materials.
26. W. Elber, in Damage Tolerance in Aircraft Structures, ASTM STP 486, American Society for Testing and Materials, 1971, p 230.
27. S. Pearson, "Initiation of Fatigue Cracks in Commercial Al Alloys and the Subsequent Propagation of Very Short Cracks," Eng. Fract. Mech., Vol 2, 1975, pp 235-247.

TABLE I. MELT ANALYSIS

S. No.	Composition - wt.%						
	Si	Fe	Cu	Mg	Zn	Co	
PHASE I							
356452	0.06	0.06	1.43/1.51	2.40/2.48	6.19/6.36	0.0	
356453	0.06/0.07	0.06	1.47/1.51	2.36/2.47	6.40/6.52	0.36/0.40	
356454	0.05/0.08	0.07	1.48/1.57	2.50/2.58	6.59/6.60	0.83/0.87	
PHASE II							
493705	0.04	0.05	1.58	2.61	8.44	0.40	
493706	0.05	0.06	2.36	2.59	6.68	0.41	
PHASE III							
493678	0.04	0.04	1.51	2.43	6.17	0.00	
493681 (1)	0.10	0.11	1.49	2.49	6.21	(2)	

NOTES: 1 - 22.9 cm diameter D.C. Cast Ingot

2 - 0.22 wt.% Cr addition

3 - Melt analyses reported for Phase I alloys are composition ranges obtained for different samples taken during atomization.

TABLE 2. POWDER SIZE AND DISTRIBUTION

S. No.	U.S. Standard Screen Analysis (wt.%)						Average Particle Diameter, μm
	-50 +100	-100 +200	-200 +325	-325			
PHASE I							
356452	trace	1.2	5.2	93.4		12.60	
356453	0.2	1.2	10.6	87.6		14.63	
356454	trace	1.0	4.4	94.4		11.97	
45 356455	0.2	1.6	4.8	93.2		12.40	
PHASE II							
493705	trace	3.4	6.2	90.3		13.97	
493706	trace	2.8	5.6	92.4		13.63	
PHASE III							
493678	trace	3.6	7.0	89.2		13.35	

TABLE 3. EXTRUSION CONDITIONS - PHASES I, II

Z , cm/cm-sec	Average Strain Rate, cm/cm-sec	Billet Temperature, °C	Tooling Temperature °C
4.30×10^3	5.91×10^{-3}	482.2	482.2
$*2.56 \times 10^{10}$	4.80×10^{-2}	426.7	426.7
1.50×10^{12}	2.75×10^{-1}	371.1	371.1

*Conditions for fabrication of Phase II extrusions.

All extrusions 20:1 extrusion ration.

Original billet 23.5 cm dia. extruded to 1.3 cm X 16.5 cm cross section.

TABLE 4. TENSILE AND NOTCH TENSILE PROPERTIES OF HOT PRESSED BILLETS*

Billet Sample Number	Product Fabricated	Product Dash No.	Tensile Strength,		Yield Strength,		Elongation, %	R.A., %	NTS/YS
			ksi	MPa	ksi	MPa			
356452-1 -2 -3 -4 -6 -7	--	-1	73.9	510	65.3	450	13	30	1.30
	FA	-2	73.8	509	65.8	454	11	24	1.28
	FABC	-3	76.8	530	68.7	474	12	29	1.20
	EZ1	-4BG	73.2	505	64.3	443	11	14	0.73
	EZ2	-6G	74.1	511	65.9	454	12	22	1.22
	EZ3	-7G	73.0	503	64.1	442	12	23	1.22
	356453-1 -2 -3 -4 -6 -7	--	-1	75.4	520	66.7	460	12	22
FA		-2	74.8	516	66.3	457	12	24	1.19
FABC		-3	76.9	530	68.9	475	11	18	1.19
EZ1		-4AG	73.8	509	64.9	447	10	20	1.17
EZ2		-6G	71.8	495	61.8	426	11	23	1.24
EZ3		-7G	75.6	521	67.3	464	11	24	1.16
356454-1 -2 -3 -4 -5 -6		--	-1	77.6	507	64.0	441	13	29
	FA	-2	74.4	513	65.3	450	10	22	1.20
	FABC	-3	71.6	454	61.8	426	9	22	1.22
	EZ1	-4AG	74.2	512	65.9	454	13	27	1.23
	EZ2	-5G	75.4	520	66.4	458	11	20	1.17
	EZ3	-6G	76.2	525	67.6	466	12	27	1.10
	356455-1 -2 -3 -4 -5 -6	--	-1	75.5	521	66.9	461	13	29
FA		-2	74.0	510	64.7	446	11	20	1.24
FABC		-3	74.6	514	65.6	452	12	26	1.22
EZ1		-4AG	73.6	507	64.4	444	13	30	1.25
EZ2		-5G	76.1	525	67.6	466	12	24	1.20
EZ3		-6G	74.0	510	64.7	446	11	26	1.24

*Samples aged 24 hours at 121°C plus 14 hours at 163°C following solution heat treatments.
All samples tested in radial direction.

TABLE 5

UNIAXIAL TENSILE PROPERTIES OF P/M BILLETS

Sample Number	Co Content (w/o)	Tensile Strength,		Yield Strength,*		El., %	R.A., %
		ksi	MPa	ksi	MPa		
356452-1	0.00	80.4	554	73.5	507	7.1	11
356453-1	0.38	81.4	561	74.5	514	8.6	13
356454-1	0.85	82.7	570	75.4	520	8.6	14
356455-1	0.42 [‡]	81.2	560	74.1	511	10.0	18
Average		81.43	560.8	74.38	512.8		
Std. Deviation		0.95	6.6	0.80	5.5		

*0.2% offset value.

[‡]Average value for blended powders.

Artificially aged 24 hours at 121°C + 4 hours at 163°C.

TABLE 6

UNIAXIAL TENSILE PROPERTIES OF P/M FORGINGS

Sample Number	Co Content (w/o)	Forging Sequencet	Tensile Strength,		Yield Strength,*		El., %	R.A., %
			ksi	MPa	ksi	MPa		
356452-2	0.00	A-D	80.8	557	74.3	512	13.6	33
-3		ABC-D	82.1	566	74.9	516	13.6	38
356453-2	0.38	A-D	81.9	565	74.9	516	12.1	33
-3		ABC-D	78.0	538	71.7	494	15.7	40
356454-2	0.85	A-D	81.6	563	73.9	510	12.9	31
-3		ABC-D	81.1	559	74.4	513	12.1	31
356455-2	0.42‡	A-D	79.7	550	71.7	494	12.9	24
-3		ABC-D	80.9	558	74.4	513	14.3	31
Average			80.76	556.8	73.78	508.7		
Std. Deviation			1.35	9.3	1.32	9.1		

*0.2% offset value.

†A-D A - upset and draw.

‡Average value for blended powders.

#Average value for blended powders.

Artificially aged 24 hours at 121°C + 4 hours at 163°C.

TABLE 7
UNIAXIAL TENSILE PROPERTIES OF P/M EXTRUSIONS

Sample Number	Co Content (w/o)	Z (Sec ⁻¹)	Tensile Strength,		Yield Strength,*		El., %	R.A., %
			ksi	MPa	ksi	MPa		
356452-4BG	0.00	1.5x10 ¹²	88.9	613	82.9	572	10.0	18
-6G		2.6x10 ¹⁰	86.1	594	80.2	553	11.4	26
-7G		4.3x10 ⁸	87.4	603	82.0	565	11.4	23
356453-4AG	0.38	1.5x10 ¹²	87.6	604	83.2	574	3.6 ⁺	8 ⁺
-6G		2.6x10 ¹⁰	86.7	598	81.2	560	11.9	29
-7G		4.3x10 ⁸	88.5	610	82.7	570	10.7	25
356454-4AG	0.85	1.5x10 ¹²	87.7	605	81.7	563	10.7	21
-5G		2.6x10 ¹⁰	87.5	603	81.2	560	10.7	25
-6G		4.3x10 ⁸	89.6	618	83.2	574	10.0	19
356455-4AG	0.42 [‡]	1.5x10 ¹²	87.7	605	82.2	567	4.3 [#]	6 [#]
-5G		2.6x10 ¹⁰	86.7	598	81.0	558	11.4	27
-6G		4.3x10 ⁸	88.5	610	83.2	574	11.4	22
Average			87.74	604.9	82.06	565.8		
Std. Deviation			1.00	6.9	1.01	7.0		

*0.2% offset value.
 #Failed outside gauge area.
 †Failed through gauge marks.
 ‡Average value for blended powders.

Artificially aged 24 hours at 121°C + 4 hours at 163°C.

TABLE 3
 CYCLIC LIVES OF P/M BILLETS
 OVER VARIOUS REGIMES OF CRACK GROWTH

Sample Number	Co Content (w/o)	Cyclic Life ($\times 10^3$ cycles)	
		1.1-3.0 cm (0.43-1.18 in.)	1.1-1.7 cm (0.43-0.67 in.) 2.4-3.0 cm (0.67-1.19 in.)
356452-1	0.00	32.14	18.93
356453-1	0.38	36.17	21.40
356454-1	0.85	25.50	15.55
356455-1	0.42 \dagger	33.41	19.60
Average		31.81	18.87
Std. Deviation		4.53	2.45

\dagger Average for blended powders.

Artificially aged 24 hours at 121°C + 4 hours at 163°C.

TABLE 9

CYCLIC LIVES OF P/M FORGINGS
OVER VARIOUS REGIMES OF CRACK GROWTH

Sample Number	Co Content (w/o)	Forging Sequence	Cyclic Life ($\times 10^3$ cycles)			
			1.1-3.0 cm (0.48-1.18 in.)	1.1-1.7 cm (0.43-0.67 in.)	2.4-3.0 cm (0.67-1.19 in.)	
356452-2	0.00	A-D	30.89	15.78	5.51	
-3		ABC-D	38.36	18.82	7.47	
356453-2	0.38	A-D	33.17	15.92	7.19	
-3		ABC-D	36.33	18.57	6.39	
356454-2	0.85	A-D	46.39	22.00	8.97	
-3		ABC-D	38.08	19.58	6.65	
356455-2	0.42 \ddagger	A-D	44.73	22.70	8.25	
-3		ABC-D	36.95	19.88	5.84	
Average			38.11	19.16	7.03	
Std. Deviation			5.26	2.50	1.18	

\ddagger Average for blended powders.

Artificially aged 24 hours at 121°C + 4 hours at 163°C.

TABLE 10

CYCLIC LIVES OF P/M EXTRUSIONS
OVER VARIOUS REGIMES OF CRACK GROWTH

Sample Number	Co Content (w/o)	Z (Sec ⁻¹)	Cyclic Life ($\times 10^3$ cycles)		
			1.1-3.0 cm (0.43-1.18 in.)	1.1-1.7 cm (0.43-0.67 in.)	2.4-3.0 cm (0.67-1.19 in.)
356452-4BG	0.00	1.5x10 ¹²	45.45	21.97	8.06
-6G		2.6x10 ¹⁰	35.37	17.77	6.48
-7G		4.3x10 ⁹	39.50	20.10	6.92
356453-4AG	0.38	1.5x10 ¹²	41.02	20.35	7.50
-6G		2.6x10 ¹⁰	33.88	17.41	5.78
-7G		4.3x10 ⁹	42.43	21.05	7.73
356454-4AG	0.85	1.5x10 ¹²	42.53	20.59	8.17
-5G		2.6x10 ¹⁰	41.88	20.04	8.28
-6G		4.3x10 ⁹	44.71	22.41	8.08
356455-4AG	0.42 [#]	1.5x10 ¹²	46.75	22.22	8.93
-5G		2.6x10 ¹⁰	42.00	21.34	7.60
-6G		4.3x10 ⁹	43.49	22.12	7.74
Average			41.58	20.61	7.61
Std. Deviation			3.81	1.64	0.86

[#]Average for blended powders.

Artificially aged 24 hours at 121°C + 4 hours at 163°C.

TABLE 11. RESULTS OF AGING STUDY FOR SELECTION OF ALLOY TEMPERERS FOR
PHASE II EXTRUSIONS

Alloy	Aging Time, 163°C	Yield Strength,		Tensile Strength,		Elong., %	R.A., %
		MPa	ksi	MPa	ksi		
CT91 (356453-6G)	4.0 (T7X1)	561	(81.2)	603	(87.5)	13.0	27
	13.0	502	(72.8)	558	(80.9)	13.0	34
	16.0 (T7X2)	481	(69.7)	542	(78.6)	15.0	40
MA88 (493706-1H)	0.5 (T7X1)	578	(83.8)	632	(91.7)	12.0	21
	* 1.0	552	(80.1)	607	(88.0)	12.5	23
	4.0	543	(78.7)	596	(86.5)	12.0	27
	13.0	502	(72.8)	550	(81.1)	13.0	36
	16.0	493	(71.5)	555	(80.5)	13.0	33
	17.5 (T7X2)	487	(70.6)	551	(79.9)	14.2	41
*19.0	468	(67.9)	540	(78.3)	16.0	40	
MA90 (493705-1H)	4.0	581	(84.3)	613	(88.9)	11.0	28
	5.0 (T7X1)	566	(82.1)	605	(87.8)	11.0	26
	* 6.0	548	(79.5)	594	(86.2)	13.0	32
	13.0	494	(71.7)	554	(80.4)	16.0	43
	14.0 (T7X2)	474	(68.8)	537	(77.9)	14.5	44
	*15.0	476	(69.0)	543	(78.6)	15.5	43
16.0	477	(69.2)	541	(78.5)	15.0	38	

*Average results for two tests.

Nominal target yield strengths: T7X1: 560 MPa (81 ksi)
T7X2: 483 MPa (70 ksi)

TABLE 12. TENSILE PROPERTIES OF PHASE II MATERIALS

Alloy	Hrs at 163°C	Yield Strength, MPa (ksi)	Tensile Strength, MPa (ksi)	Elongation, %	Reduction in Area, %
<u>Extrusions</u>					
Zn/Mg/Cu/Co					
CT91	4.0 (T7X1)	560 (81.2)	598 (86.7)	11.9	29
	16.0 (T7X2)	481 (69.7)	542 (78.6)	13.4	40
MA88	0.5 (T7X1)	578 (83.8)	632 (91.7)	12.0	21
	17.5 (T7X2)	487 (70.6)	551 (79.9)	14.2	41
MA90	5.0 (T7X1)	566 (82.1)	605 (87.8)	11.0	26
	14.0 (T7X2)	474 (68.8)	537 (77.9)	14.5	44
55					
7050-T76511	--	514 (74.6)	576 (83.6)	12.4	31
<u>Hand Forgings</u>					
CT91	T7X1	516 (74.8)	565 (82.0)	12.1	33
	T7X2	425 (61.6)	493 (71.5)	15.9	46
MA88	T7X1	508 (73.7)	584 (84.7)	13.1	24
	T7X2	436 (63.2)	507 (73.5)	15.2	44
MA90	T7X1	522 (75.7)	574 (83.3)	12.4	31
	T7X2	454 (65.6)	518 (75.1)	13.8	38

TABLE 13. CRACK LENGTHS AT FRACTURE FOR CCT SPECIMENS
FROM PHASE II HAND FORGINGS

Specimen No.	Alloy and Temper	a *		a ₂ *		Figure
		cm	(in.)	cm	(in.)	
356453-B2-LT2	CT91-T7X2	4.62	1.82	3.12	1.23	39
493706-1-LT1	MA88-T7X1	4.47	1.76	3.20	1.26	41
493706-2-LT1	MA88-T7X2	2.54	1.00	4.42	1.74	41
493706-1-LT2	MA88-T7X1	2.67	1.05	4.70	1.85	39
493705-1-LT1	MA90-T7X1	4.57	1.80	3.45	1.36	41
493705-2-LT1	MA90-T7X2	2.92	1.15	3.56	1.40	41
493705-1-LT2	MA90-T7X1	3.43	1.35	4.45	1.75	39
493705-2-LT2	MA90-T7X2	3.25	1.28	4.80	1.89	39

*See Figure 7 for CCT specimen configuration.

TABLE 14. CALCULATED PLANE STRAIN MONOTONIC PLASTIC ZONE SIZES
FOR EXPERIMENTAL MATERIALS

$\overline{MPa\sqrt{m}}$	$\frac{\Delta K}{(\text{ksi}\sqrt{\text{in.}})}$	$\overline{MPa\sqrt{m}}$	$\frac{K_{\text{max}}}{(\text{ksi}\sqrt{\text{in.}})}$	\overline{MPa} (82 ksi)	\overline{MPa} (75 ksi)	\overline{MPa} (70 ksi)
2.2	2.0	3.3	3.0	4.8	5.7	6.5
3.3	3.0	5.0	4.5	10.7	12.7	14.7
4.4	4.0	6.6	6.0	19.0	22.8	26.1
5.5	5.0	8.3	7.5	30.0	35.5	40.9
6.6	6.0	9.9	9.0	43.0	51.2	58.8
7.7	7.0	11.6	10.5	58.2	69.6	80.0
8.8	8.0	13.2	12.0	76.0	91.0	104.5
9.9	9.0	14.9	13.5	97.0	115.2	132.0
11.0	10.0	16.5	15.0	119.0	142.2	163.3

57

565 MPa = approximate yield stress for P/M-T7X1 extrusions.

517 MPa = yield stress for I/M 7050-T76511 extrusions.

483 MPa = approximate yield stress for P/M-T7X2 extrusions.

TABLE 15. SHORT-TRANSVERSE MECHANICAL PROPERTIES OF PHASE III HAND FORGINGS

Sample Number	Material	Stress Relief?	Tensile Strength, MPa	Tensile Strength, (ksi)	Yield Strength, MPa	Yield Strength, (ksi)	Elongation in 25 mm, %	R.A., %	NTS/YS	$K_Q, K_{Ic},$ MPa \sqrt{m}
493681	7XXX I/M	Yes	509.5	(73.9)	483	(70.1)	2.0	2.0	0.86	20.2
	7XXX I/M	Nc	479	(69.5)	>460.5#	(66.8)	1.0	1.5	<0.81#	22.3*
493678	7XXX P/M	Yes	480	(69.6)	437	(63.4)	2.5	2.5	1.32	40.5
	7XXX P/M	No	525	(76.2)	497	(72.1)	1.0	1.5	1.10	24.0*
354703	CT91	No	538	(78.0)	500	(72.5)	2.0/7.0	7.0	1.26	36.1*

58

NOTES

Tensile and notched tensile properties are average values from duplicate tests.

K_Q values are single test values only.

Alloy 354703 has comparable composition and fabrication history vs CT91 alloy 493678 of Phase III (see Table 16, Reference 3).

#Second tensile test failed before 0.2% offset at higher stress than yield strength recorded for initial test.

*ASTM E399 not satisfied because of excessive crack curvature. These values are not valid K_{Ic} measurements.

TABLE 16. AVERAGE¹ X-RAY RESIDUAL STRESS INDICATIONS ON FCG SPECIMENS

Original Parent Slab: Residual Stress State: Stress Orientation:	Residual Stress Indications (MPa)									
	T/2 Specimen					Surface Specimen ²				
	Nonstress Rel.		Stress Rel.			Nonstress Rel.		Stress Rel.		
	L	S	L	S		L	S	L	S	
Location ³										
A	-21	+19	-30	-40		-50	+9	-41	-26	
B	-28	+7	-55	-38		-64	+3	-55	-38	
Avg A & B	-24.5	+13	-42.5	-39		-57	+3	-48	-32	
D	-121	--	-59	--		-97	--	-79	--	
E	-97	--	-76	--		-62	--	-31	--	
Avg D & E	-109	--	-67.5	--		-79.5	--	-55	--	

- NOTES: 1. Averaged for P/M and I/M materials.
 2. Locations identified in Figure 58.
 3. Measurements made only for one surface specimen.

SI conversion: 1 ksi=6.894 MPa.

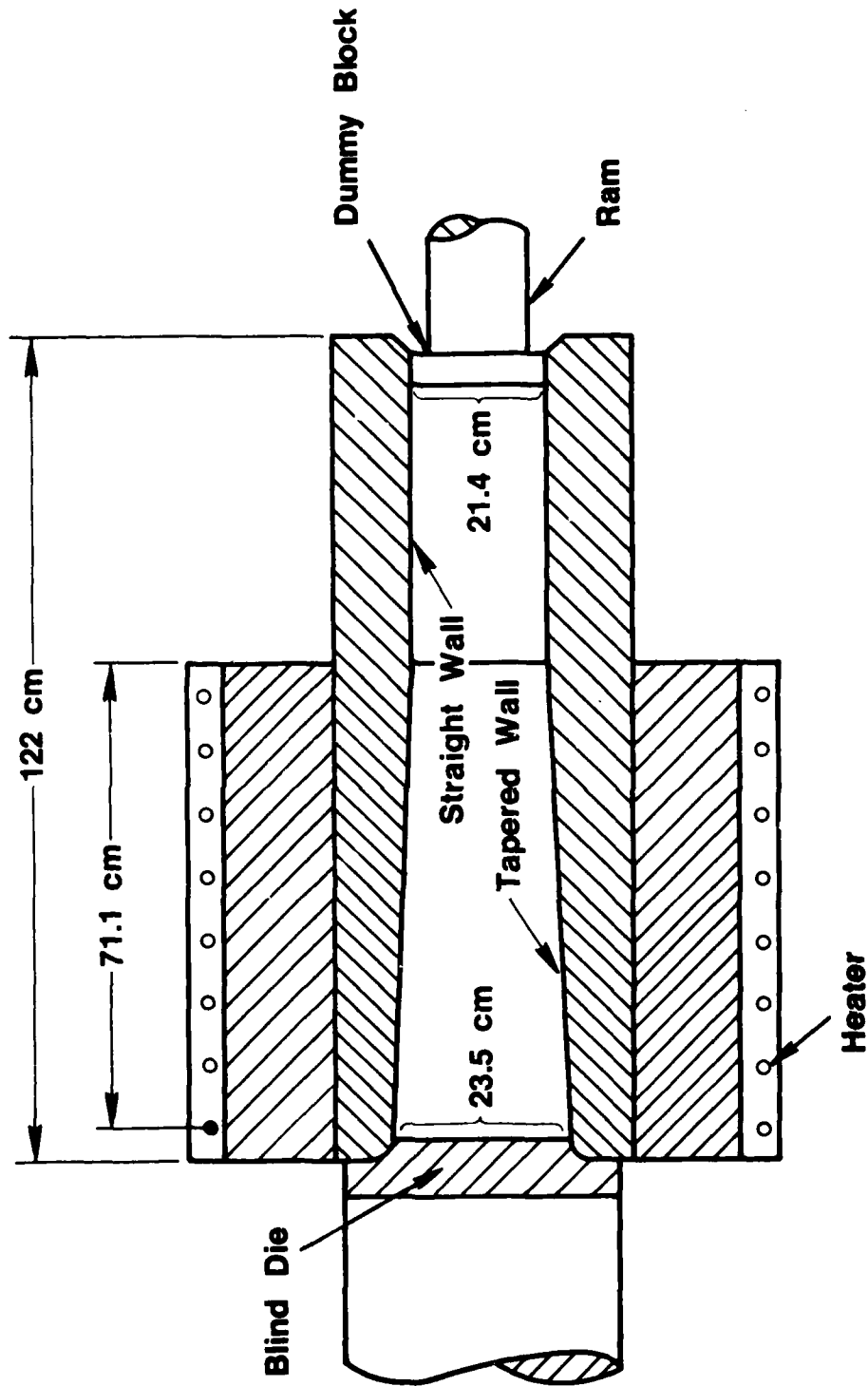


Figure 1. Schematic diagram of 21.4 cm hot compacting cylinder.

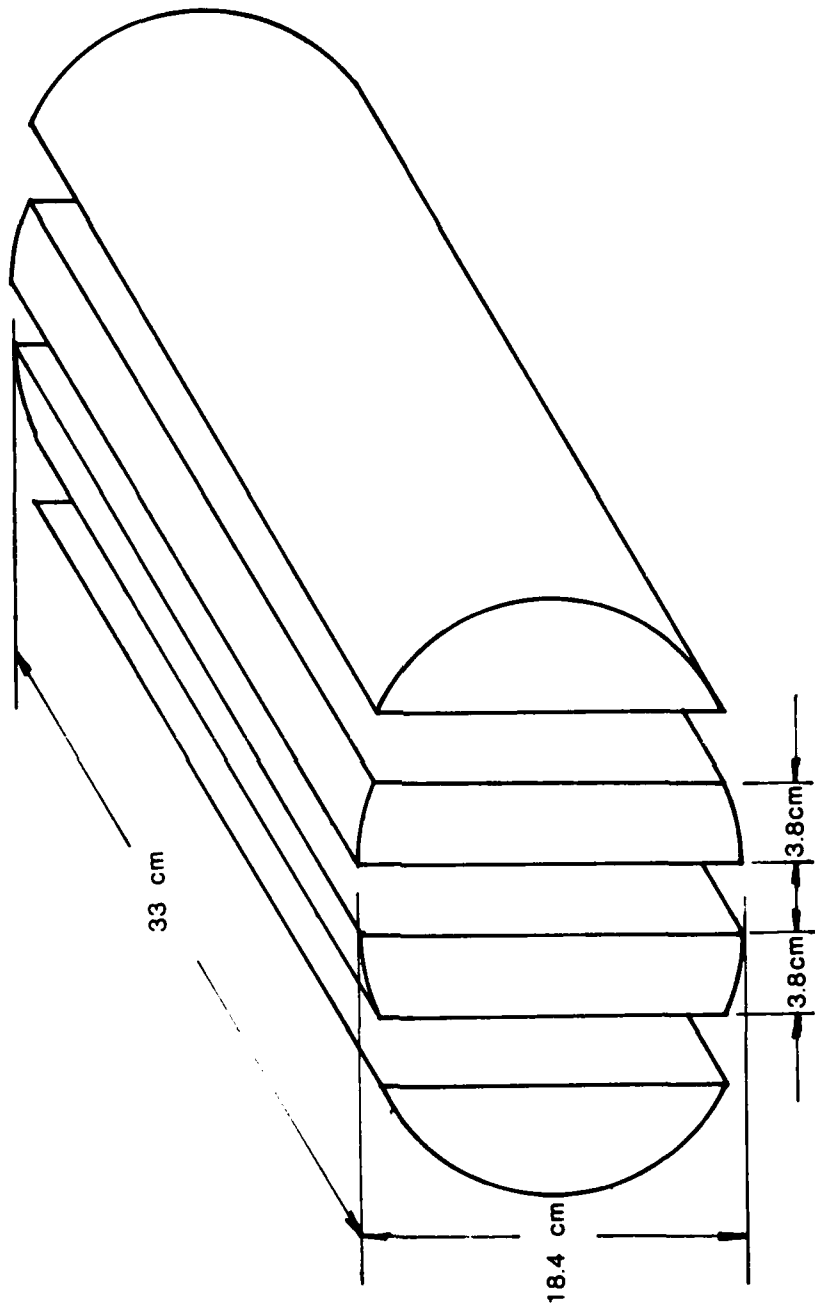


Figure 2. Sectioning layout for testing of Phase I hot-pressed billets.

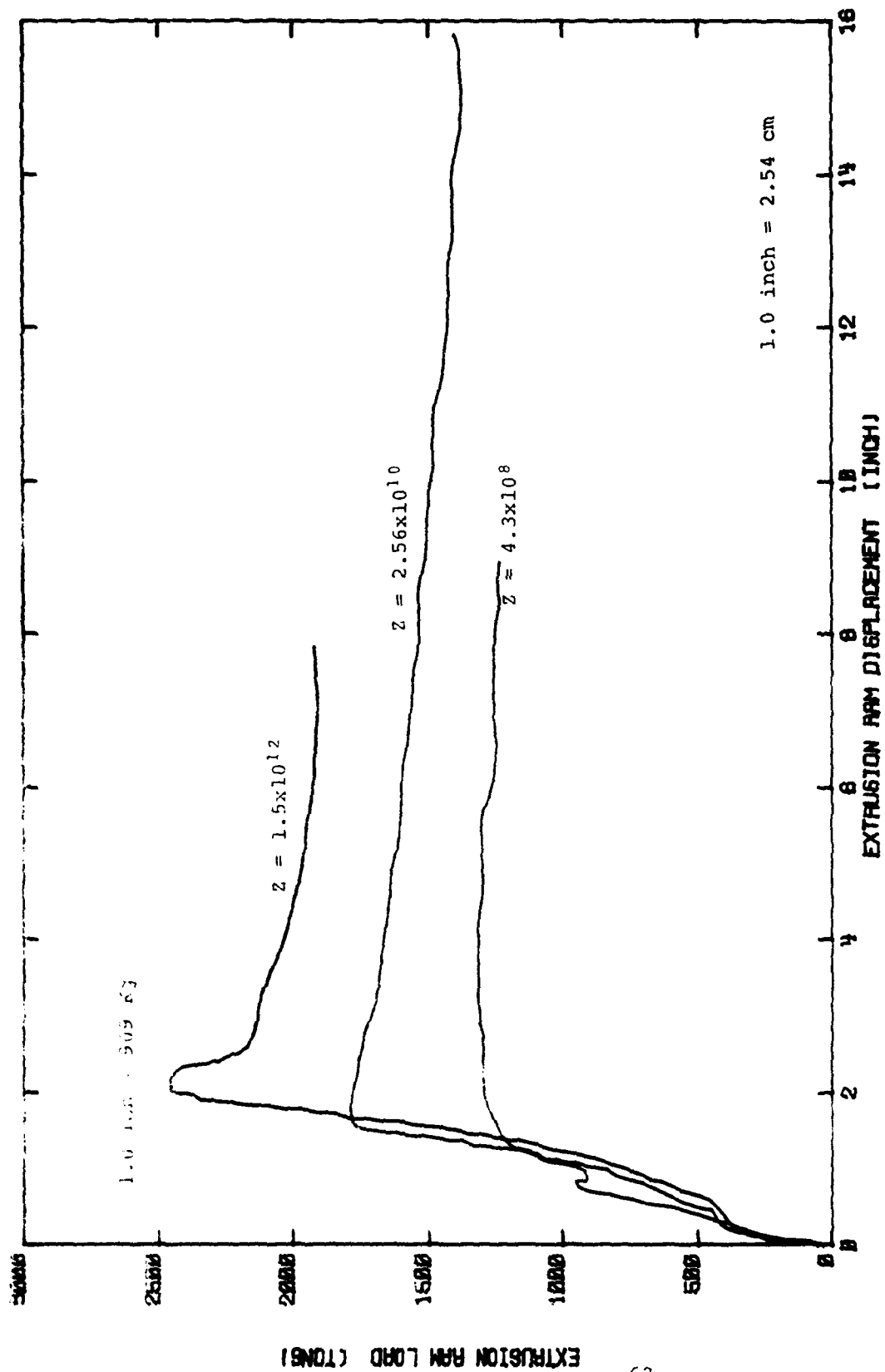


Figure 3. Extrusion load versus ram displacement for Phase I P/M extrusions.

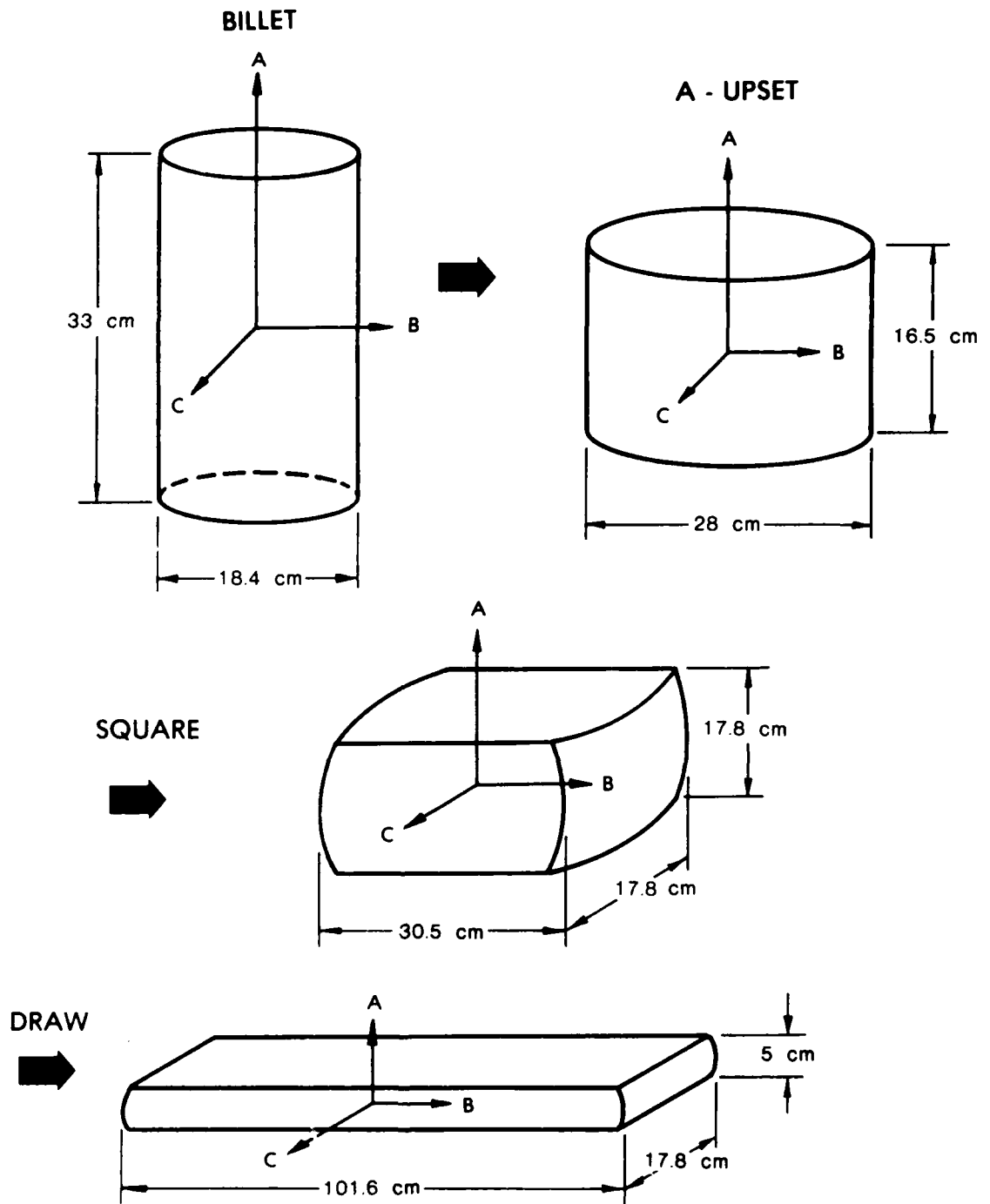


Figure 4. Forging sequence for production of A-upset and draw hand forgings.

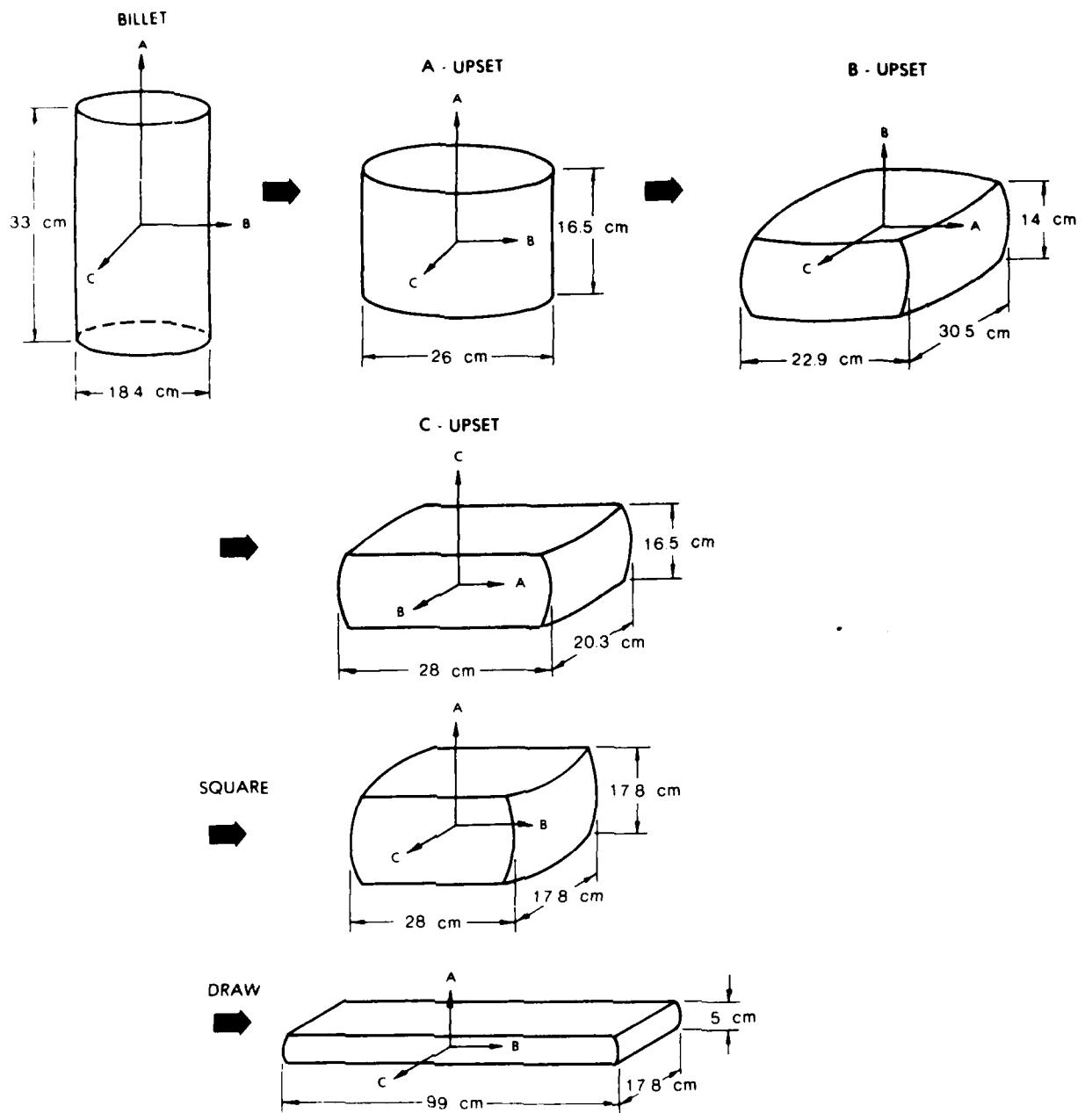
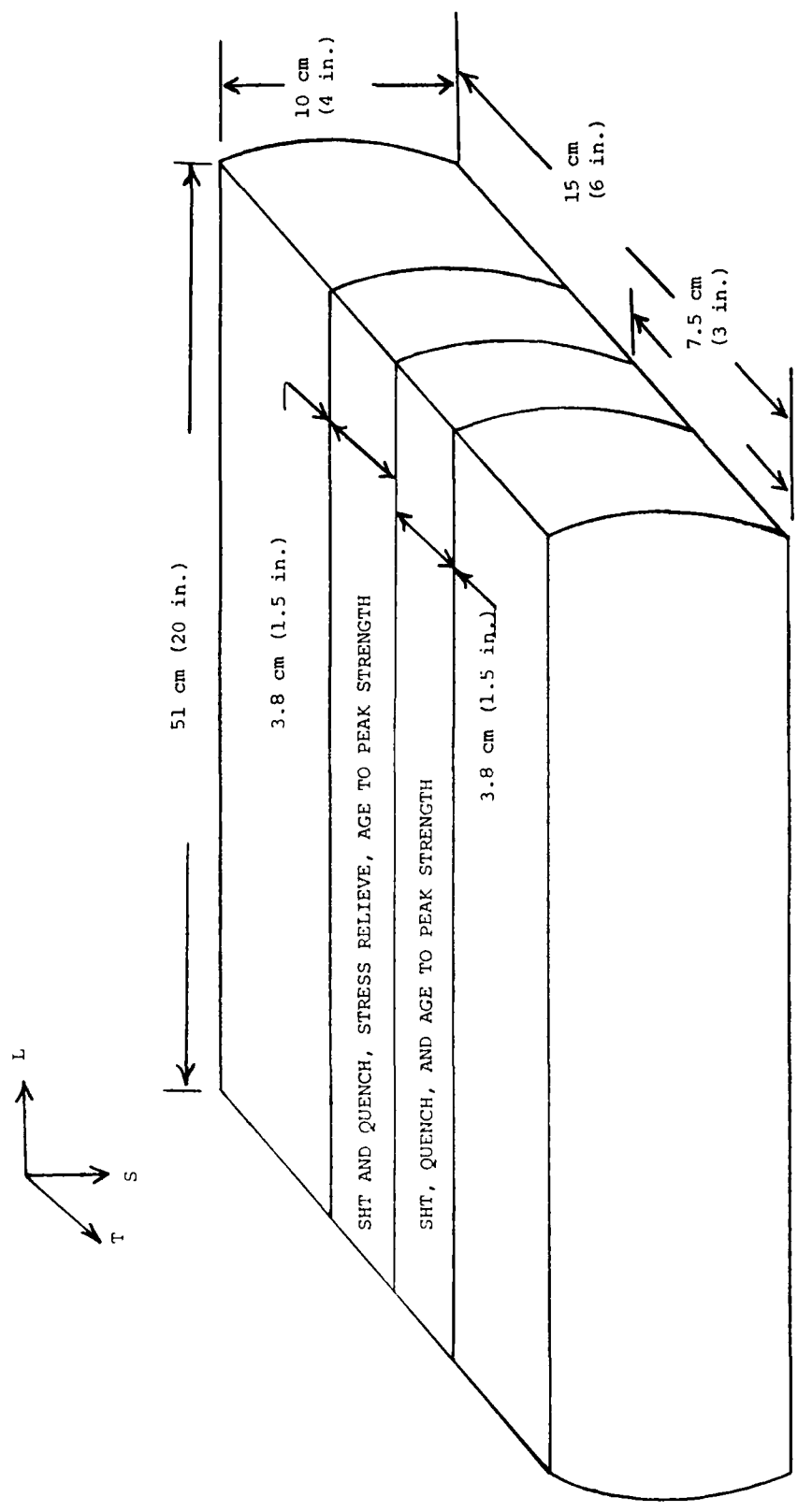


Figure 5. Forging sequence for production of ABC-upset and draw hand forgings.



ALL DIMENSIONS APPROXIMATE

MATERIALS: Co FREE P/M CT91 (MA87)
I/M 7175

Figure 6. Slabs removed from Phase III A-upset and draw hand forgings for subsequent heat treatment and mechanical testing.

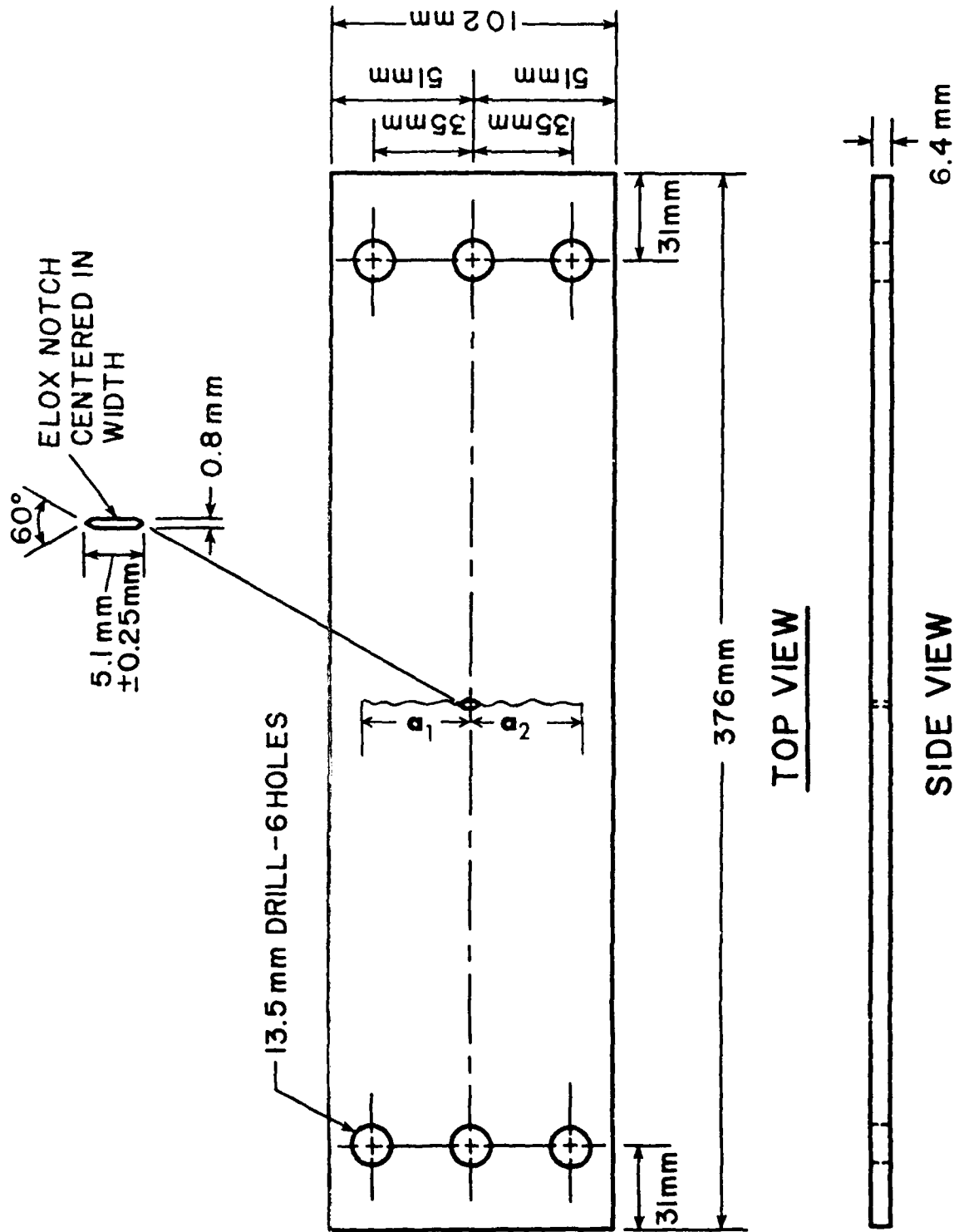


Figure 7. CCT specimen geometry used for Phase I and Phase II fatigue crack growth tests, L-T orientation.

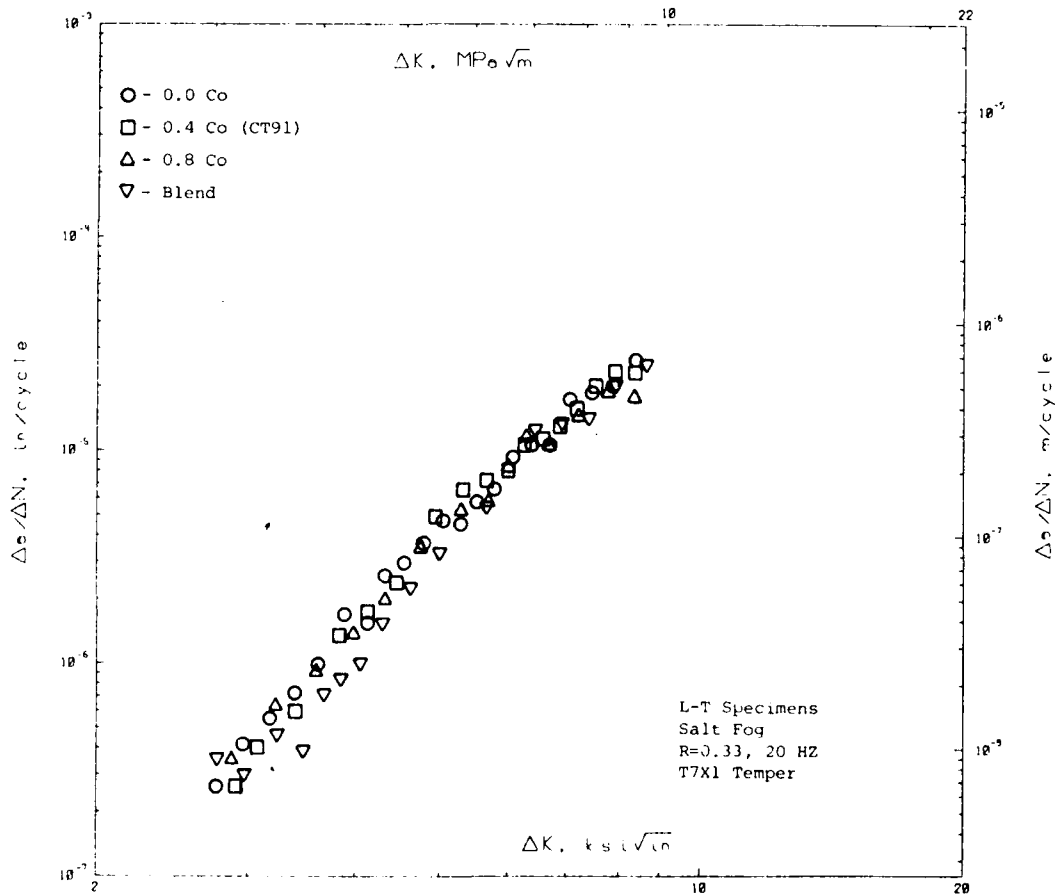


Figure 8. Fatigue crack growth data for Phase I A-upset and draw hand forgings tested in salt fog atmosphere.

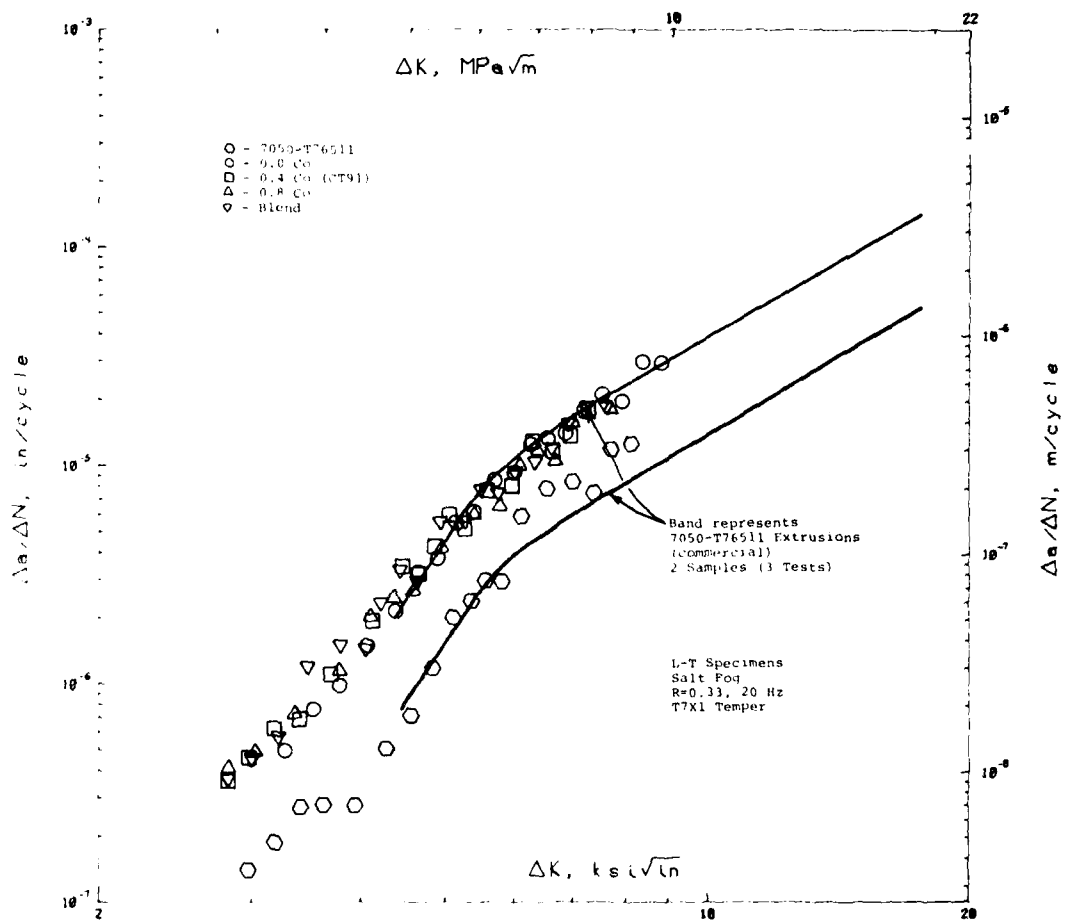


Figure 9. Fatigue crack growth data for Phase I medium Z extrusions tested in salt fog atmosphere.

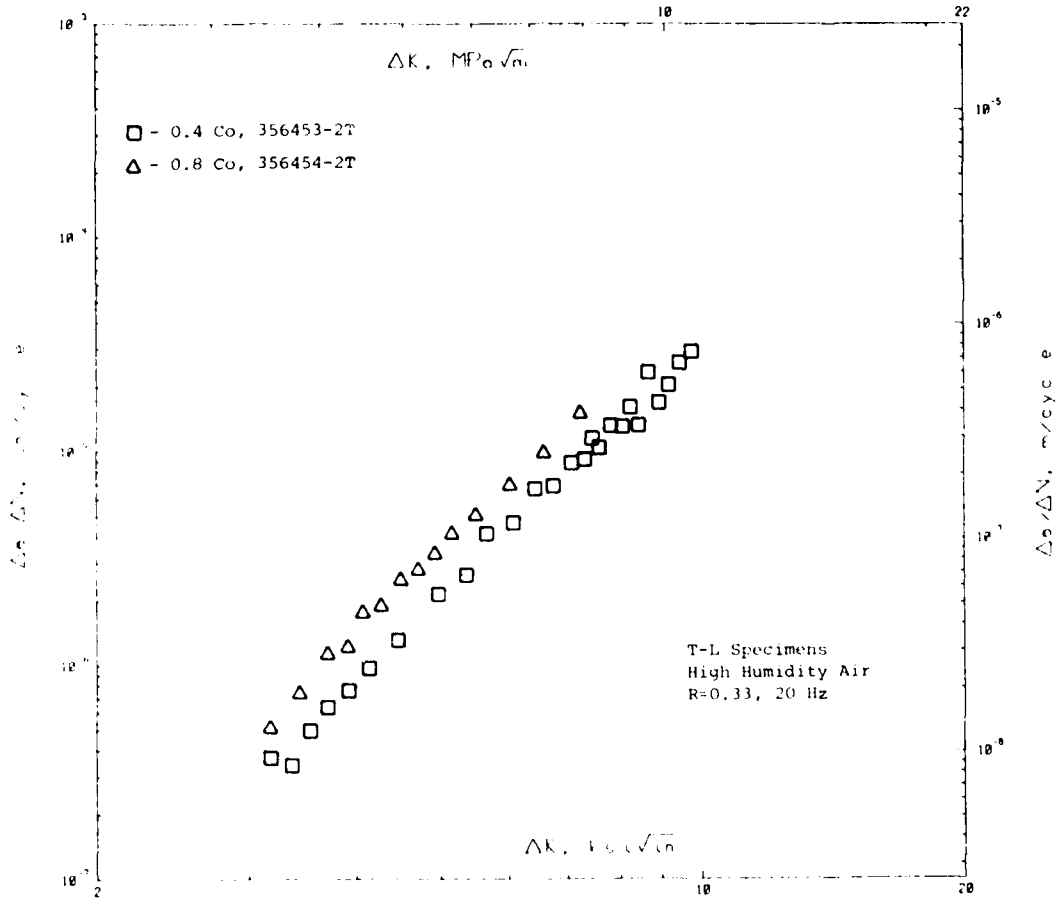


Figure 10. Fatigue crack growth data for T-L specimens from Phase I A-upset and draw hand forgings tested in humid air.

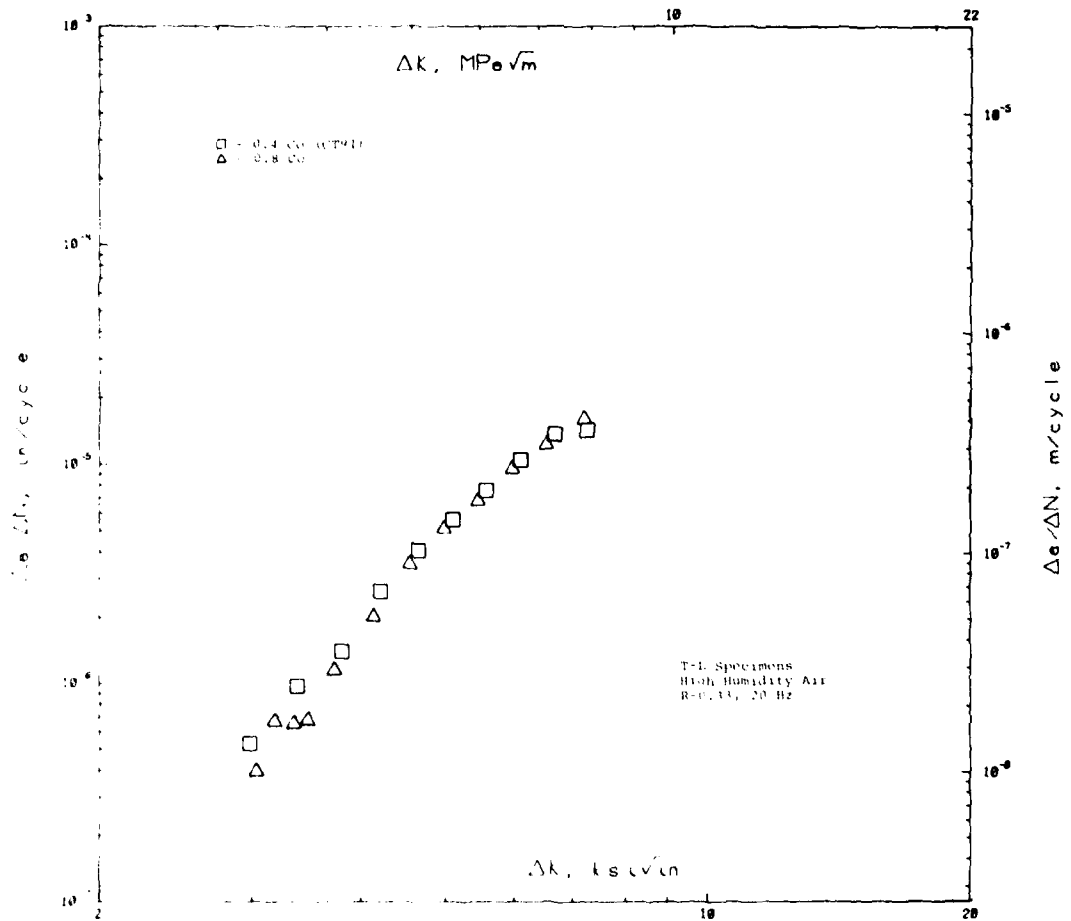


Figure 11. Fatigue crack growth data for T-L specimens from Phase I medium Z extrusions tested in humid air.

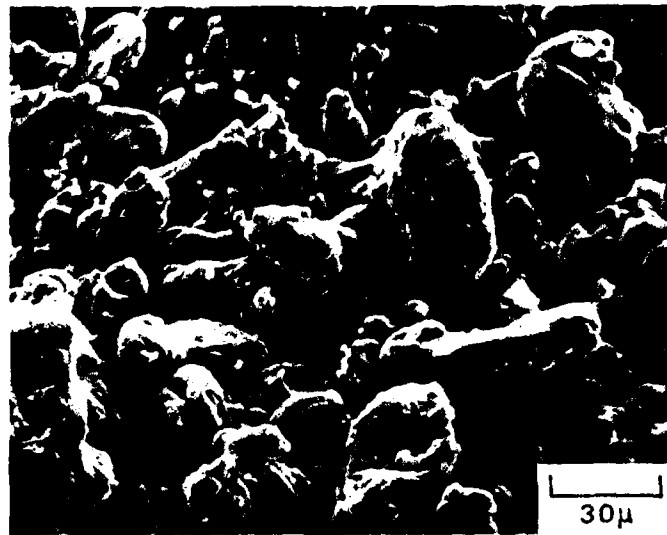


Figure 12. Scanning electron micrographs of as-atomized alloy 0.4 Co (CT91) powder.

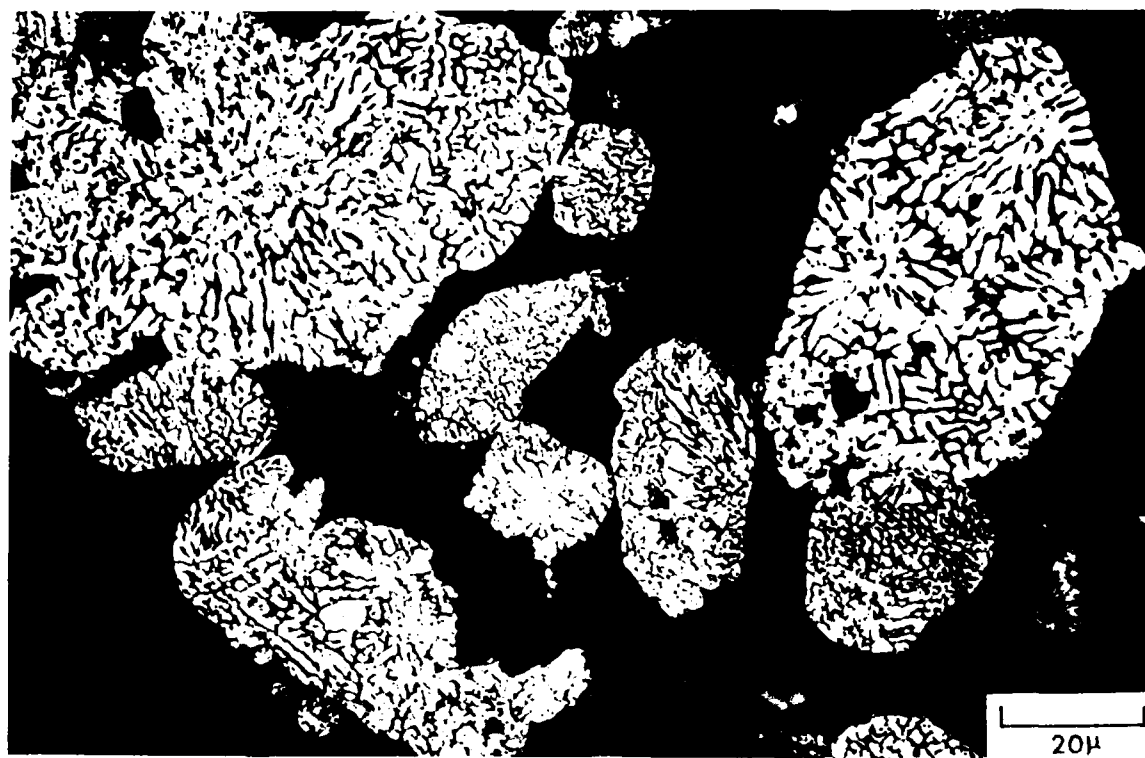


Figure 13. Optical micrograph of polished and etched atomized alloy CT91 powder particles.

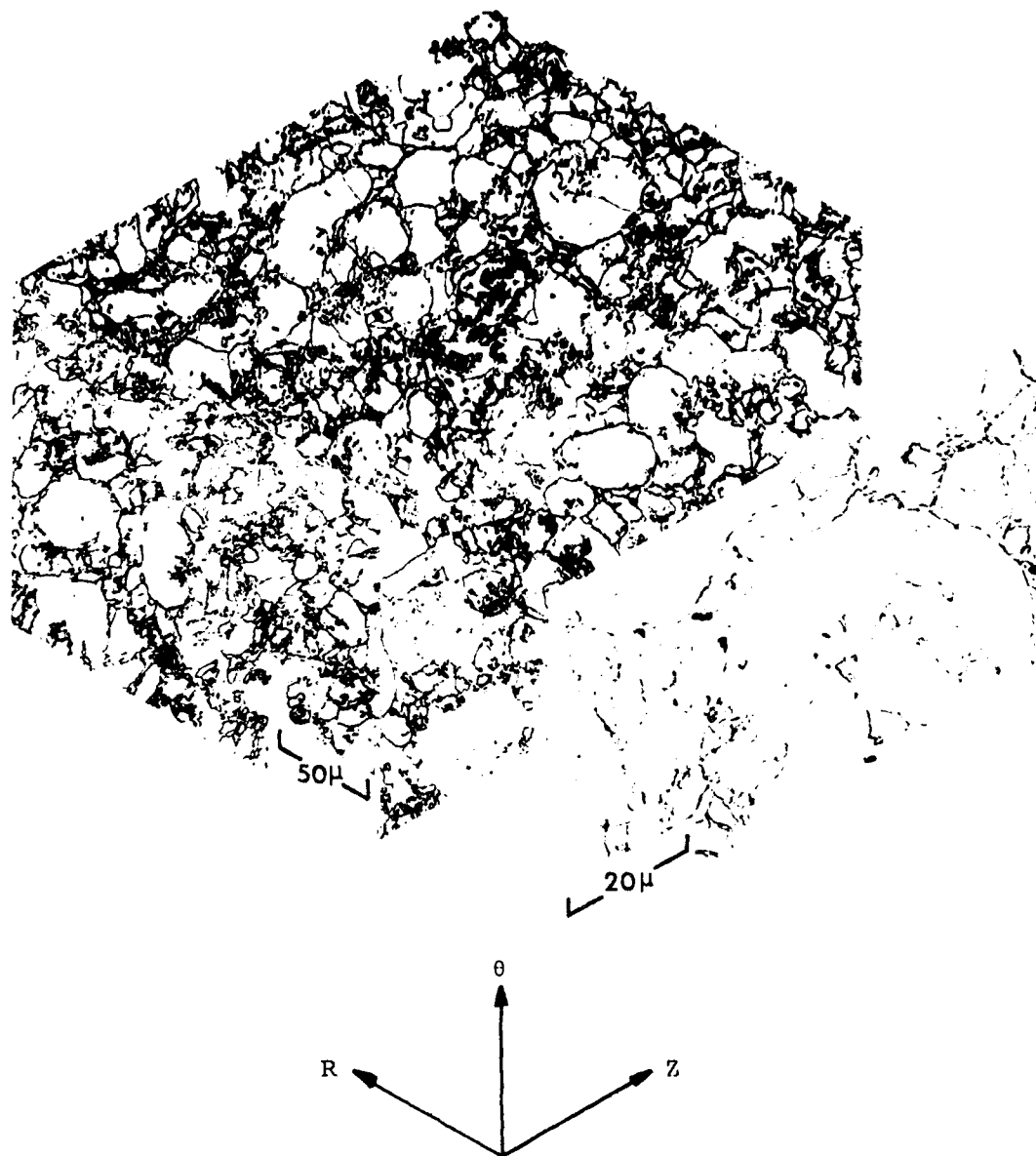


Figure 14. Optical microstructure of P/M billet, S-356452, 0.0 Co.

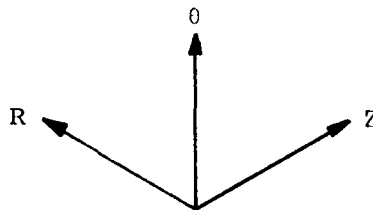
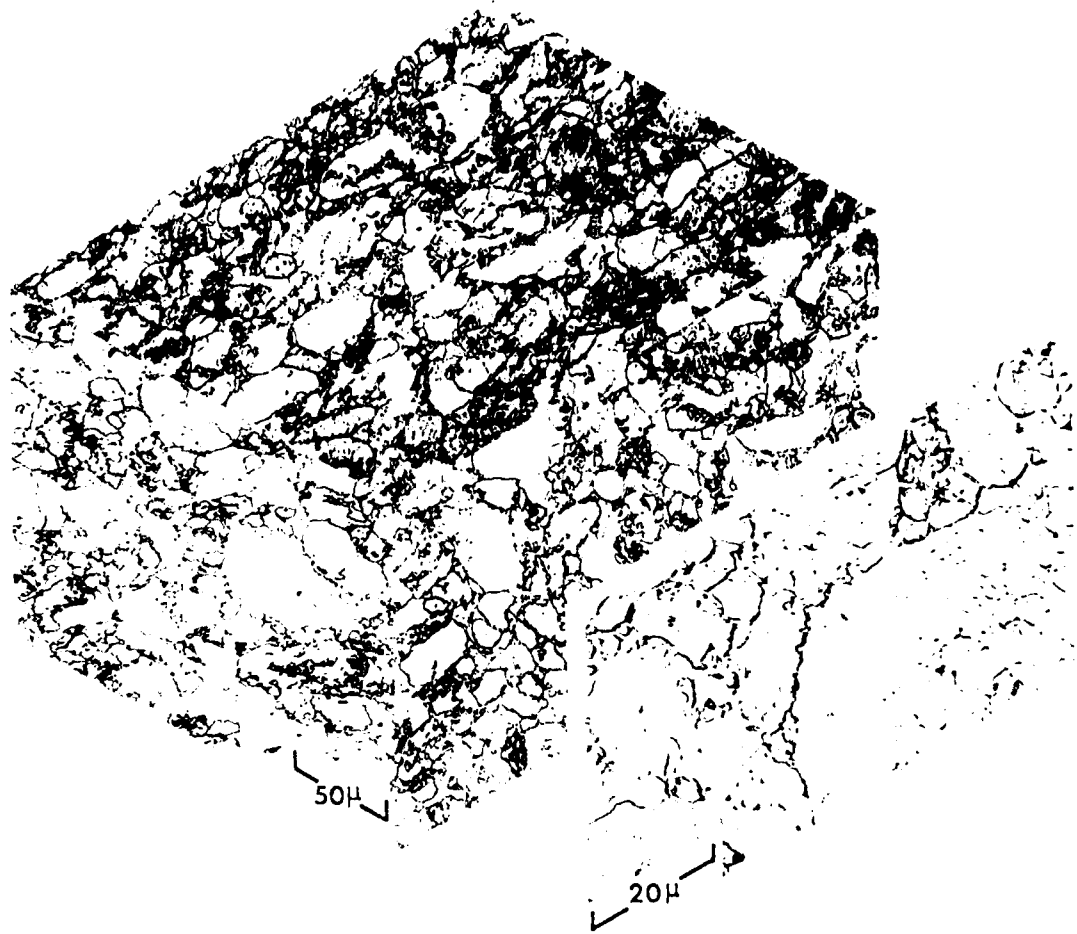


Figure 15. Optical microstructure of P/M billet, S-356453, 0.4 Co (CT91).

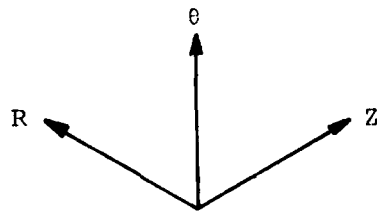
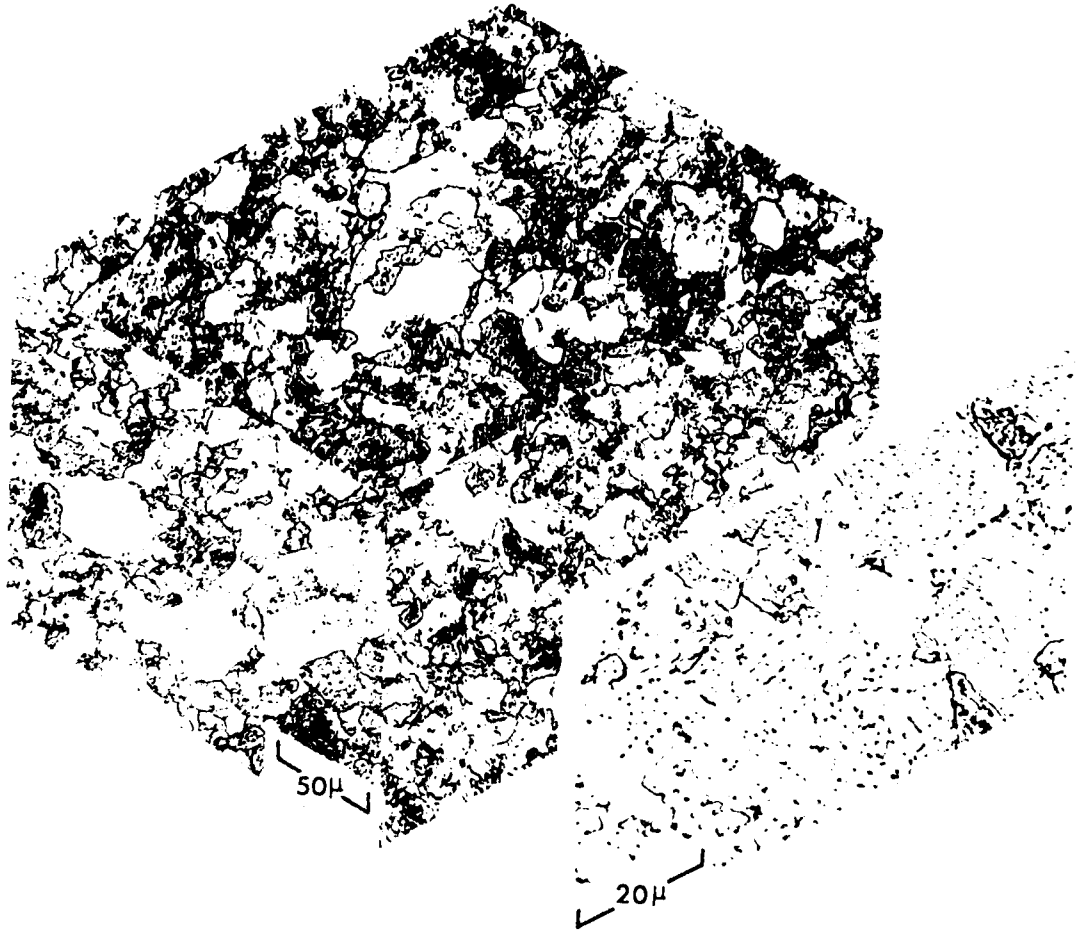


Figure 16. Optical microstructure of P/M billet, S-356454, 0.8 Co.

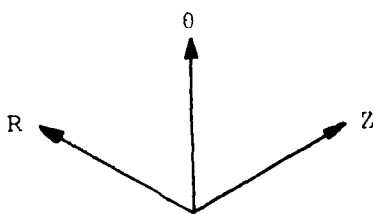
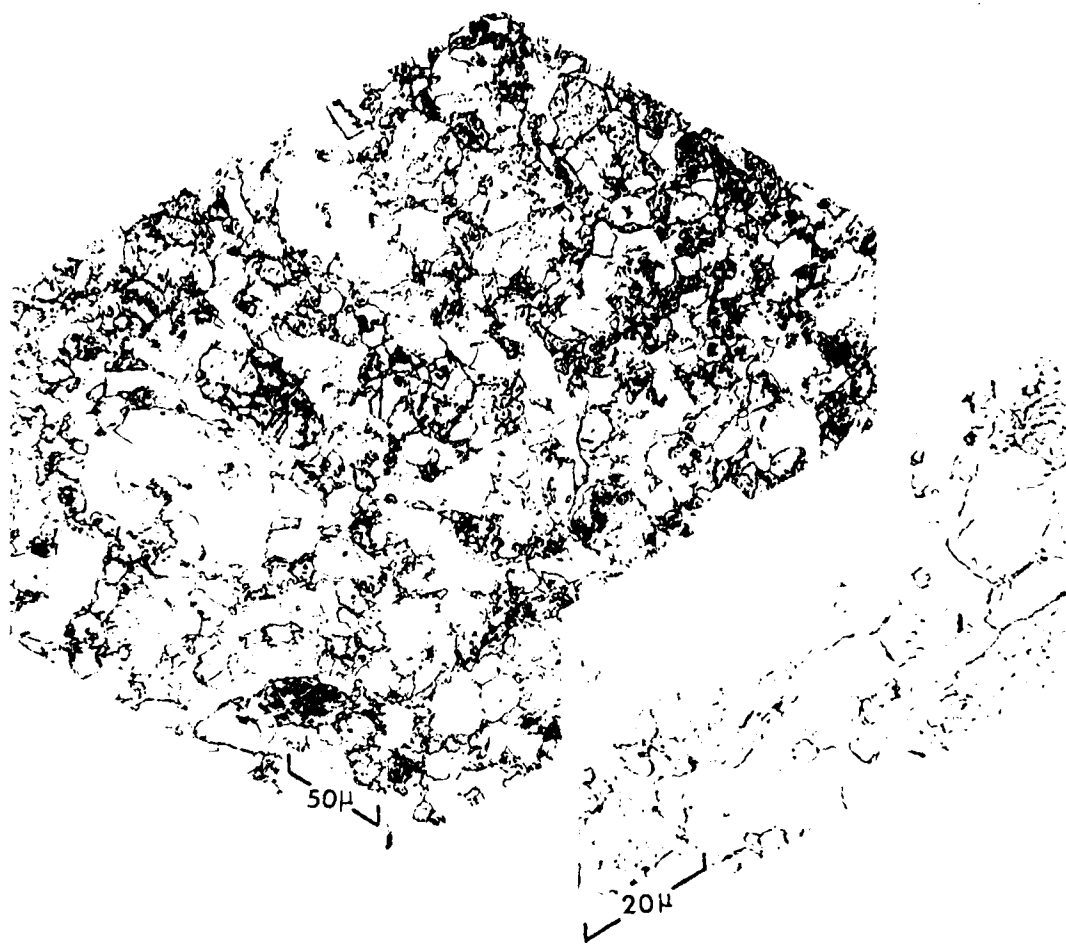


Figure 17. Optical microstructure of P/M billet, S-356455, blend.

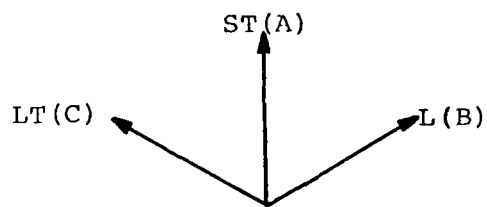
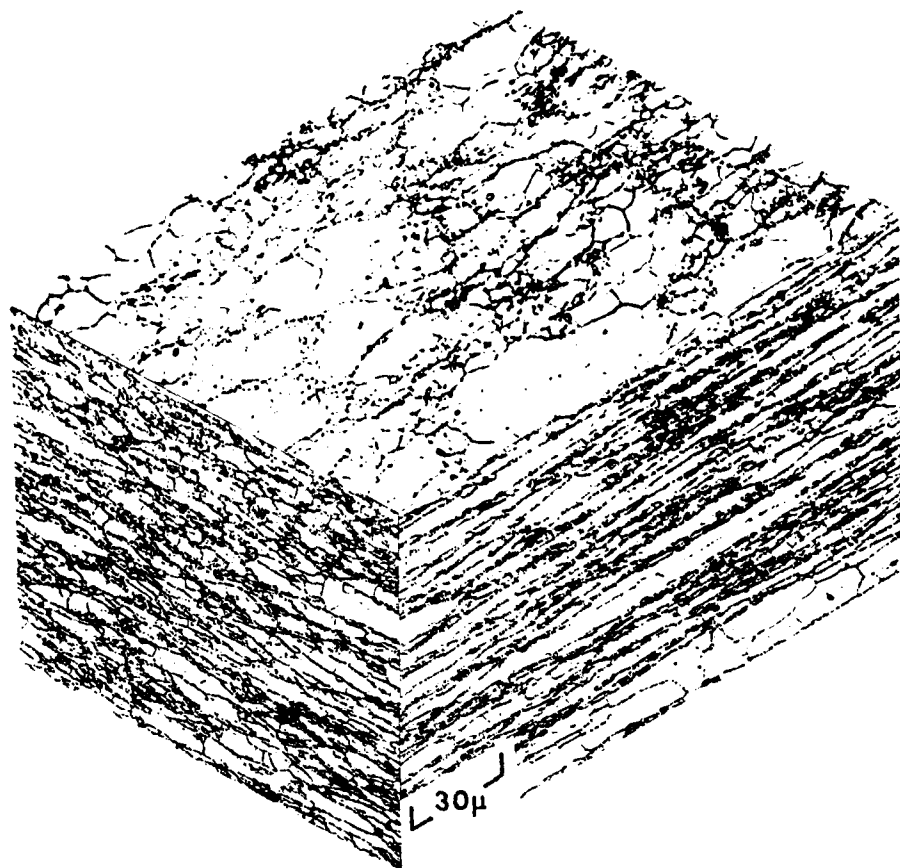


Figure 18. Optical microstructure of 0.0 Co A-upset and draw hand forging, S-356452-2T.

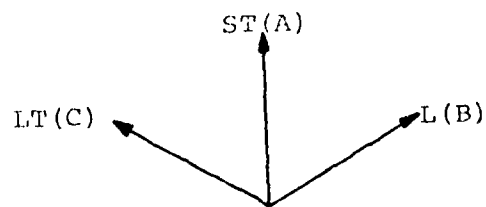
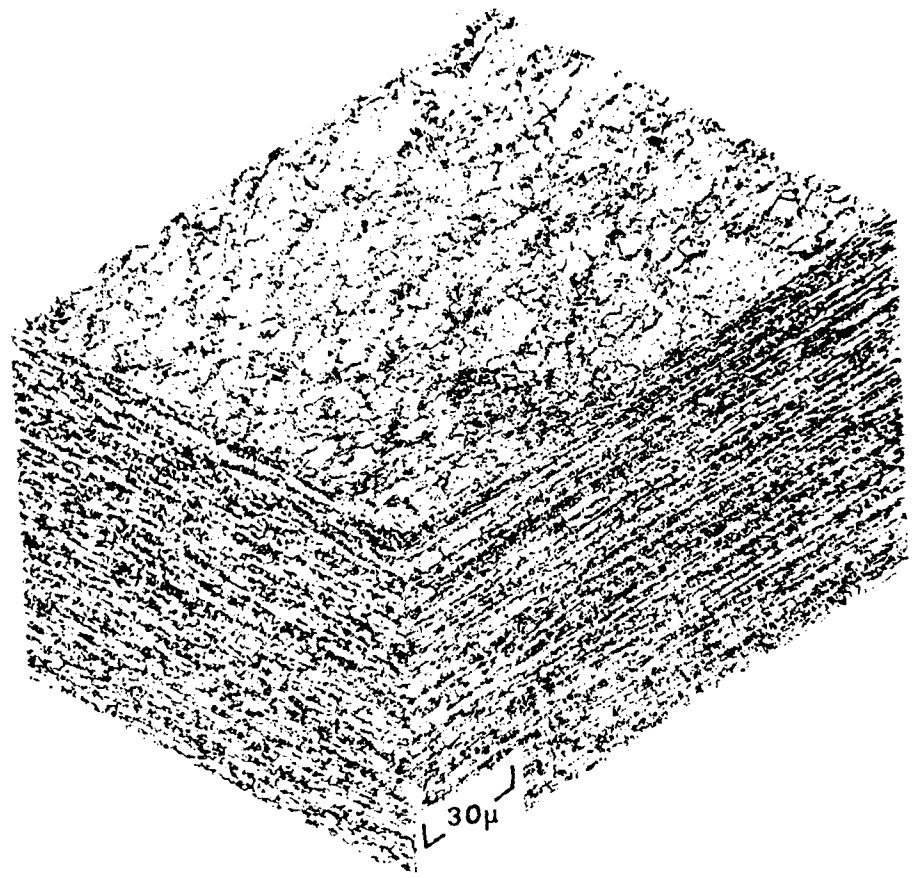


Figure 19. Optical microstructure of 0.0 Co ABC-upset and draw hand forging, S-356452-3T.

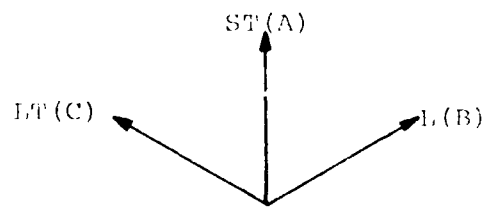
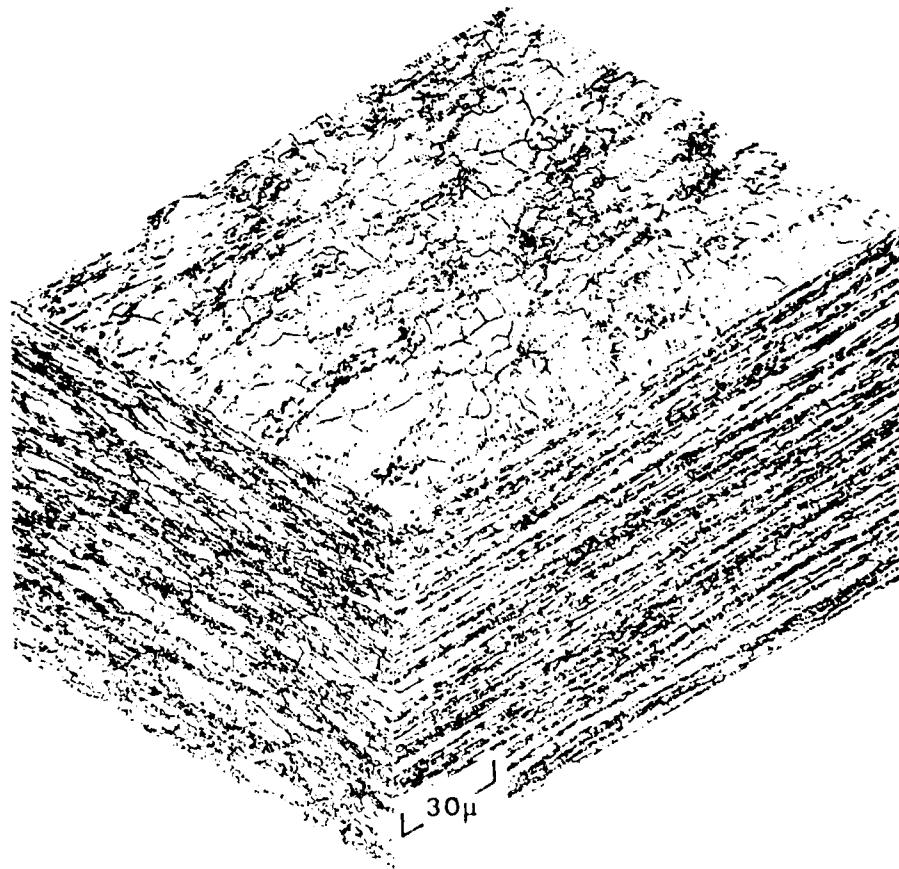


Figure 20. Optical microstructure of 0.4 Co A-upset and draw hand forging, S-356453-2T (CT91).

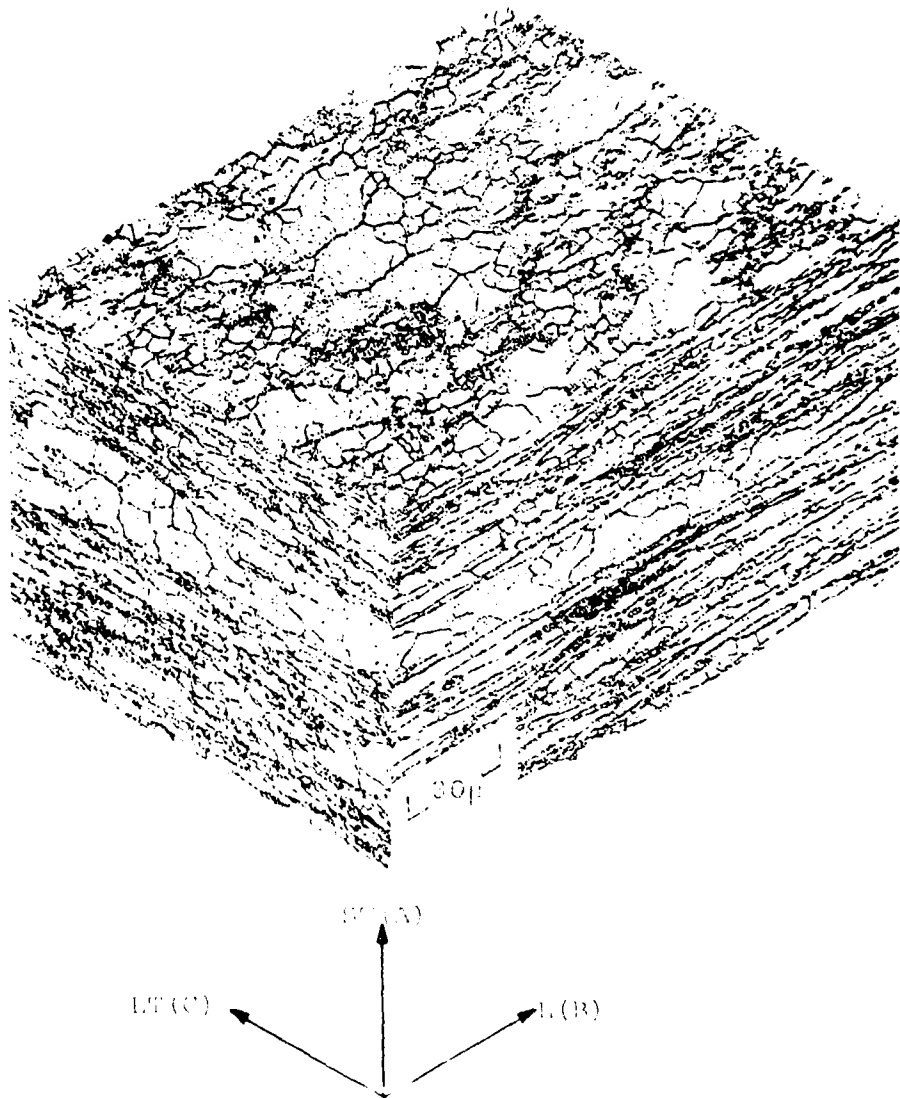


Figure 21. Optical microstructure of 0.4 Co ABC-upset and draw hand forging, S-356453-3T (CT91).

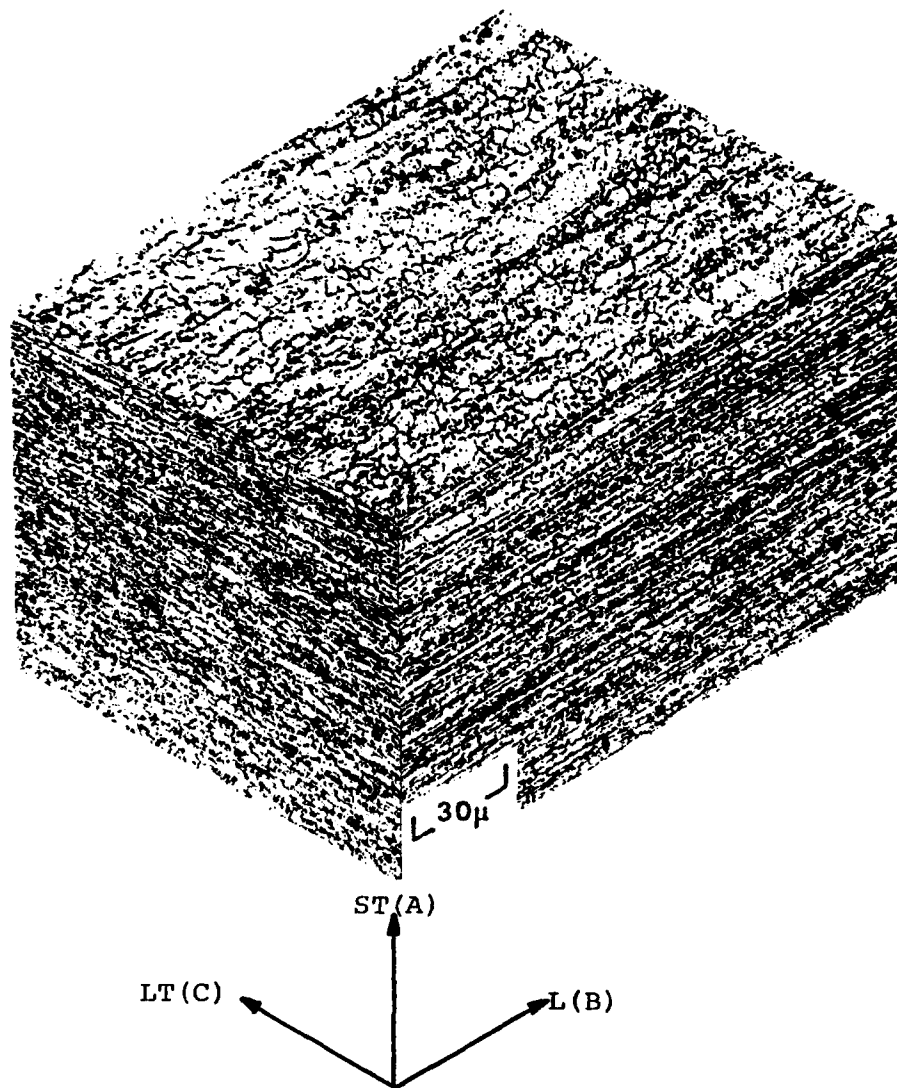


Figure 22. Optical microstructure of 0.8 Co A-upset and draw hand forging, S-356454-2T.

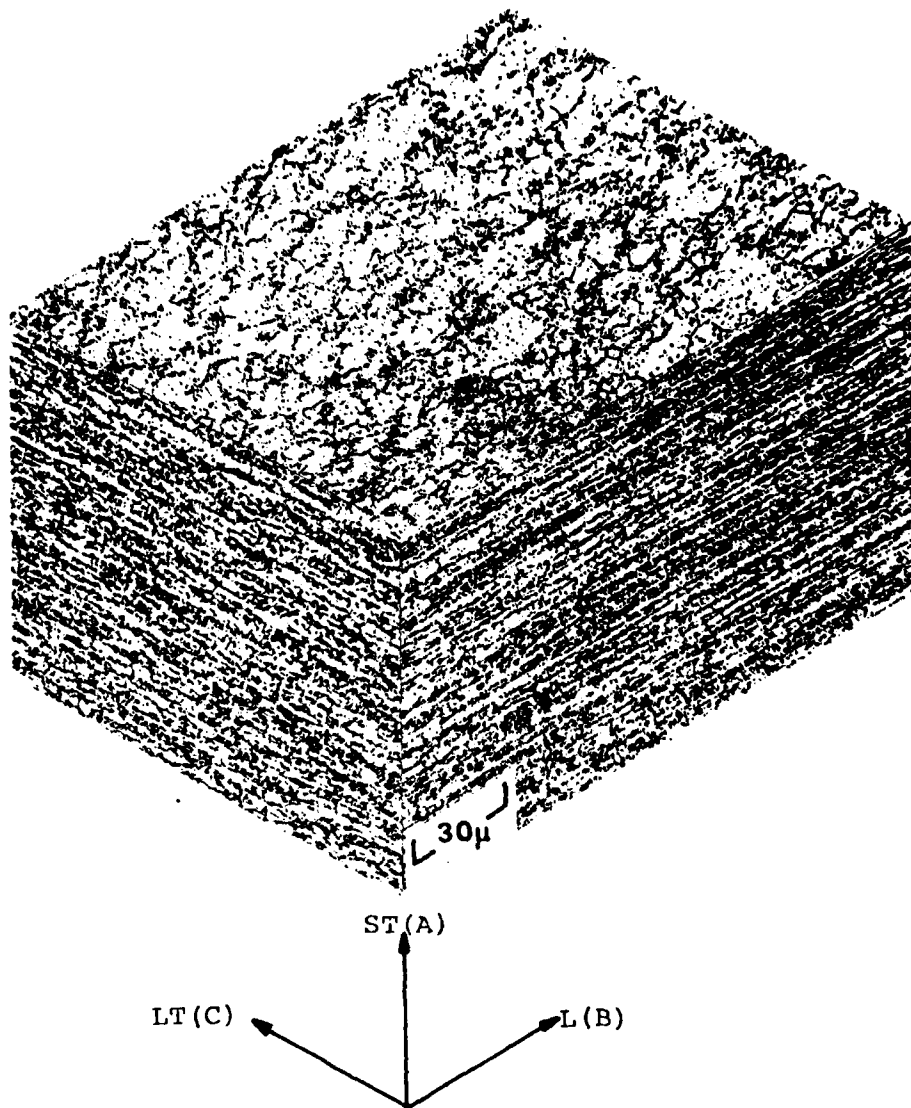


Figure 23. Optical microstructure of 0.8 Co ABC-upset and draw hand forging, S-356454-3T.

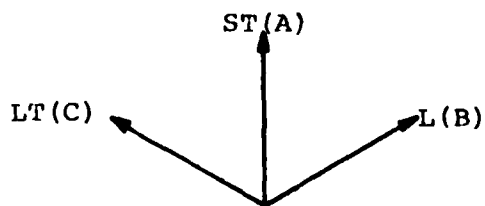
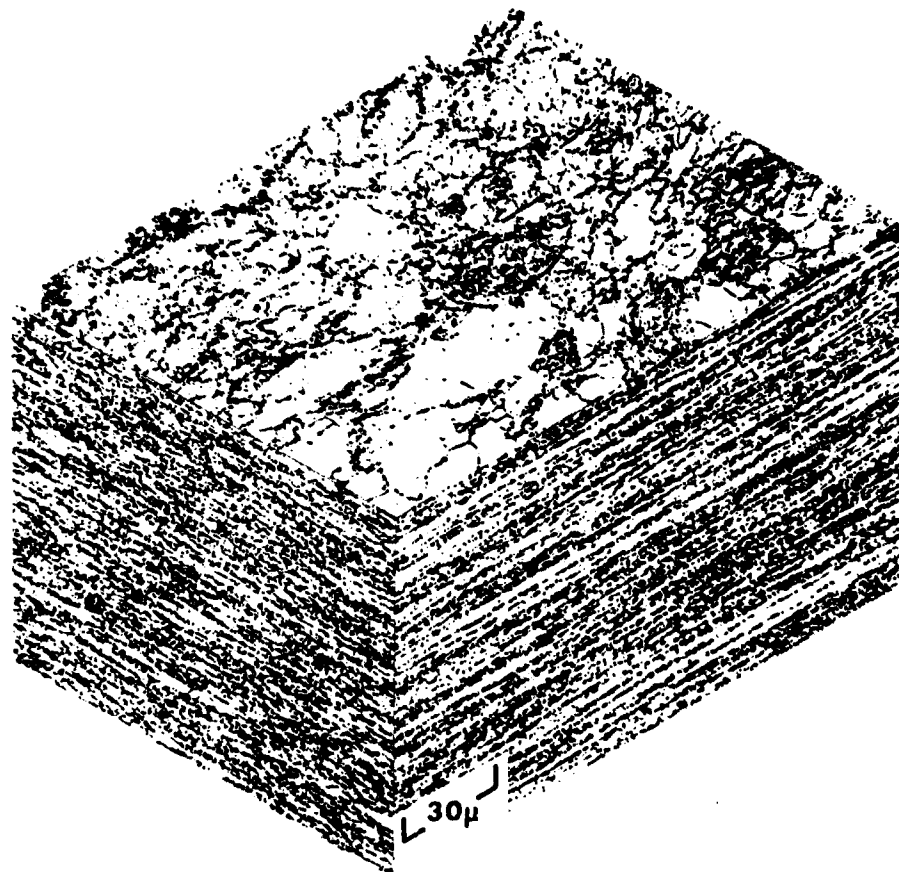


Figure 24. Optical microstructure of blended powder A-upset and draw hand forging, S-356455-2T.

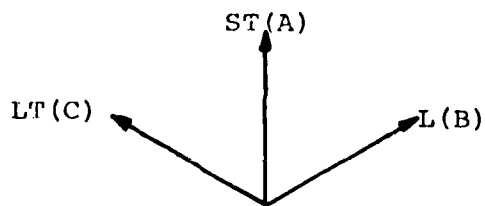
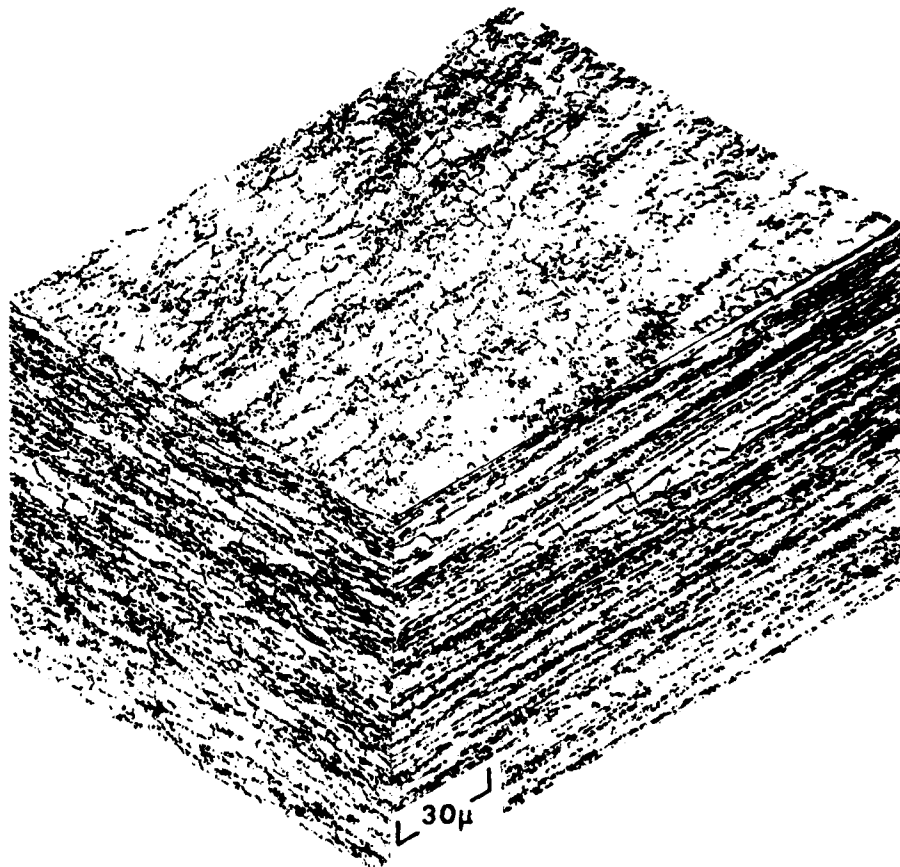


Figure 25. Optical microstructure of blended powder ABC-upset and draw hand forging, S-356455-3T.

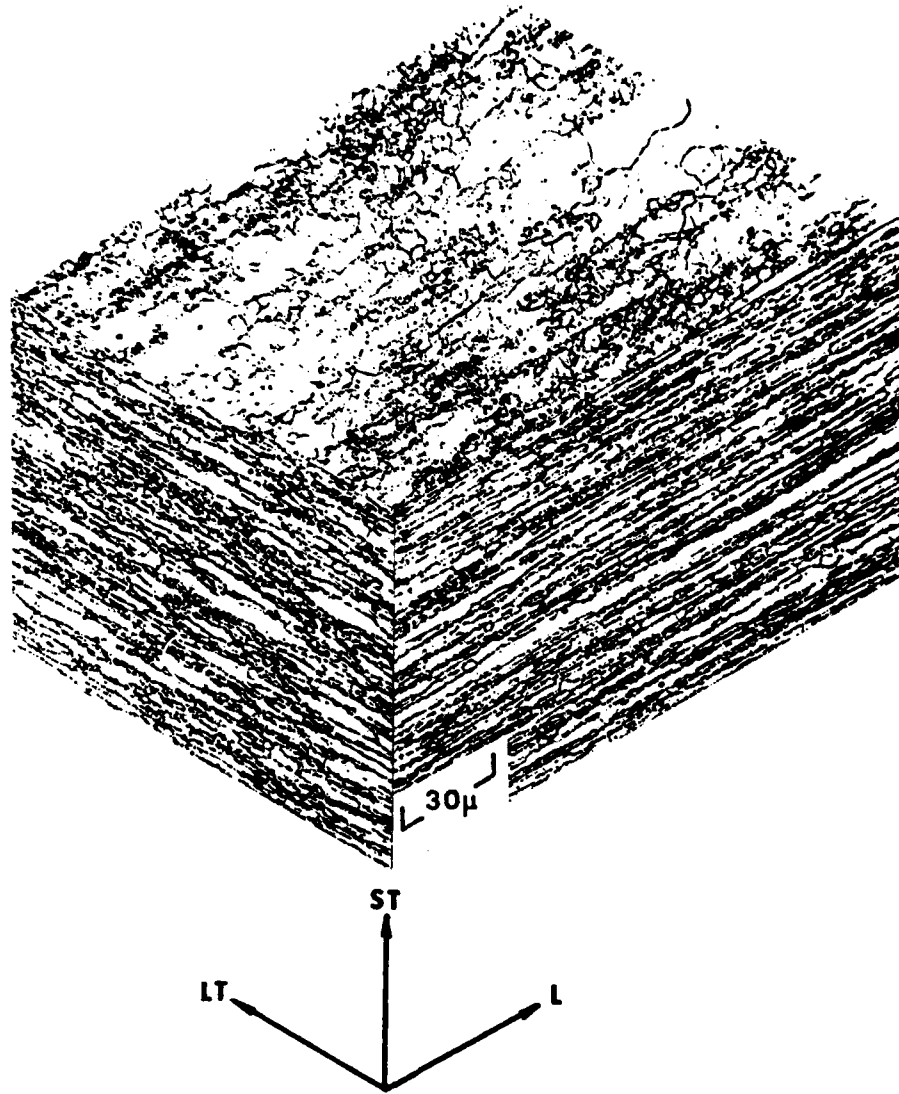


Figure 26. Optical microstructure of 0.0 Co medium Z extrusion, S-356452-6G.

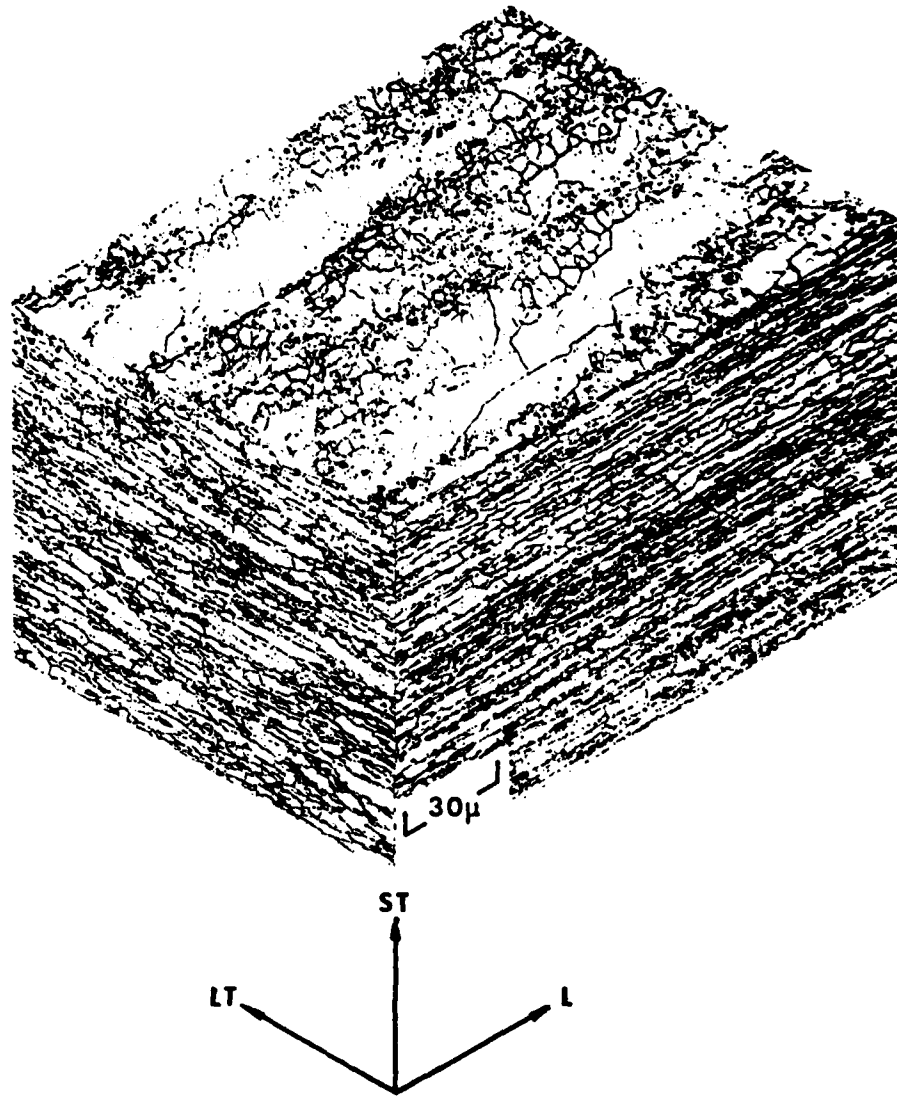


Figure 27. Optical microstructure of 0.4 Co medium Z extrusion, S-356453-6G (CT91).

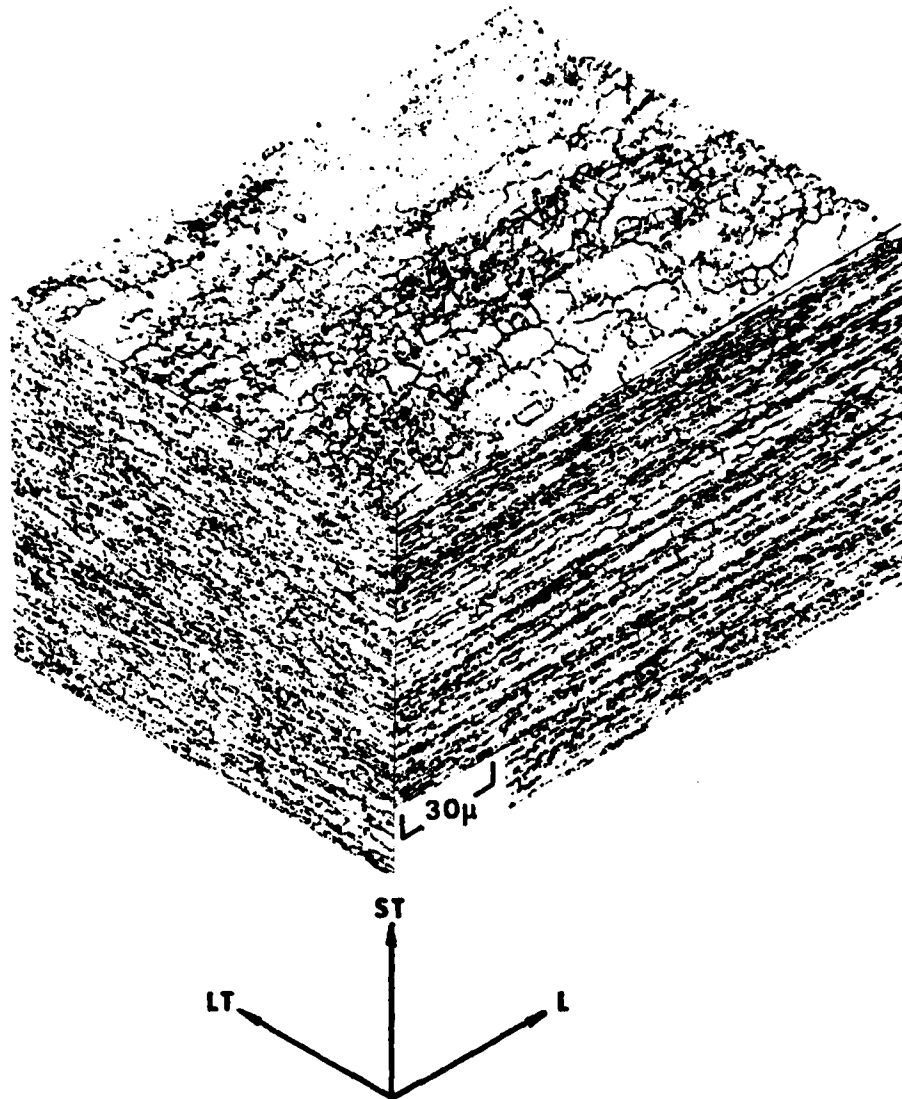


Figure 28. Optical microstructure of 0.8 Co medium Z extrusion, S-356454-5G.

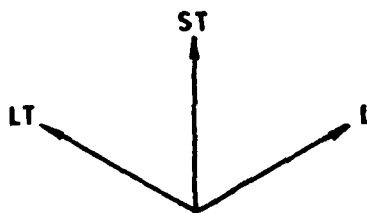
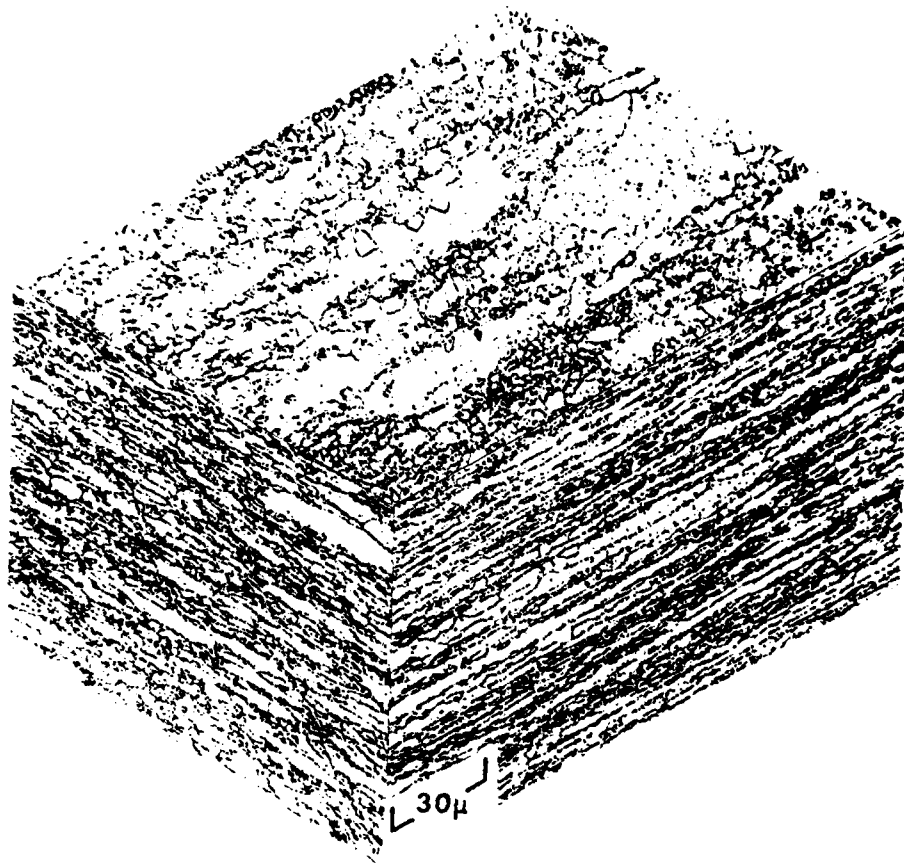


Figure 29. Optical microstructure of blended powder medium Z extrusion, S-356455-5G.

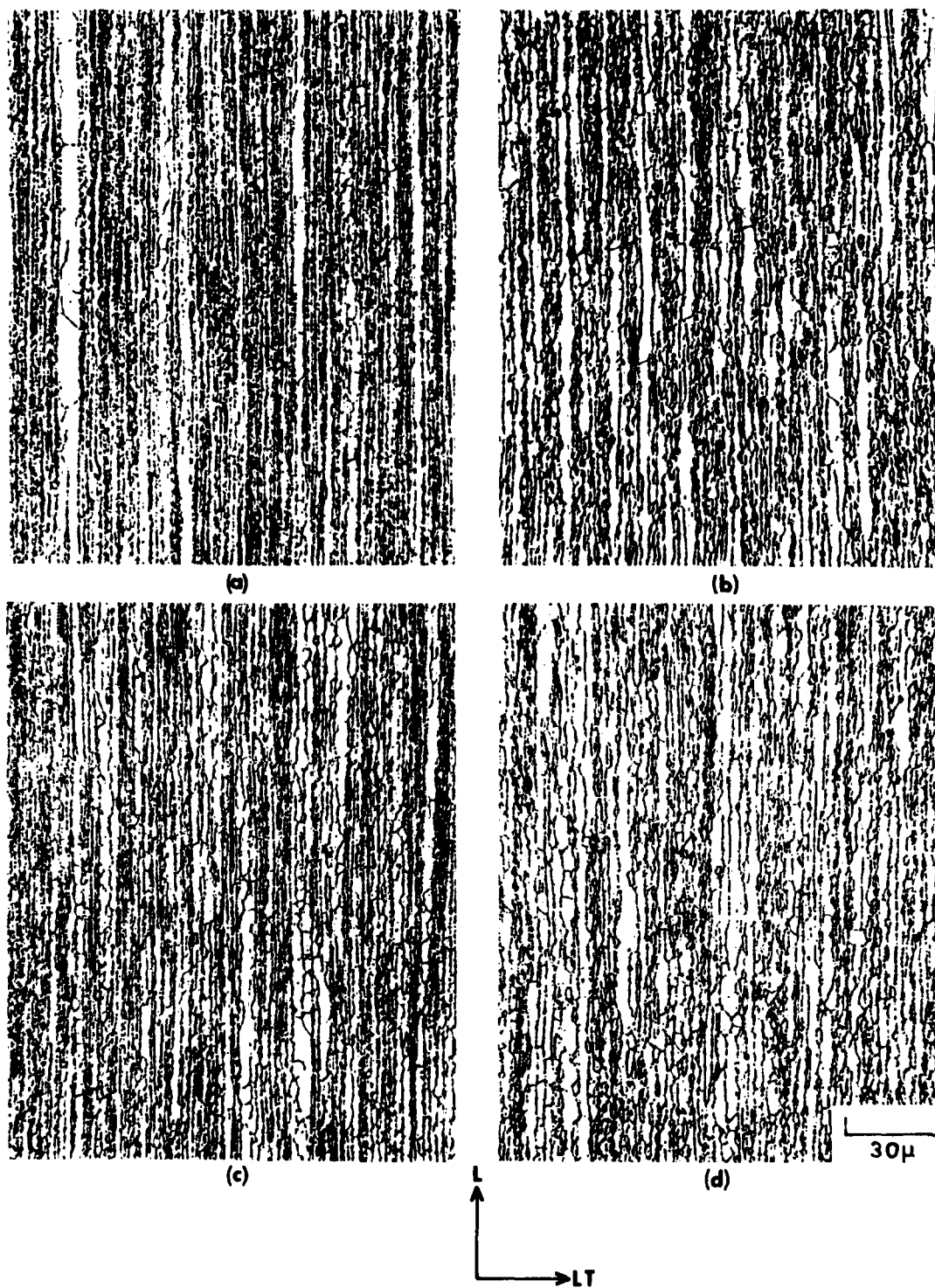


Figure 30. Longitudinal micrographs of Phase I high and low Z extrusions: (a) high Z, 0.0 Co, S-356452-4BG, (b) low Z, 0.0 Co, S-356452-7G, (c) high Z, 0.4 Co, S-356453-4AG (CT91), and (d) low Z, 0.4 Co, S-356453-7G (CT91).

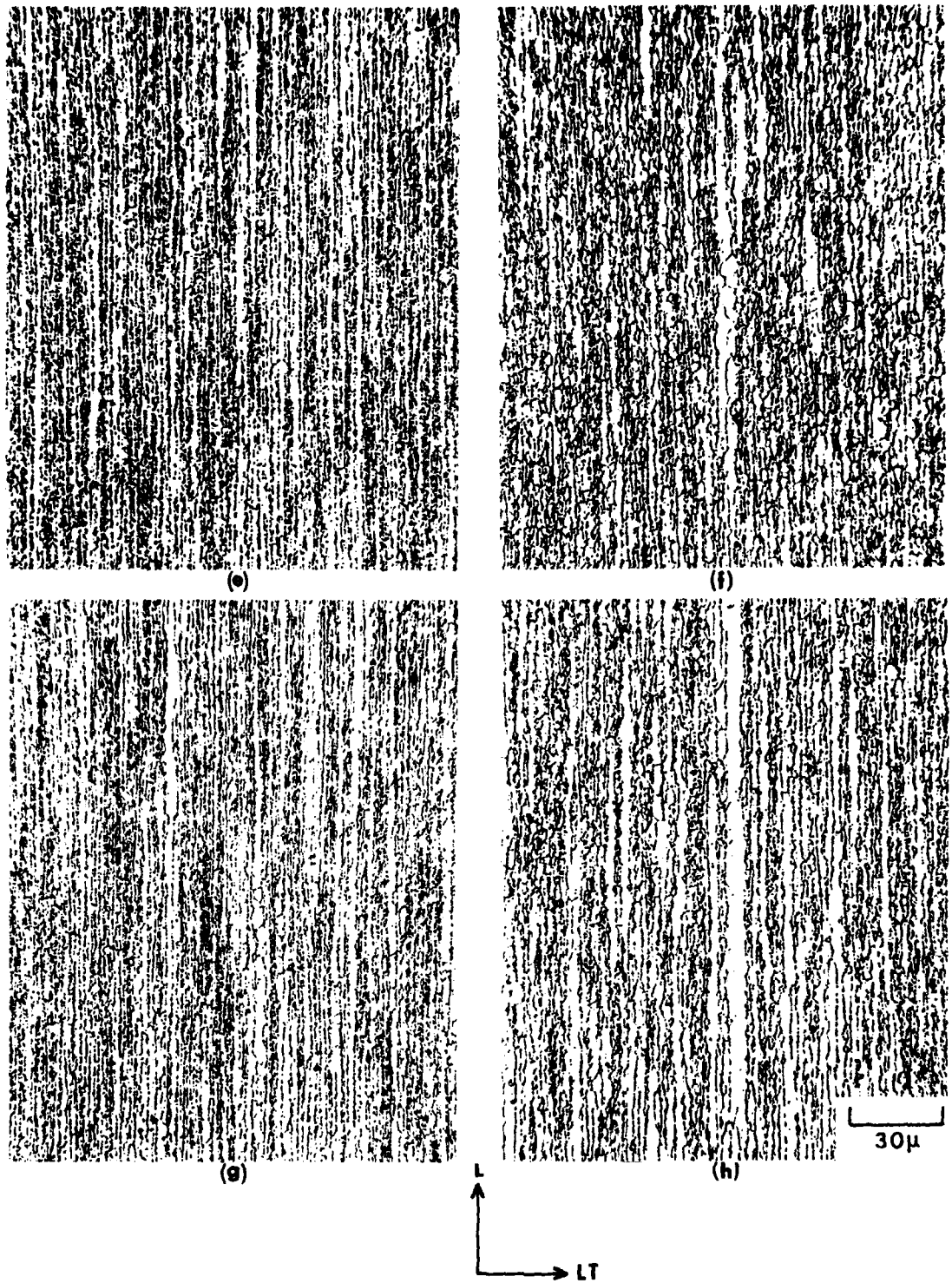
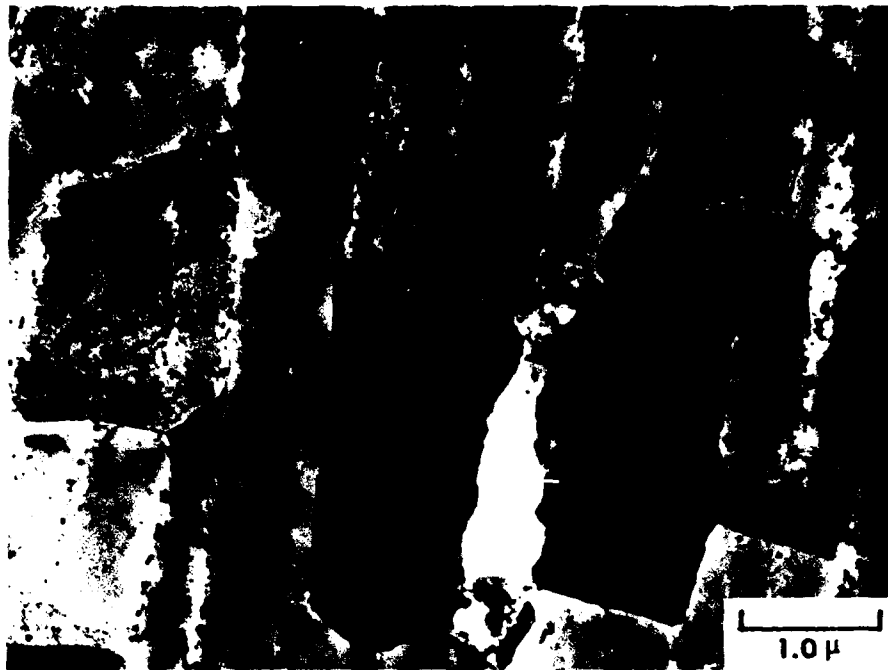
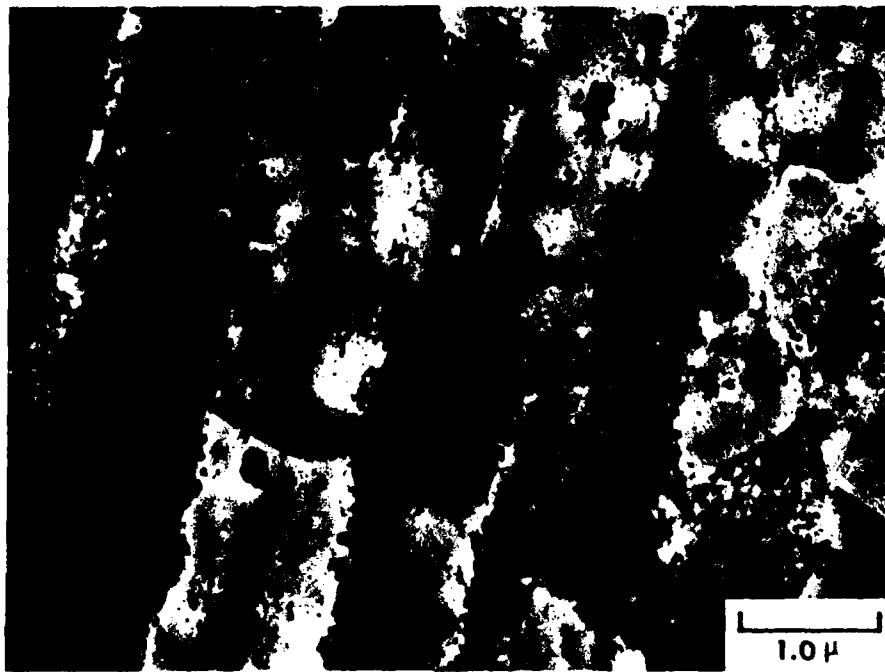


Figure 30. (Continued) (e) high Z, 0.8 Co, S-356454-4AG, (f) low Z, 0.8 Co, S-356454-6G, (g) high Z, blend, S-356455-4AG, and (h) low Z, blend, S-356455-6G.

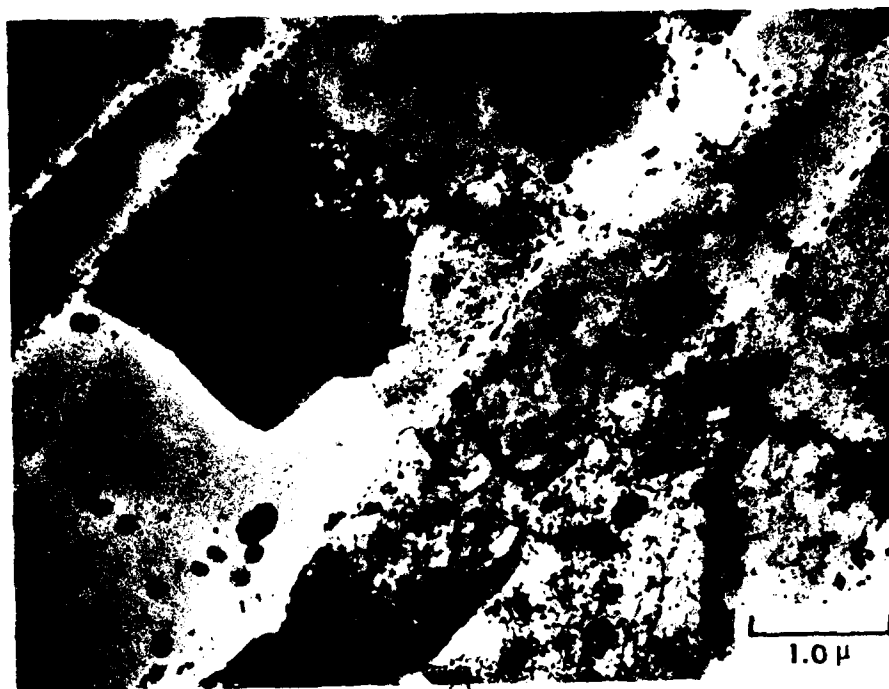


(a)

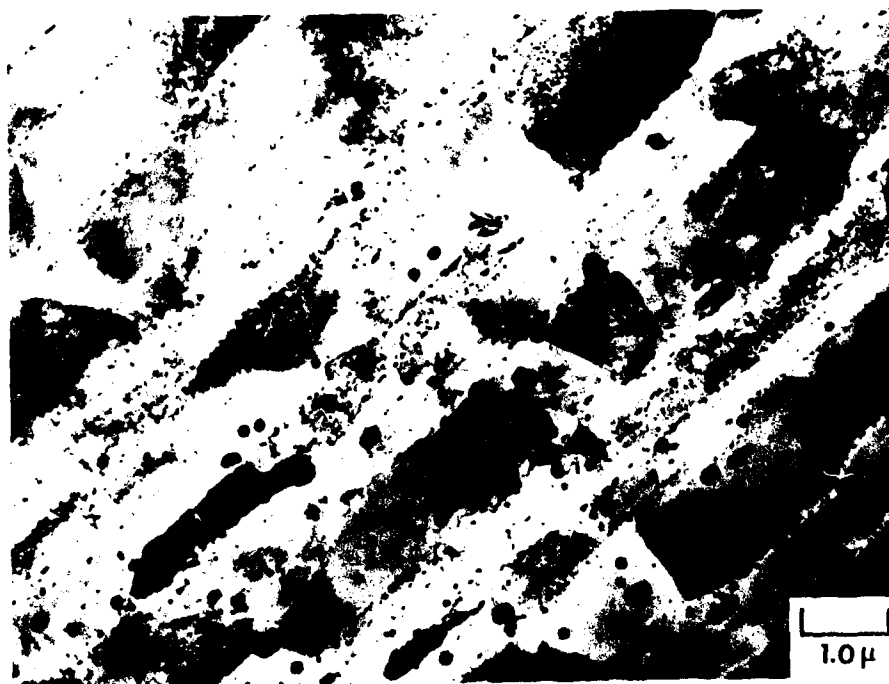


(b)

Figure 31. Transmission electron micrographs of Phase I high Z extrusions in T7X1 temper: (a) 356452-4BG, 0.0 Co, and (b) 356453-4AG, 0.4 Co (CT91).



(c)



(d)

Figure 31. (Continued) TEM's of Phase I extrusion: (c) and (d) 356455-4AG, Blend.

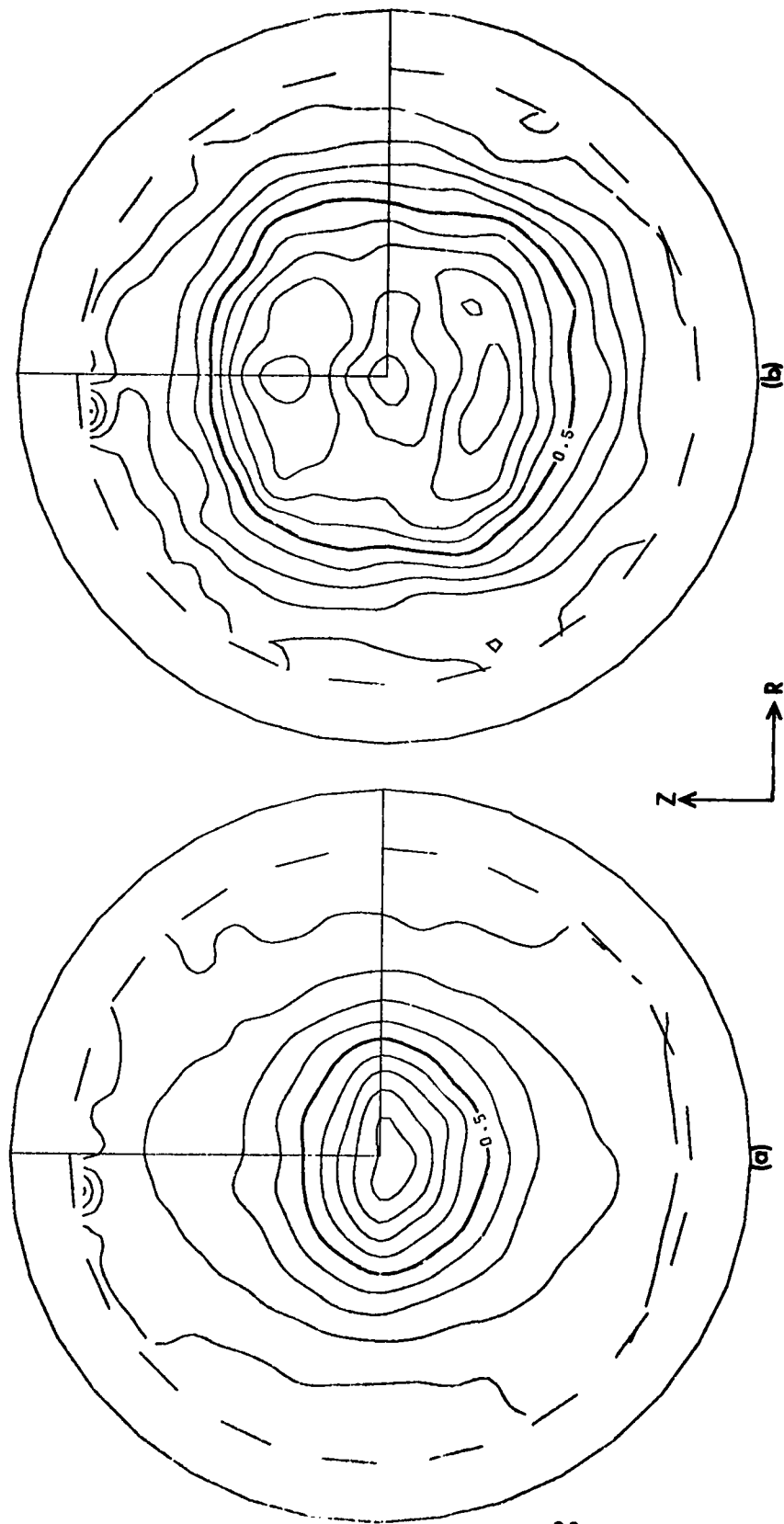


Figure 32. Pole figures showing degree of preferred orientation for CT91 hot-pressed billet, S-356453: (a) (200) and (b) (220).

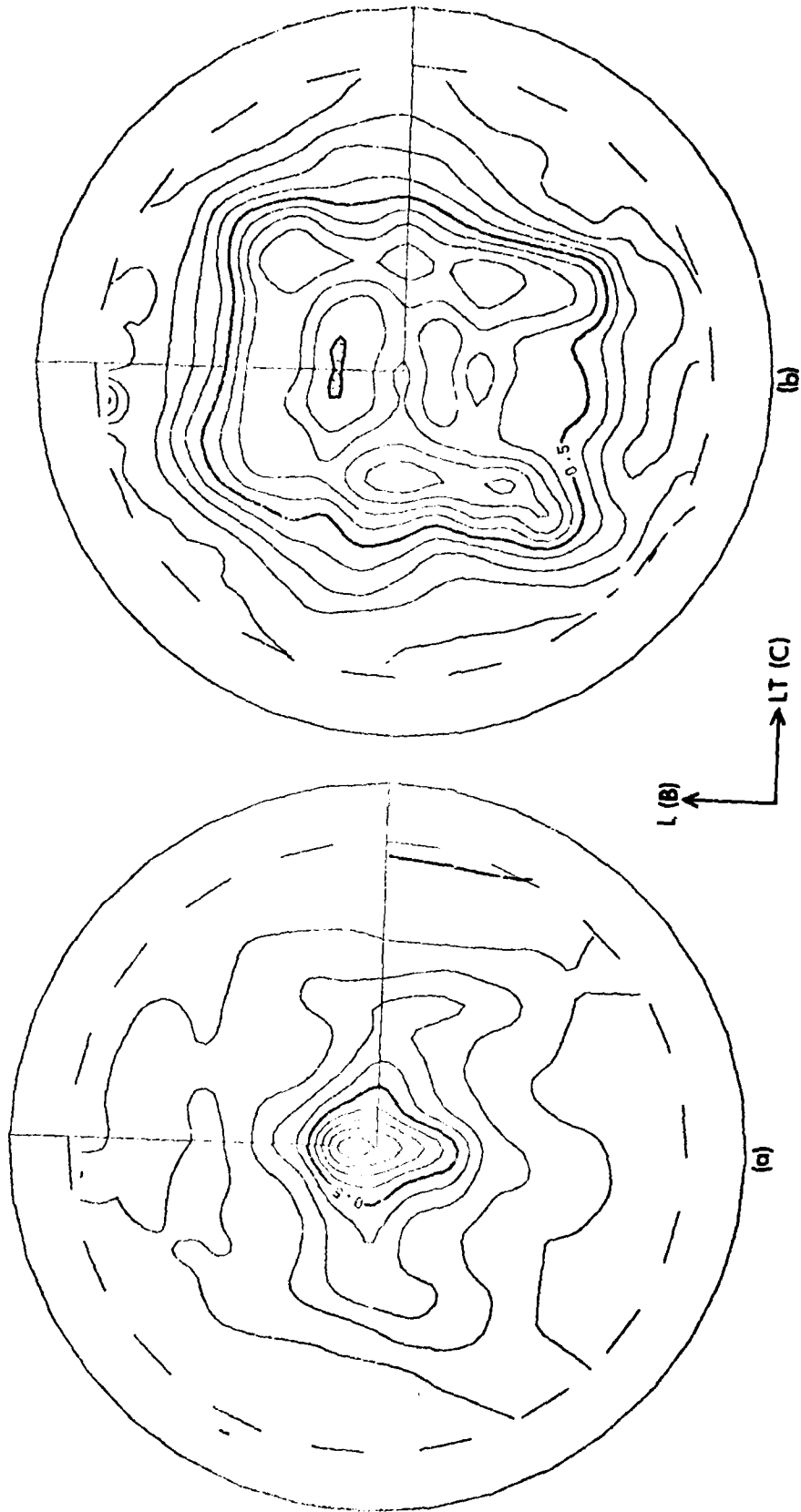


Figure 33. Pole figures showing degree of preferred orientation for CT91 A-upset and draw hand forging, S-356453-2T: (a) (200) and (b) (220).

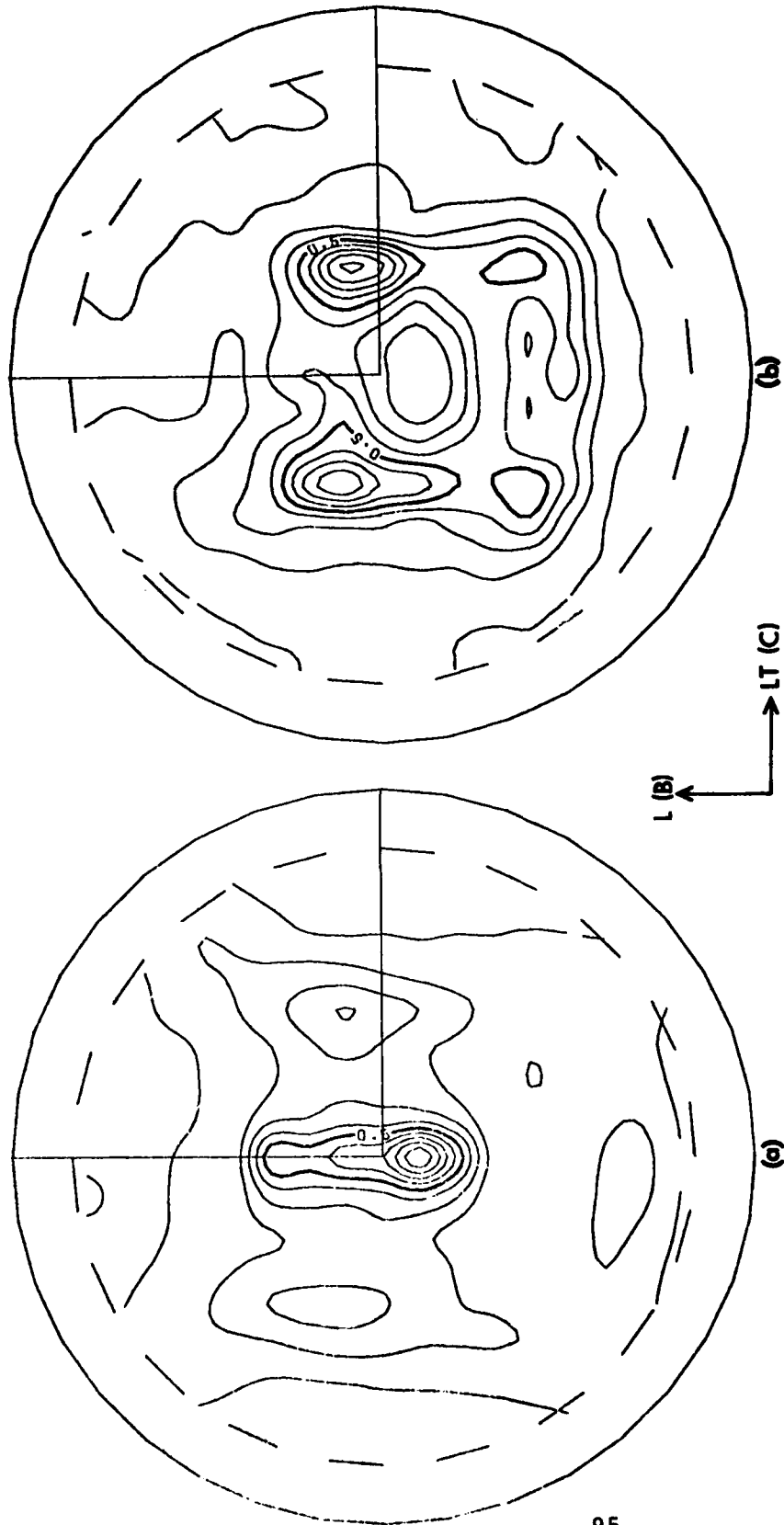


Figure 34. Pole figures showing degree of preferred orientation for CT91 ABC-upset and draw hand forging, S-356453-3T: (a) (200) and (b) (220).

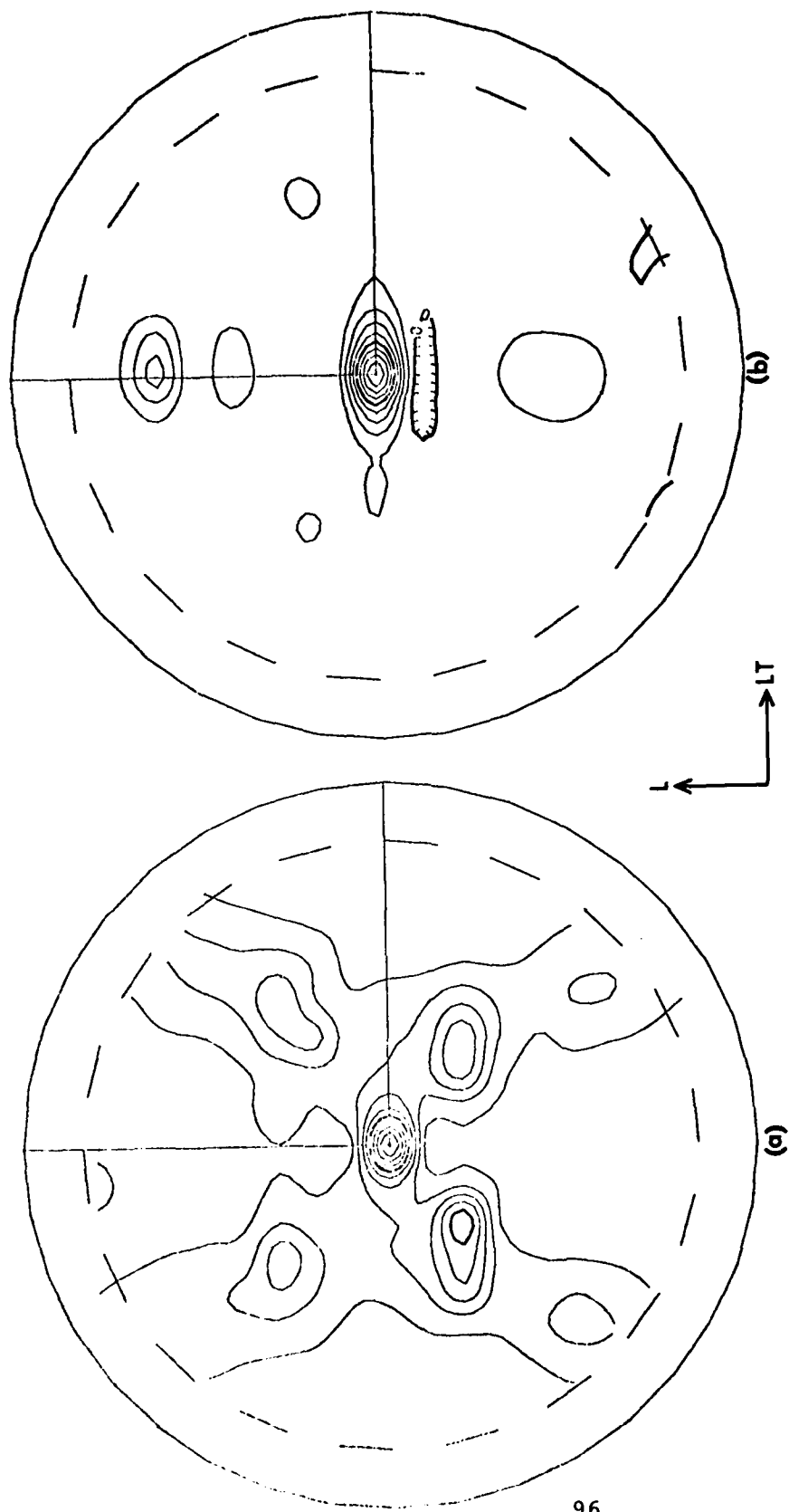


Figure 35. Pole figures showing degree of preferred orientation for CT91 high Z extrusion, S-356453-4AG: (a) (200) and (b) (220).

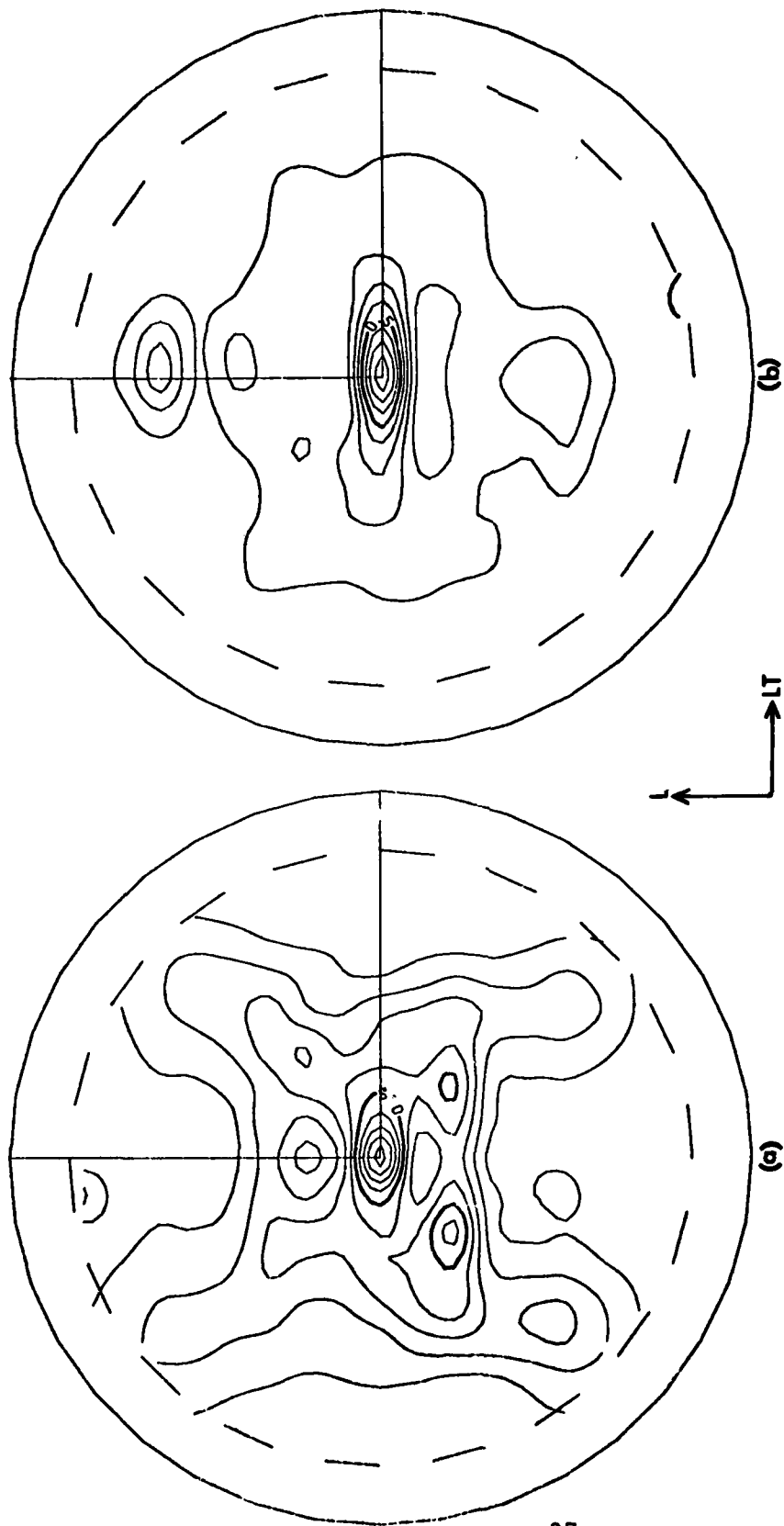


Figure 36. Pole figures showing degree of preferred orientation for Cr91 low Z extrusion, S-356453-7G: (a) (200) and (b) (220).

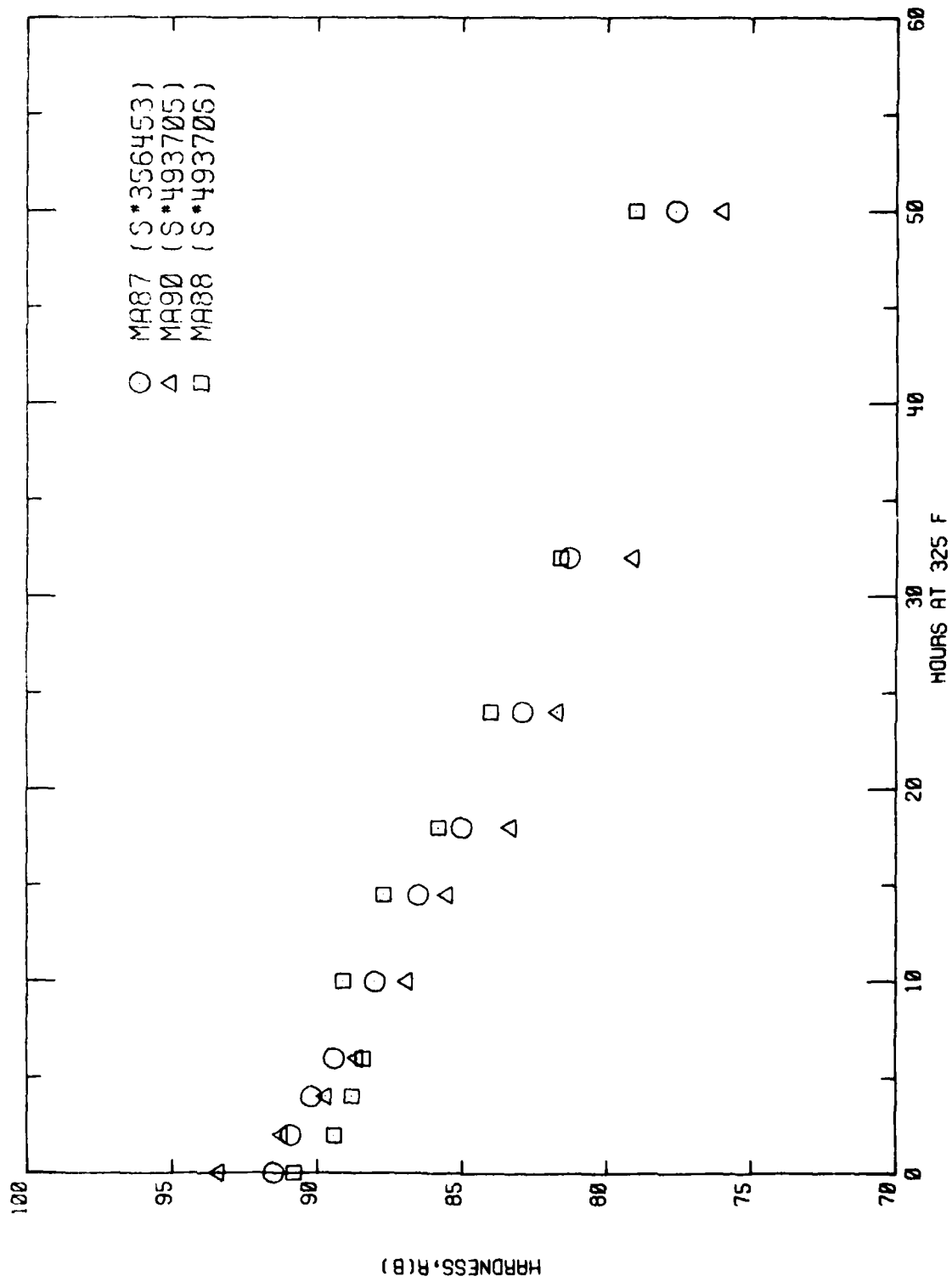


Figure 37. Rockwell B hardness versus second-step aging time at 163°C (325°F) for Phase II extrusions. All materials were aged initially for 24 hours at 121°C (250°F).

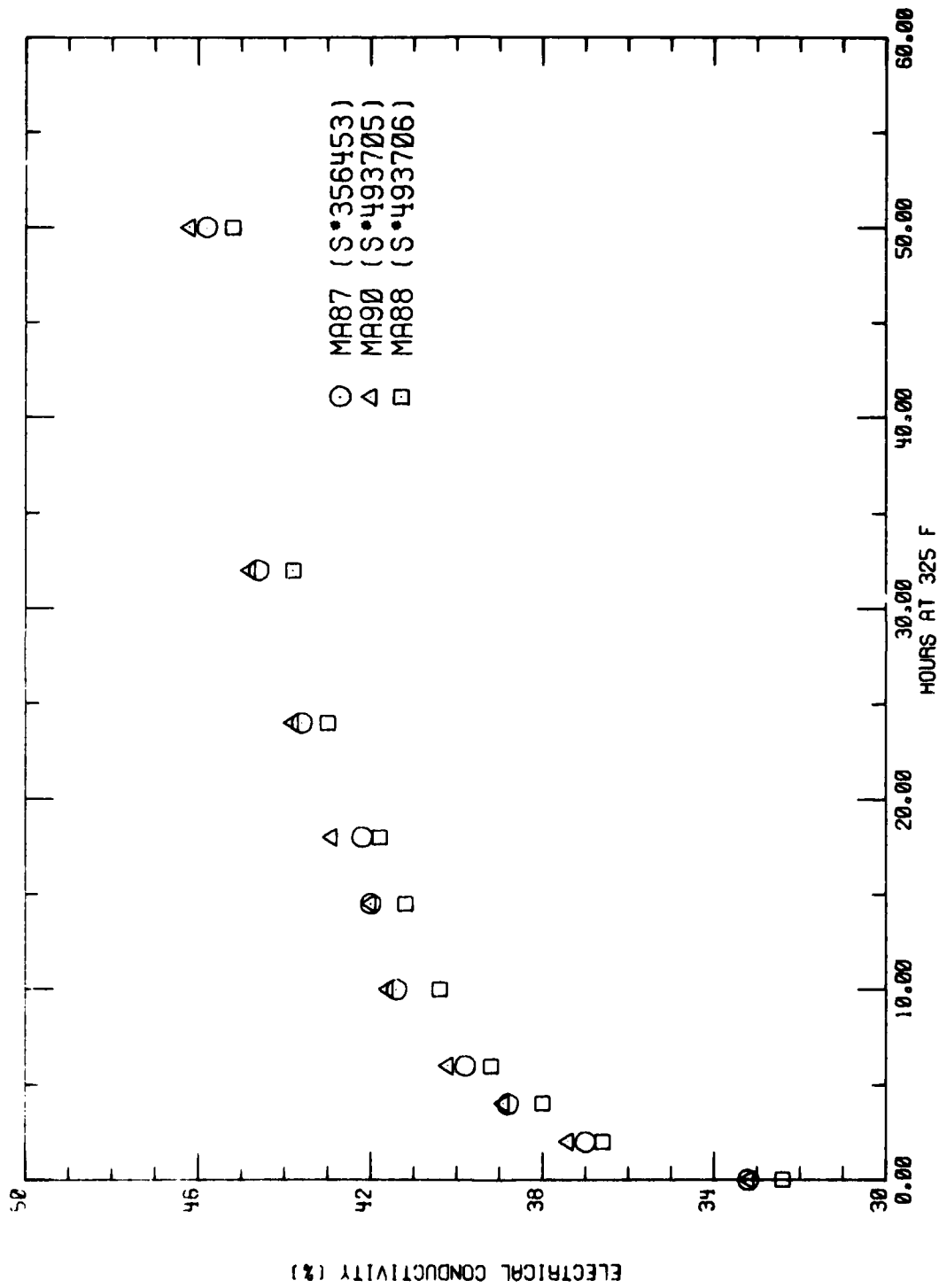


Figure 38. Electrical conductivity versus second-step aging time at 163°C (325°F) for Phase II extrusions. All materials were aged initially for 24 hours at 121°C (250°F).

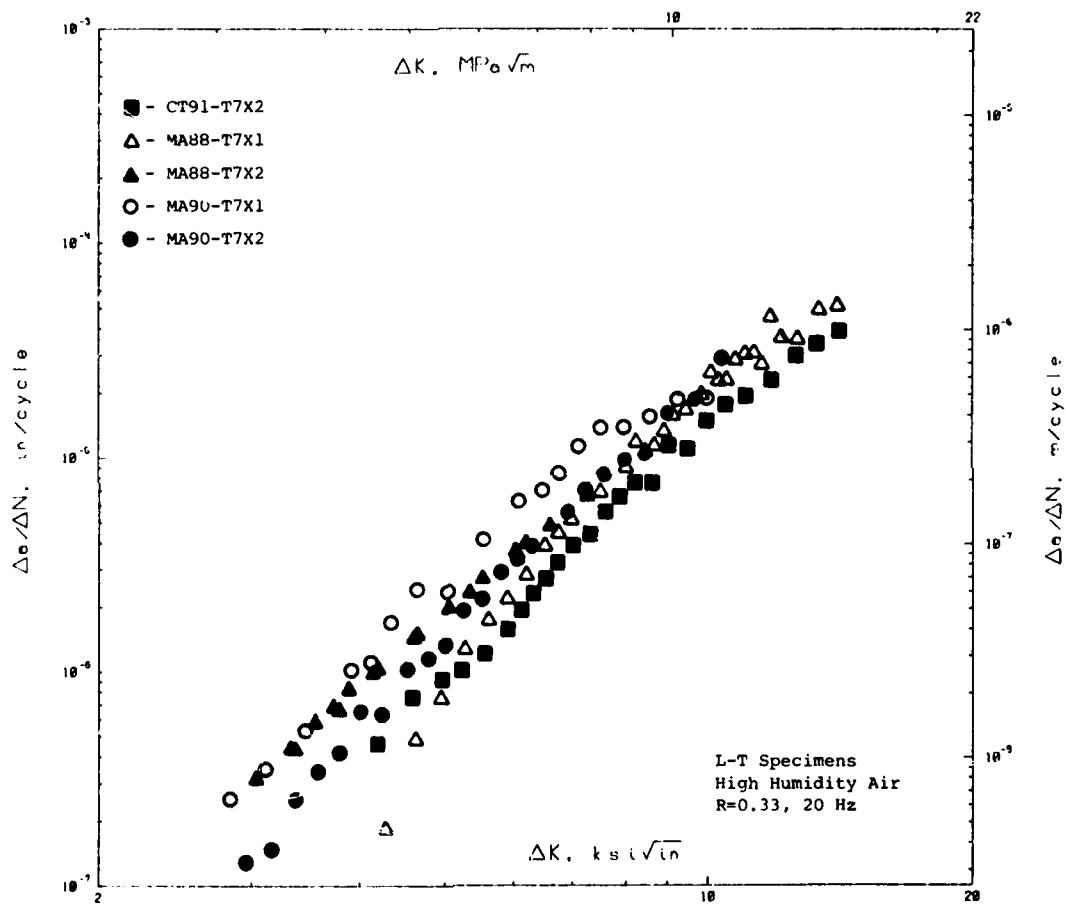


Figure 39. Fatigue crack growth data for Phase II hand forgings tested in humid air.

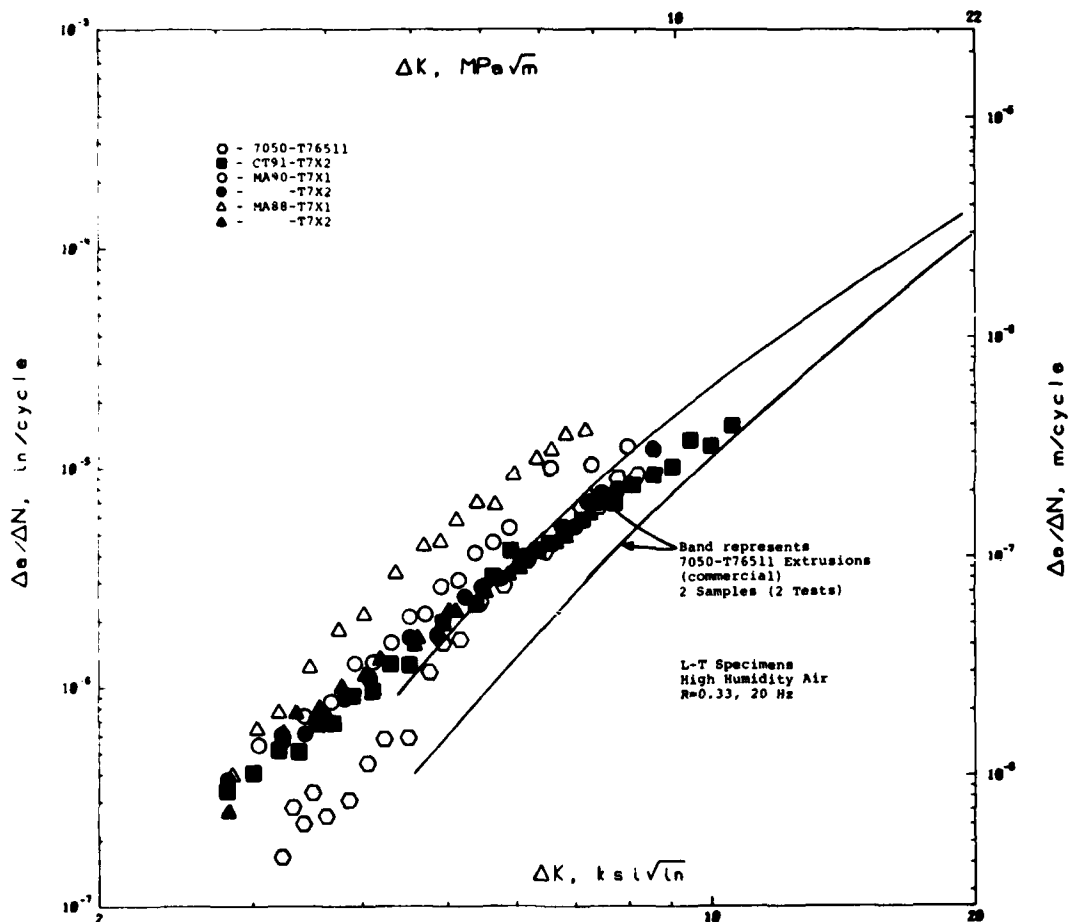


Figure 40. Fatigue crack growth data for Phase II extrusions tested in humid air.

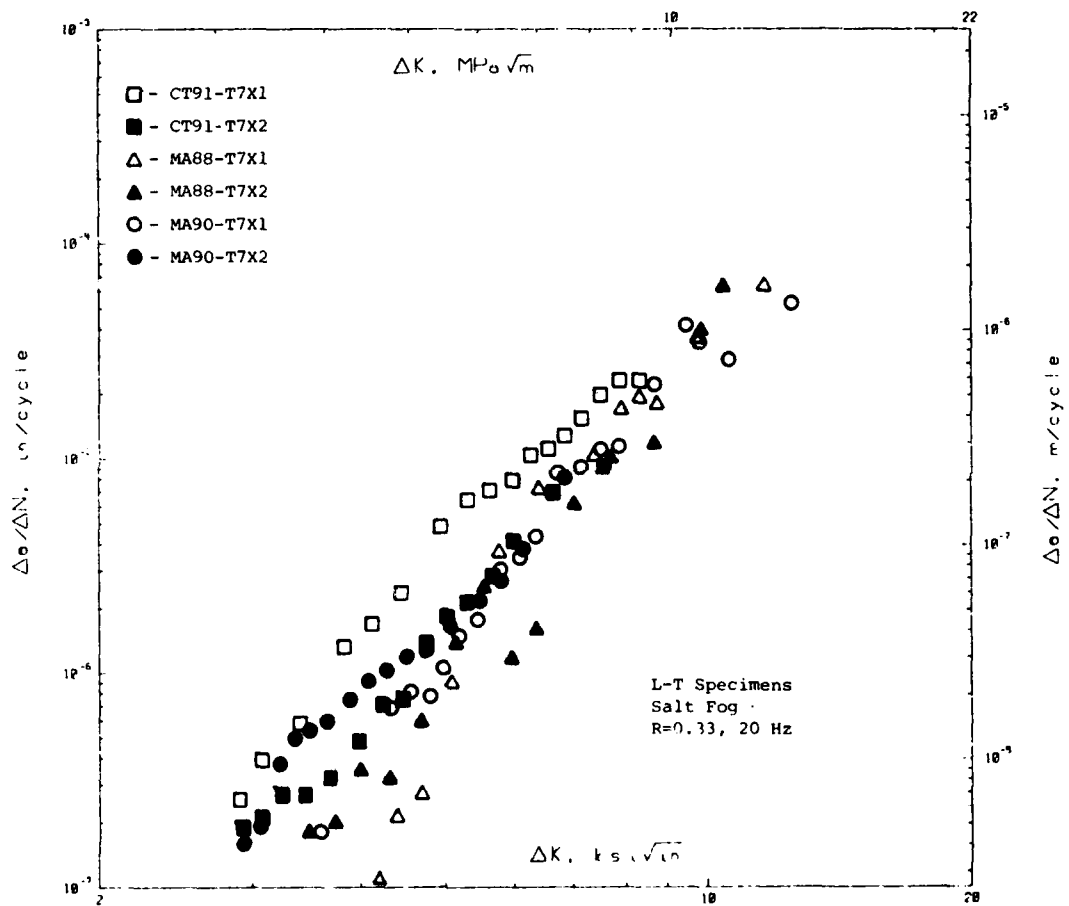


Figure 41. Fatigue crack growth data for Phase II hand forgings tested in salt fog atmosphere.

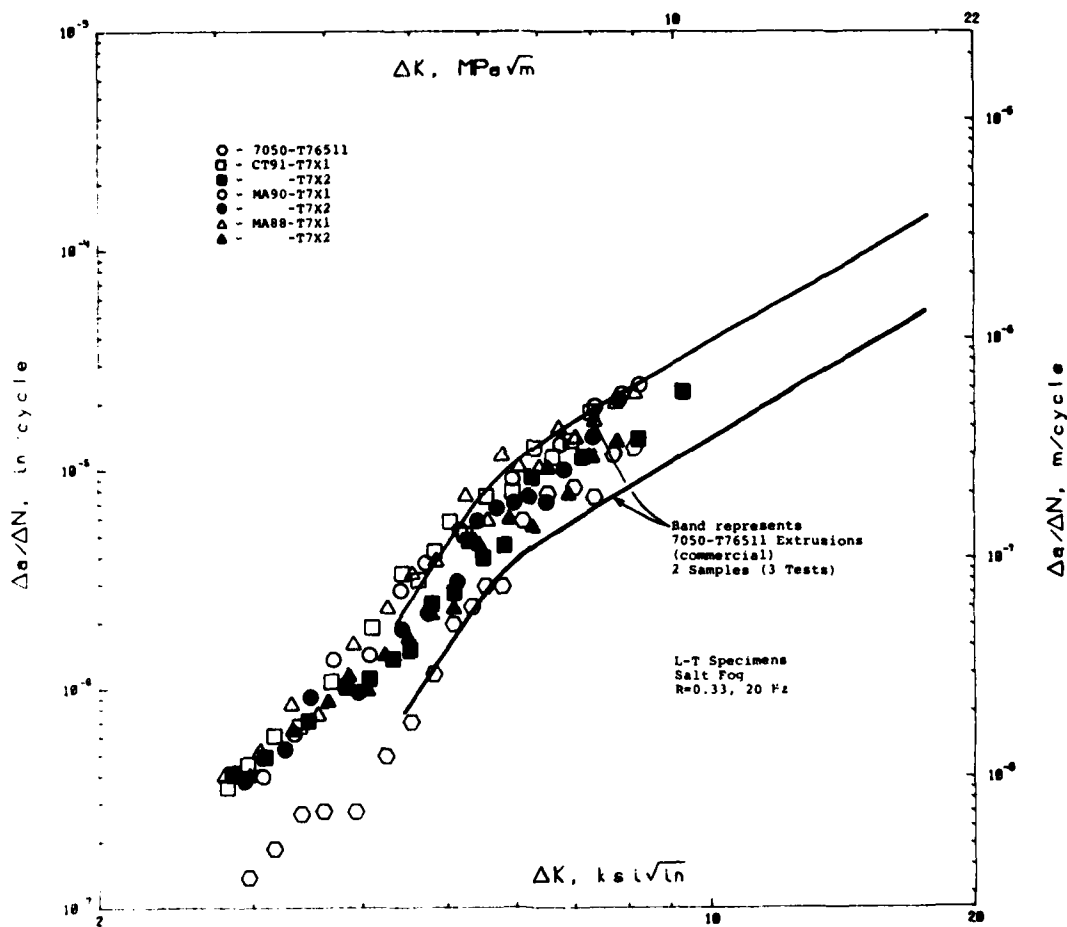


Figure 42. Fatigue crack growth data for Phase II extrusions tested in salt fog atmosphere.

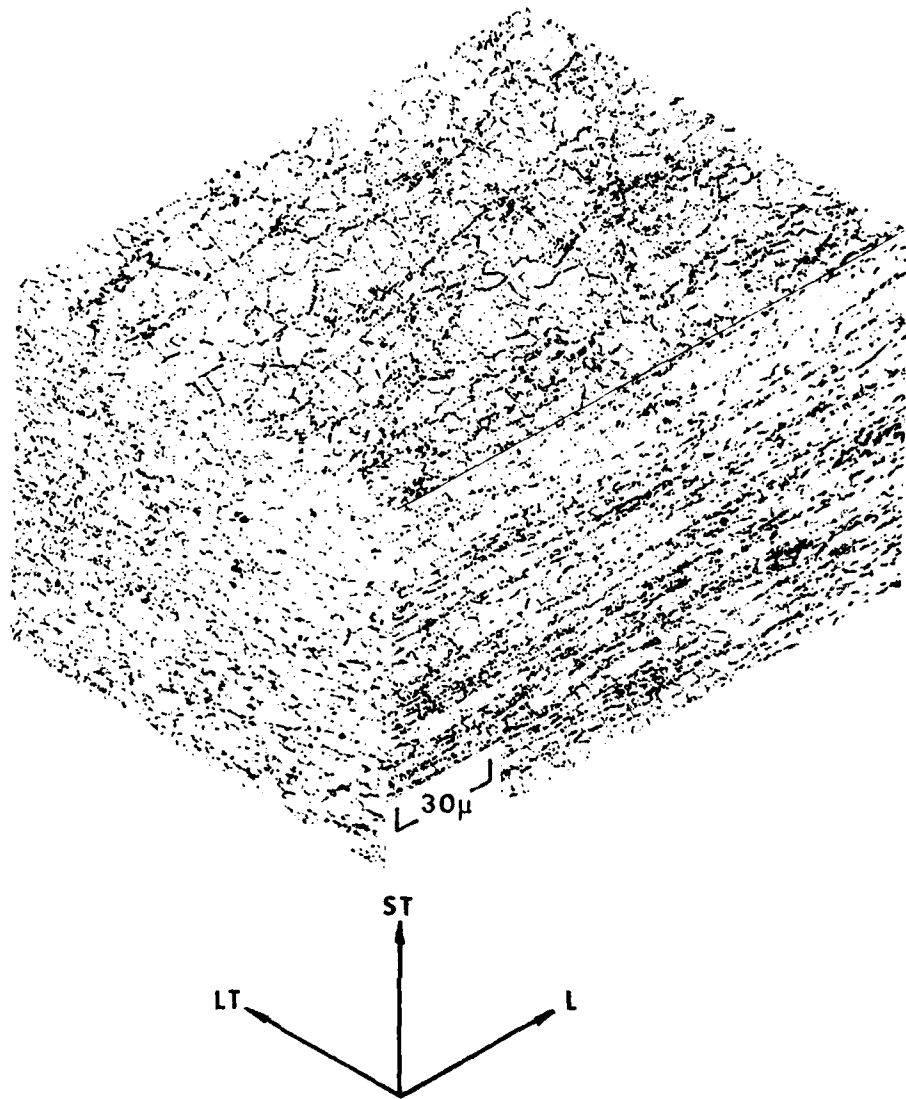


Figure 43. Optical microstructure of MA88 A-upset and draw hand forging, S-493706.

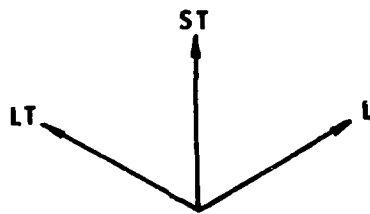
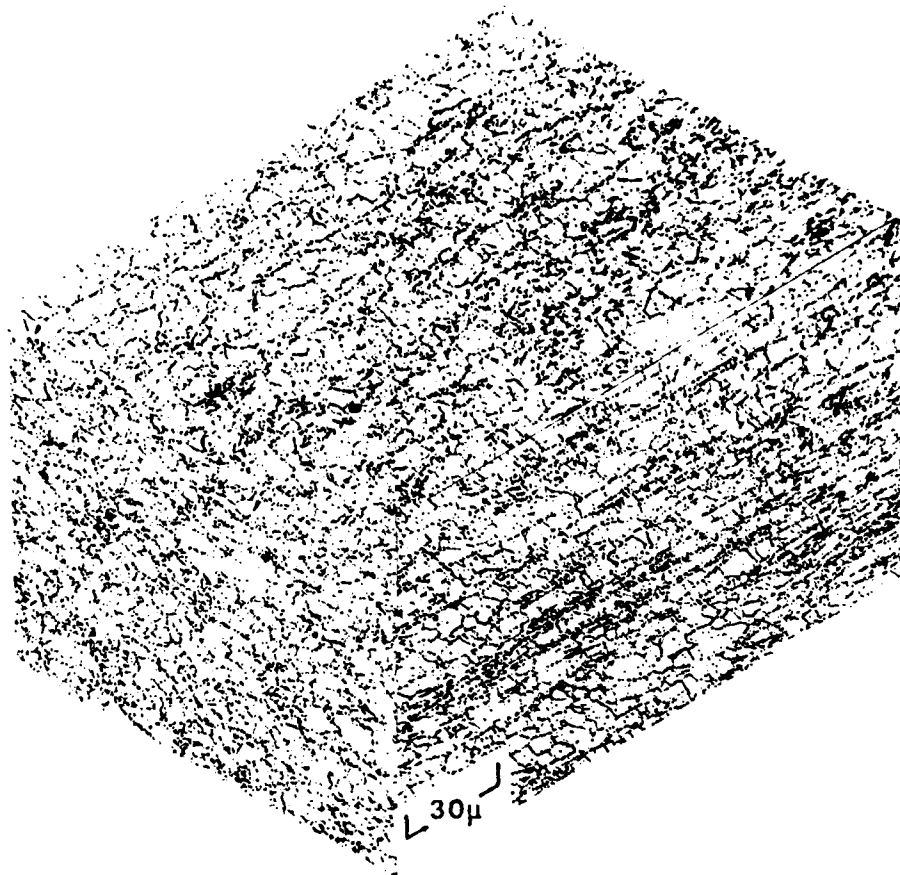


Figure 44. Optical microstructure of MA90 A-upset and draw hand forging, S-493705.

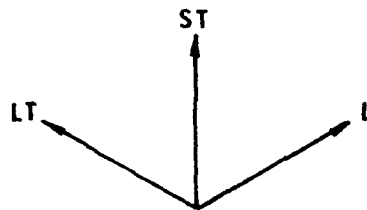
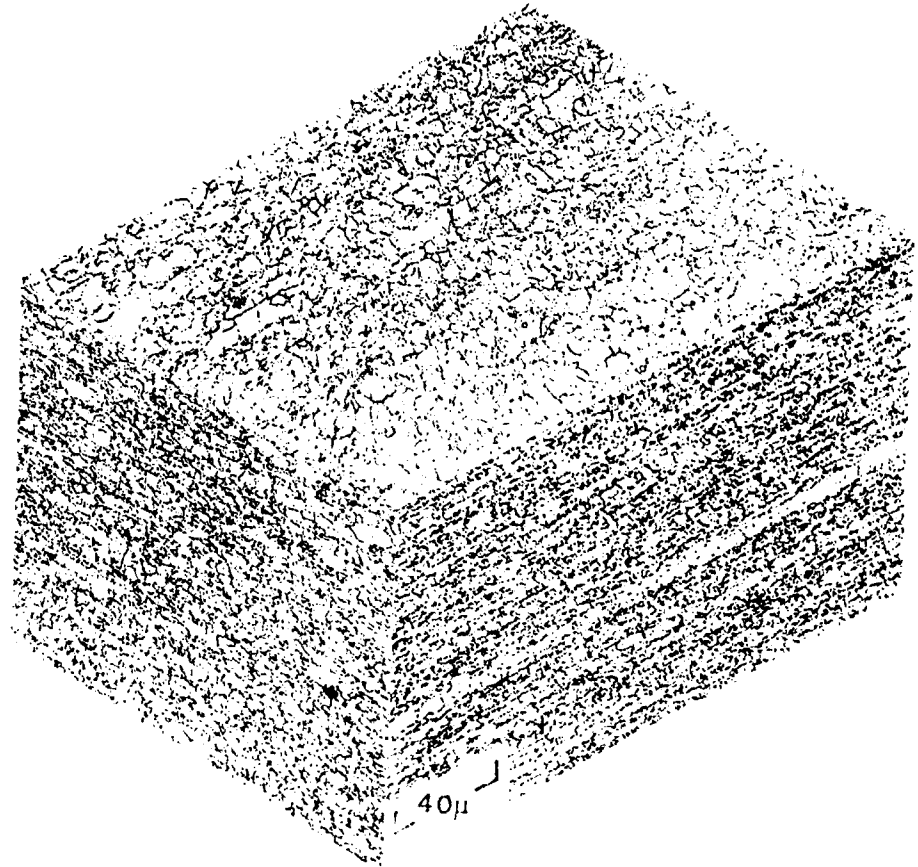


Figure 45. Optical microstructure of MA88 extrusion, S-493706-1G.

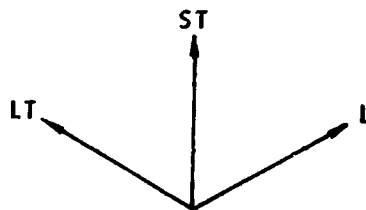
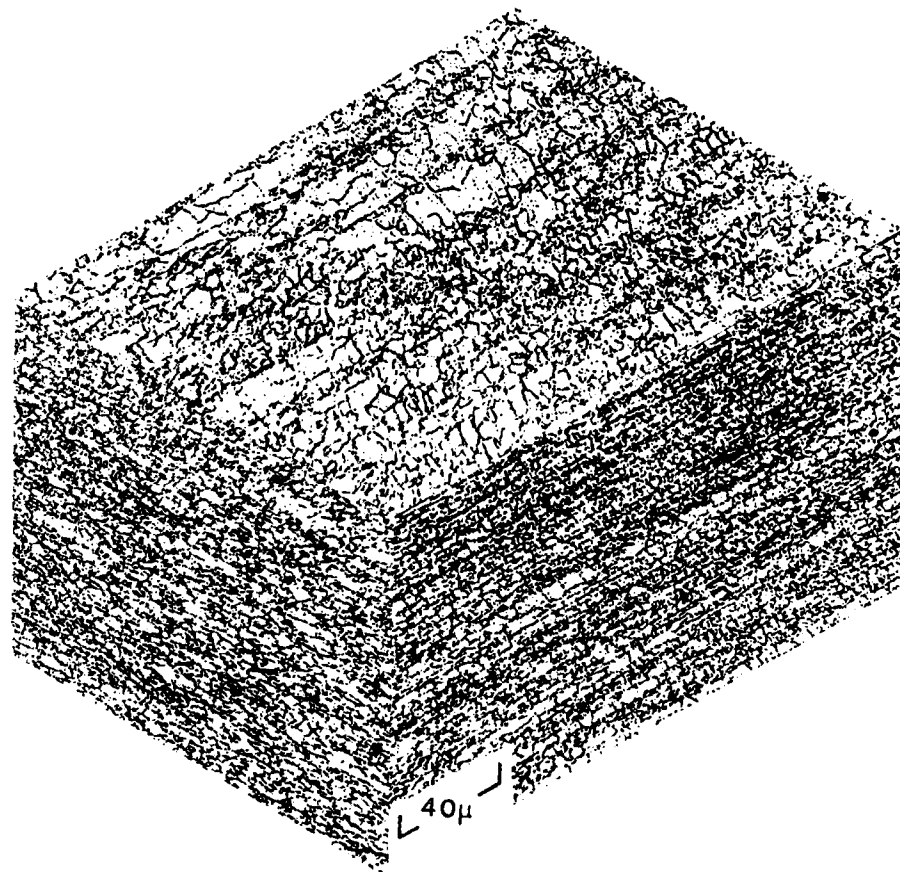


Figure 46. Optical microstructure of MA90 extrusion, S-493705-1G.

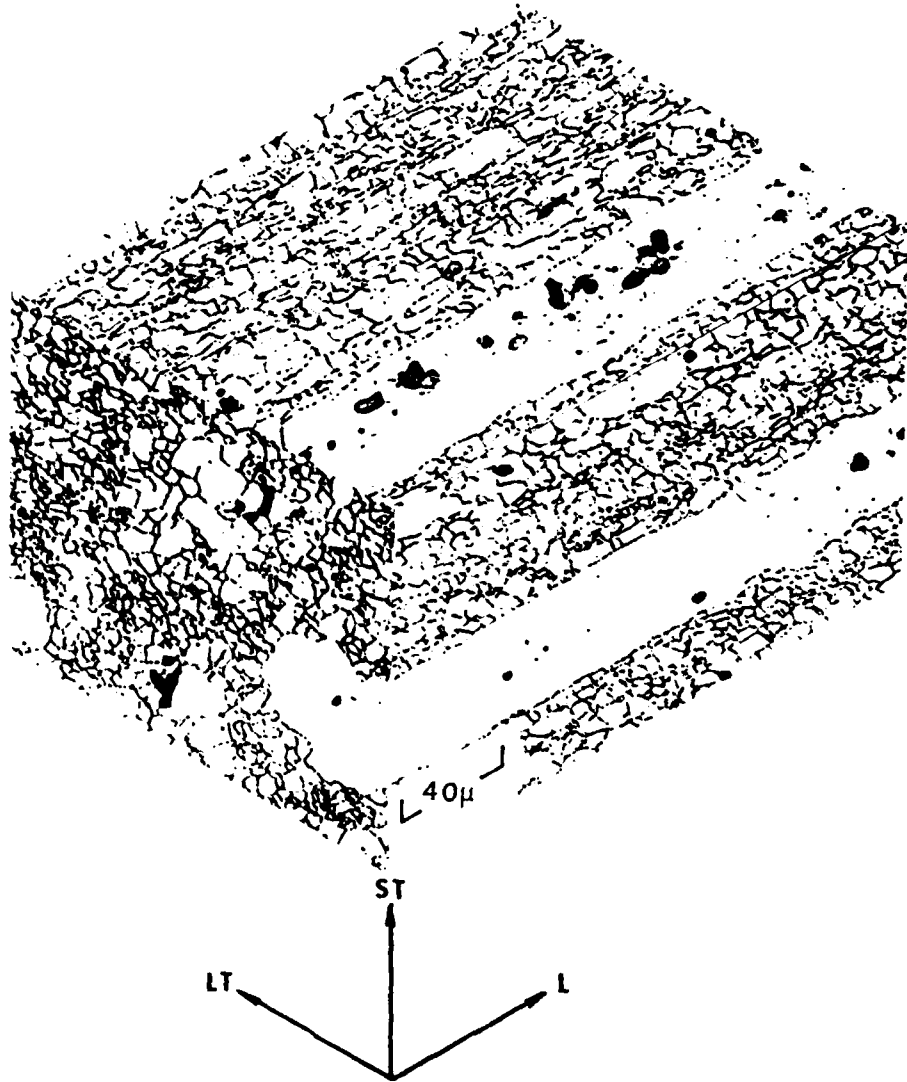


Figure 47. Optical microstructure of commercially-produced 7050-T76511 extrusion used for control in FCG evaluations.

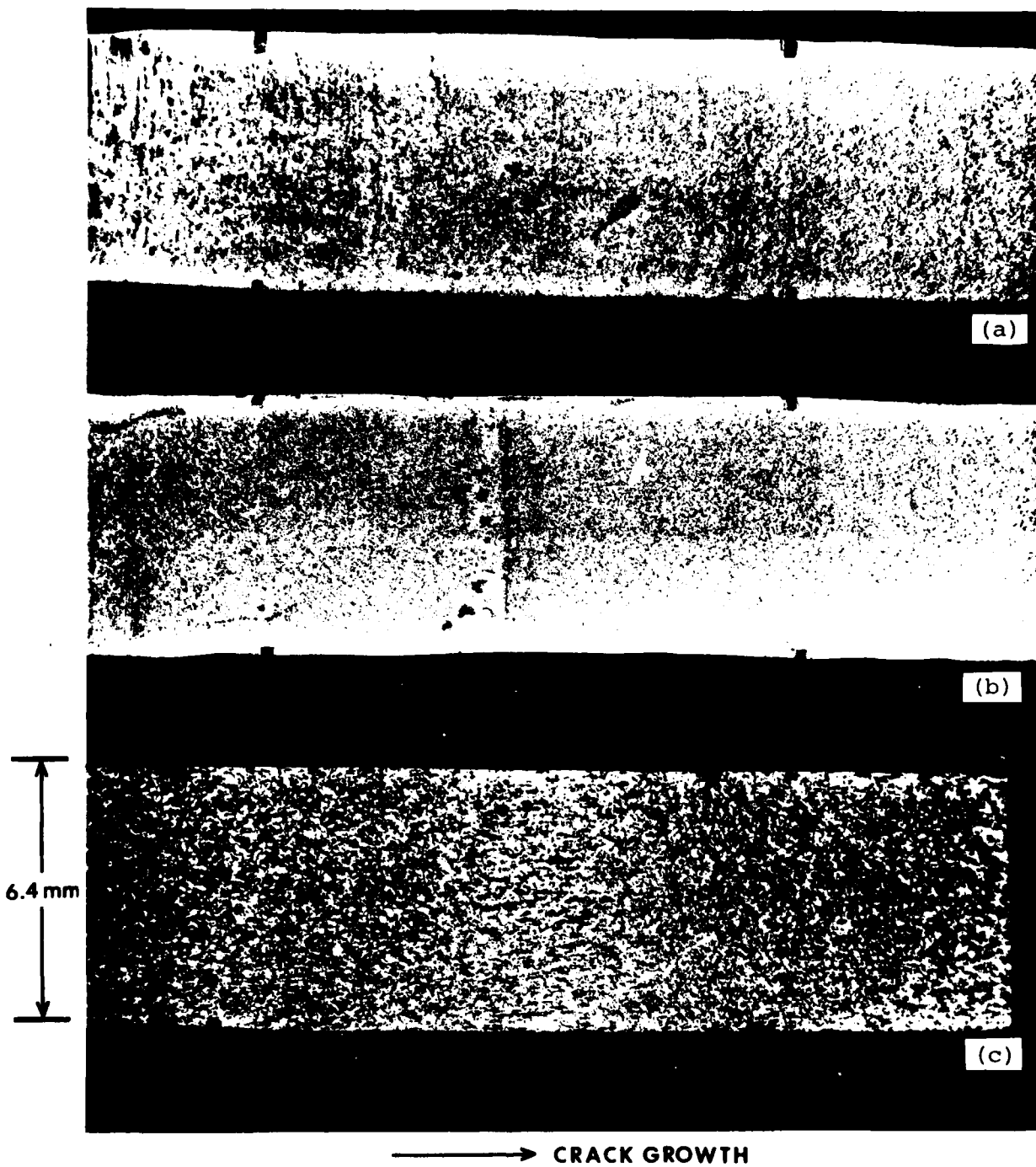


Figure 48. Macrophotographs of fractured FCC specimens from salt fog tests: (a) CT91, T7X1 temper, (b) CT91, T7X2 temper, and (c) 7050-T76511.

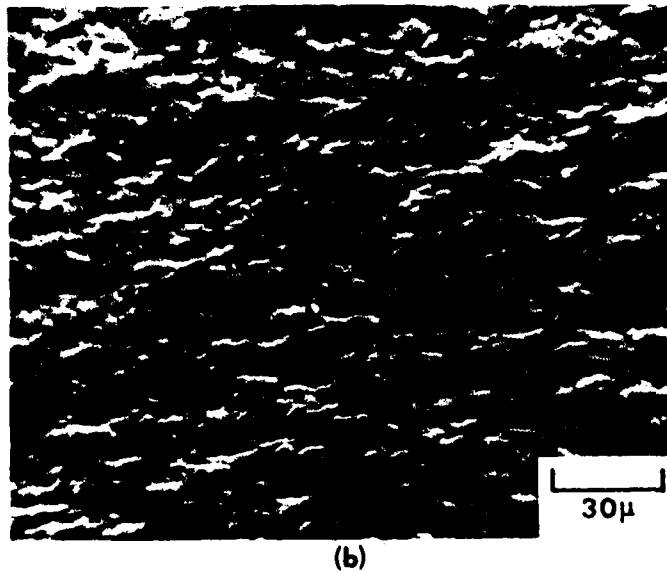
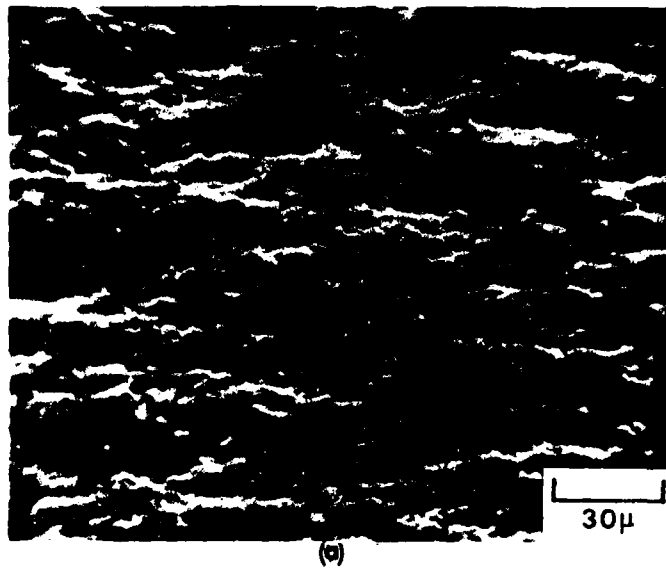
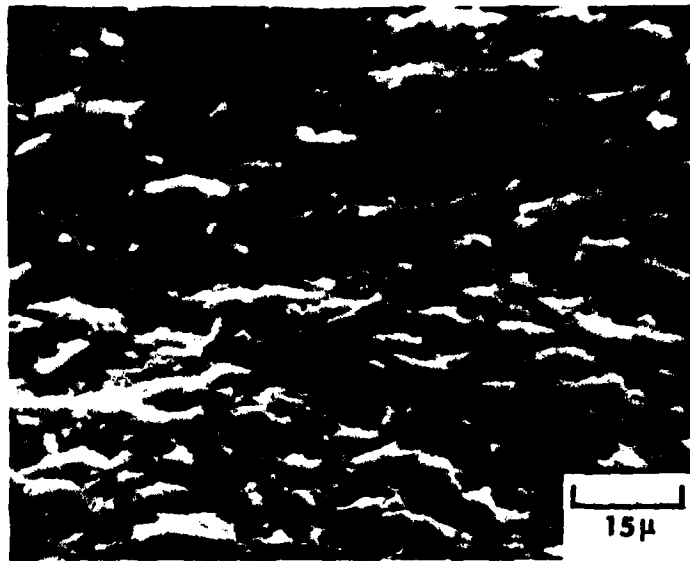
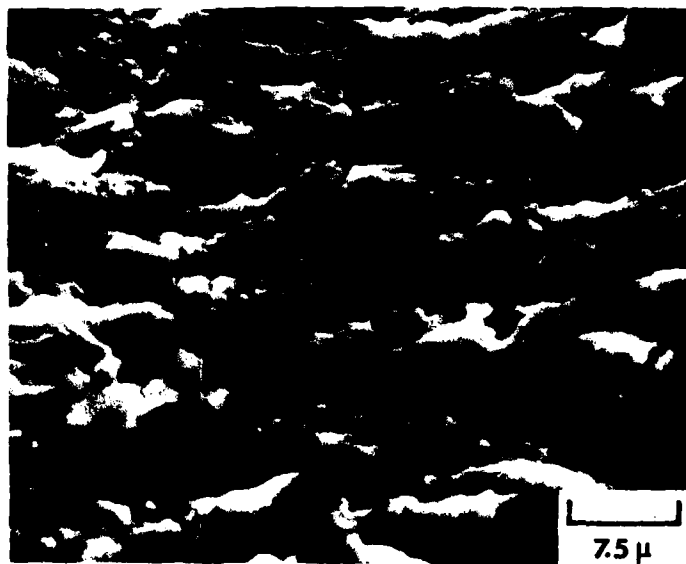


Figure 49. Fractographs of CT91 extrusion FCG specimens tested in salt fog atmosphere, $\Delta K \sim 7 \text{ MPa}\sqrt{\text{m}}$: (a) T7X1 temper and (b) T7X2 temper. Crack growth direction is left to right.

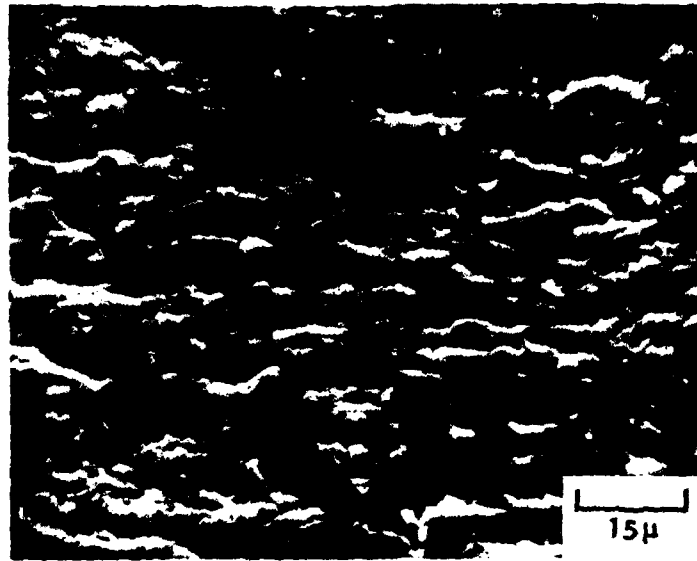


(a)

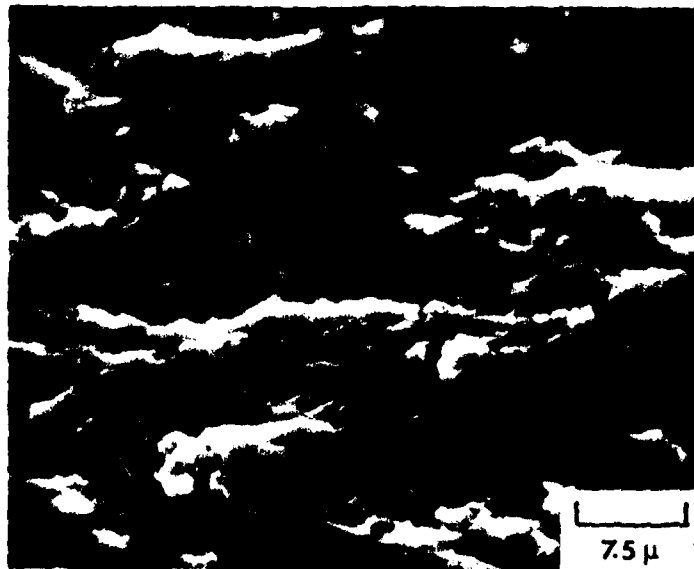


(b)

Figure 50. Fractographs of P/M alloy extrusion FCG specimens tested in salt fog atmosphere, $\Delta K \sim 7 \text{ MPa}\sqrt{\text{m}}$: (a) and (b) MA88-T7X2, (c) and (d) MA90-T7X2. Crack growth direction is left to right.

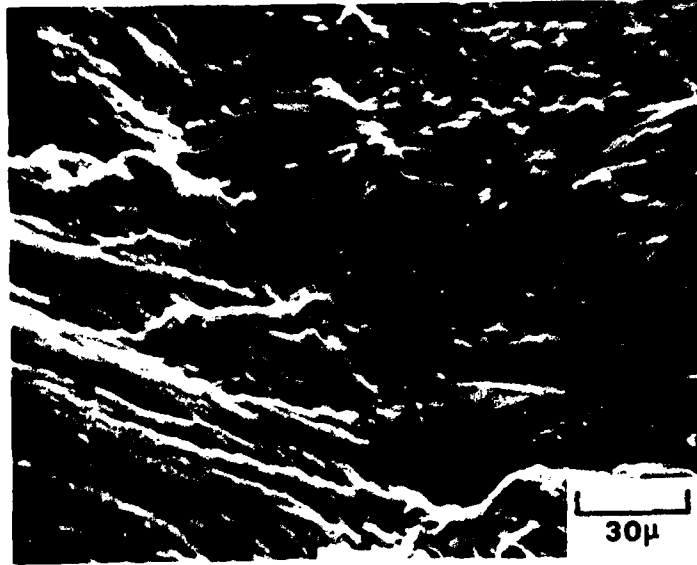


(c)

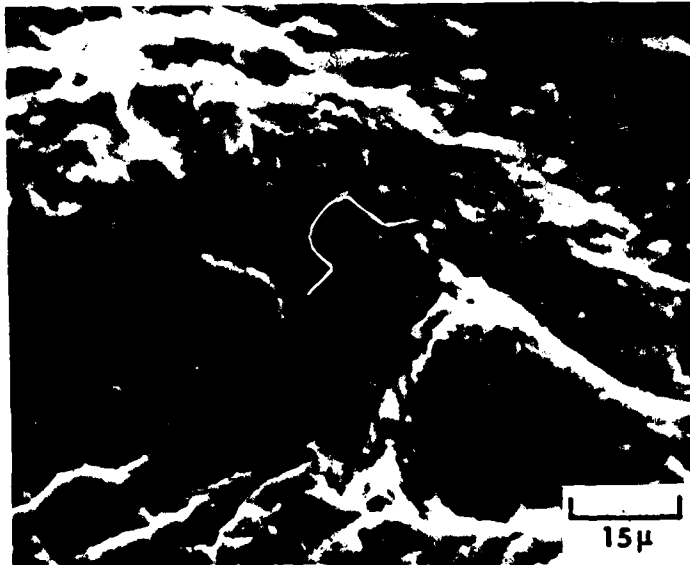


(d)

Figure 50. (Continued) Fractographs of MA90-T7X2 FCG specimens tested in salt fog atmosphere.



(a)



(b)

Figure 51. Fractographs of 7050-T76511 extrusion FCG specimen tested in salt fog atmosphere, $\Delta K \sim 7 \text{ MPa}\sqrt{\text{m}}$: (a) low magnification, (b) higher magnification of similar area. Crack growth direction is left to right.

Yield Strength = 517 MPa
R = 0.33



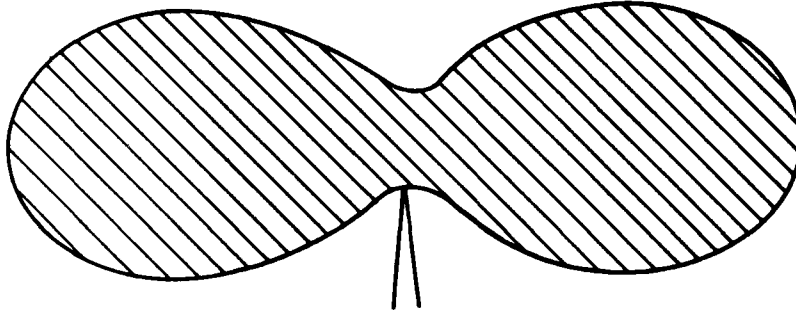
$\Delta K = 3.0 \text{ MPa}\sqrt{\text{m}}$

$r_p \approx 13 \mu\text{m}$



$\Delta K = 5.0 \text{ MPa}\sqrt{\text{m}}$

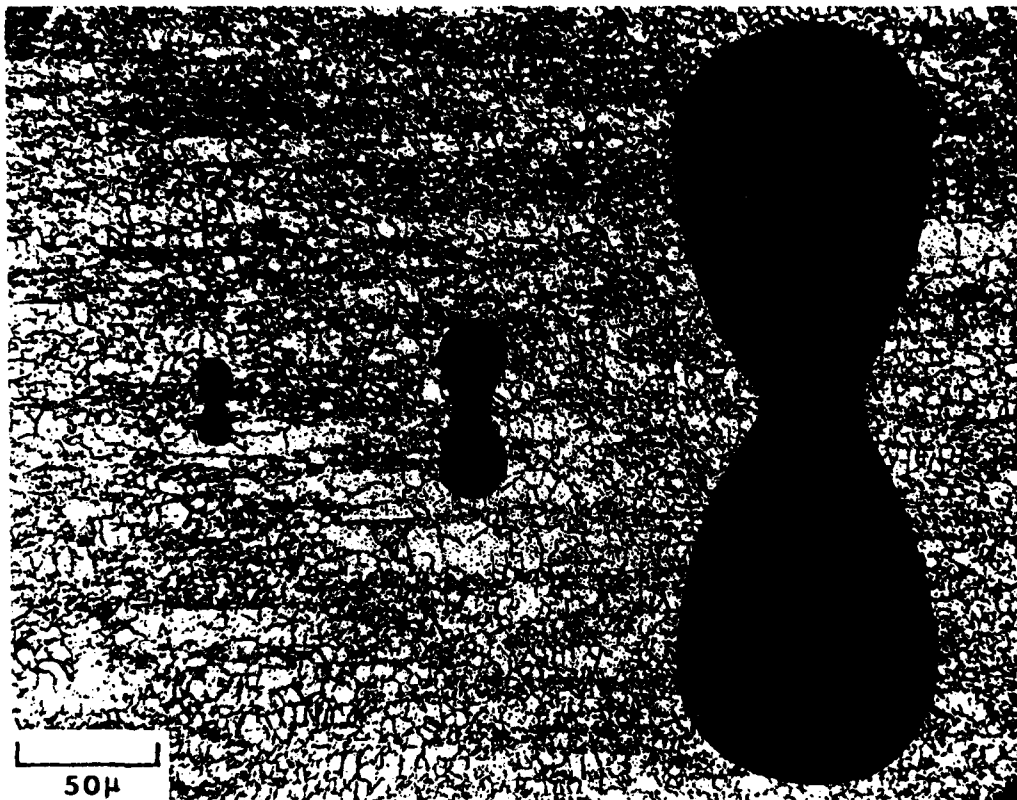
$r_p \approx 36 \mu\text{m}$



$\Delta K = 10.0 \text{ MPa}\sqrt{\text{m}}$

$r_p \approx 142 \mu\text{m}$

Figure 52. Schematic diagram of monotonic plastic zone size (r_p) as a function of ΔK .

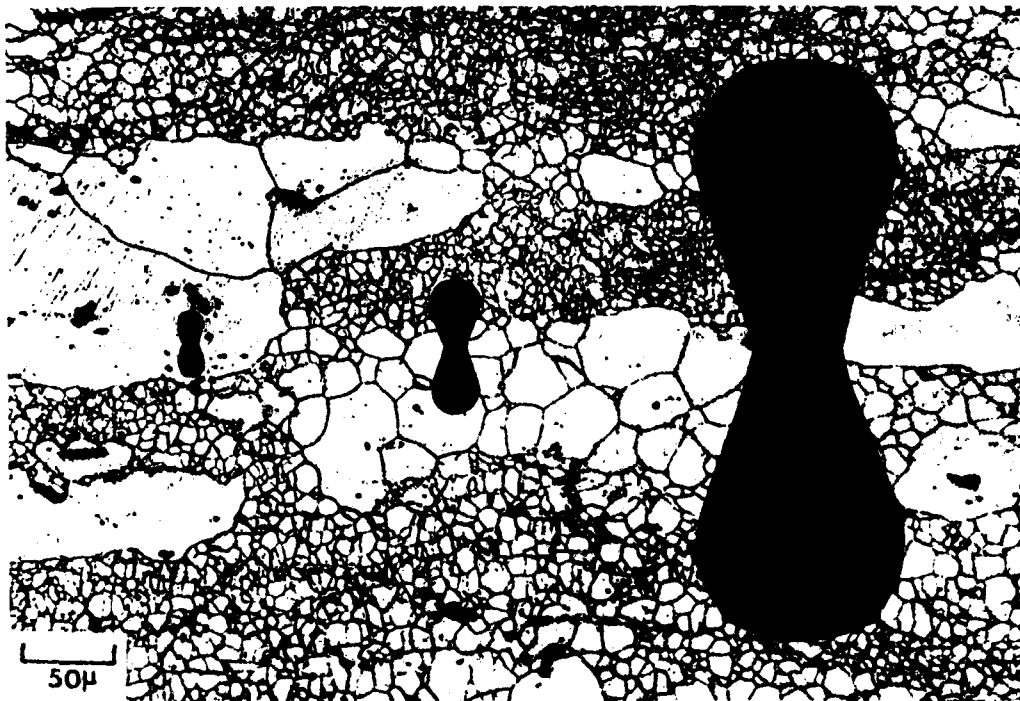


$\Delta K = 3.0$

5.0

10.0 $\text{MPa}\sqrt{\text{m}}$

Figure 53. Schematic superposition of monotonic plastic zones and microstructures for: (a) CT91-T7X1 and (b) 7050-T76511, showing relative sizes of r_p and microstructural features. Plastic zone sizes illustrated here from left to right are for $\Delta K = 3.0, 5.0, \text{ and } 10.0 \text{ MPa}\sqrt{\text{m}}$.



AK = 3.0

5.0

10.0 MPa \sqrt{m}

Figure 53. (Continued) (b) Monotonic plastic zone size vs microstructure for 7050-T76511.

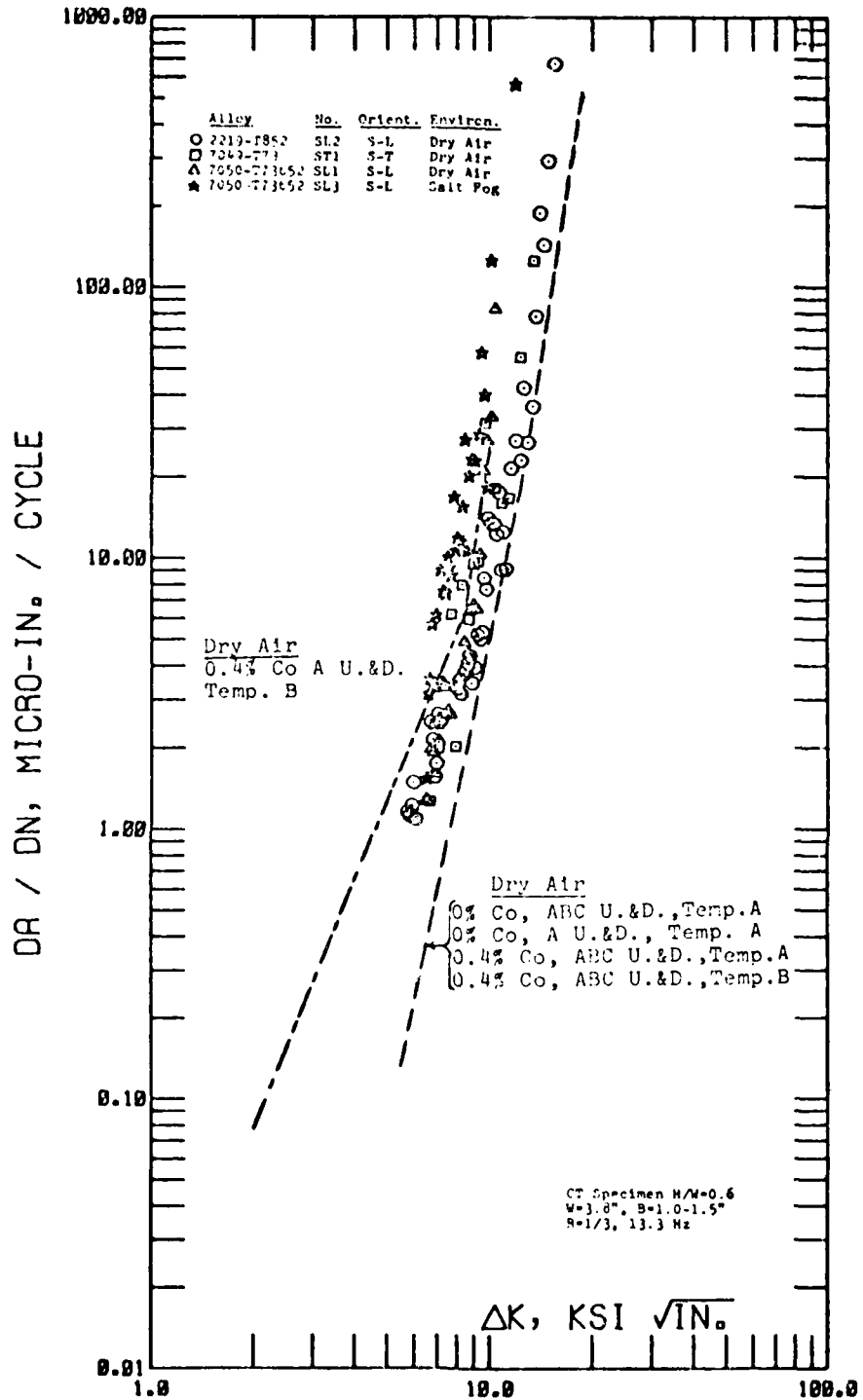


Figure 54. FCG data for short-transverse specimens taken from P/M hand forgings, Reference 3.
(SI conversion: 1 in.=2.54 cm, 1 ksi√in.=1.1 MPa√m)

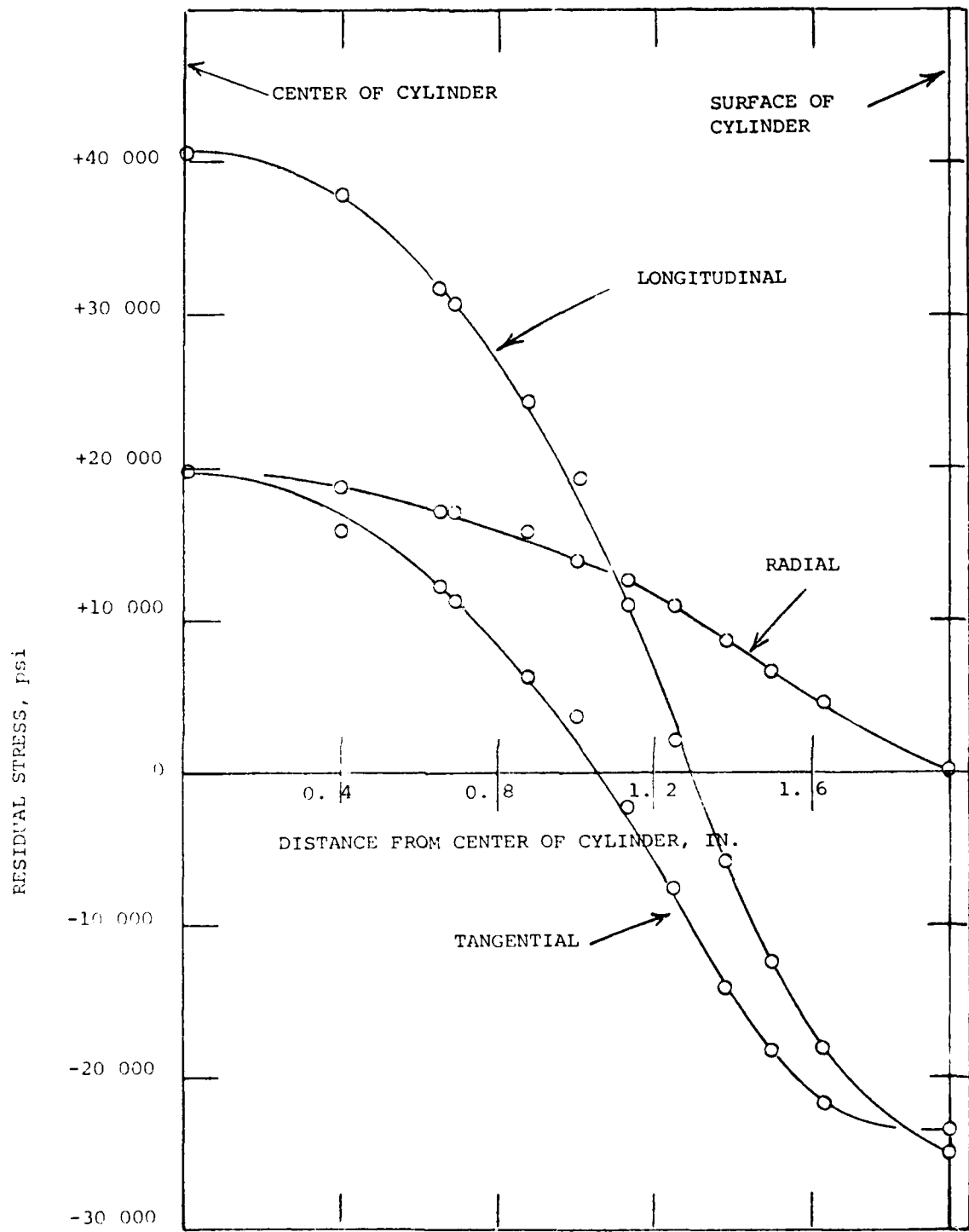


Figure 55. Residual stress distribution in 7075 cylinder quenched in cold water spray.
 (SI conversion: 1 in.=2.54 cm, 1000 psi=6.894 MPa).

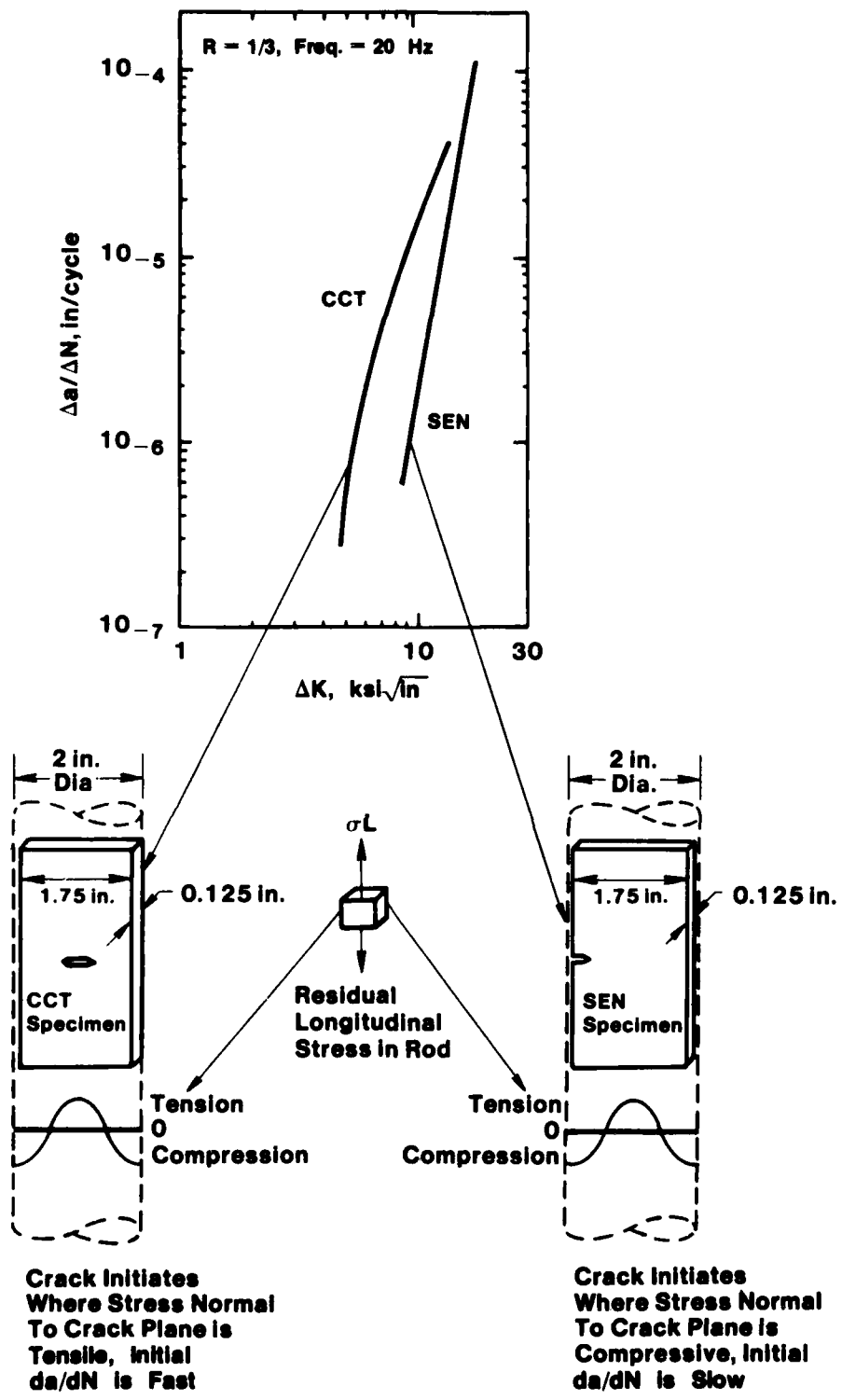
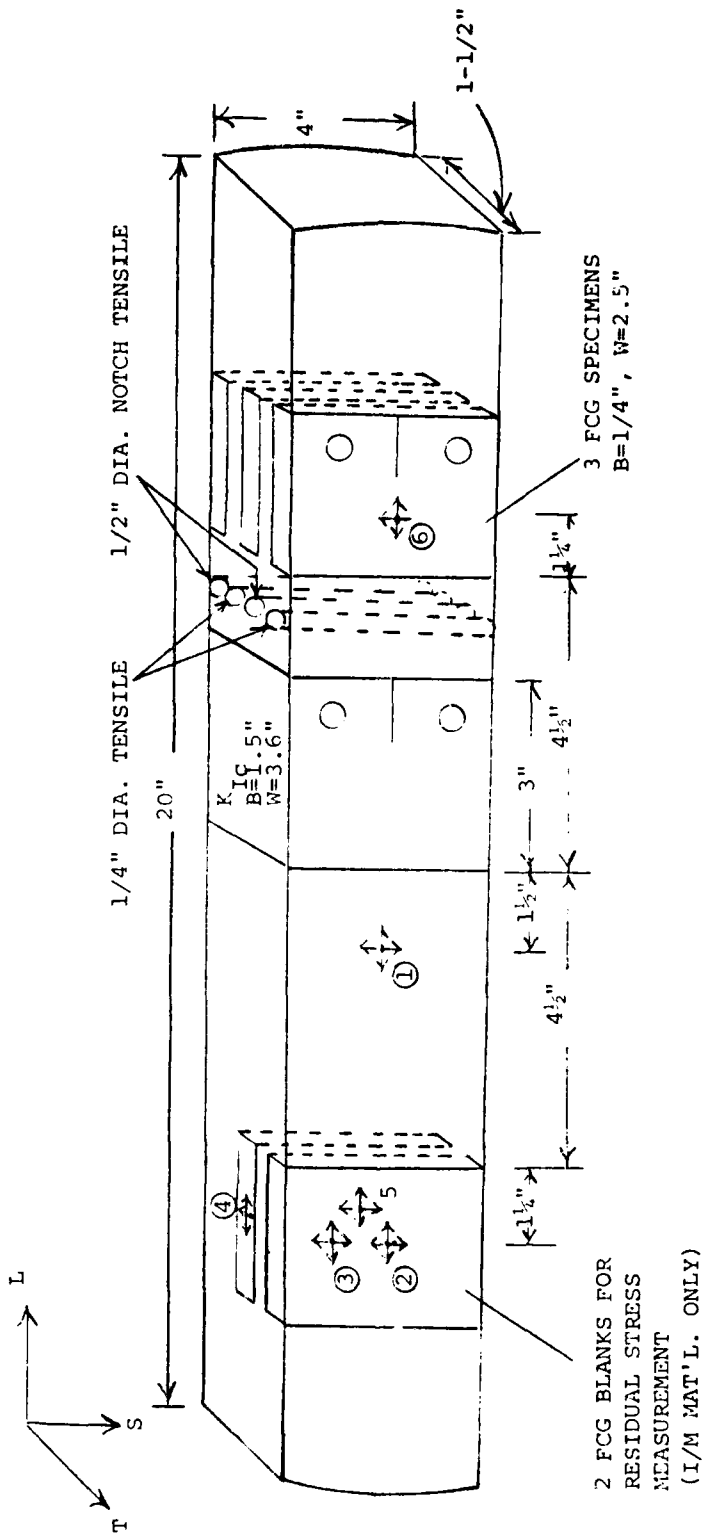


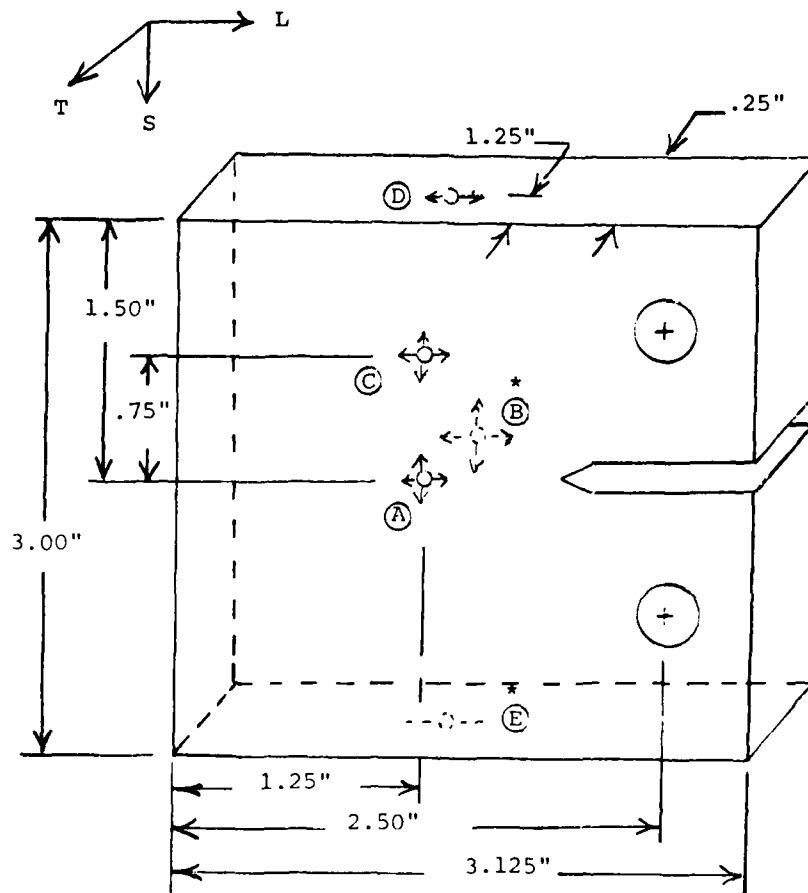
Figure 56. Proposed explanation for observed effect of specimen type on FCG rates established from nonstress-relieved 7XXX P/M extruded rod.
 (SI conversion: 1 in.=25.4 mm, 1 ksi $\sqrt{\text{in.}}$ = 1.1 MPa $\sqrt{\text{m}}$)

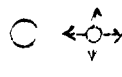


⇄ INDICATES LOCATION AND DIRECTION OF RESIDUAL STRESS MEASUREMENT BY X-RAY METHOD PRIOR TO REMOVING SPECIMENS

* LOCATION ⑤ ON REAR SURFACE DIRECTLY OPPOSITE LOCATION ②

Figure 57. Location of Phase III test specimens and residual stress measurements in parent slab.
 (SI conversion: 1 in.=25.4 mm)

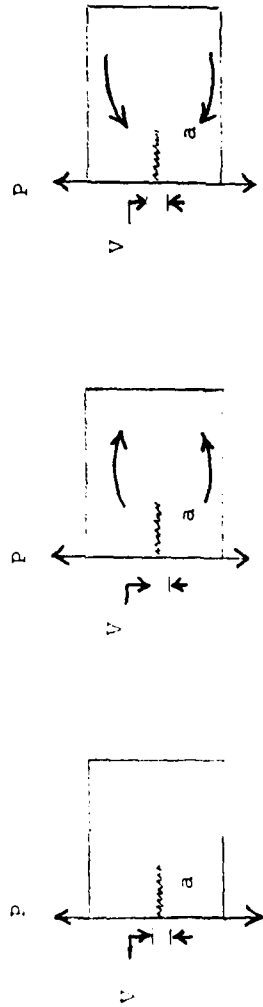



 INDICATIONS LOCATION AND DIRECTION OF RESIDUAL STRESS MEASUREMENT BY X-RAY METHOD

(*) INDICATES LOCATIONS B AND E ARE RESPECTIVELY ON OPPOSITE SURFACE TO LOCATIONS A AND D

METRIC CONVERSION: 1 IN. = 25.4 mm

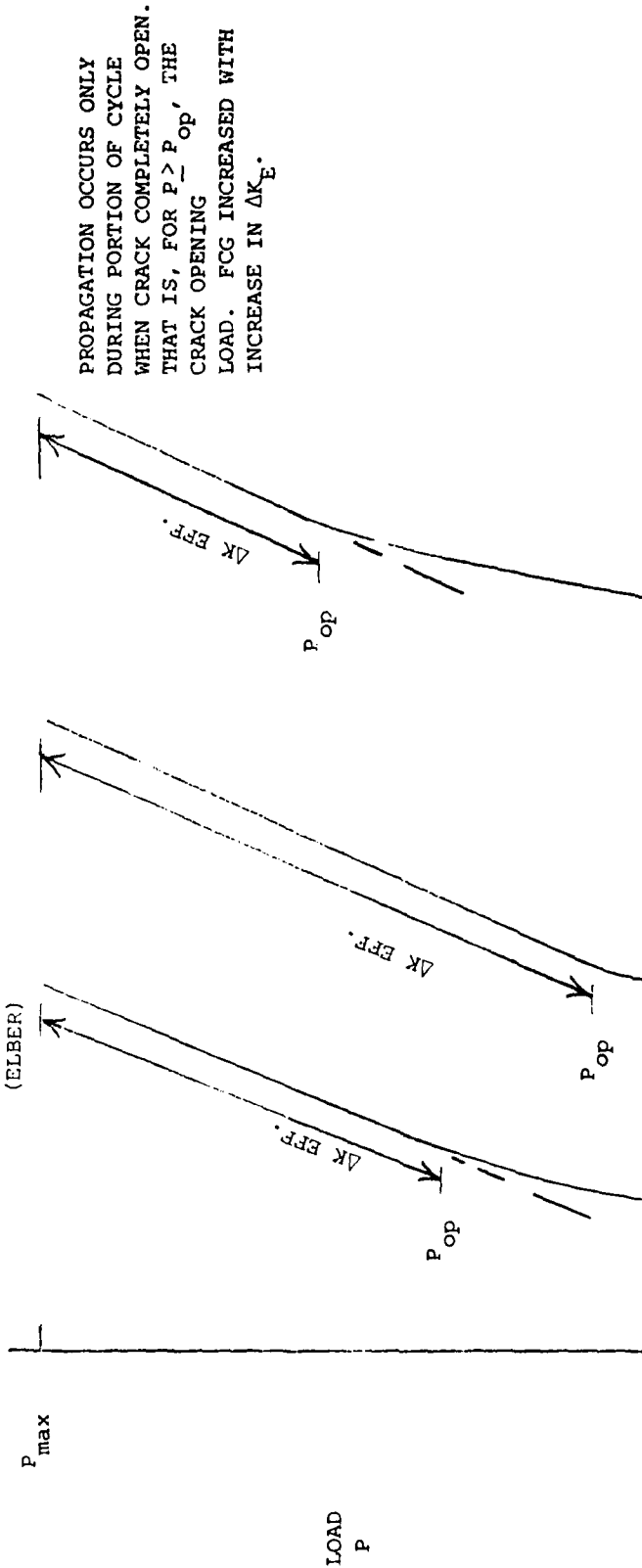
Figure 58. Location and orientation of X-ray residual stress measurements on FCG test specimens.



1. MATERIAL FREE OF RESIDUAL STRESS OPENING LOAD ATTRIBUTED TO CRACK CLOSURE (ELBER)

2. TENSION RESIDUAL STRESS + CRACK CLOSURE, P_{op} DECREASE

3. COMPRESSION RESIDUAL STRESS + CRACK CLOSURE, P_{op} INCREASE



PROPAGATION OCCURS ONLY DURING PORTION OF CYCLE WHEN CRACK COMPLETELY OPEN. THAT IS, FOR $P > P_{op}$, THE CRACK OPENING INCREASES WITH INCREASE IN ΔK_E .

CRACK OPENING DISPLACEMENT - V

Figure 59. Effect of residual stresses on load-COD trace in bulk material surrounding the crack tip.

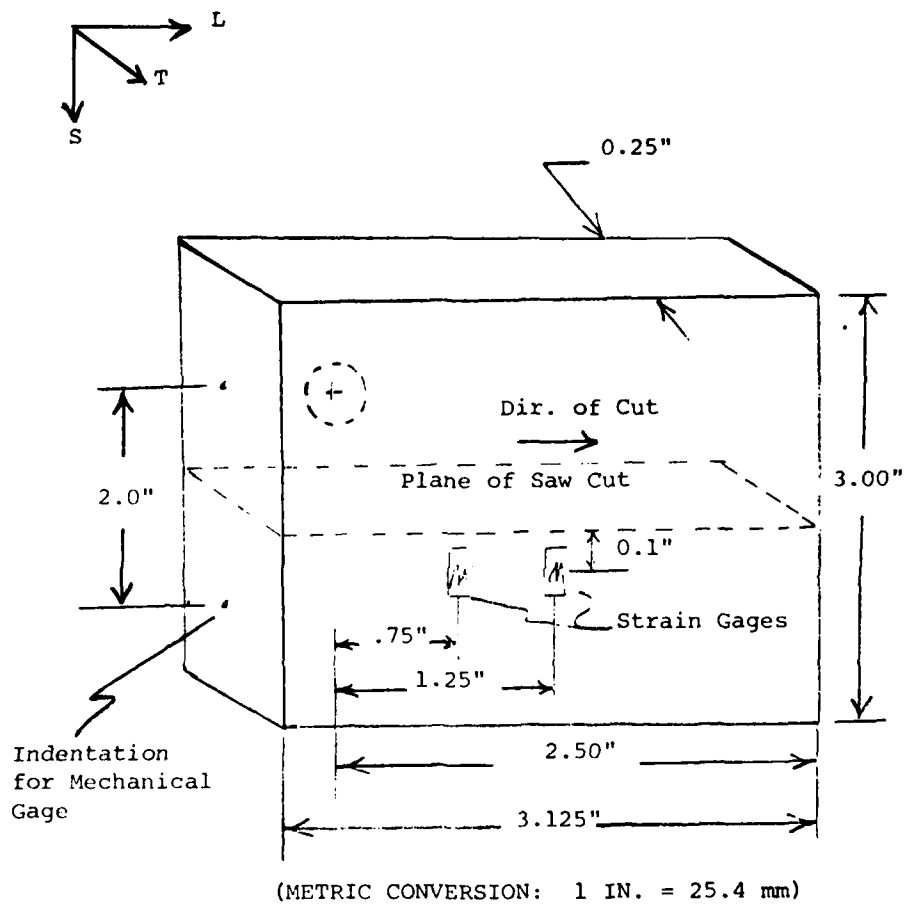
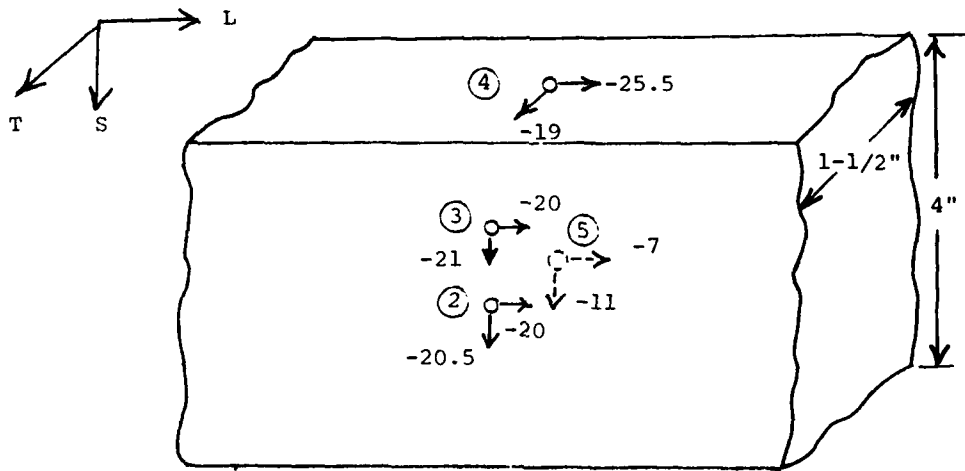


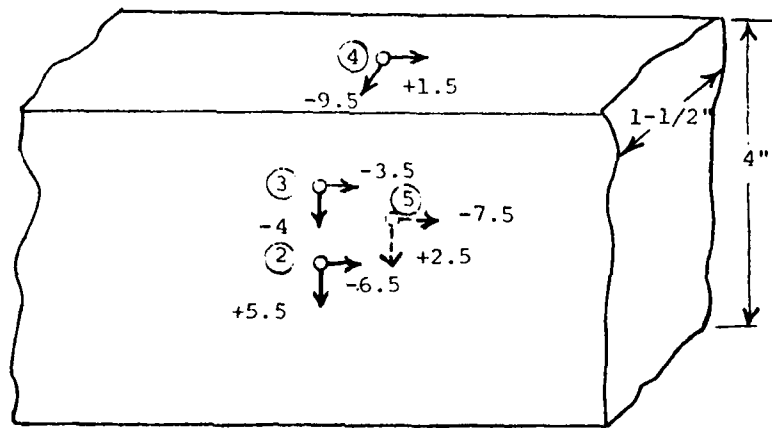
Figure 60. Location of displacement measurements in CT specimen blanks simulating FCG by progressive sawcuts.



NONSTRESS RELIEVED

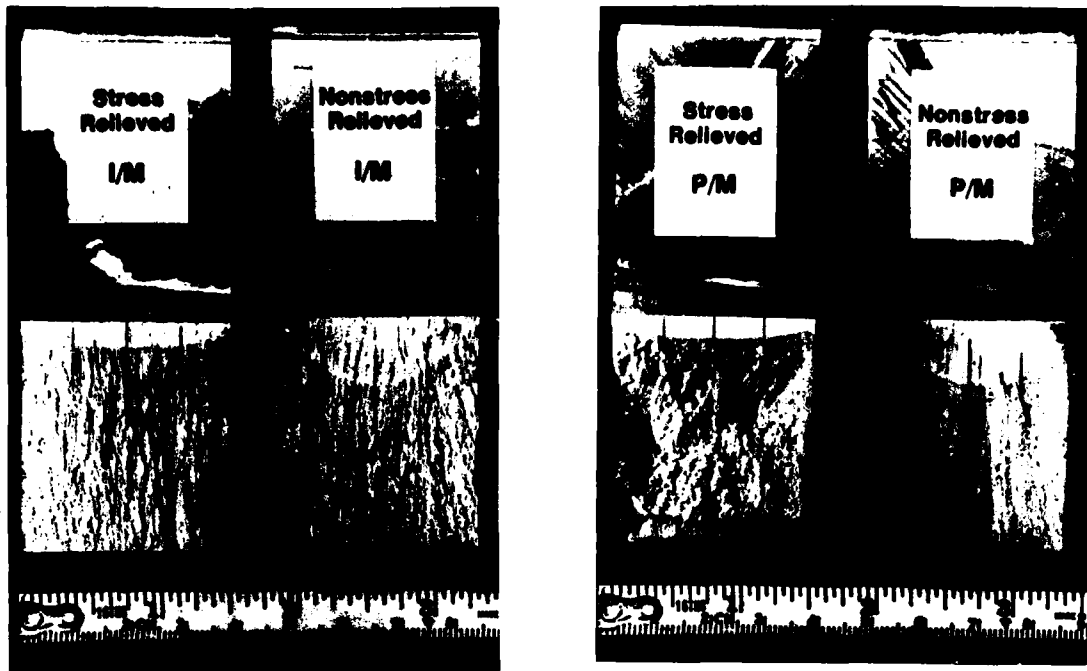
METRIC CONVERSION: 1 IN. = 25.4 mm

STRESSES GIVEN IN ksi
(1 ksi = 6.9 MPa)



STRESS RELIEVED

Figure 61. Average residual stress measurements in parent slabs. (Results averaged for P/M and I/M materials.)



Broken Fracture Toughness Specimen Halves

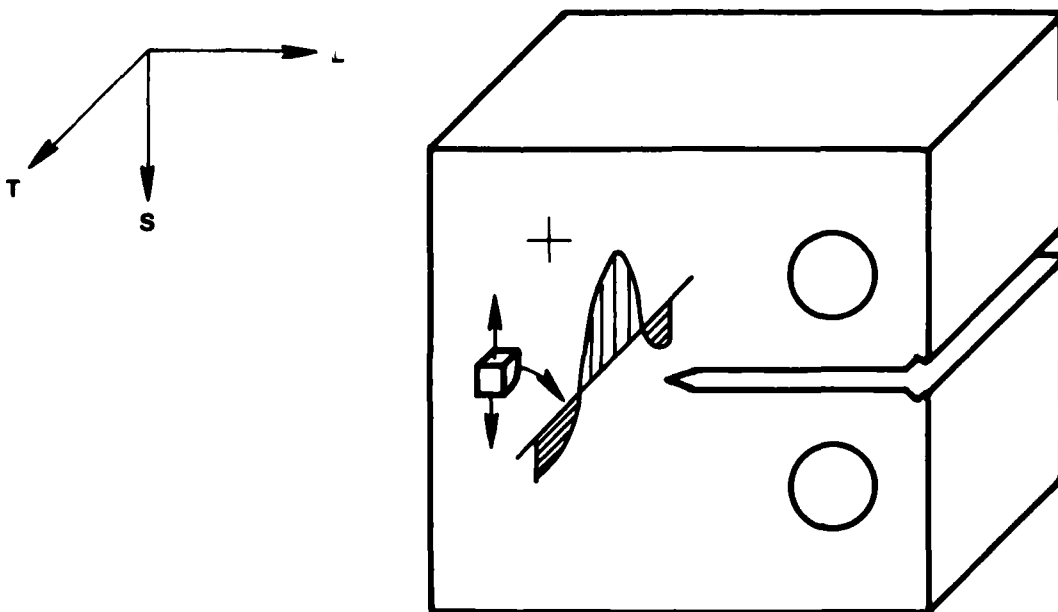
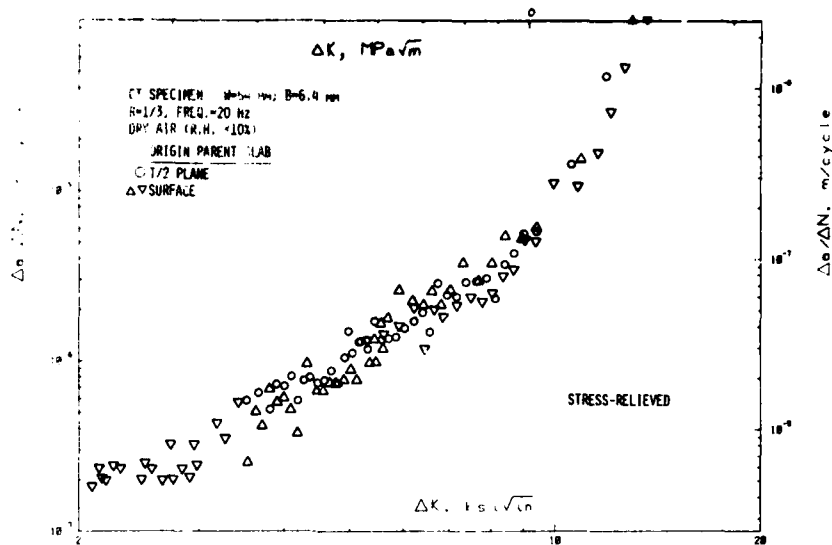
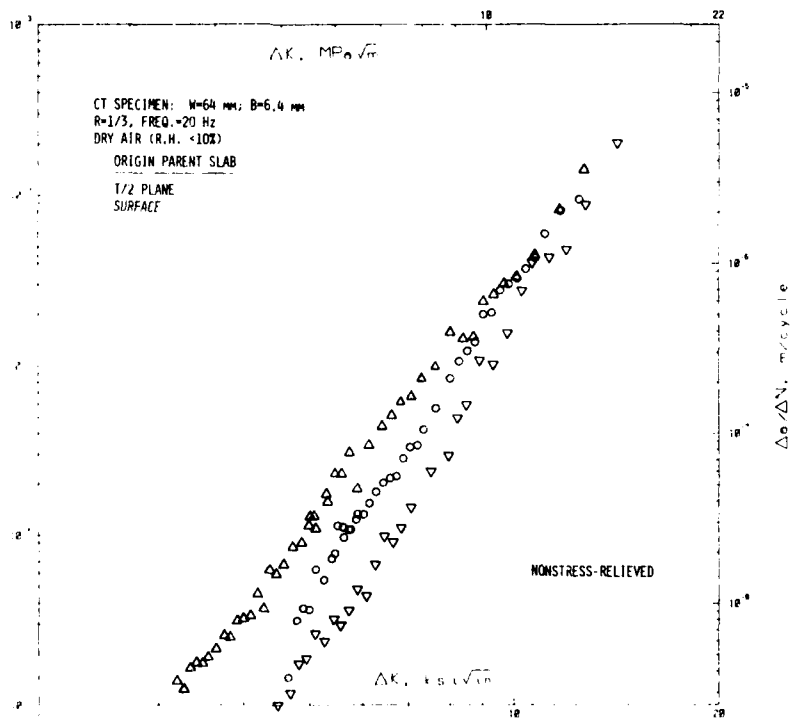


Figure 62. Through-thickness residual stress distribution which causes crack curvature in nonstress-relieved materials.

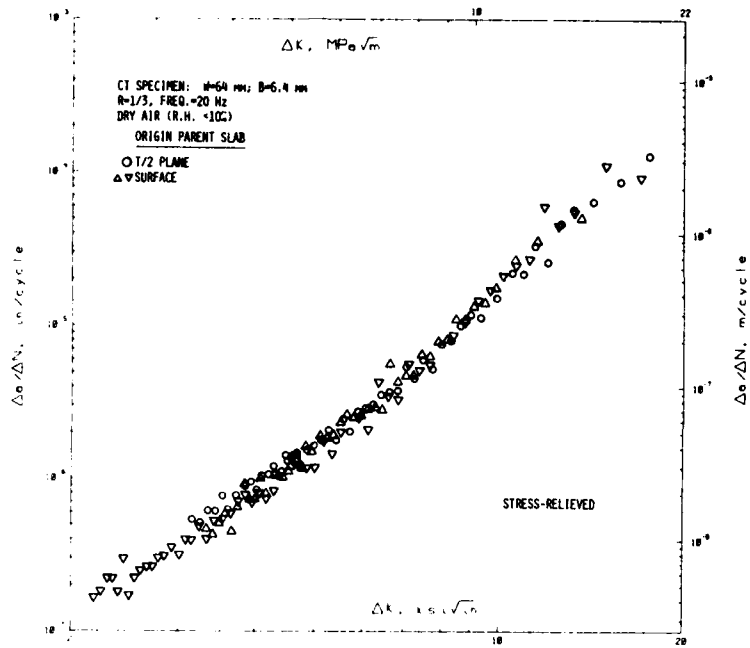


(a)

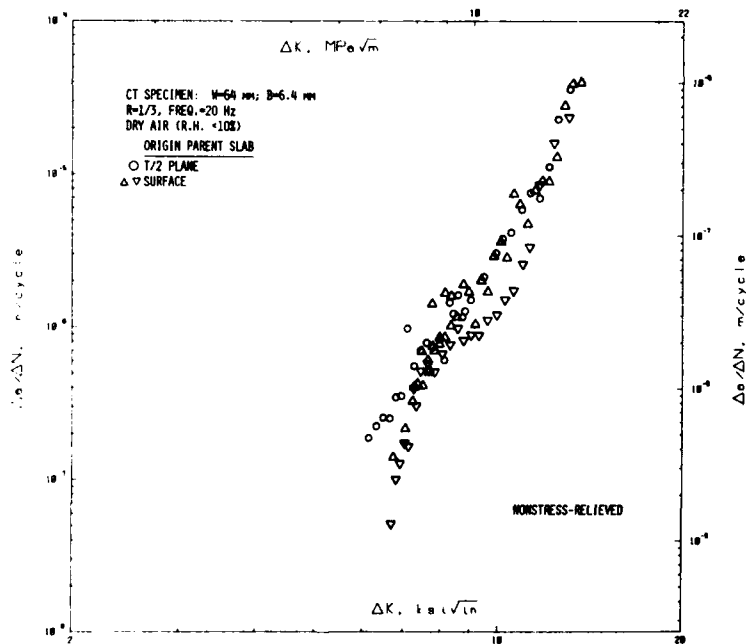


(b)

Figure 63. Effect of stress relief on S-L FCG rates in MA87-T7X2 hand forging: da/dN vs ΔK for (a) stress-relieved and (b) nonstress-relieved slabs.



(a)



(b)

Figure 64. Effect of stress relief on S-L FCG rates in 7XXX-T7X2 hand forging: da/dN vs ΔK for (a) stress-relieved and (b) nonstress-relieved slabs. 127

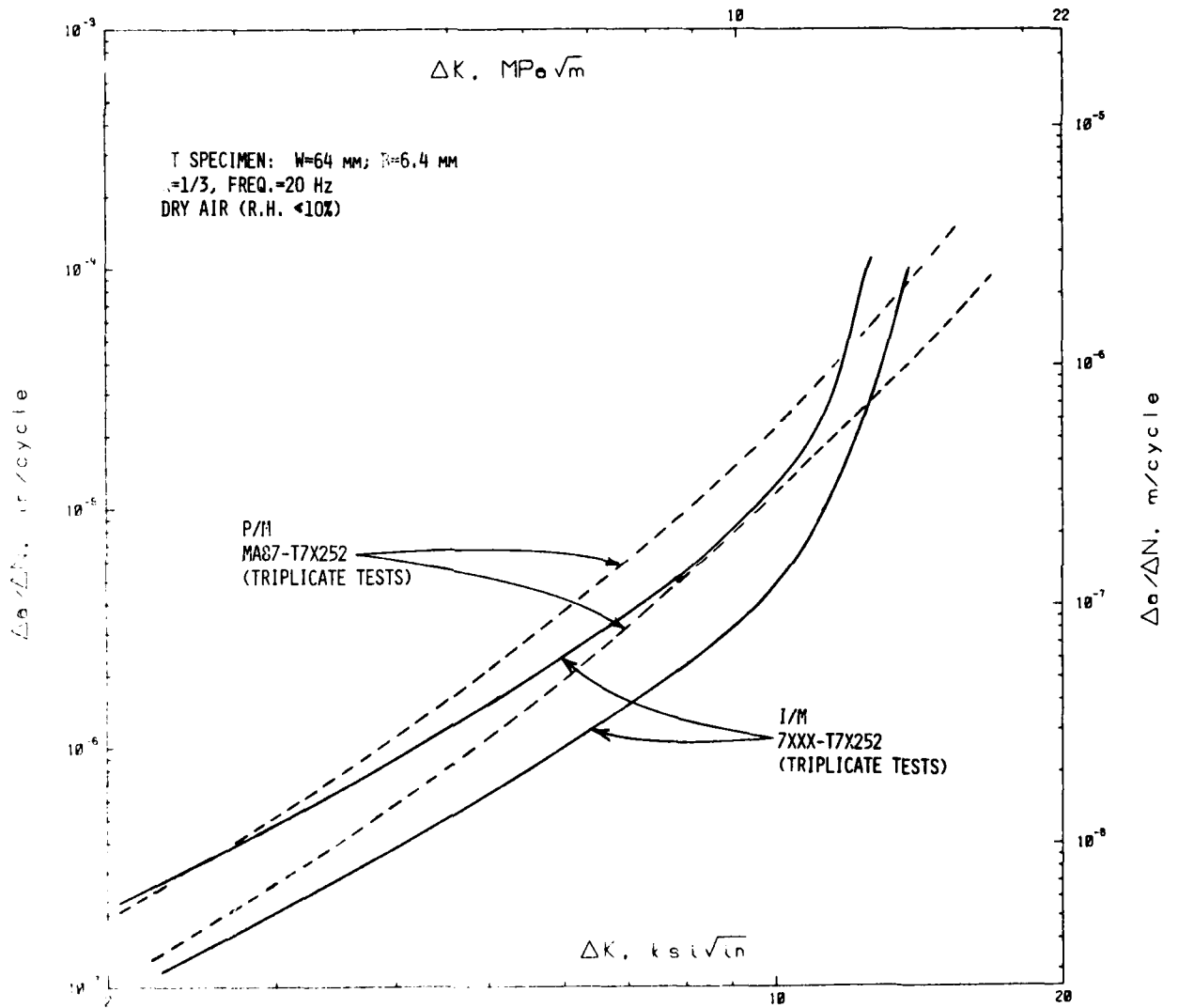


Figure 65. Comparison of S-L FCG rates in stress-relieved P/M and I/M hand forgings.

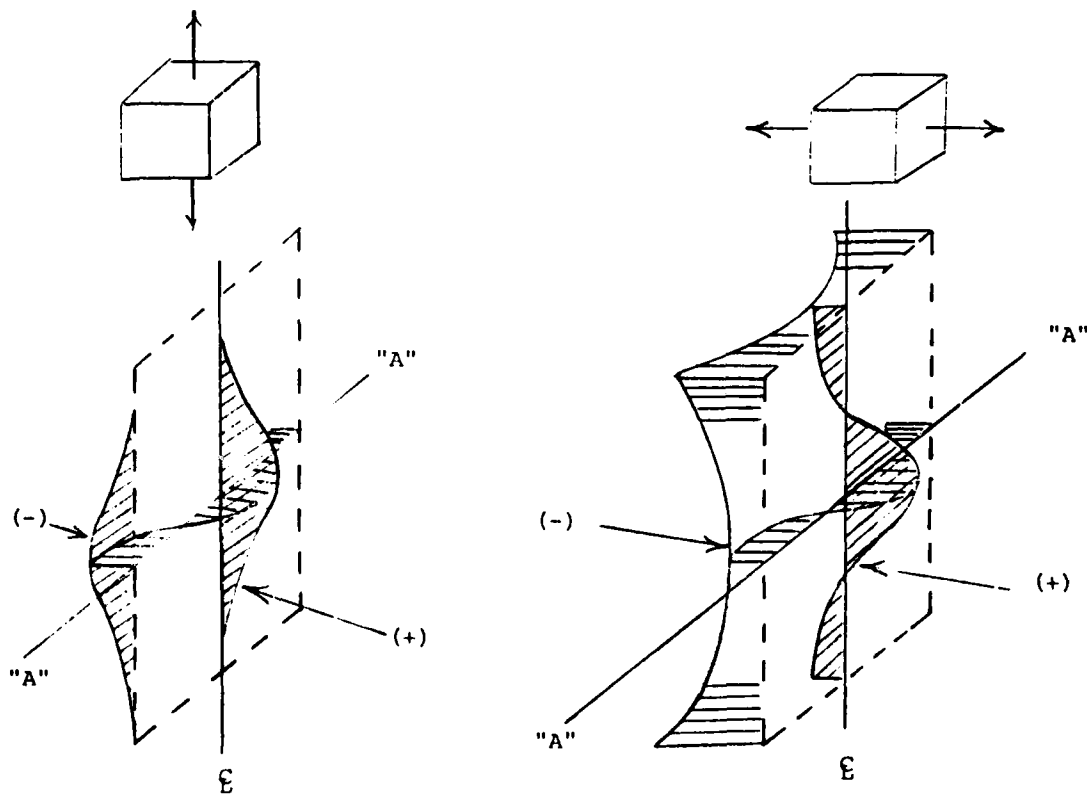
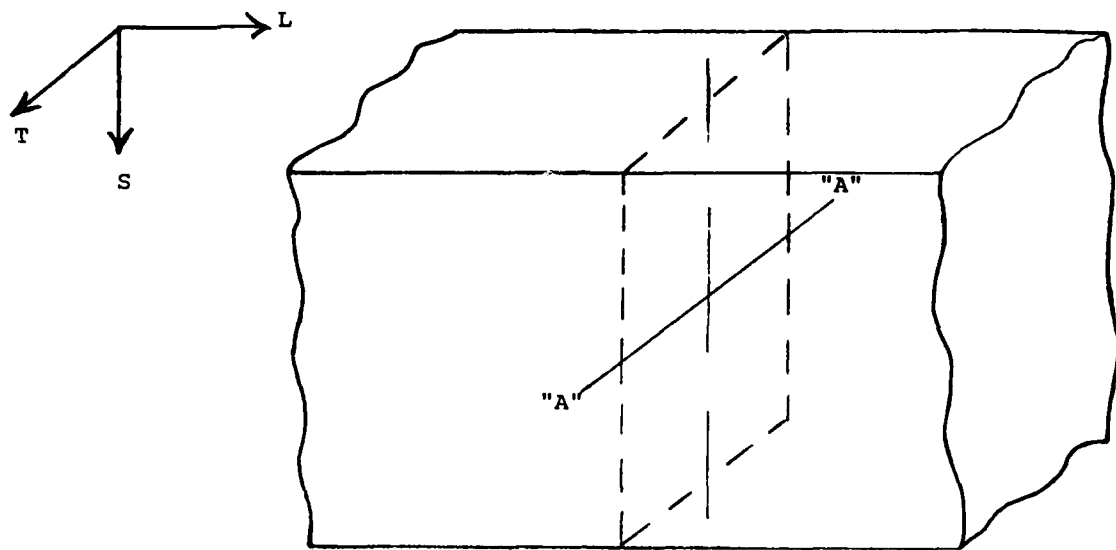


Figure 66. Typical residual stress distribution on rectangular section "A-A".

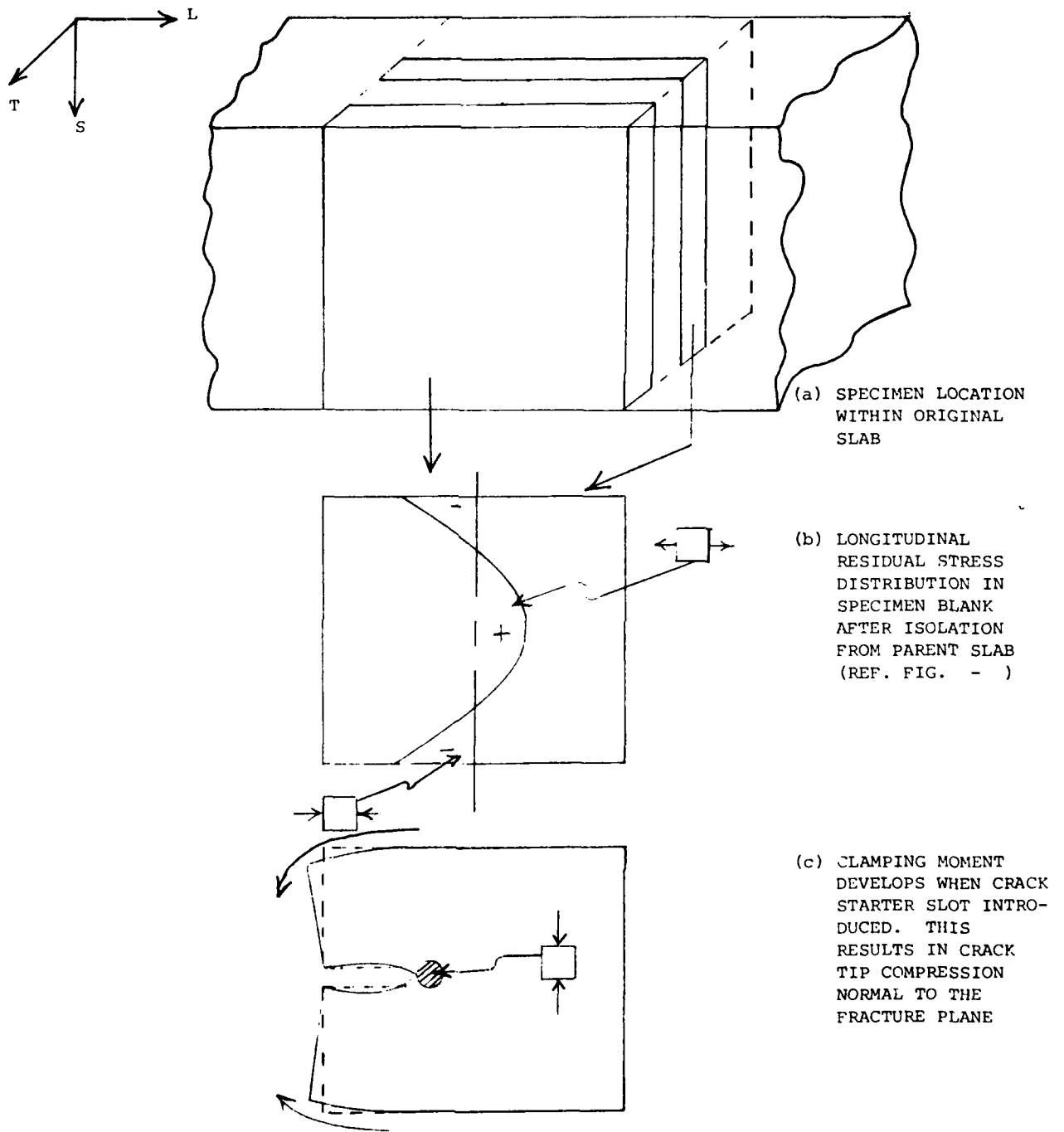


Figure 67. Effect of longitudinal residual stress on FCG measurement in S-L CT specimen taken from non-stress-relieved material.

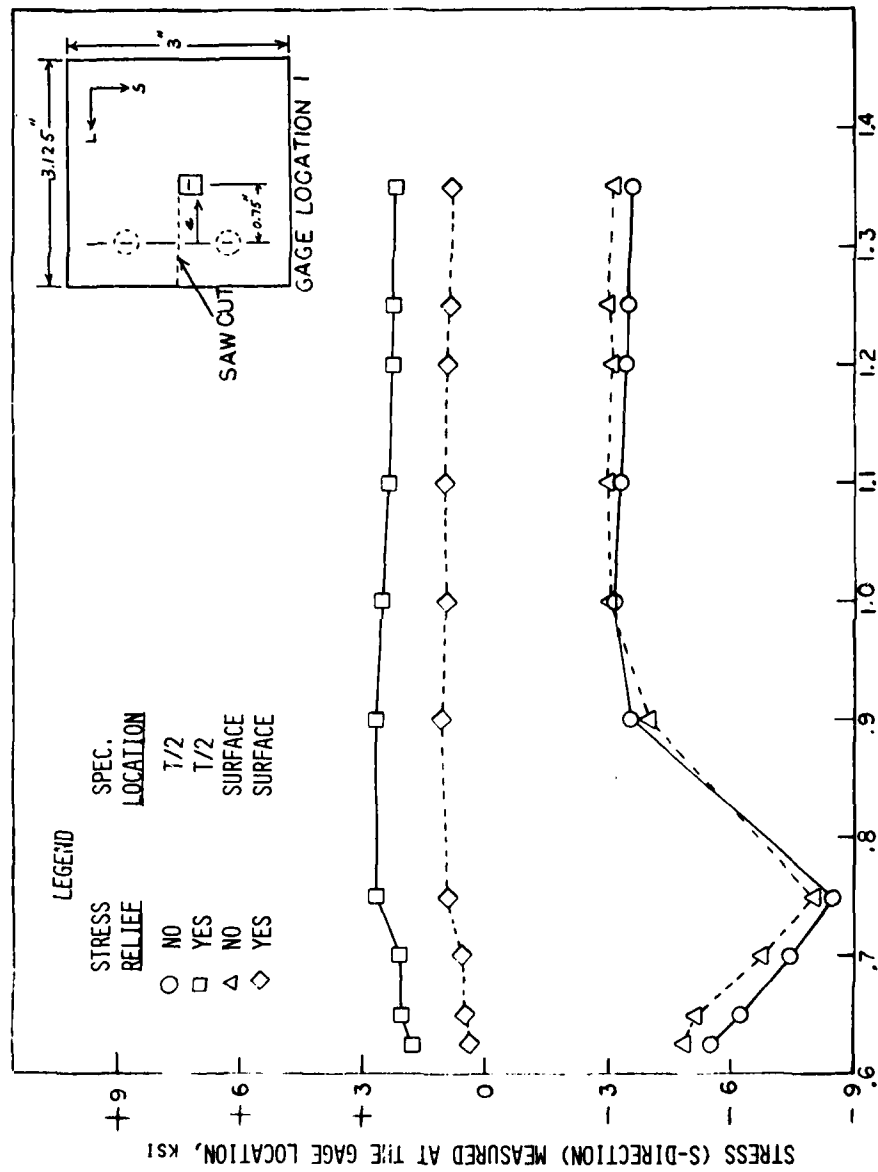
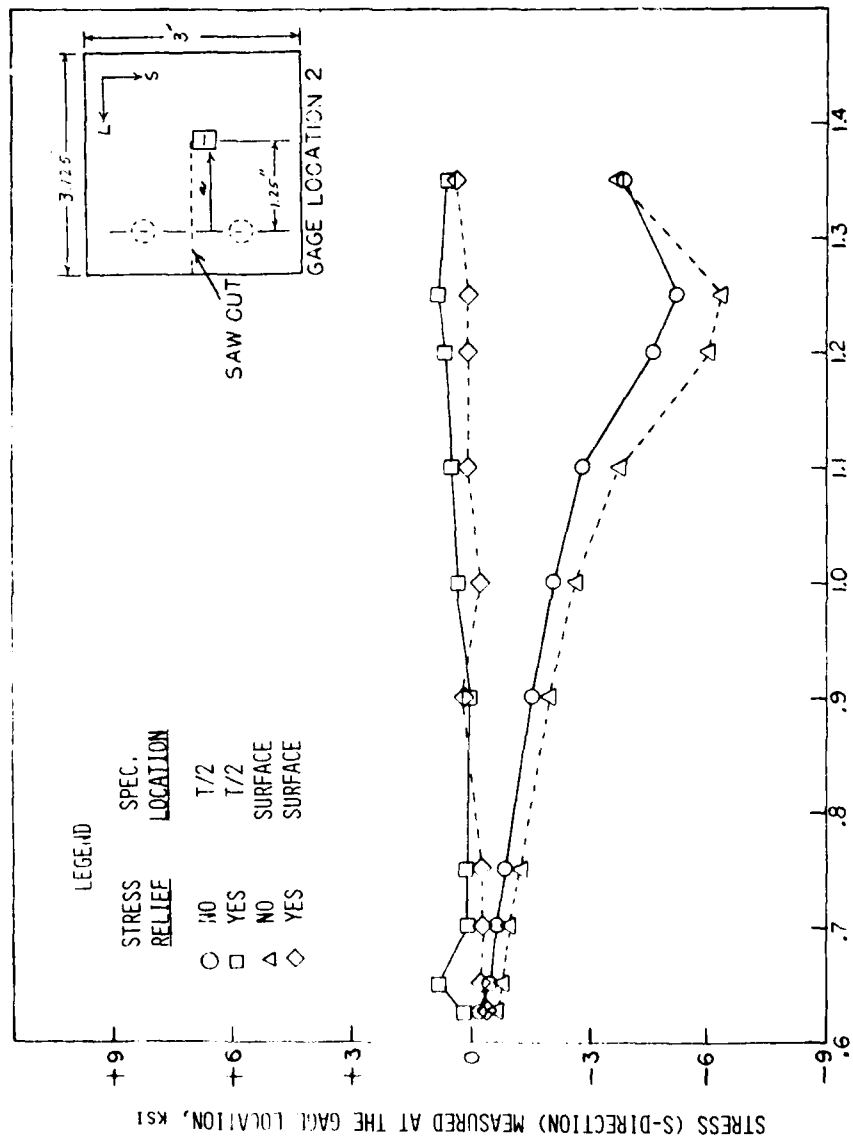


Figure 68. (a) Stress redistribution following sawcuts to simulate a propagating crack in a compact tension specimen for gauge location 1, $a = 19.05$ mm (0.75 in.). (SI conversion: 1 in.=25.4 mm, 1 ksi=6.894 MPa)



DISTANCE OF SAWCUT MEASURED FROM C. OF PINHOLES, A, IN.

Figure 68. (Continued) (b) Stress redistribution following sawcuts to simulate a propagating crack in a compact tension specimen for gage location 2, a = 31.8 mm (1.25 in.). (SI conversion: 1 in.=25.4 mm, 1 ksi=6.894 MPa)

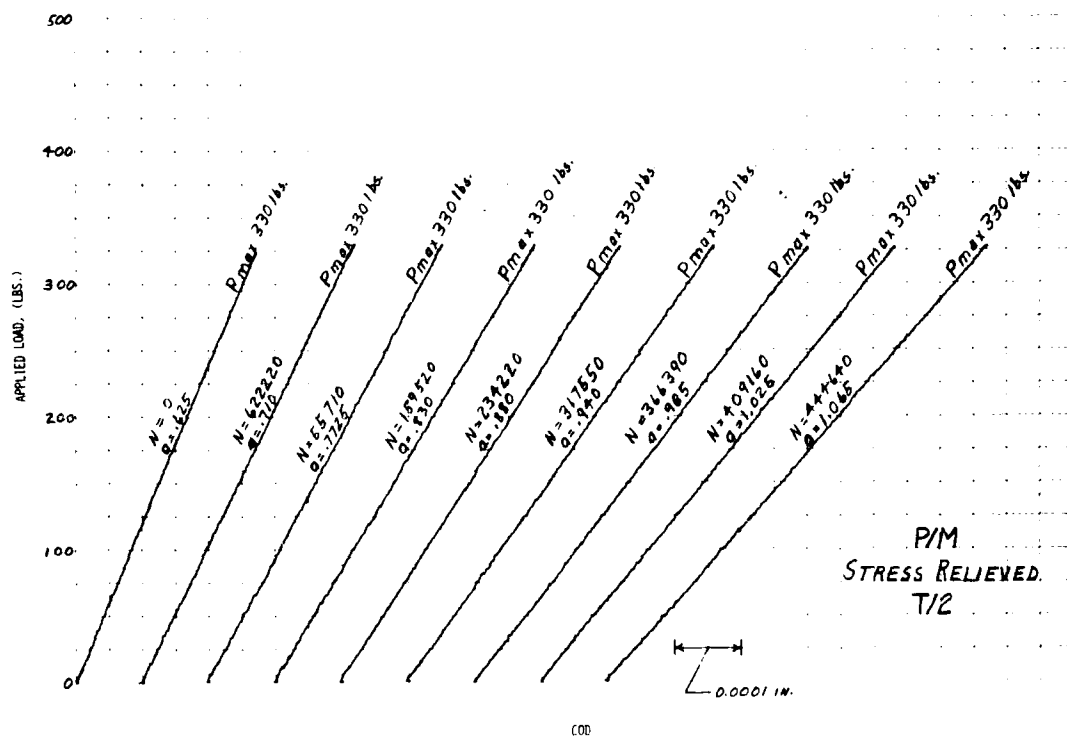
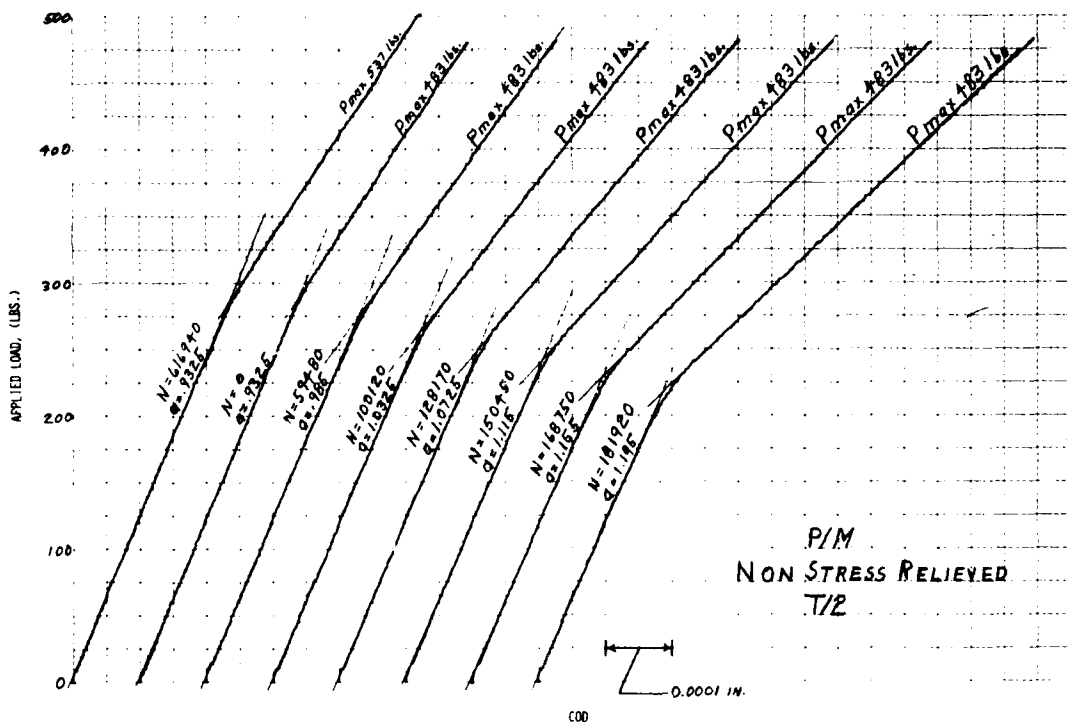


Figure 69. Characteristic Load-COD traces established on stress-relieved and nonstress-relieved P/M FCG specimens.
(SI conversion: 1 in.=25.4 mm, 1 lb=4.4 N)

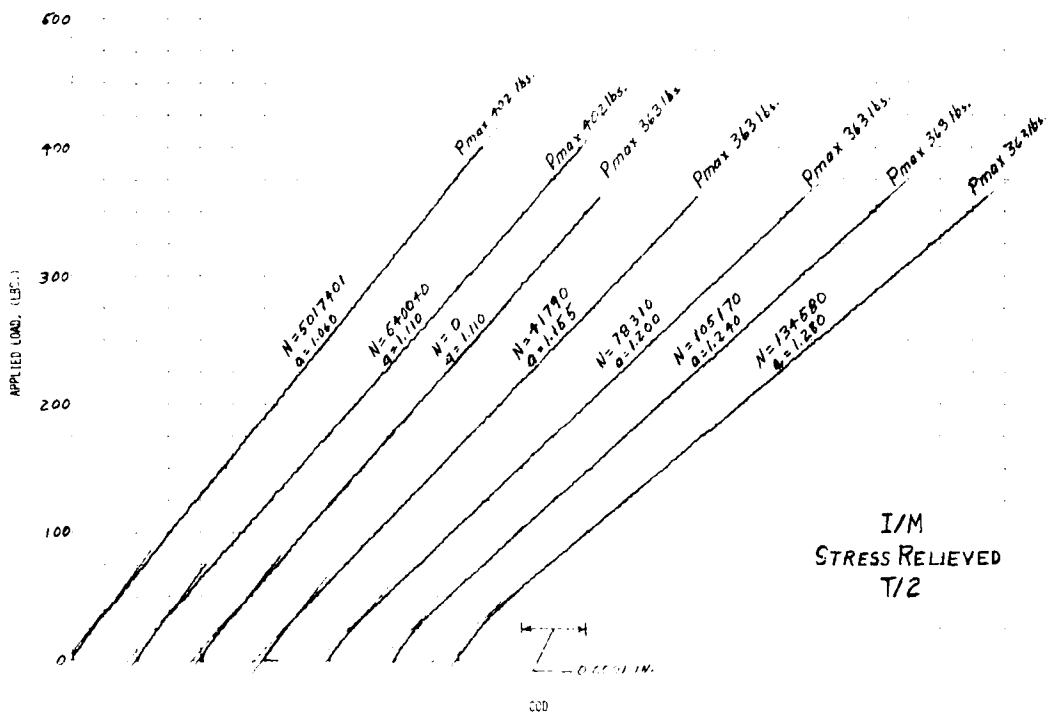
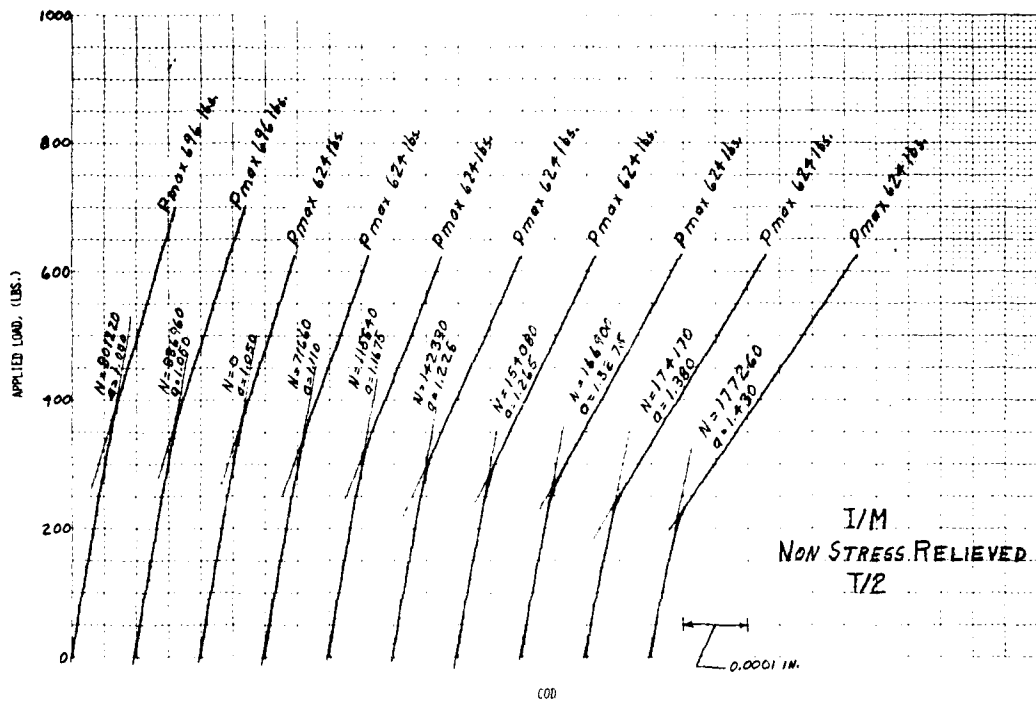


Figure 70. Characteristic Load-COD traces established on stress-relieved and nonstress-relieved I/M FCG specimens.

(SI conversion: 1 in.=25.4 mm, 1 lb=4.4 N)

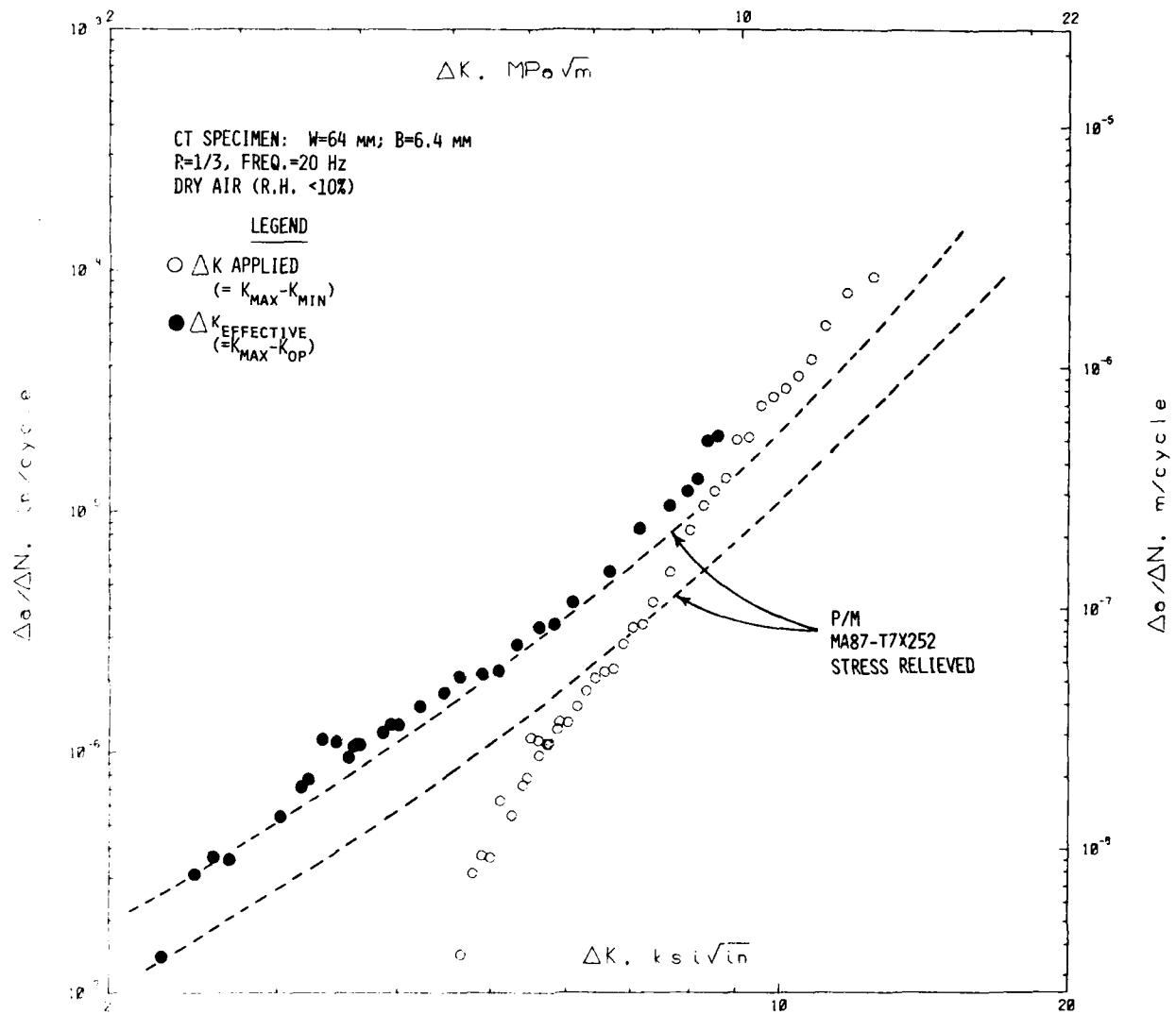


Figure 71. Corrected FCG rates in nonstress-relieved P/M hand forgings.

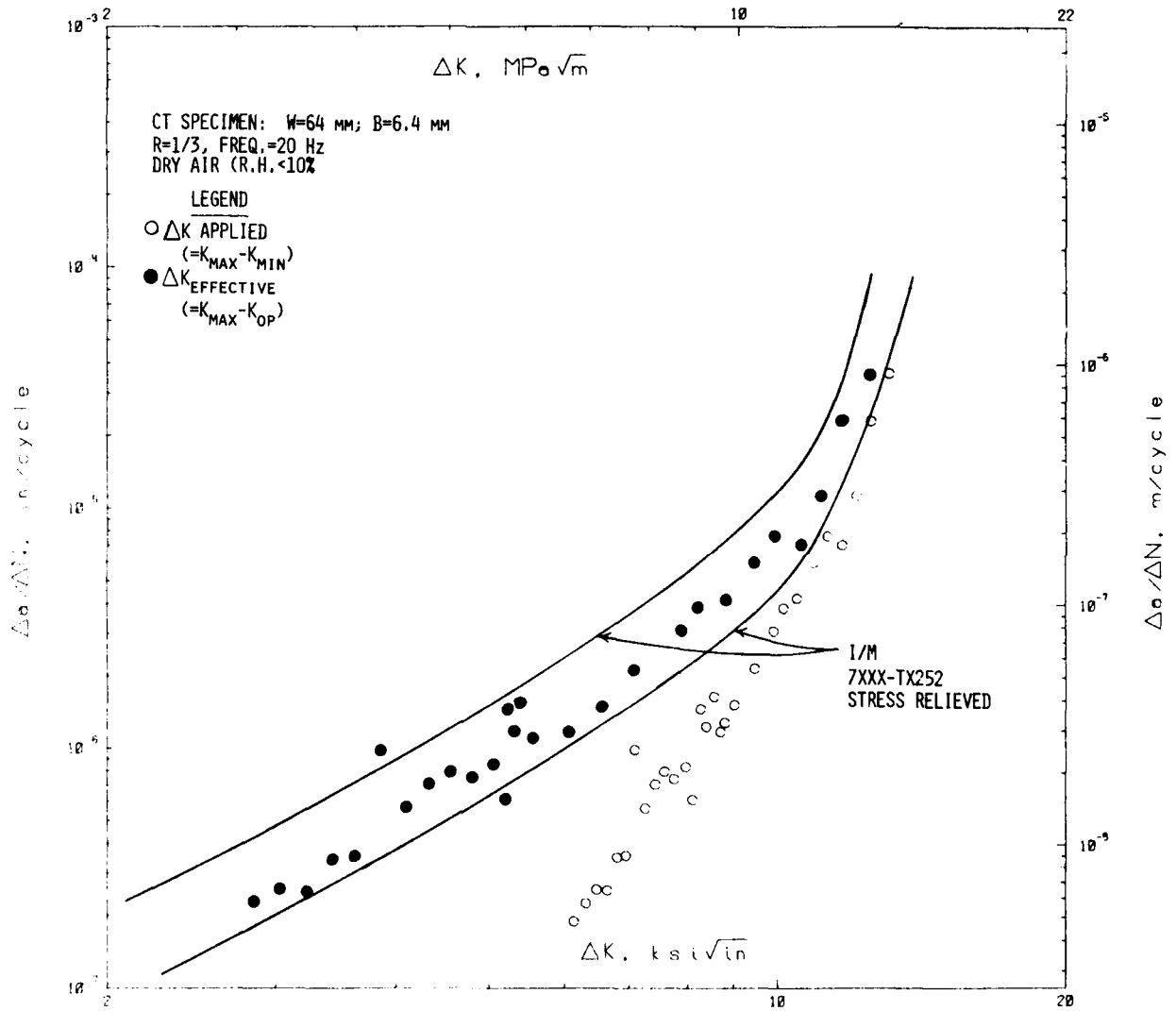
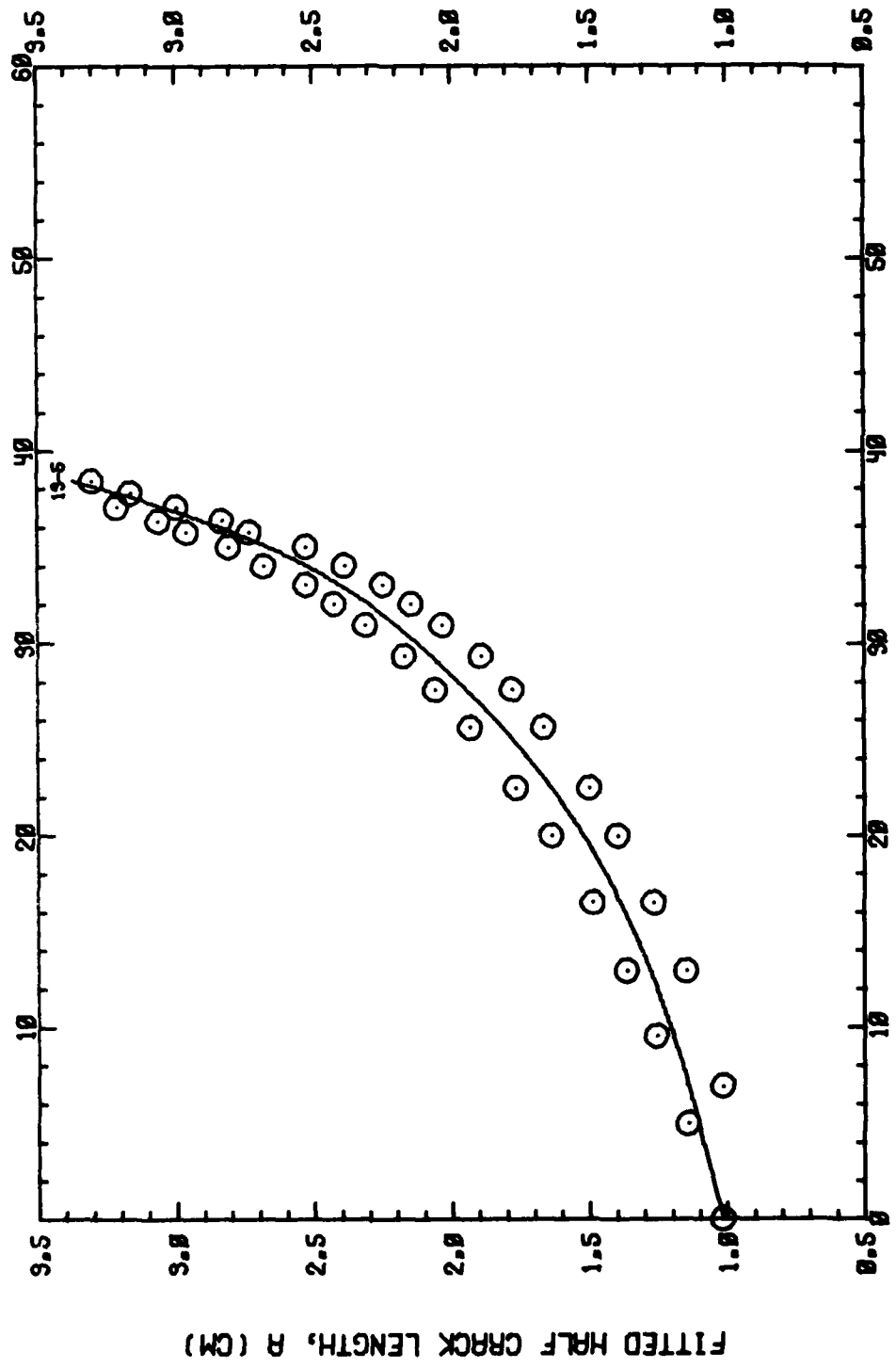


Figure 72. Corrected FCG rates in nonstress-relieved I/M hand forgings.

APPENDIX

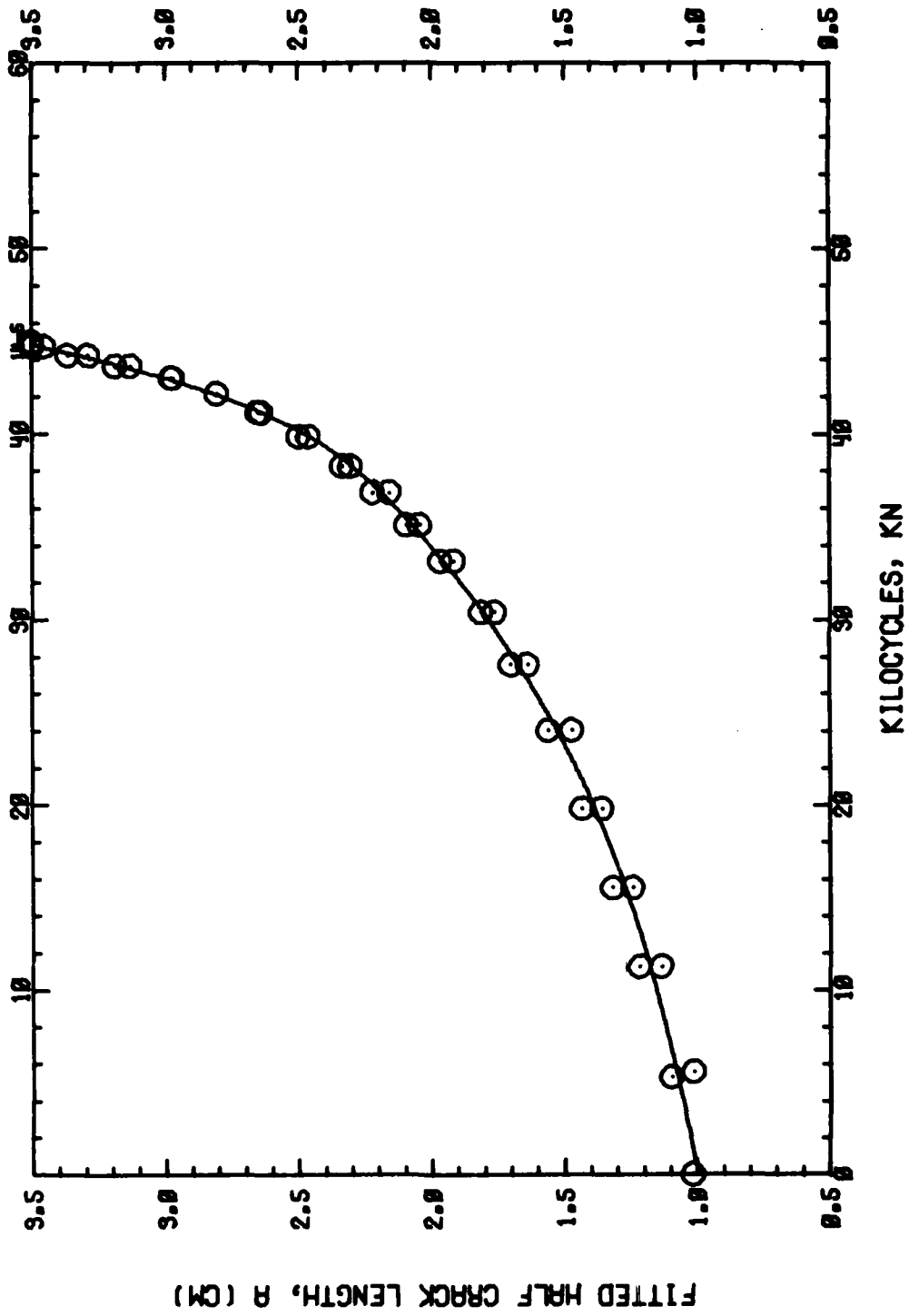
FATIGUE CRACK GROWTH RESULTS FOR PHASE I MATERIALS
TESTED IN HUMID AIR



KILOCYCLES, KN

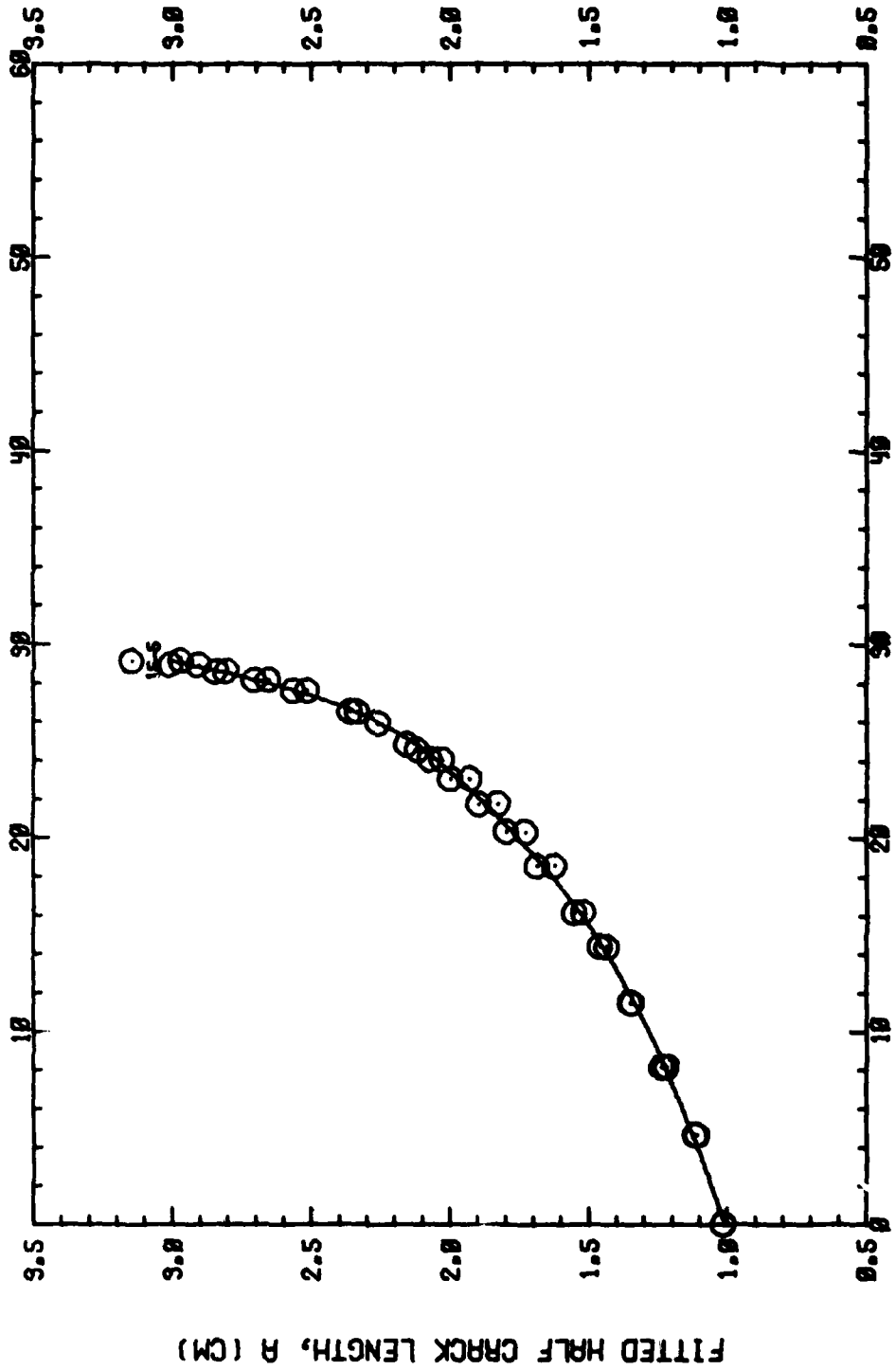
S-356452-1

Figure A1. Crack length versus cycles for 0.0 Co billet tested in humid air.



S-356453-1

Figure A2. Crack length versus cycles for 0.4 Co billet tested in humid air.



KILOCYCLES, KN

S-356454-1

Figure A3. Crack length versus cycles for 0.8 Co billet tested in humid air.

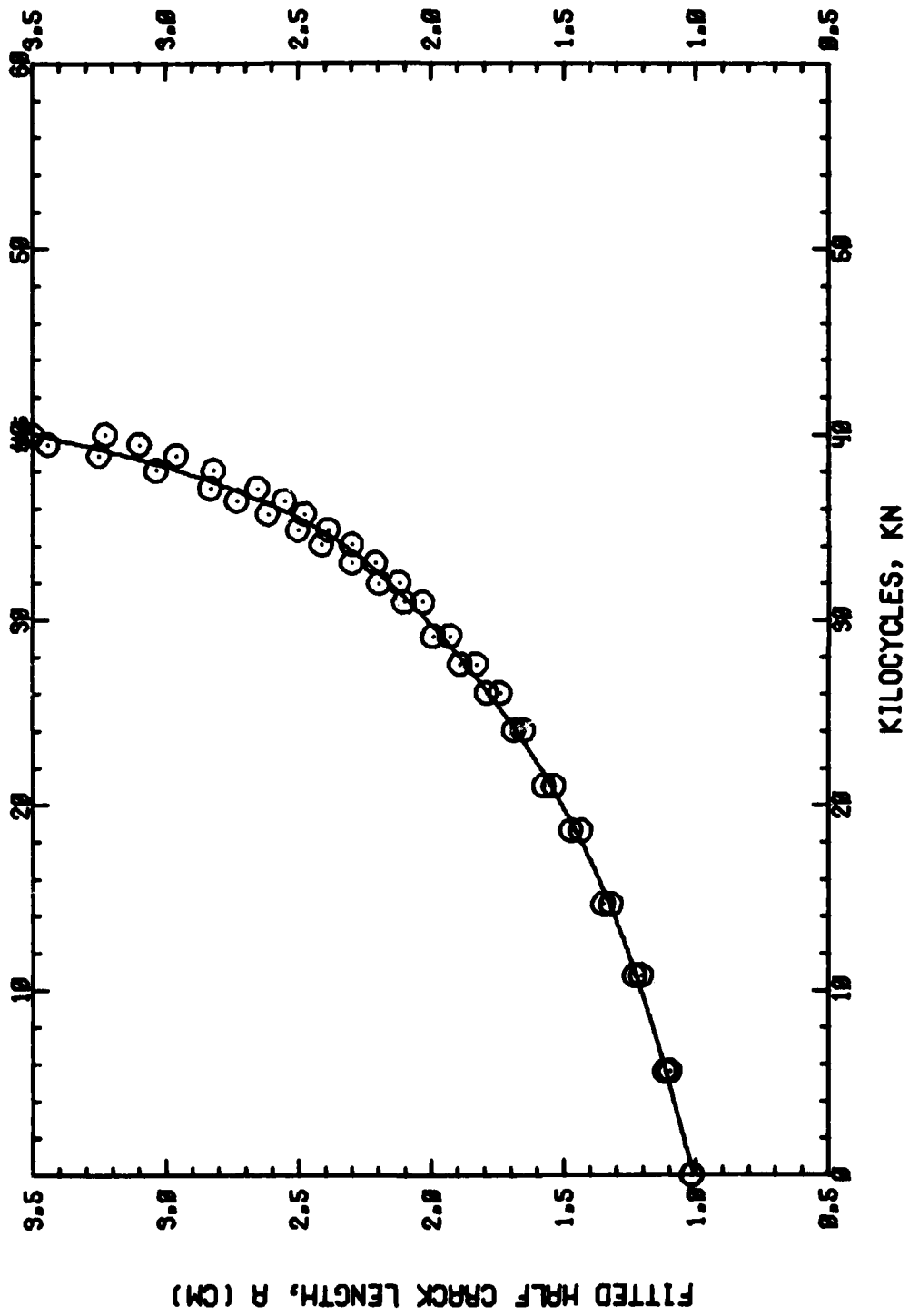


Figure A4. Crack length versus cycles for blended powder billet tested in humid air.

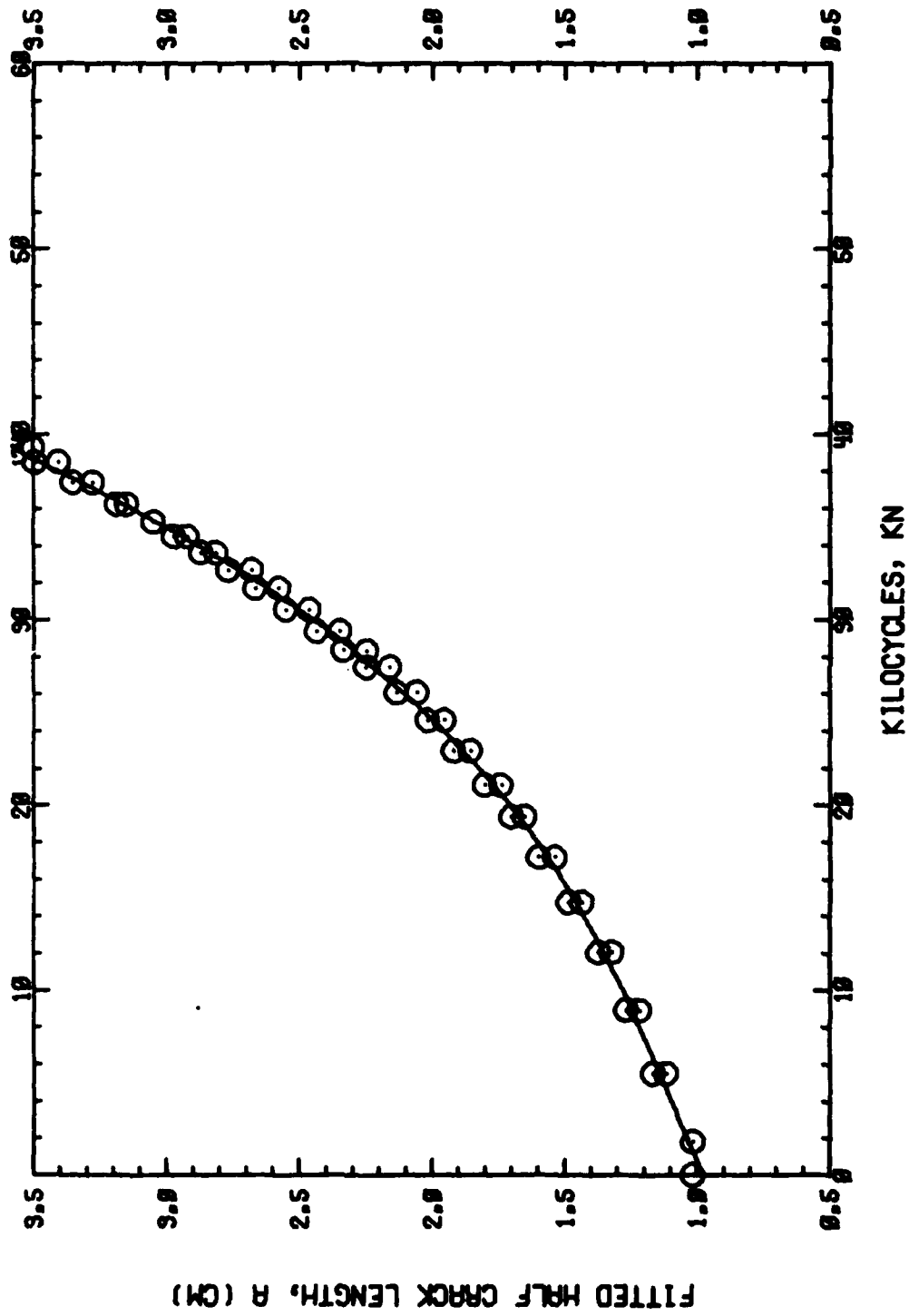
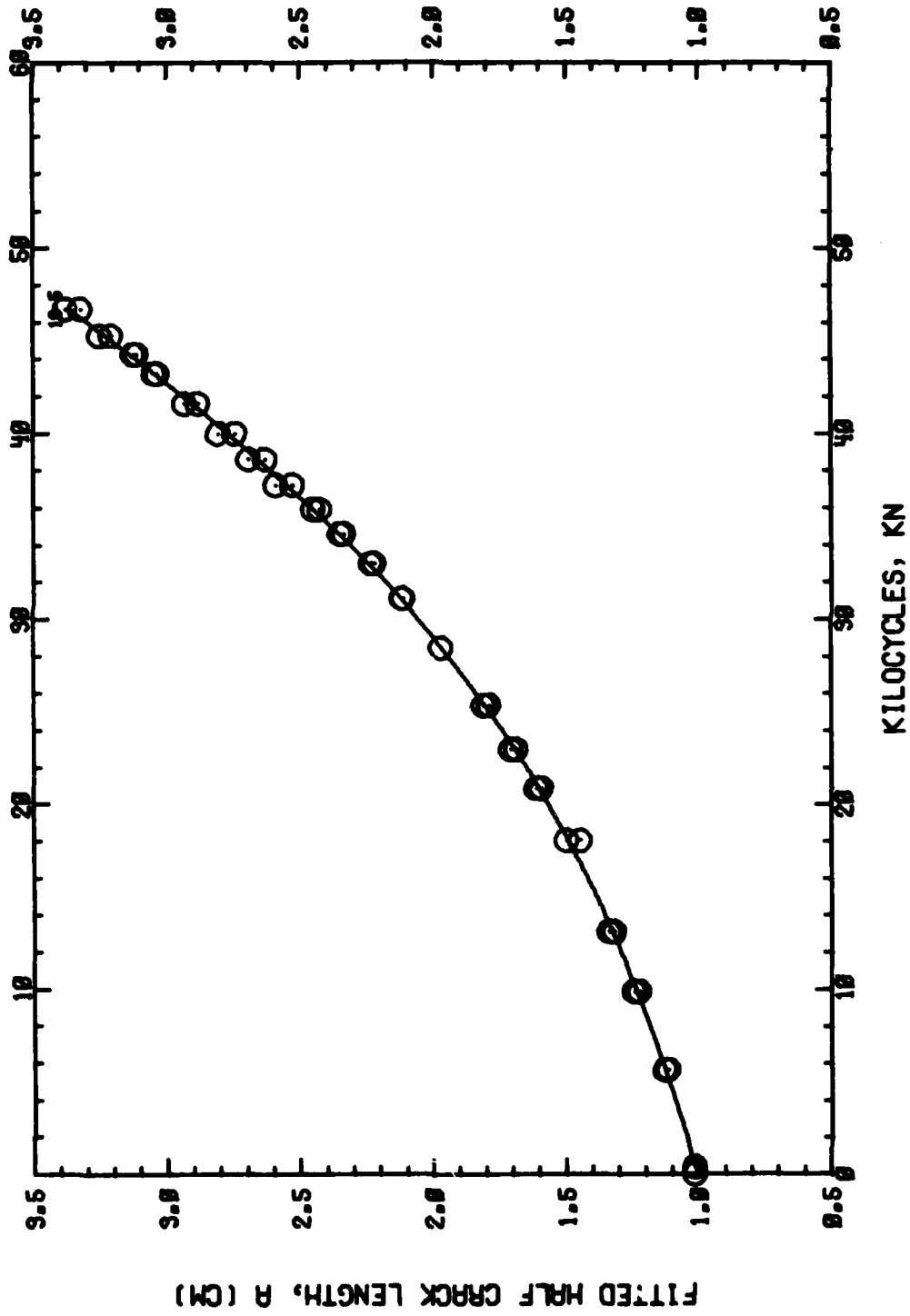
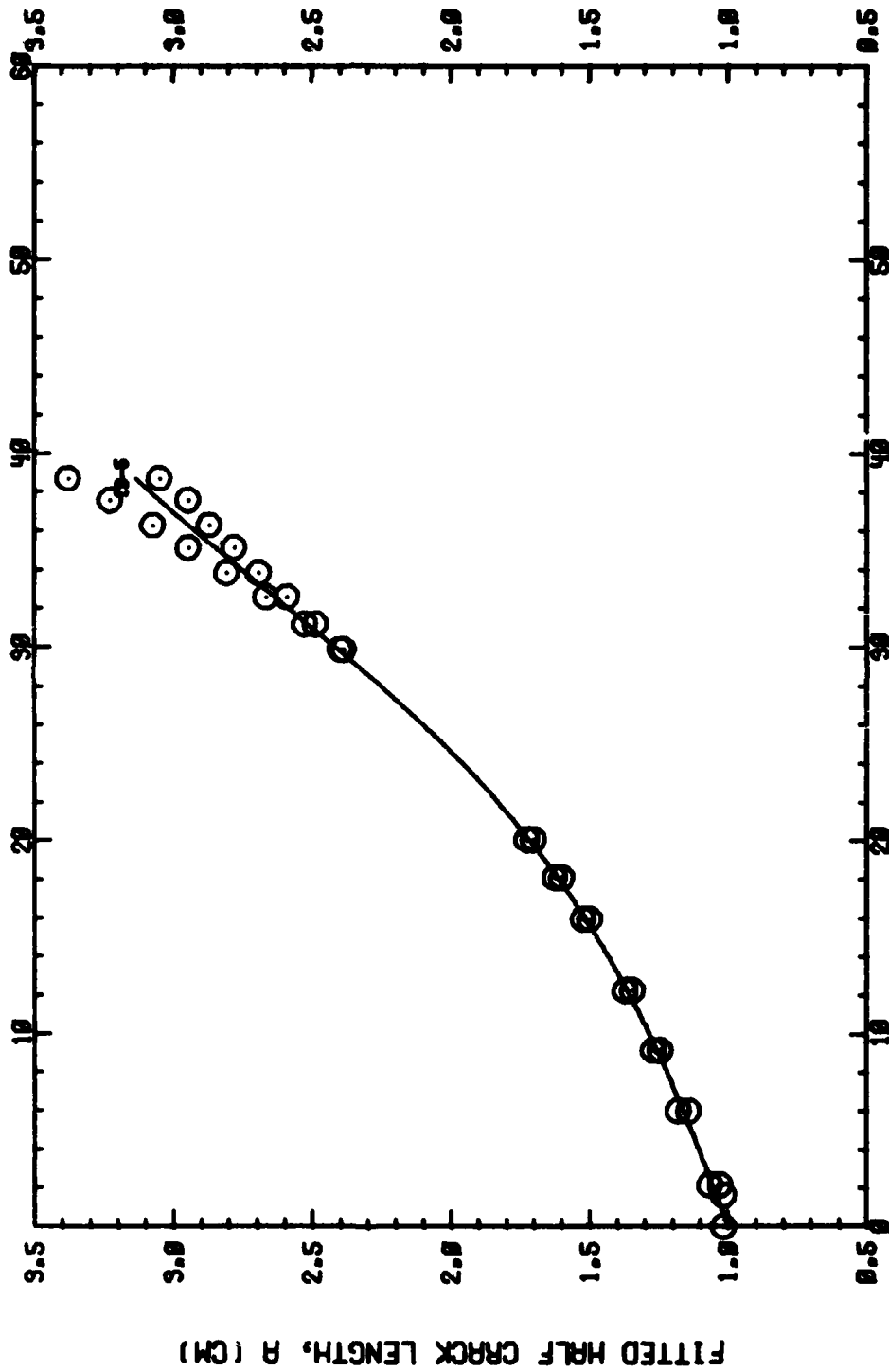


Figure A5. Crack length versus cycles for 0.0 Co A hand forging tested in humid air.
S-356452-2T



S-356452-3T

Figure A6. Crack length versus cycles for 0.0 Co ABC hand forging tested in humid air.

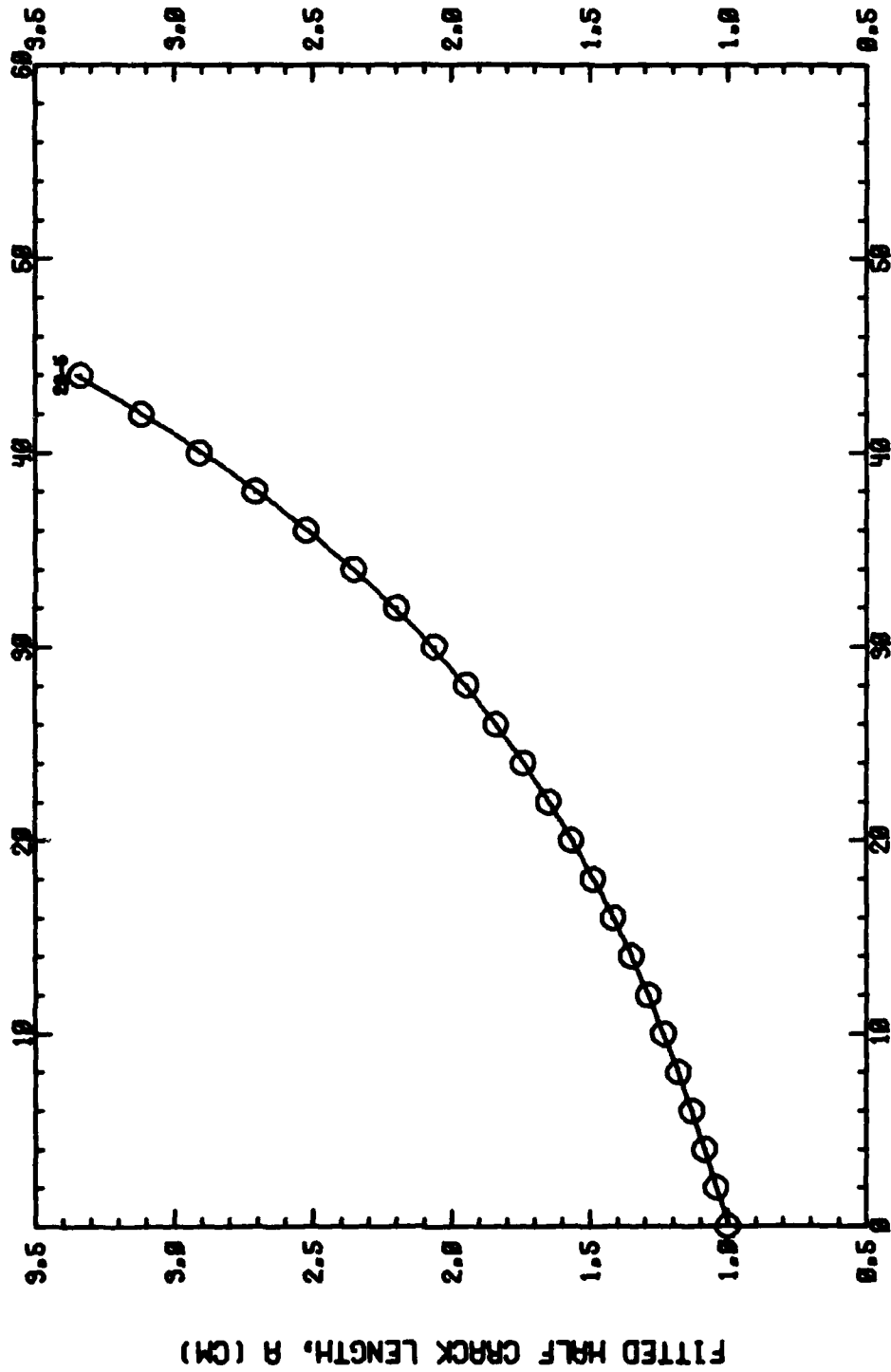


KILOCYCLES, KN

S-356453-2T

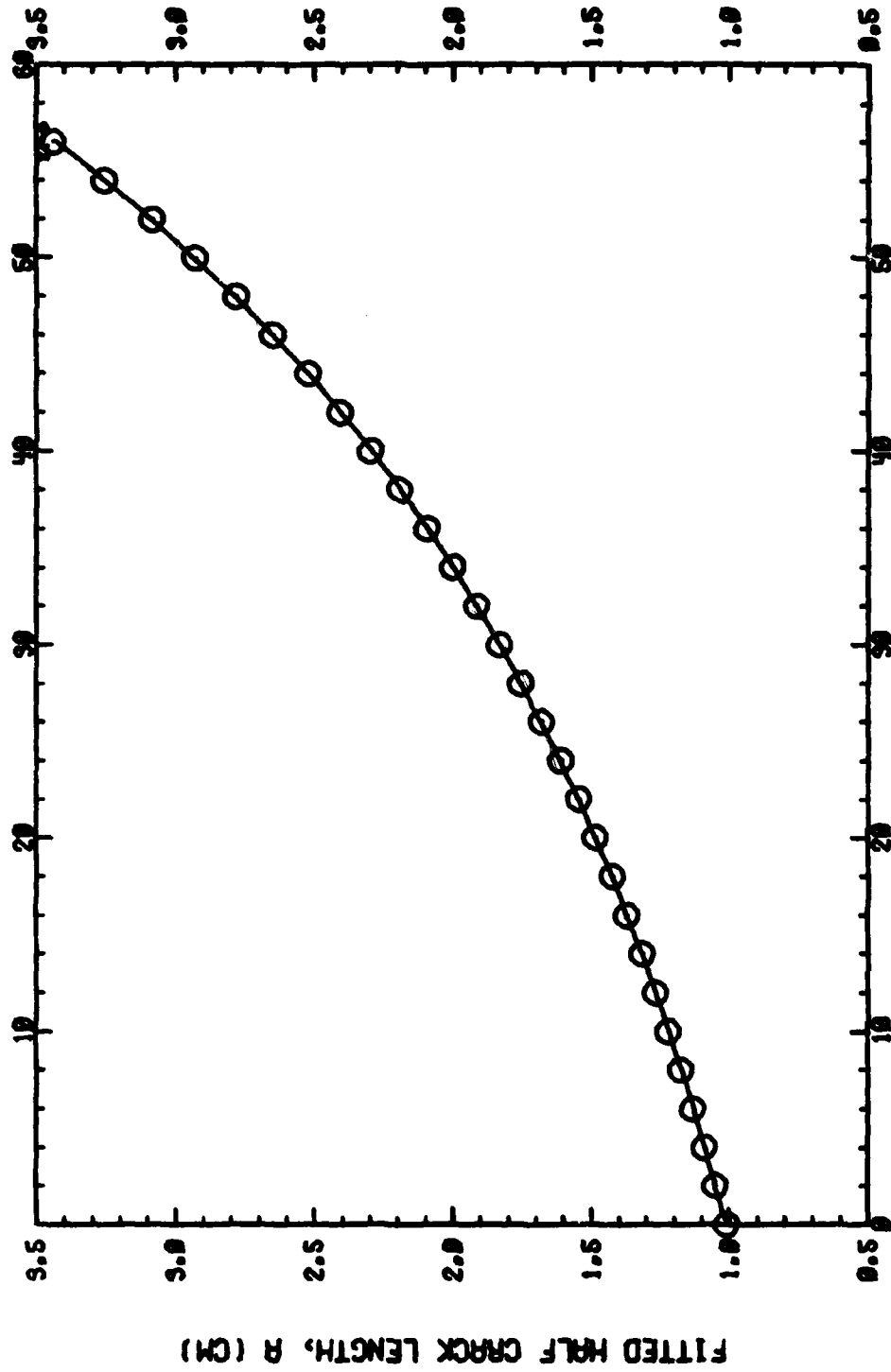
FITTED HALF CRACK LENGTH, a (CM)

Figure A7. Crack length versus cycles for 0.4 Co A hand forging tested in humid air.



KILOCYCLES, KN
S-356453-3T

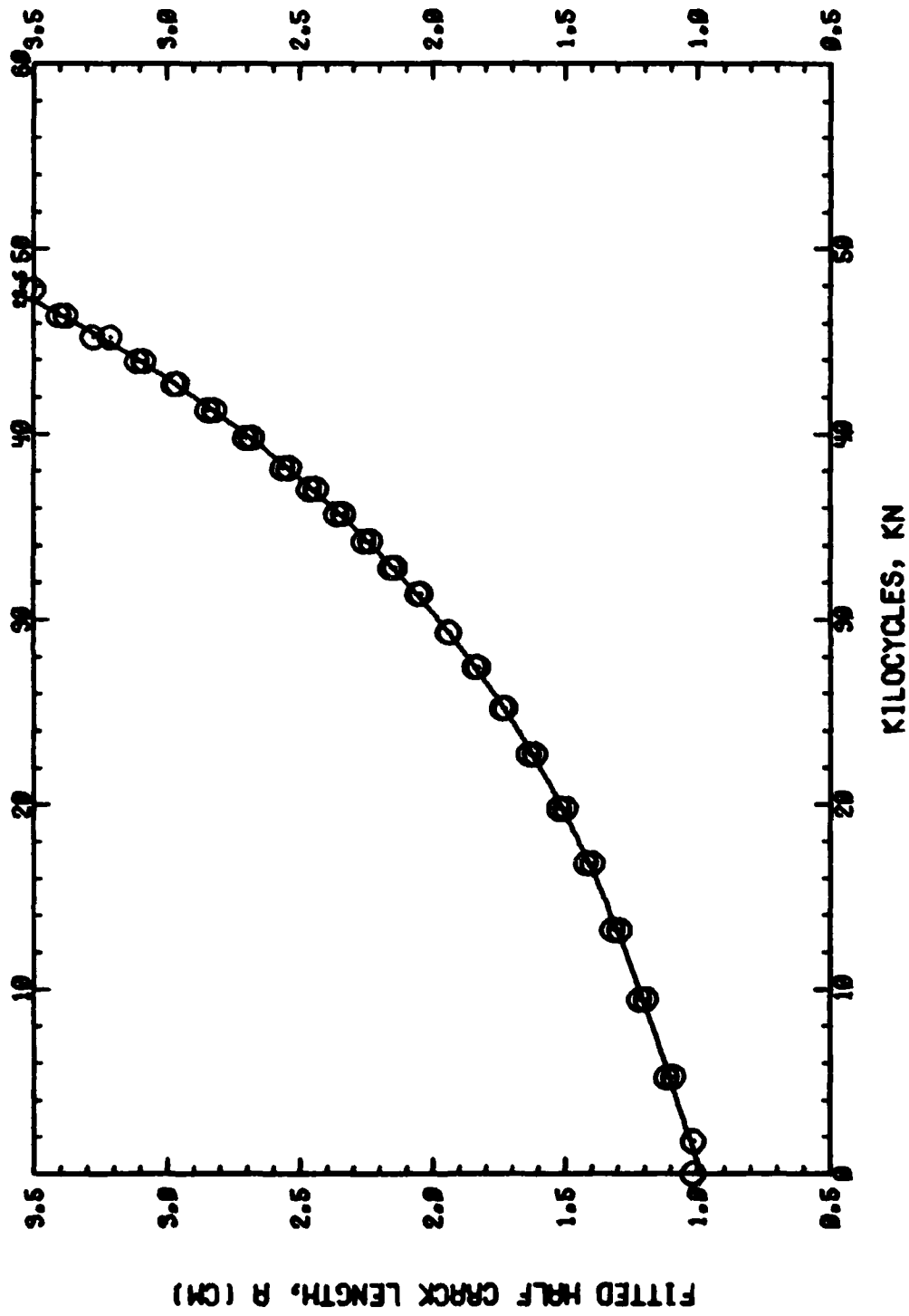
Figure A8. Crack length versus cycles for 0.4 Co ABC hand forging tested in humid air.



KILOCYCLES, KN

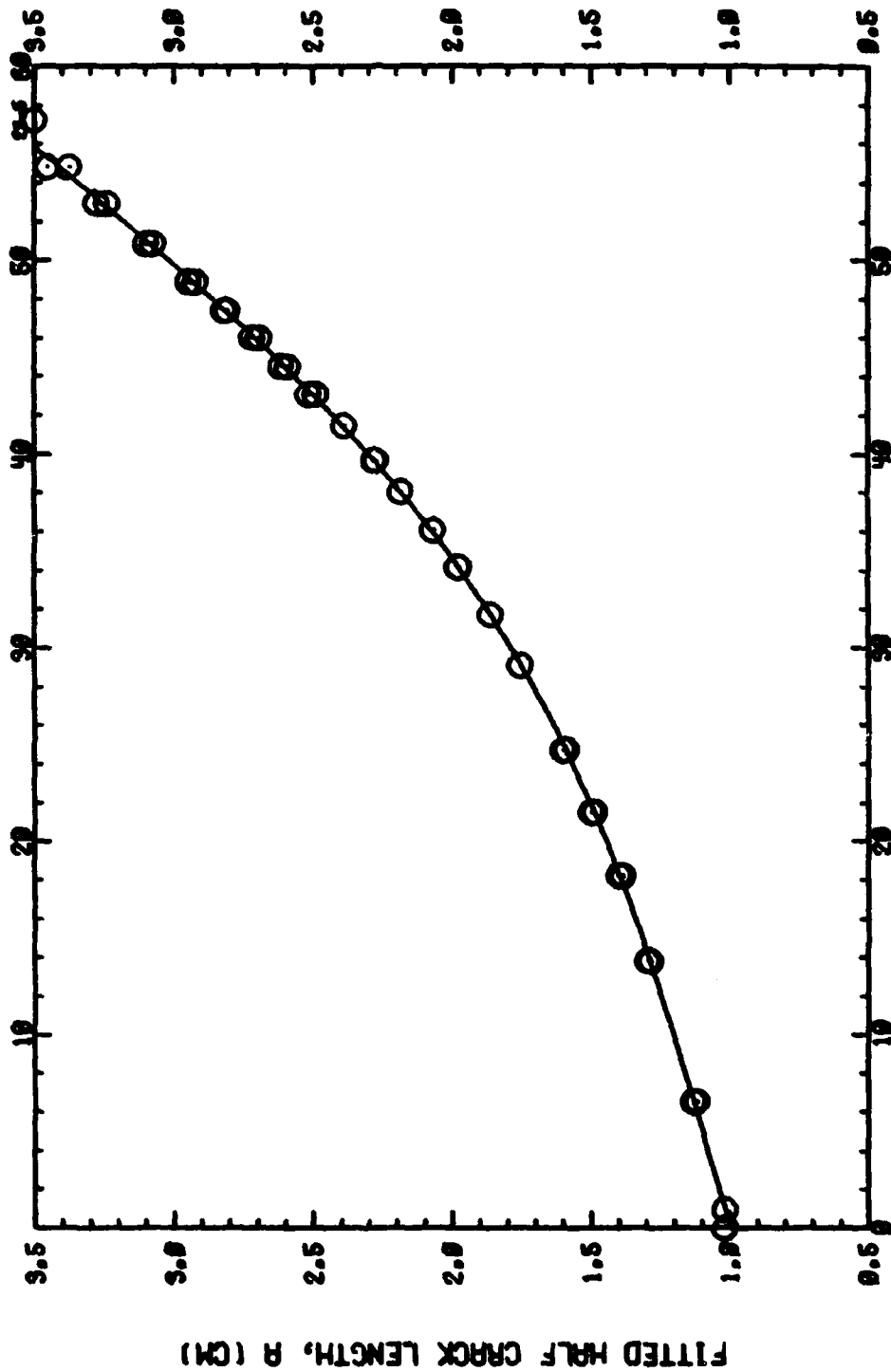
S-356454-2T

Figure A9. Crack length versus cycles for 0.8 Co A hand forging tested in humid air.



S-356454-3T

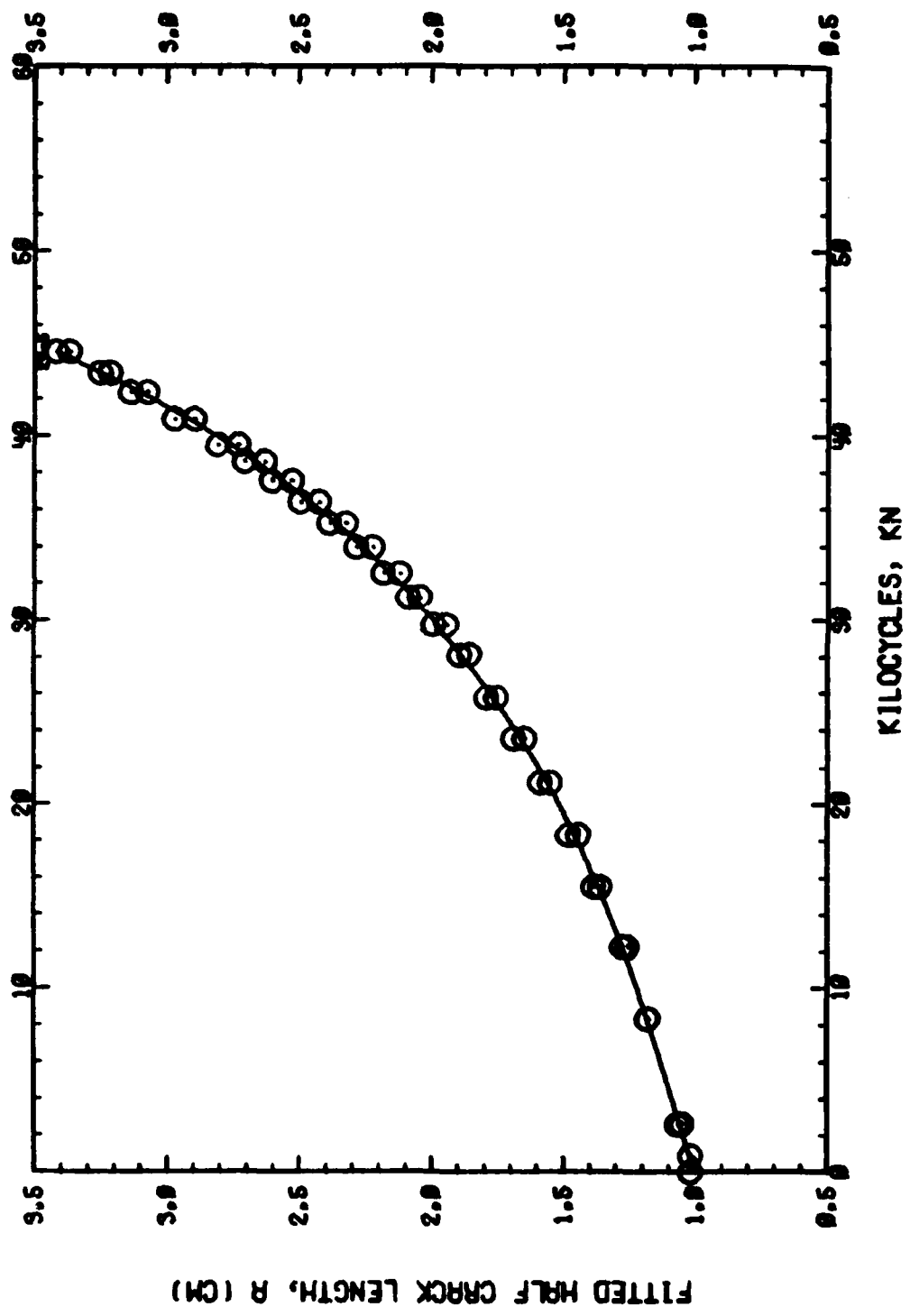
Figure A10. Crack length versus cycles for 0.8 Co ABC hand forging tested in humid air.



KILOCYCLES, KN

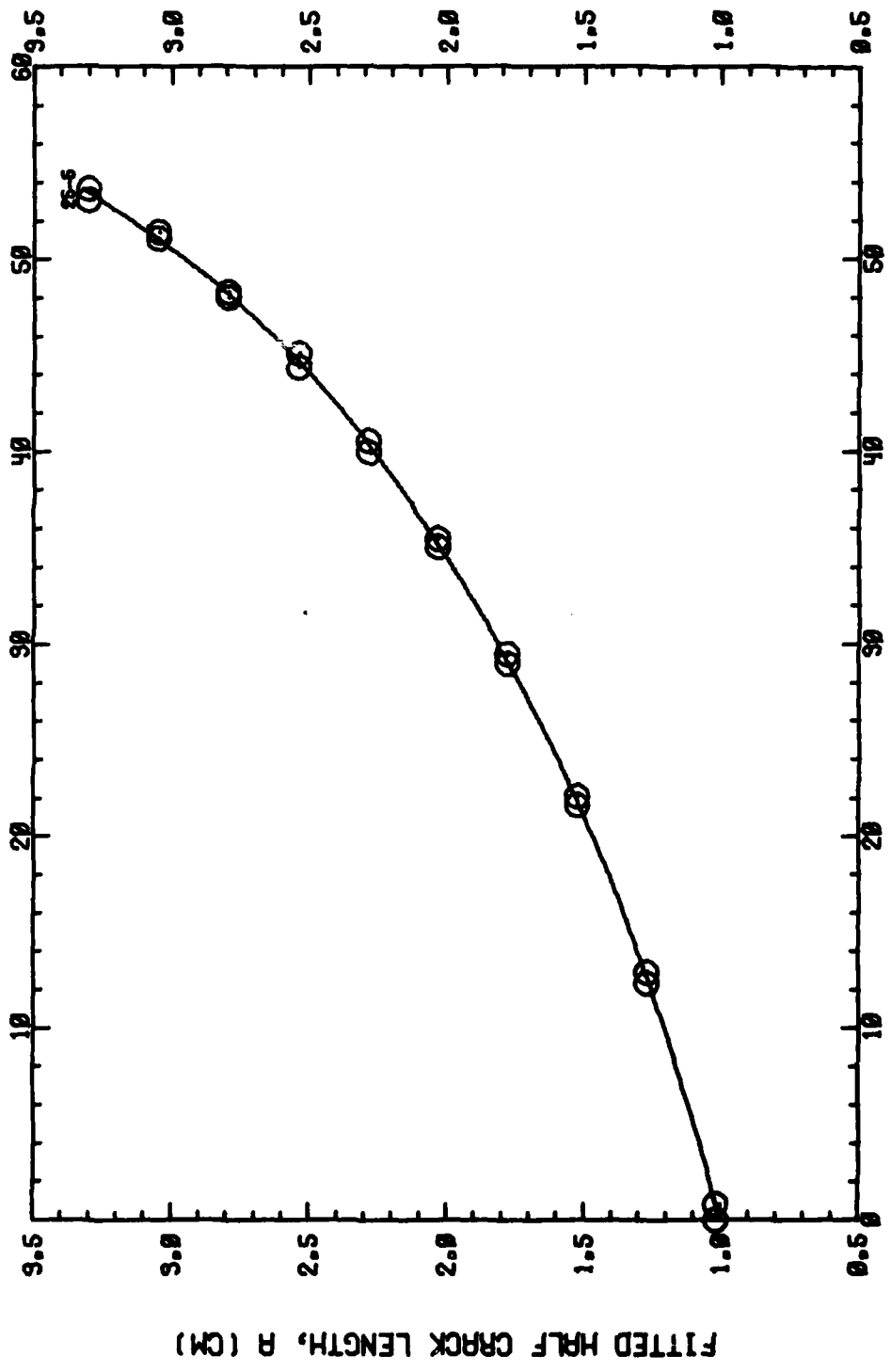
S-356455-2T

Figure A11. Crack length versus cycles for blended powder A forging tested in humid air.



S-356455-3T

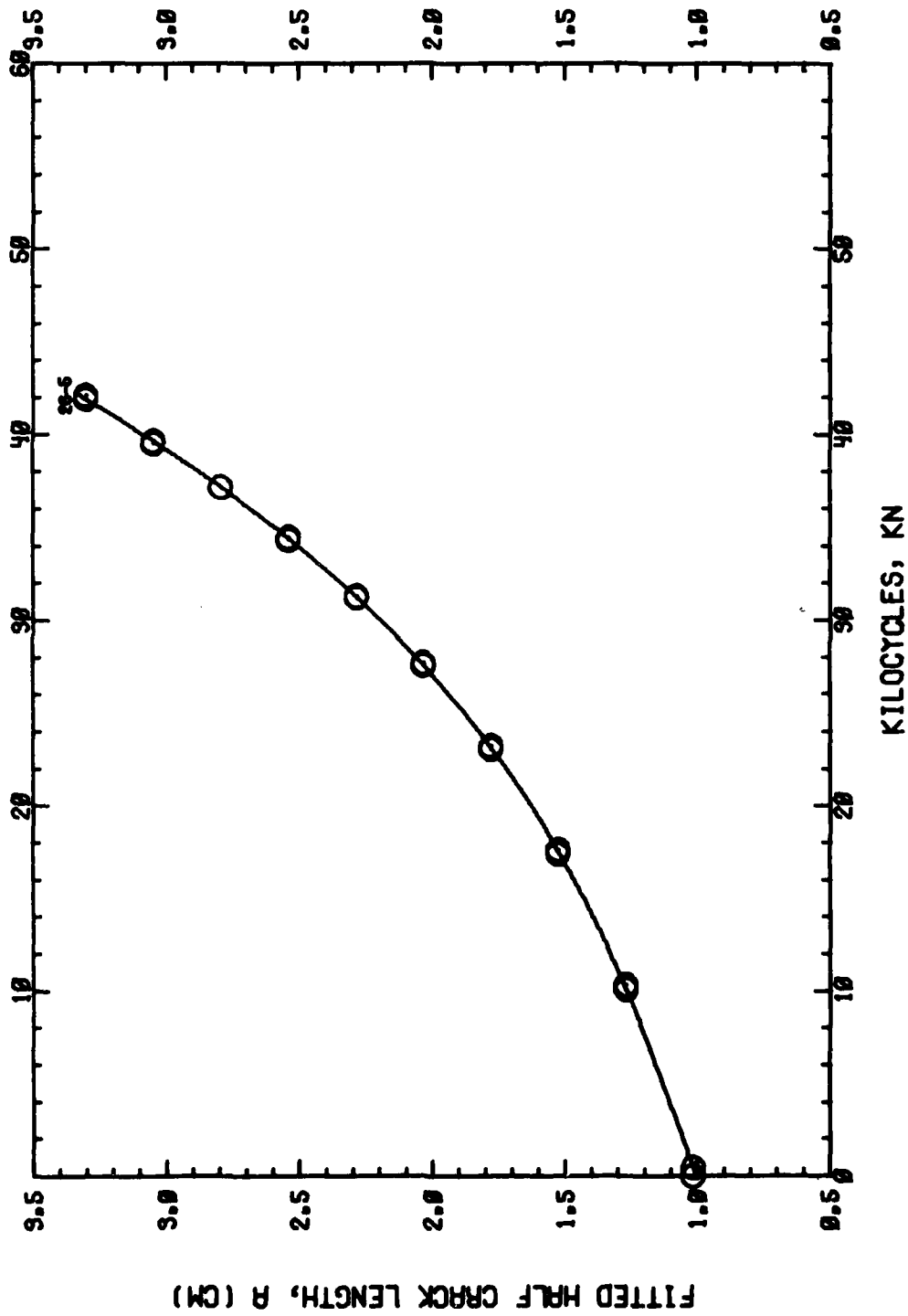
Figure A12. Crack length versus cycles for blended powder ABC forging tested in humid air.



KILOCYCLES, KN

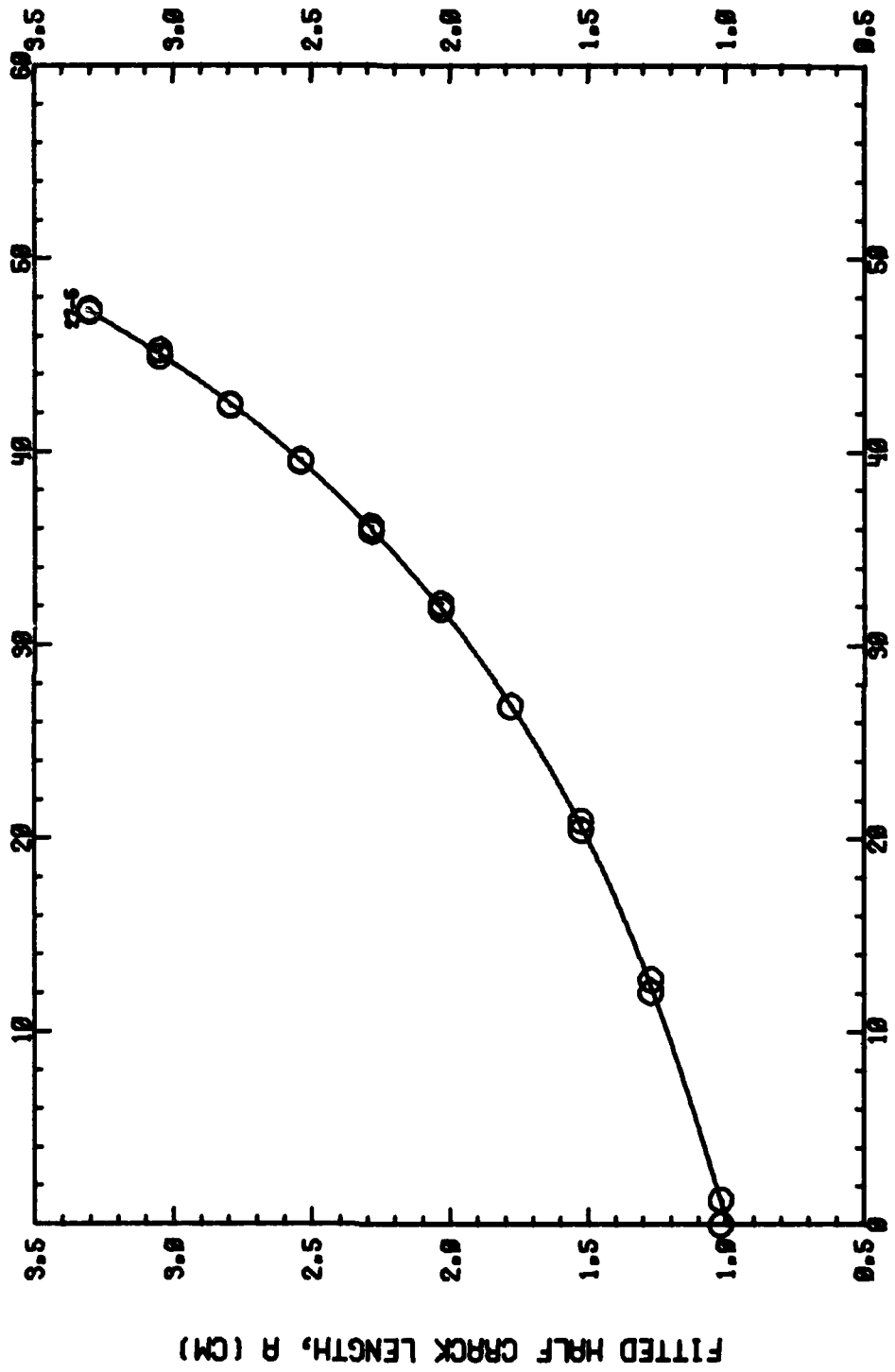
S-356452-4BG

Figure A13. Crack length versus cycles for 0.0 Co high Z extrusion tested in humid air.



S-356452-60

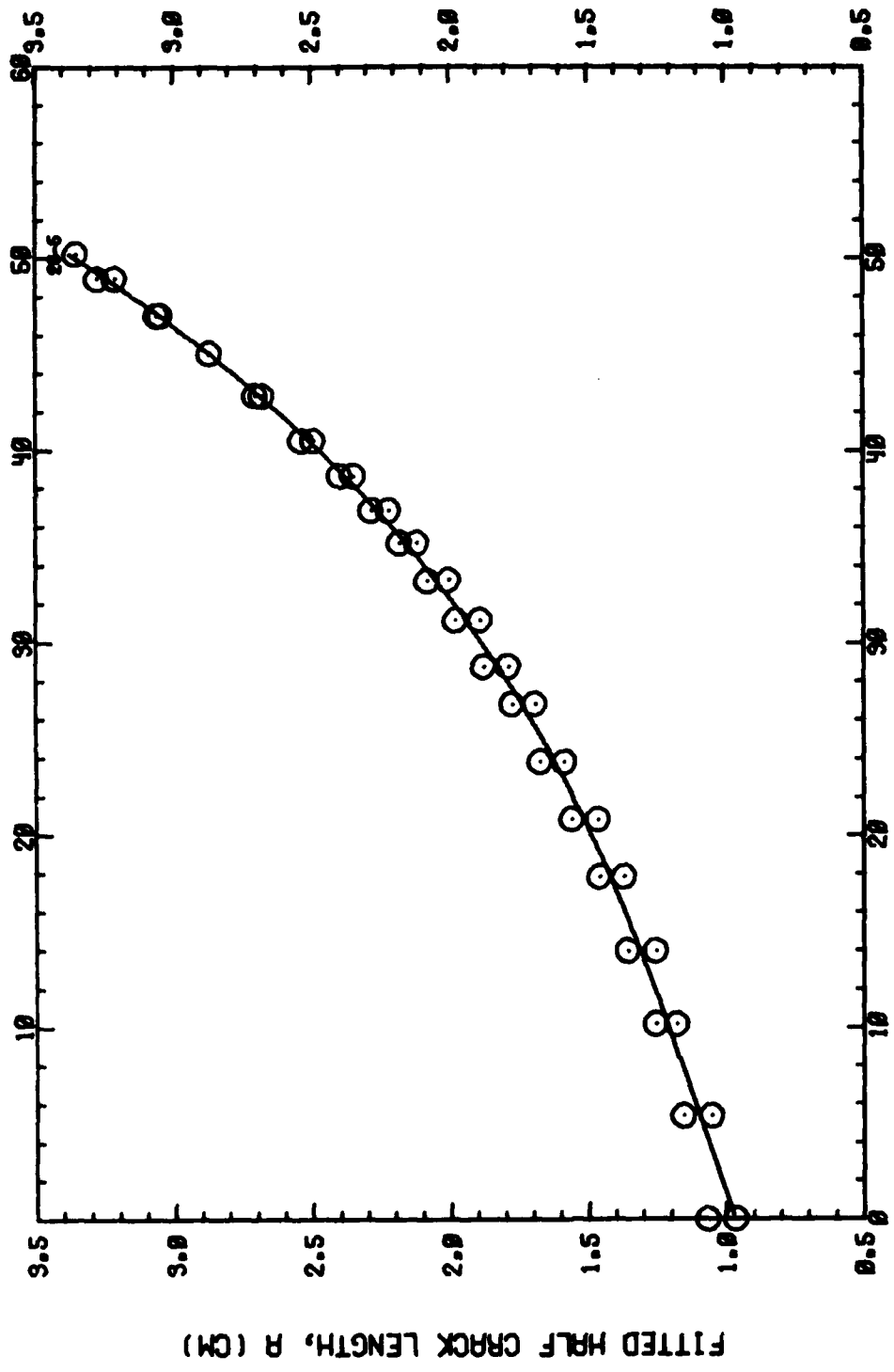
Figure A14. Crack length versus cycles for 0.0 Co medium Z extrusion tested in humid air.



KILOCYCLES, KN

S-356452-7G

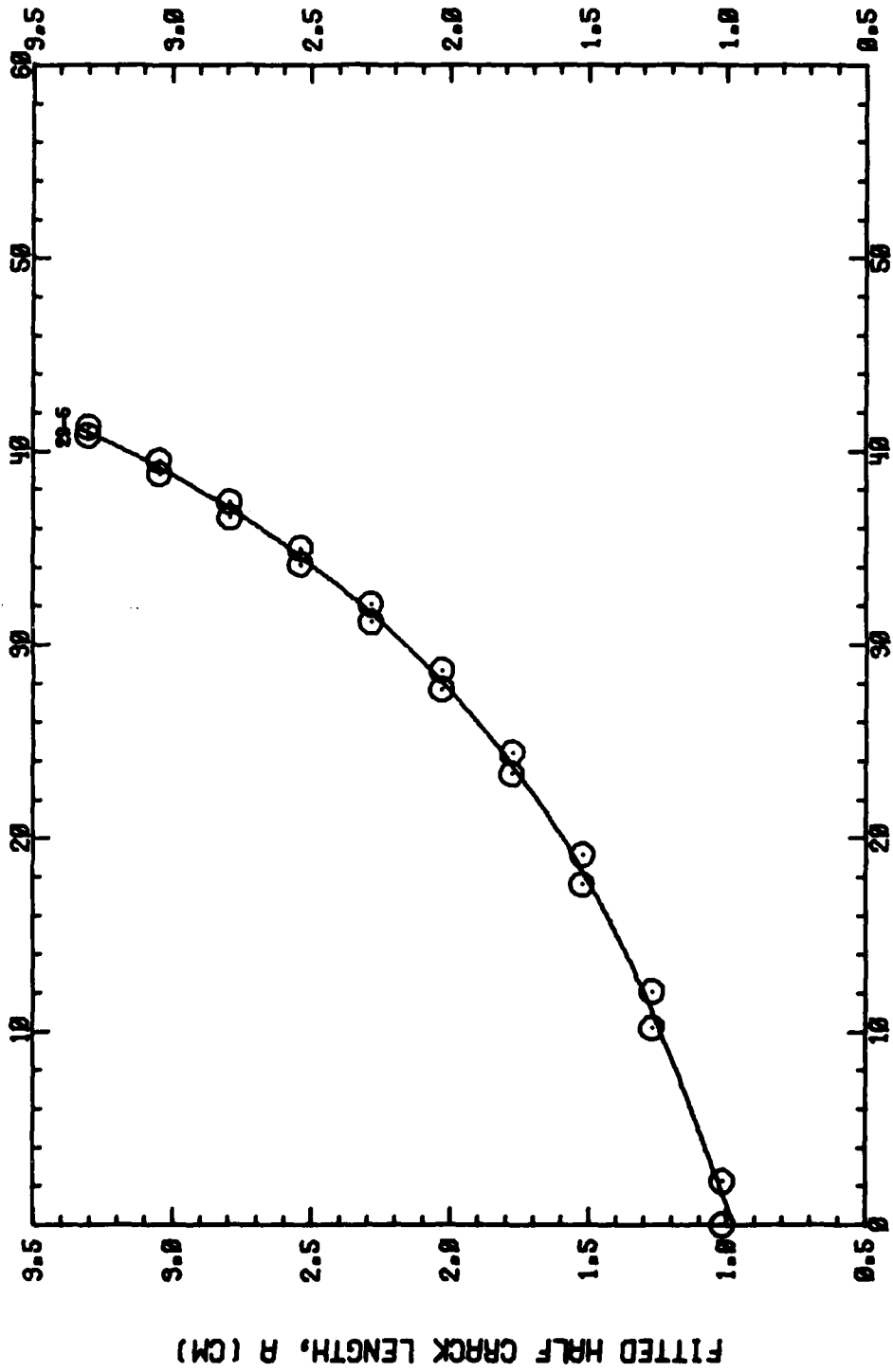
Figure A15. Crack length versus cycles for 0.0 Co low Z extrusion tested in humid air.



KILOCYCLES, KN

S-356453-4AG

Figure A16. Crack length versus cycles for 0.4 Co high Z extrusion tested in humid air.



KILOCYCLES, KN

S-356453-6G

Figure A17. Crack length versus cycles for 0.4 Co medium Z extrusion tested in humid air.

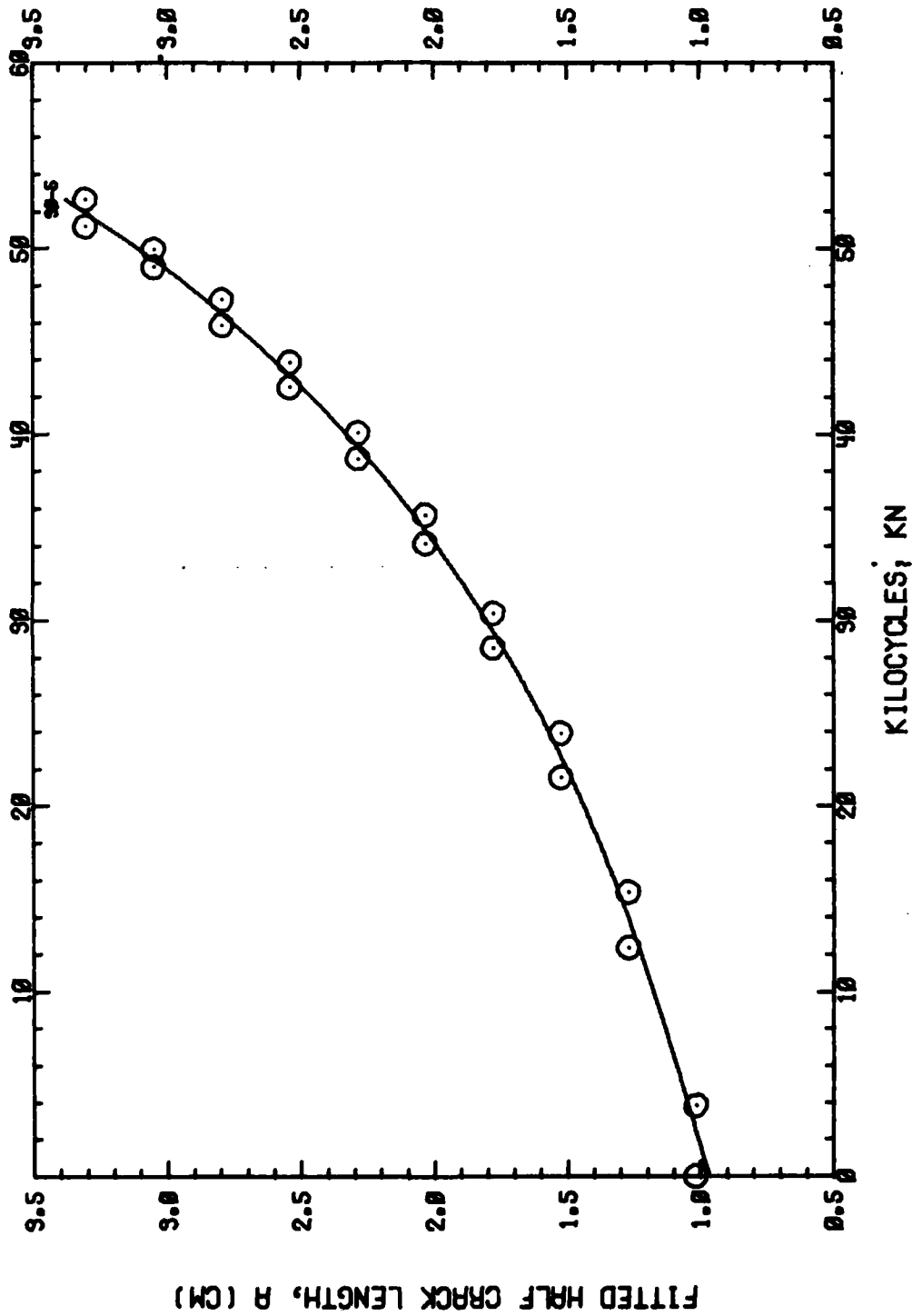
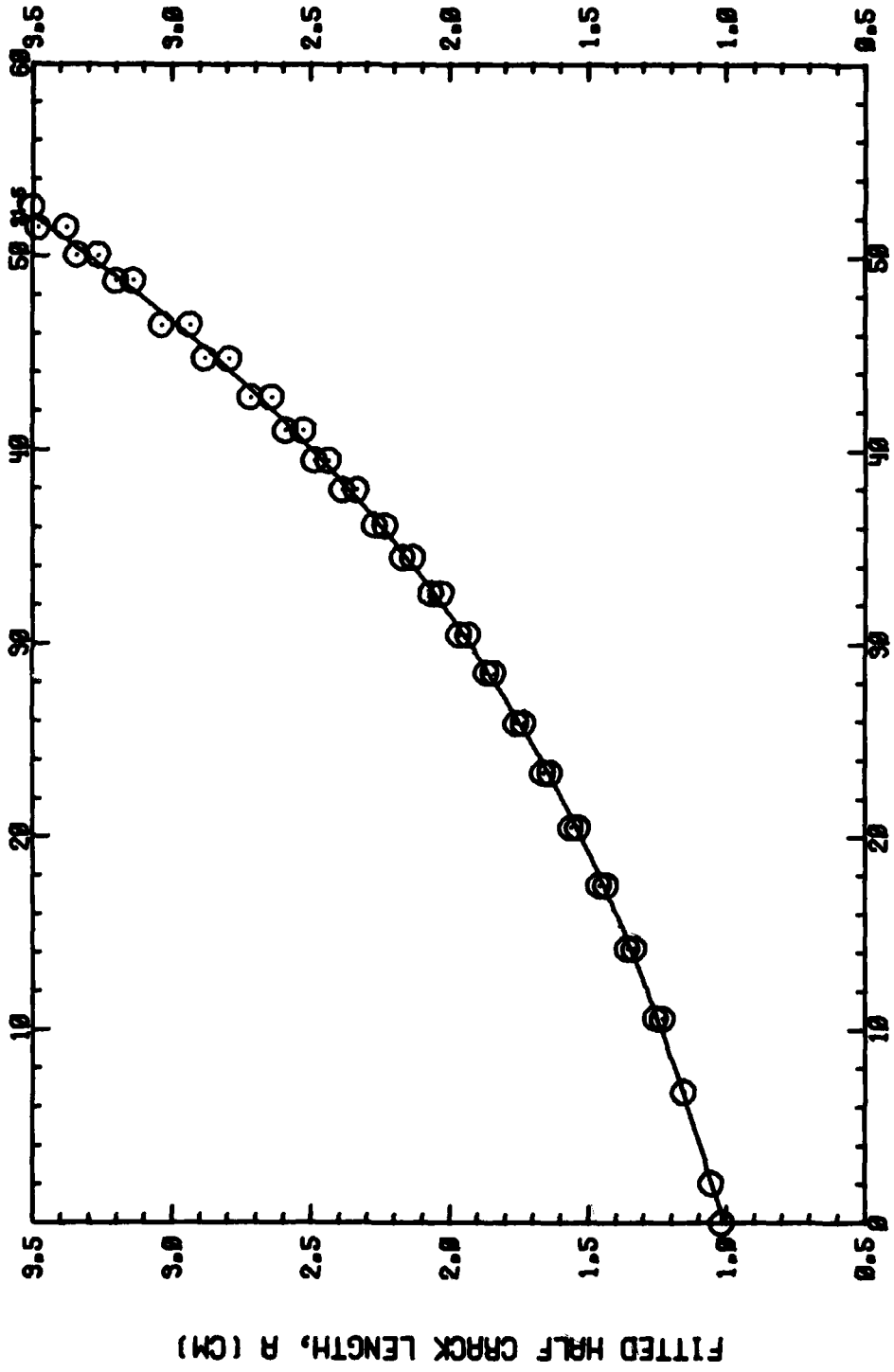


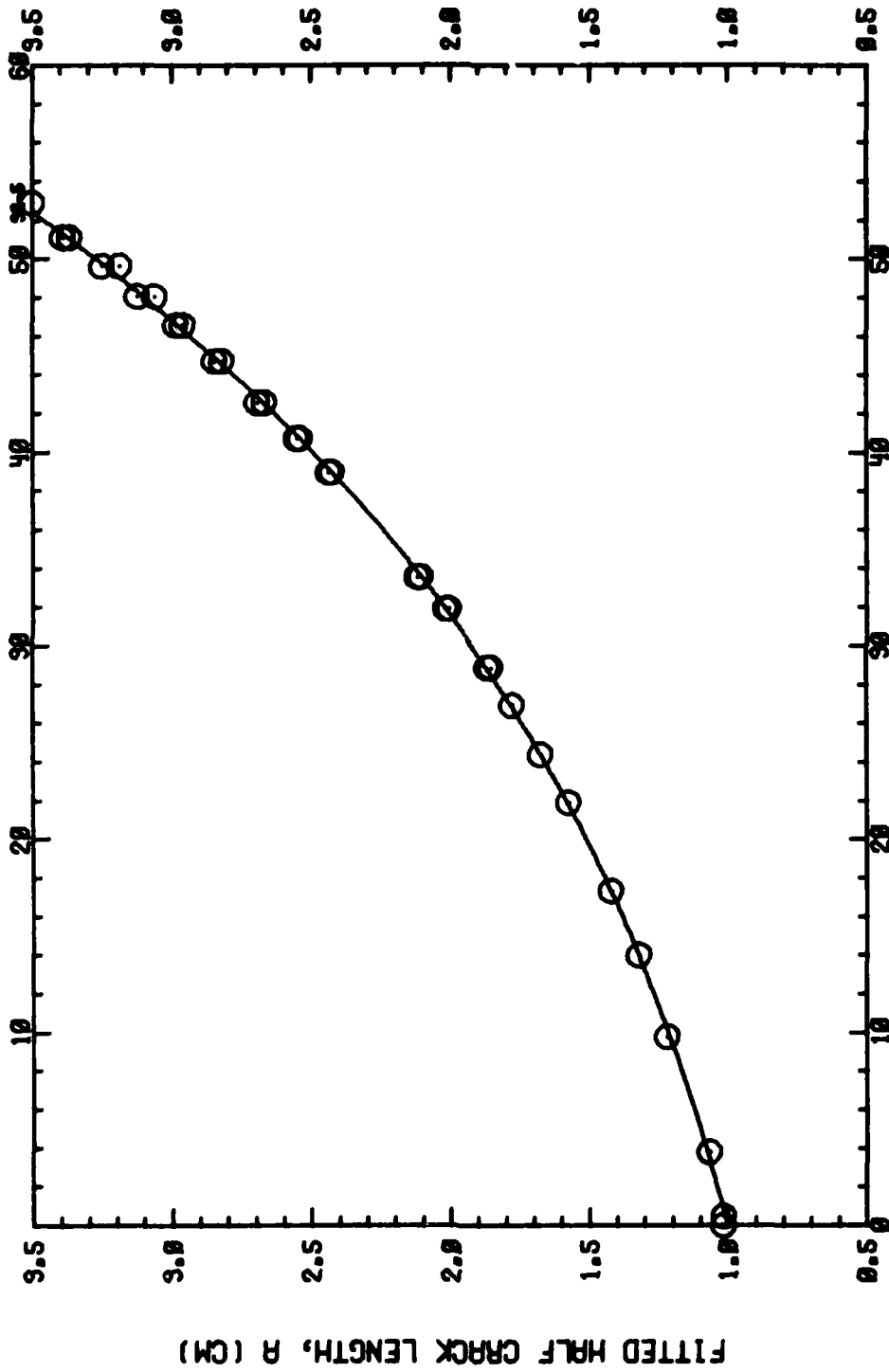
Figure A18. Crack length versus cycles for 0.4 Co low Z extrusion tested in humid air.



KILOCYCLES, KN

S-356454-4AG

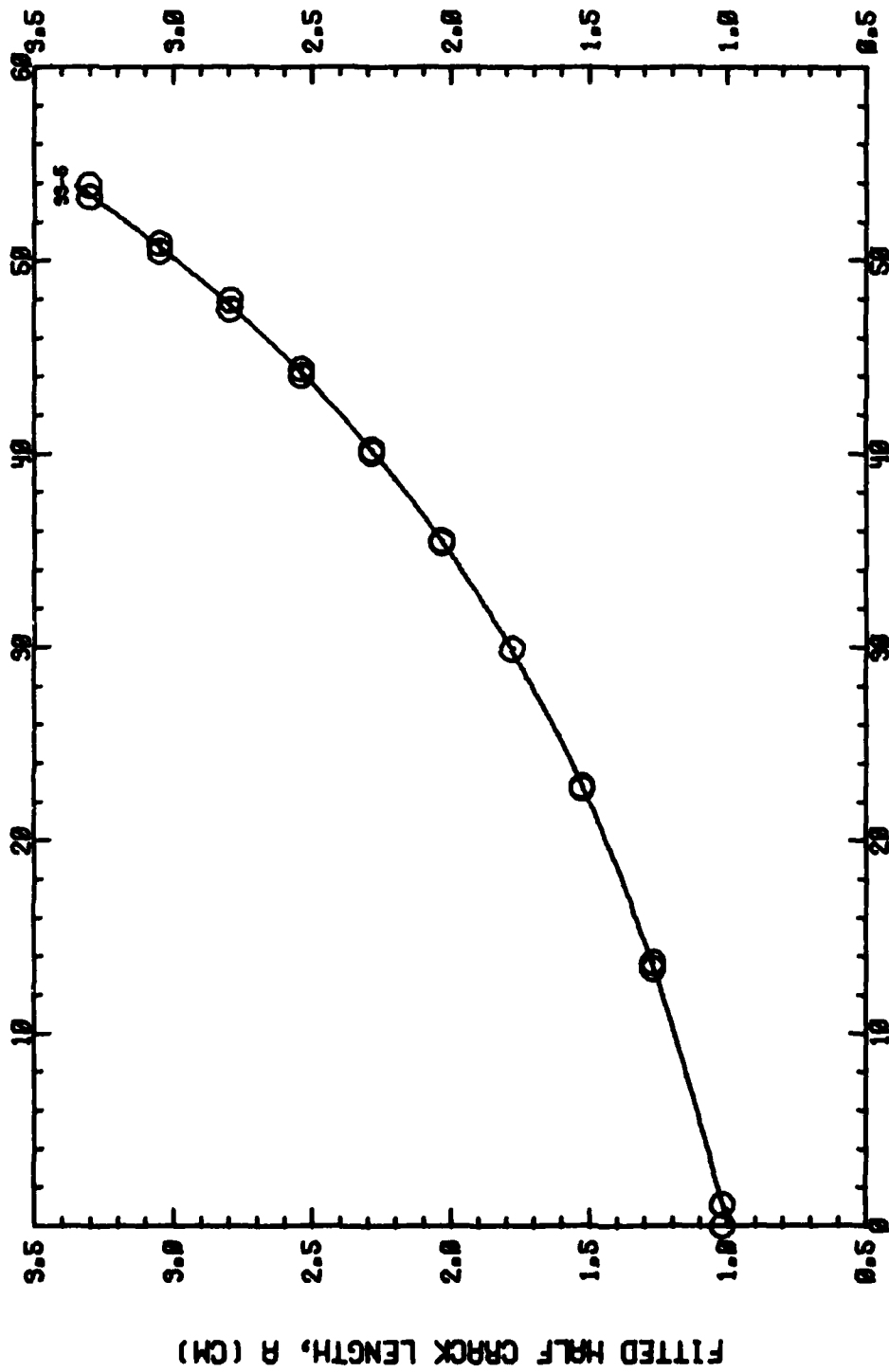
Figure A19. Crack length versus cycles for 0.8 Cc high % extrusion tested in humid air.



KILOCYCLES, KN

S-356454-5G

Figure A20. Crack length versus cycles for 0.8 Co medium Z extrusion tested in humid air.



KILOCYCLES, KN

S-356454-6G

Figure A21. Crack length versus cycles for 0.8 Co low Z extrusion tested in humid air.

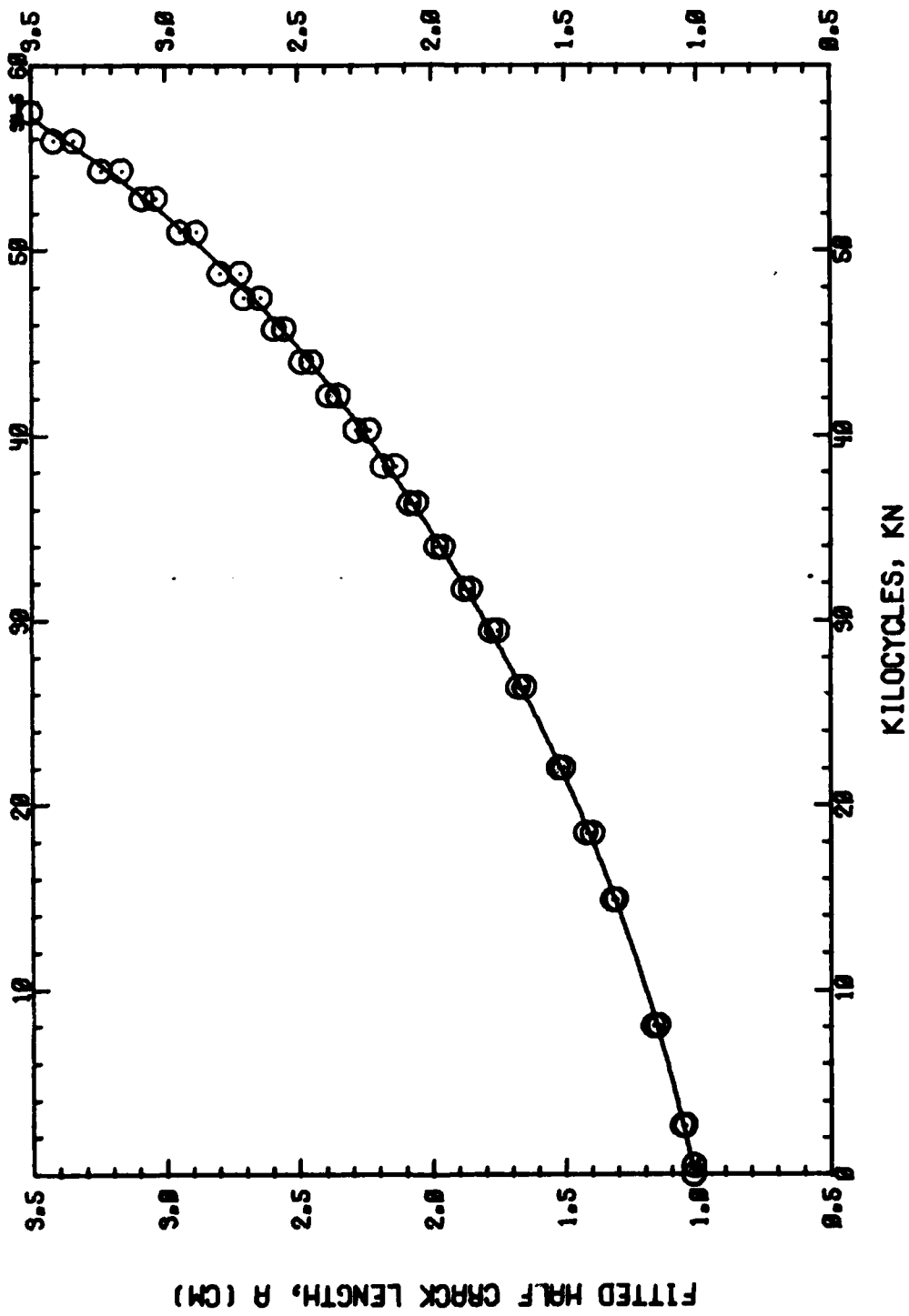
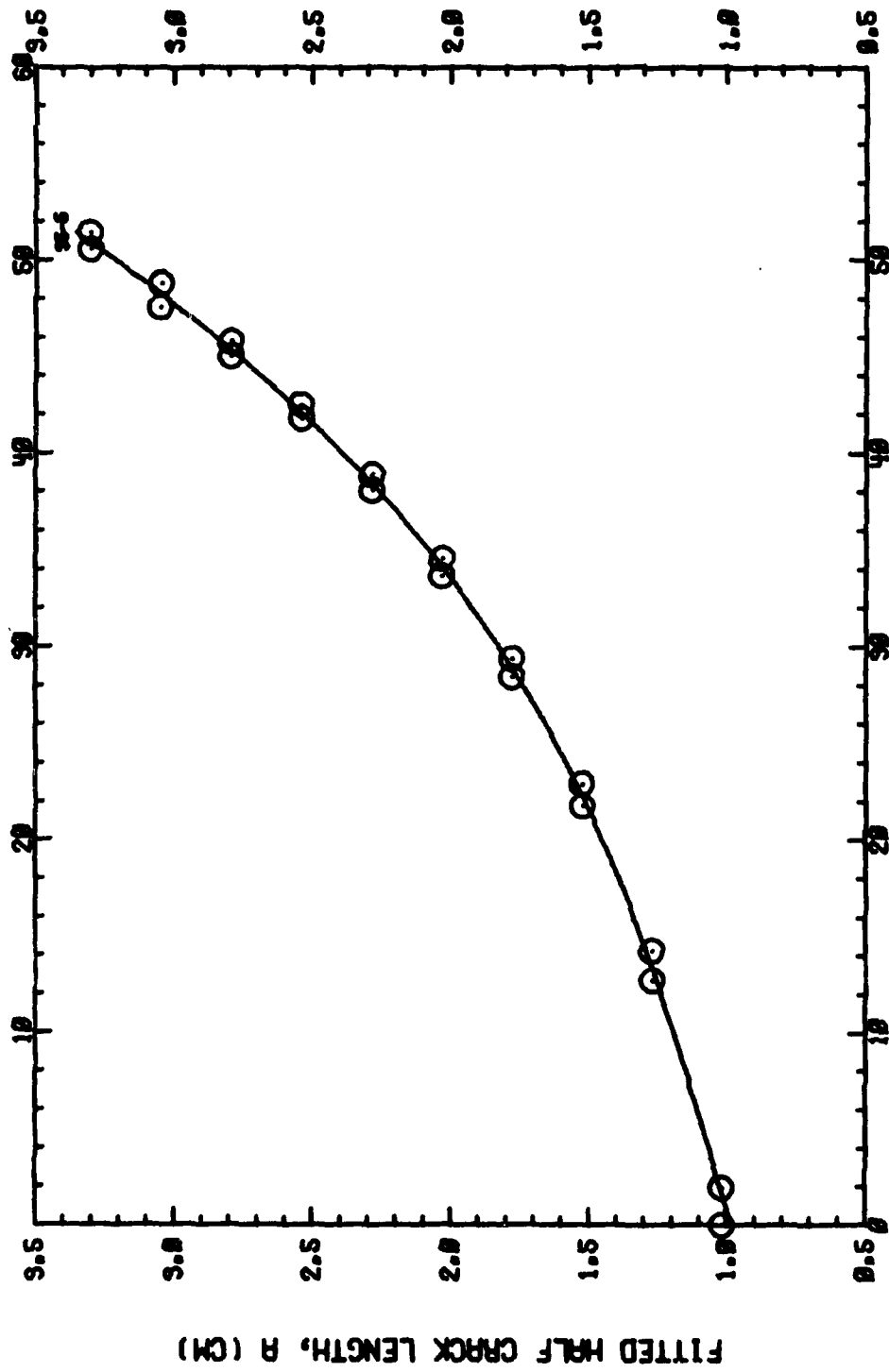


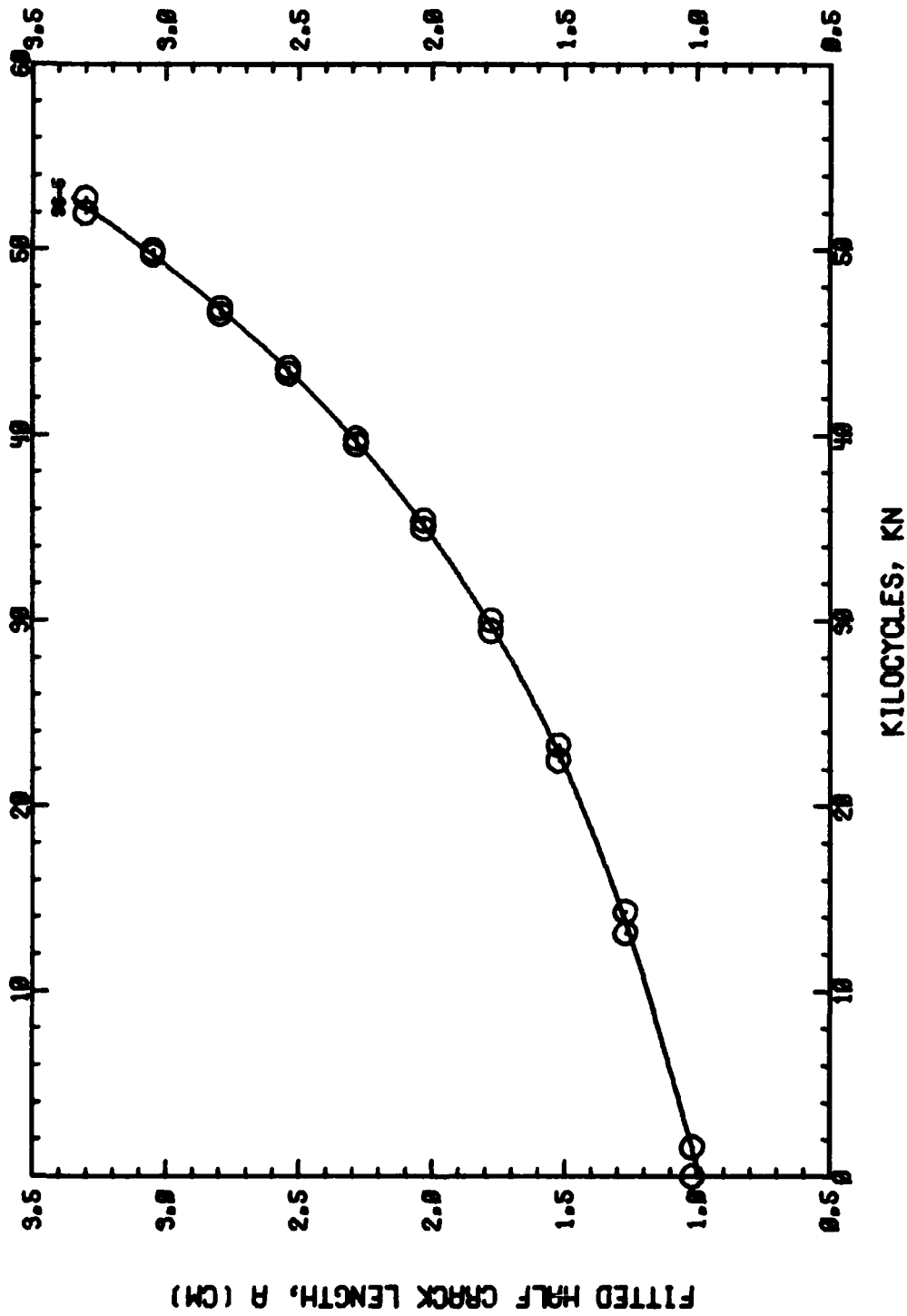
Figure A22. Crack length versus cycles for blended powder high z extrusion tested in humid air.



KILOCYCLES, KN

S-356455-50

Figure A23. Crack length versus cycles for blended powder medium Z extrusion tested in humid air.



S-356455-6G

Figure A24. Crack length versus cycles for blended powder low Z extrusion tested in humid air.